FUNDAMENTAL CHARACTERISATION OF THERMAL INFLUENCE IN HOT MIX ASPHALT REPAIR

A thesis submitted for the degree of Doctor of Philosophy

by

Juliana Byzyka

Department of Civil and Environmental Engineering, Brunel University London

December 2018

To

My husband & our baby

Mum

&

Dad

Abstract

The study focuses on the issue of hot mix asphalt pothole repairs, the performance of which is greatly reduced by repair edge disintegration. This is caused by low interface temperatures which result in low density interfaces and poor repair bonding. The study examined heat flow in shallow and deep pothole excavations under controlled pre-heating done in heating-cooling cycles, referred as "dynamic heating", and the effect of asphalt thermal properties on this. Dynamic heating was applied with an experimental infrared heater operating between 6.6 kW and 7.7 kW heat power and with the heater being stationary or moving above simulated potholes at offsets of 130 mm and 230 mm. The study also examined heat flow in traditional non-heated shallow repairs, referred as "static repairs", and dynamic shallow repairs and the effect of pothole pre-heating in repair adhesion. Finite Element modelling was also used to enhance understanding of heat flow in the executed repairs. Then, the bonding properties and rutting resistance of the repairs were assessed using shear bond tests (SBT's) and wheel track tests (WTT's) respectively. The results showed that irrespective of excavation depth, heating power and heater offset, temperature distribution in the pothole excavation and inside the slabs under dynamic heat was non-uniform. Dynamically heating pothole excavations for approximately 10 minutes yields better heat distribution than 20 minutes heating time while minimising the possibility of asphalt overheating. The temperature profile at the interface of the dynamically heated repair is improved when compared to static repair suggesting better interface adhesion. A significant role in this profile is played by thermal contact conductance which determines the resistance to pavement-repair thermal conduction per unit area at the repair interface. This was reflected in the assessment and simulation of the repairs with the latter generating reasonable transient temperature profiles within the dynamically heated pothole excavation, at the interface of the repairs, and inside the host pavement. Further, the shear strength at the bottom and side interfaces of dynamically heated repairs was 78.2% and 68.4% higher respectively than that of static repairs. On average, static and dynamic repairs showed repair interface rutting depths of 14.82 mm and 10.36 mm respectively. It was concluded that dynamically heating a pothole excavation increases repair interface adhesion and repair durability.

Publications

1. Byzyka, J., Rahman, M. and Chamberlain, D. A. (2019) 'Thermal influence in the performance of static and dynamic hot mix asphalt pothole repairs', the *98th Transportation Research Board Annual Meeting.* Washington, D.C., 8-12 January. <u>In press</u>. (Chapter 8)

2. Byzyka, J., Rahman, M. and Chamberlain, D. A. (2019) 'Experimental investigation of temperature distribution in non - heated and pre - heated hot mix asphalt patch repair', *7th International Conference in Bituminous Mixtures and Pavements*. Thessaloniki, 12-14 June. <u>In press.</u> (Chapter 6)

3. Byzyka, J., Rahman, M. and Chamberlain, D. A. (2018) 'An innovative asphalt patch repair pre-heating method using dynamic heating', *Construction and Building Materials*, 188, pp. 178-197. (Chapter 4)

4. Byzyka, J., Rahman, M. and Chamberlain, D. A. (2018) 'An improved interface temperature distribution in shallow hot mix asphalt patch repair using dynamic heating', *International Journal of Pavement Engineering*. <u>In press.</u> (Chapter 6)

5. Byzyka, J., Rahman, M. and Chamberlain, D. A. (2018) 'Thermal analysis of hot mix asphalt pothole repair by finite element method', submitted for publication at the Journal of Transportation Engineering, Part B: Pavements. <u>Under review</u>. (Chapter 7)

6. Byzyka, J., Chamberlain, D. A. and Rahman, M. (2017) 'A novel control pothole repair system using radiant heat for long lasting patch repairs', *the 96th Transportation Research Board Annual Meeting*. Washington D.C., 8-12 January. (Chapter 3)

7. Byzyka, J., Rahman, M. and Chamberlain, D. A. (2017) 'A three-dimensional finite element analysis of temperature distribution in hot mix asphalt pothole repair', *the 10th International Conference on the Bearing Capacity of Roads, Railways and Airfields.* Athens, 28-30 June.

8. Byzyka, J., Chamberlain, D.A. & Rahman, M. (2017) 'Development of advanced temperature distribution model in hot - mix asphalt patch repair', *Proceedings of the Institution of Civil Engineers-Transport*, pp. 1-11. (Chapter 3)

9. Byzyka, J., Rahman, M. and Chamberlain, D. A. (2017) 'Thermal segregation of asphalt material in road repair', *Journal of Traffic and Transportation Engineering (English Edition)*, 4(4), pp. 360-371.

10. Byzyka, J., Rahman, M. and Chamberlain, D. A. (2016) 'Thermal segregation of asphalt material in road repair', *the 8th International Conference Maintenance and Rehabilitation of Pavements*. Singapore, 27-29 July. <u>Paper received Best Paper Award</u>.

Acknowledgements

Many thanks to friends and family for believing in me. To my godmother for always having that extra hug for me.

To my husband for his love, support and patience and our baby who we are looking forward to meeting in a few months. To mum for her continuous encouragement and strength. This accomplishment would not have been possible without you both.

To dad – you are very missed.

Declaration

I declare that this Thesis was carried out in accordance with the requirements of the University's Regulations and Code of Practice for Research Programs and that it has not been submitted for any other academic award. Except where indicated by specific reference in the text, this work is my own work. Work done in collaboration with, or with the assistance of others, is indicated as such. I have identified all material in this report which is not my own work through appropriate referencing and acknowledgement. Where I have quoted or otherwise incorporated material which is the work of others, I have included the source in the references. Any views expressed in the Thesis, other than referenced material, are those of the author.

Juliana Byzyka
Brunel University London
December 2018

Contents

Table of figures

Table of tables

Chapter 1

Introduction

This chapter introduces the research background, aims and objectives of the research, the research methodology and the layout of the Thesis. The tasks conducted in order to achieve the research objectives are also described.

1.1   Research background

Asphalt is a material bound with bitumen as a binding agent. It consists of aggregate, bitumen and air voids with aggregate making 94% to 95% of hot mix asphalt mass (Prowell, Zhang and Brown, 2005). Although an asphalt pavement can expand and contract under temperature variations and movement, it still deteriorates. The main causes of pavement distresses are repeated traffic loading, environmental conditions, asphalt ageing, week subgrade and poor pavement structure (Walker, 1984; Mfinanga, Ochiai and Yasufuku, 1996; Chatti, Salama and Mohtar, 2004; Lesueur and Youtcheff, 2013). Typical failure modes are cracking, rutting, ravelling and potholing (Adlinge and Gupta, 2013).

In addition to traffic and temperature related damage, exposure to water causes aggregate dislodging, stripping and ravelling. Ravelling results from water infiltration into the pavement which weakens the mastic and the mastic-aggregate bond. Repeated traffic loading and water action leads to initial stripping, severe ravelling and then to potholing (Dawson, 2008). Therefore, many potholes usually appear after wet weather conditions and are dramatically increased after freezing and thawing cycles (Lavin, 2003). Potholes are well known for causing traffic disruptions and accidents to road users.

Over recent years, the use of high-quality materials, that will protect the surface layer of an asphalt pavement from weather conditions and high traffic loading, have been tried (Texas Department of Transportation, 2011). However, increasing traffic volumes and heavier loads, allied to repeated adverse weather are causing significant deterioration of the UK road network, resulting in millions of potholes and failed areas (i.e cracking, stripping, and ravelling). The Automobile Association (AA) survey, in which more than 22,000 people participated, revealed

that 33% of participants have confronted damage to their vehicles due to potholes on roads. In 2013, the number of potholes, which has grown with the passage of the years, was found to have increased up to 30% compared to the start of 2012 (Knapman, 2013).

According to the AA report in 2014, road deterioration in the UK had risen by 40% by March 2014 in comparison with October 2013 figures (The Automobile Association (AA), 2016). In 2015, the annual local authority road maintenance (ALARM) survey reported that 2.67 million potholes were filled in England and Wales (Asphalt Industry Alliance, 2015). Between 2015 and 2018, the number of potholes filled dropped to 1.17 million. However, a quick repair is undoubtedly going to fail prematurely. The situation becomes worse when the 2018 ALARM report states that more than 38,600 km of local road will need to be repaired in 2018/19 (Asphalt Industry Alliance, 2018). The poor riding condition of UK roads has generated significant public dissatisfaction as road distress not only creates dangerous driving conditions but also high repair bills for their vehicles.

Usually, the reasons for premature pothole repair failure are because (a) the patching material is laid on failed areas and it is likely that the underlying materials are in poor condition, (b) the quality of the repairs offered by the contractor differs as the skill levels of the teams responsible for the repairs varies, and (c) fast cooling is observed at the edges of the repair due to cold underlying asphalt layer resulting in low density interfaces and weak points prone to premature failure. Other reasons that confirm the failure of road maintenance are the lack of technical quality due to a lack of established guidelines or test methods, inadequate compaction, poor surface preparation and overall inferior workmanship, as well as the lack of appropriate guidelines for maintenance engineers on materials suitability in every patch repair situation.

Heating the underlying layer, prior to pothole filling and compaction, could possibly enhance the bonding between the cold host pavement and the new hot-fill mix, decrease early edge disintegration and repair failure and increase overall repair life, decrease repetitions of patching and costs in labour, equipment, traffic control and long disruption times (Nazzal, Kim and Abbas, 2014). Infrared, microwave or induction heating systems are used for this purpose and have been studied by other researchers such as Clyne, Johnson and Worel (2010), Uzarowski et *al.* (2011), Freeman and Epps (2012), Leininger (2015) and Obaidi, Gomez-Meijide and Garcia (2017).

Infrared technology has been used in pothole repair operations and repair of asphalt cracks for more than thirty years, although not reported under controlled conditions. The effect of thermal properties of asphalt mixtures in the heating process has not been considered nor the influence of other parameters such as pothole geometry, environmental conditions and temperatures achieved within the repair build. In addition, temperatures at the repair interfaces of current repair practices have not been yet examined and correlated to repair failure. Further, heat flow in asphalt pavement under infrared heat and during repair activity by also not previously been reported.

1.2   Research objectives

The study aims to derive and evaluate a controlled pre-heated repair method through full scale experimentation, scientifically based materials, construction, application and parametric modelling for durable hot mix asphalt (HMA) pothole repair. The research program was divided into four areas: firstly, a patented experimental infrared heater was studied and its operation was investigated in empty pothole excavations of various depths to determine optimum pothole pre-heating methods; secondly, non-heated and infrared heated pothole repairs were executed using the optimum pre-heating methods, temperatures at the repair interfaces were quantified, and HMA thermal properties were studied to understand heat flow in the repairs; thirdly, pothole repairs were simulated using the finite element method to further understand how temperatures are distributed in pothole repairs; fourthly, non-heated and pre-heated pothole repair interface strength and durability to failure was assessed.

The objectives of the research are:

1. Comprehensive literature review on asphalt pavement failures, current asphalt repair activities in terms of materials, methods, life cycle and parametric modelling;
2. Design and execute a detailed laboratory experimental programme to develop an optimum infrared heating method by a controlled infrared heater at the interfaces of shallow and deep pothole excavations in HMA pavement;
3. Develop an accurate temperature distribution profile in a pothole repair in an HMA pavement;
4. Investigate the influence of thermal parameters such as thermal conductivity, thermal diffusivity, thermal radiation and specific heat capacity in HMA repair;

5. Develop a transient thermal parametric HMA repair model with appropriate parametric options and calibrate against an experimental study;

6. Investigate the influence of the dynamic operation of the infrared heater for optimum repair performance.

1.3   Research methodology and outline

To achieve the six individual research objectives, the tasks of Figure 1.1 were undertaken. The tasks are described in detail below the figure and their position within the Thesis is outlined.
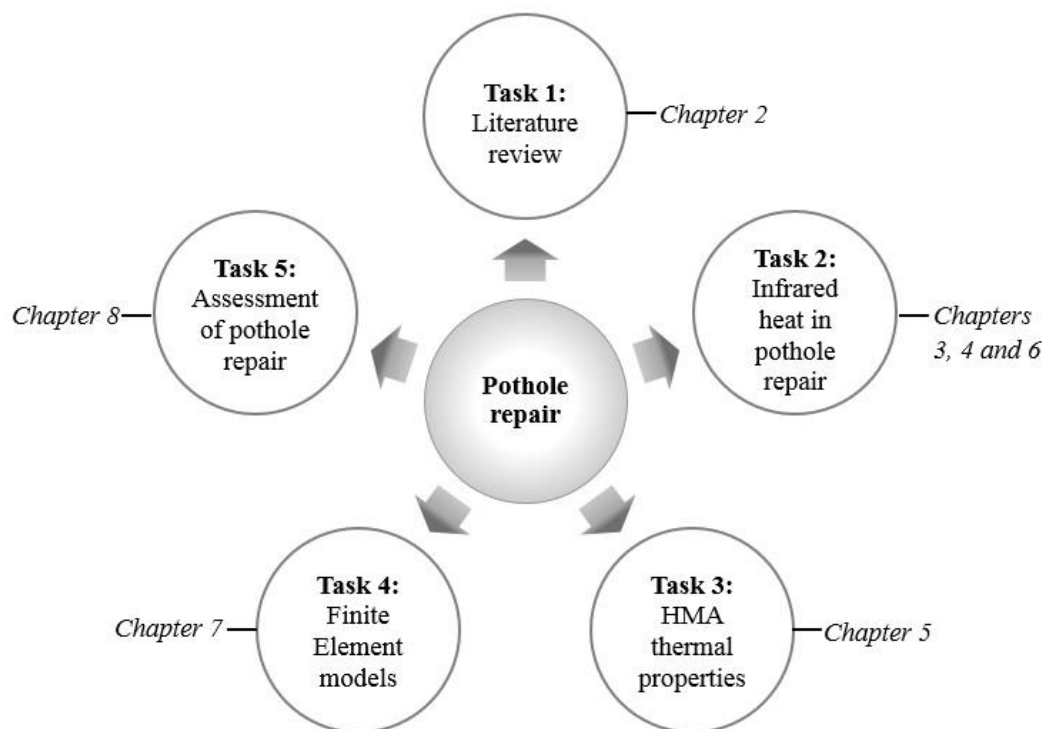
Figure 1.1 Research methodology tasks

Task 1: Literature review (*Chapter 2*)

a) Complete a review of general background of asphalt, pavement structures and deteriorations of asphalt pavements

b) Review of existing pothole repair methods

c) Identify parameters affecting pothole repair performance and durability

d) Identify the gaps in the literature

e) Establish testing methods and British or International Standards for thermal conductivity measurements for a range of asphalt pavement materials

f) Determine testing methods and British or International Standards for quantifying and comparing the performance of pothole repairs

g) Determine simulation of pothole repairs by three-dimensional (3D) thermal Finite Element (FE) modelling

From b and c, the gap in knowledge was identified.

Task 2: Infrared heat in pothole repair (*Chapters 3, 4 and 6*)

a) Study the operation, temperature and heat power outputs of an experimental infrared heater (*Chapter 3*)

b) Simulate pre-heated pothole excavations of various depths in the laboratory to identify temperature feedback controls within the repair build, mainly using extractable thermocouples. The analysis includes 45 mm, 75 mm and 100 mm deep pothole excavations designed in HMA slabs (*Chapter 4*)

c) Simulate non-heated and pre-heated pothole repairs in the laboratory to quantify temperatures at the repair interfaces using extractable thermocouples. The analysis is done only in 45 mm deep pothole repairs constructed in HMA slabs (*Chapter 6*)

Task 3: HMA thermal properties (*Chapter 5*)

Complete measurements of thermal conductivity and calculation of capacitance parameters for a range of asphalt mixtures that were also used to perform laboratory experiments described in Chapters 4 and 6. Thermal conductivity measurements are done at room and elevated temperatures in order to use the results to calibrate the pothole repair simulation models of the research.

Task 4: Finite element models (*Chapter 7*)

Develop 3D FE modelling of pothole repairs to gain understanding of internal temperature response to applied infrared heating and those of non-heated repairs in relation to experimental work.

Task 5: Assessment of pothole repairs (*Chapter 8*)

Complete and evaluate pothole repairs by both traditional patching (non-heated pothole repair) and pre-heated patching methods determined from the research. The selected tests are shear bond test and immersion wheel tracking test.

Chapter 2

Literature review

In this chapter, asphalt pavement is initially introduced and parameters causing pavement failures are identified. Then, the pothole, the major asphalt pavement failure mode that this research is concerned about, is discussed in terms of pothole repair methods, failure mechanisms and parameters affecting repair durability. Since debonding emerges from the literature as a major pothole repair failure mechanism, heating technologies are reviewed that may be used in the repair operations and increase repair adhesion. Radiative heat flow in asphalt pavement is then introduced followed by a review of simulation modelling that helps to identify basic principles and parameters for the thermal behaviour of asphalt in pre-heated pothole repairs. The chapter ends by addressing the gap in the literature that motivated this research. Figure 2.1 below shows the organisation of this chapter. The chapter aims to address the first objective of the research.
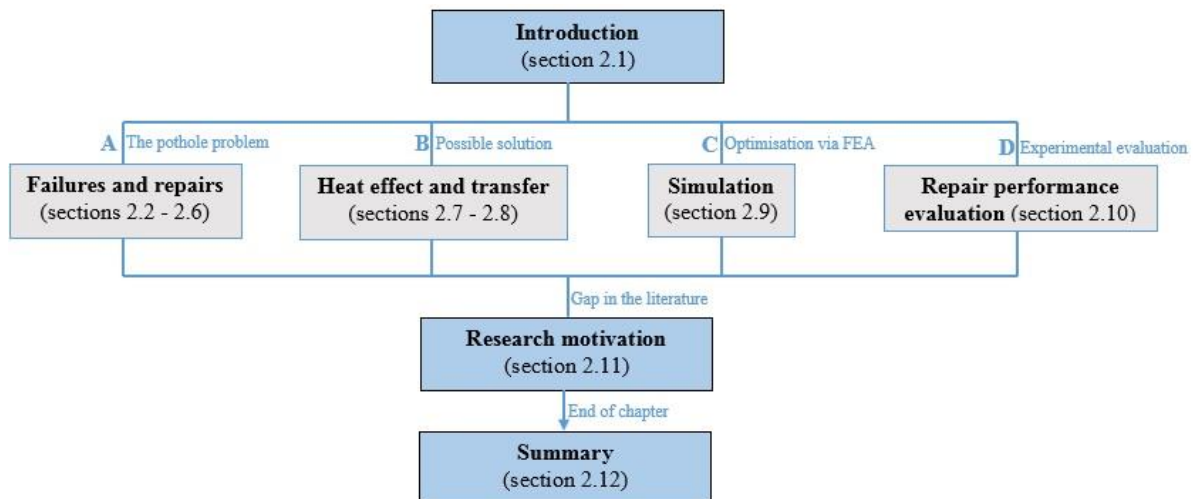
Figure 2.1 Literature review chapter flow chart

2.1   Introduction

Pavements constitute an important asset of developed countries such as the UK. They contribute to the economic and social well-being at all levels. Pavements are widely divided in to flexible (asphalt based structure), rigid (concrete based structure) and composite pavements. In the UK, 95% of the road network is asphalt pavement. The role of the asphalt pavement is to successfully facilitate traffic loading and distribute this to the subgrade without causing significant deformation to the soil. It should also be less permeable to water ingress, offer skid resistance, resistance to tire polishing and smooth riding to the road users (Nikolaides, 2014). A typical asphalt pavement consists of, starting from top to bottom, the surface or wearing course, binder course, base, sub-base, capping layer and subgrade (Thom, 2008). Figure 2.2 shows low and high volume asphalt pavement profiles.

Thin asphaltic 'chip-seal' (<30 mm)

Unbound aggregate layer(s)
= Base & Sub-base

Natural or imported (fill) subgrade

(a)

Asphaltic
surfacing & base layers

Unbound aggregate Sub-base

Soil improvement layer (capping)

Natural or imported (fill) subgrade

(b)
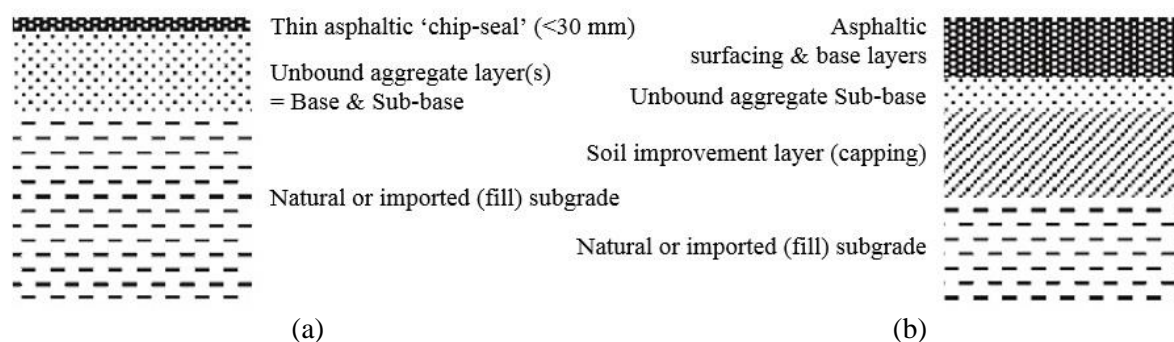
Figure 2.2 Asphalt pavement layer distribution: (a) low volume; (b) higher volume (Dawson, 2008, p.6, image has been modified to standardised font)

The subgrade is the natural soil. It is composed of heavy clays, silts, sands and rock mixtures. The strength of the pavement is considerably affected by the strength of the soil defined by its stiffness and resistance to deforming under repeated traffic loading. The same parameters determine the strength of granular materials. The capping, sub-base and base layers consist of granular materials such as gravel, crushed rock and granulated industrial by-products or hydraulically bound materials made of aggregate or soil mixed with a binding agent such as Portland cement or fly ash and water. Hydraulically bound materials are characterised by their stiffness, tensile strength and fatigue resistance. The base course may also be of asphalt which is the material of the binder and surface courses (Thom, 2008).

2.2   Parameters causing failure to asphalt pavement

Asphalt pavement deteriorates due to individual factors or a combination of them. These factors are traffic loading, climate, bitumen ageing (Walker, 1984; Mfinanga et al., 1996; Adlinge and Gupta, 2013; Lesueur and Youtcheff, 2013; Chatti, Salama and El Mohtar, 2004), weak subgrade and poor pavement construction practices (Adlinge and Gupta, 2013). Well known failures are fatigue or alligator cracking; thermal or transverse cracking; longitudinal cracking; block cracking; reflective cracking; slippage cracking; rutting; shoving; corrugation; depression; overlay bumps; ravelling or stripping; and potholes; all shown in Figure 2.3.

2.2.1 Effect of traffic loading

Under the wheel load, pavement deteriorates due to deflection or bending caused in the surface course (Figure 2.4). As the pavement bends, the upper part of the surface course is compressed, and the lower part is stretched. Repeated bending leads eventually to fatigue cracking and failure of the pavement (Walker, 1984; Lesueur and Youtcheff, 2013). The greater the axle load and its number of repetitions, the higher the deflection of the pavement and the shorter its lifespan. To protect the pavement from axle loads both surface and base courses have a significant role. The surface course must be strong or thick enough to endure wheel induced stresses. The base course is dual role is to successfully distribute the wheel load into the subgrade without damaging it and protect the pavement against moisture damage (Walker, 1984). Pavement deteriorations due to traffic are fatigue cracking, rutting, loss of skid resistance, bleeding, block and reflective cracking and others (Lesueur and Youtcheff, 2013).

2.2.2 Effect of climate

Air temperature and rainfall significantly affect the performance of asphalt pavement. The temperature influences the creep properties of the asphalt, the thermally induced stresses, the low-temperature cracking, the fatigue cracking, the rutting and the performance of the subgrade. The effect of air temperature on the soil is significant during freeze-thaw cycles (Mfinanga et *al*., 1996). The dramatic effect of rainfall in the asphalt and the underlying soil layer is seen when water penetrates the pavement through top-down or bottom-up cracks (Dawson, 2008). Moisture damages the bonding of the asphalt, reduces the strength of the soil and decreases the support of the pavement causing alligator cracking, stripping, rutting (Mfinanga et *al*., 1996; Adlinge and Gupta, 2013), flushing and potholing (Lesueur and Youtcheff, 2013).

Fatigue or alligator cracking
(Shatnawi, 2008, p.1-8)

Thermal or transverse cracking
(Uxbridge, London, UK 2016)

Longitudinal cracking
(Uxbridge, London, UK
2016)

Block cracking
(Uxbridge, London, UK 2016)

Reflective cracking
(Shatnawi, 2008, p.1-8)

Slippage cracking
(Washington Asphalt
Pavement Association, 2018)
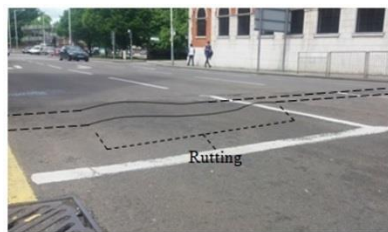
Rutting
(Uxbridge, London, UK 2016)

Shoving
(Pavement Interactive, 2018a)

Corrugation
(Pavement Interactive, 2018a)

Depression
(Pavement Interactive, 2018b)

Overlay bump
(Shatnawi, 2008, p.1-11)

Ravelling or stripping
(Uxbridge, London, UK
2016)

Pothole
(Uxbridge, London, UK 2016)

Figure 2.3 Asphalt pavement failures (photos are author's own unless otherwise stated)
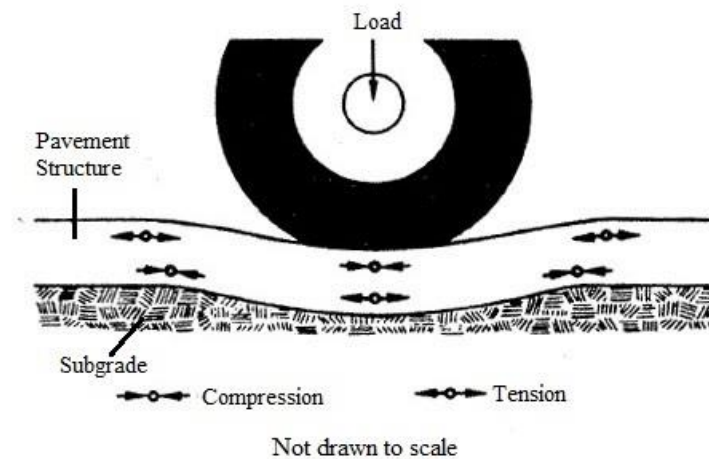
Figure 2.4 Impact of repeated traffic loading in asphalt pavement (Walker, 1984, p.1)

2.2.3 Effect of bitumen ageing

Bitumen chemical composition changes with time and reduces the performance of asphalt pavement. The first effect of this chemical change is short-term and long-term ageing (Thom, 2008; Lesueur and Youtcheff, 2013). The second effect is bitumen absorption by the aggregates (Thom, 2008). Short-term ageing of bitumen happens during mixing, transporting and compaction. whereas, long-term ageing occurs during the service life of the pavement. As a result, asphalt becomes vulnerable, it cracks and eventually fails (Thom, 2008; Lesueur and Youtcheff, 2013). Common failures are stripping, accelerated ageing and cracking (Lee et *al.*, 1990).

2.2.4 Effect of subgrade strength

The performance of asphalt pavement is significantly reduced by poor subgrade (Adlinge and Gupta, 2013). Soil must be prepared to endure traffic loading during the lifecycle of the pavement. If neglected, the pavement fails, and fatigue cracking appears on pavement surface course.

2.2.5 Effect of construction quality

Poor construction work in terms of material quality, layer thickness, compacting equipment and moisture ingress during construction also lead to pavement failure. Well known distresses are cracking, distortion, disintegration and loss of skid resistance (Roberts et *al.*, 1991; Shatnawi, 2008; Nikolaides, 2014).

One result of the described failures from traffic loading, climate, bitumen ageing, subgrade strength and construction quality is the pothole. This is shown in Figure 2.5 and further discussed in the following section.
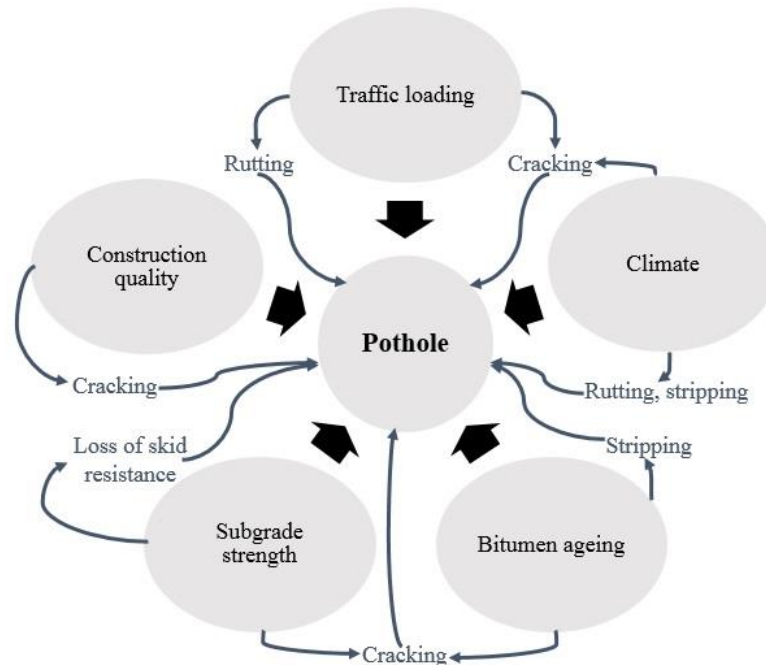
Figure 2.5 The pothole problem

2.3   Potholes

Even though the asphaltic surfacing of an asphalt pavement is designed to be a less permeable layer compared to the other layers of the pavement (sub-base, capping and subgrade), water does permeate into it. The ingress of water into the pavement and repeated traffic loading deteriorate the mastic and the aggregate mastic-bond of the asphalt causing initially stripping which develops into severe ravelling and then to the creation of potholes (Dawson, 2008; Thom, 2008; Adlinge and Gupta, 2013).

Potholes appear in the form of small or large bowl-shaped holes on the pavement surface (Shatnawi, 2008; Lavin, 2003). Prolonged cold wet weather on periods with cyclic freeze-thaw conditions, such as occur in the UK, accelerate pothole development, (Lavin, 2003; Thom, 2008) cause high maintenance costs and generate significant public dissatisfaction (Thom, 2008) as road distress not only creates dangerous driving conditions but also high repair bills for vehicles. Figure 2.6 shows the sequence of a pothole formation.

(i)   Stage 1   Water is forced into a cracked pavement

(ii)   Stage 2   Water travels along the interface between the asphalt (AC) and the compacted aggregate base

(iii) Stage 3   Asphalt lifts to allow pressure to dissipate, but also allows more water to be pumped into the crack

(iv)   Stage 4   Asphalt is dislodged due to traffic action and water pressure
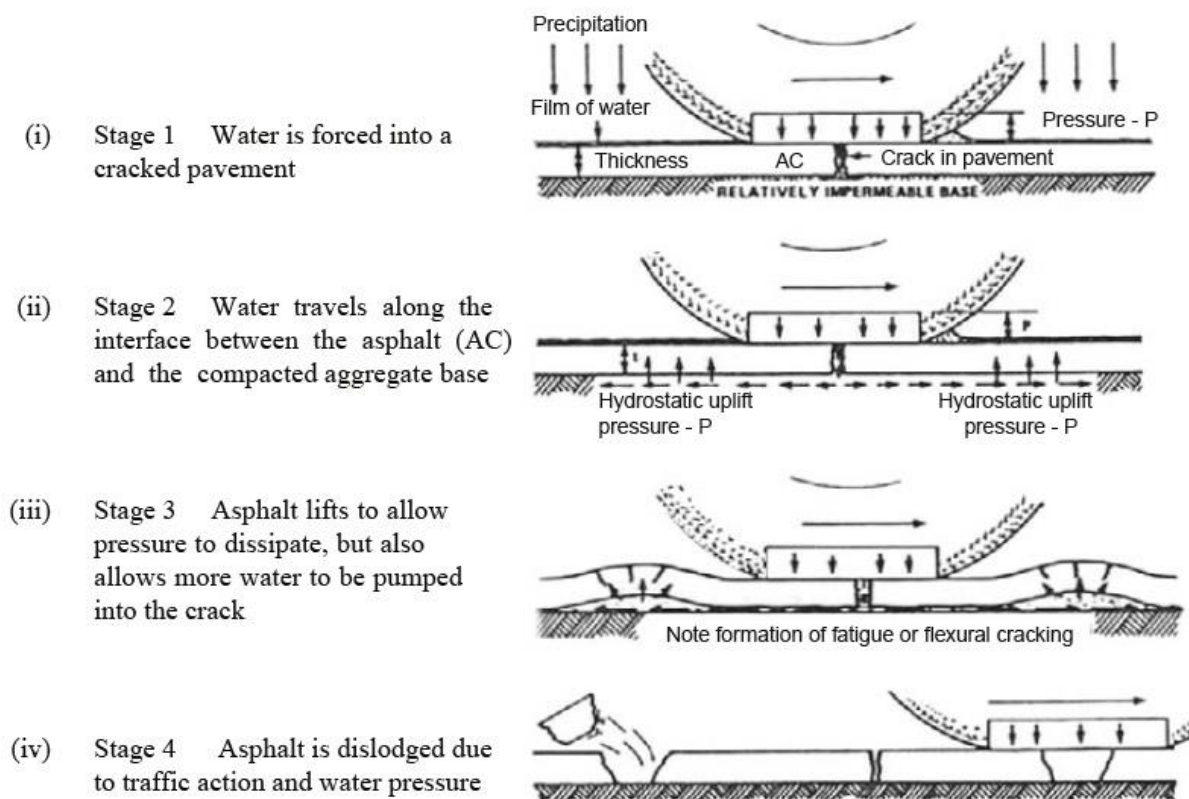
Figure 2.6 Developmental pothole (Greke, 1979, cited in Dawson, 2008, p.180)

2.4   Pothole repairs

Common repair methods are pothole filling and patching. Pothole filling is performed as an emergency repair using cold asphalt mixes, mainly during winter. Well known pothole filling methods are: "throw and go", "throw and roll", semi-permanent and injection. Conversely, patching is a permanent repair and is used to repair, as well as potholes, alligator cracking, depression, rutting, corrugations and slippage cracking (Lavin, 2003). HMA is mainly used in patching.

2.4.1 Temporary repairs

"Throw and go" is a simple and fast repair process. It is mainly done during the cool months of the year. The material is simply thrown into the hole and allowed to be compacted by the passing vehicles. Cold asphalt or stockpile mixtures are used to fill the holes which are not cleaned or dried prior to filling it with asphalt. "Throw and roll" is similar to throw and go. The difference between the two processes is that the compaction of the fill mixture for the throw and roll method is done by the dump truck that transports the fill material at the repair site (Figure 2.7(a)). Therefore, the "throw and roll" repair method is likely to be more durable than

the throw and go repair. However, both methods aim to just quickly fill the pothole and reduce the risks of road accidents due to pavement failure until a permanent repair is planned and executed (Lavin, 2003).

Spray injection is a pothole repair method performed during cold weather. The patching material is either cold asphalt or stockpile mixture. The repair starts by cleaning the pothole from loose material, debris and water. Then, tack coat is applied and the patching material is injected into the pothole with high pressure (Lavin, 2003; Kwon et *al.*, 2018) (Figure 2.7(b)).

| (a) | (b) |

Figure 2.7 (a) Throw and roll; (b) Spray injection repair methods (McDaniel et *al.*, 2014, (a) p.6 and (b) p.7, label added by author)

Semi-permanent repair is a durable temporary repair method due to better adhesion of the fill material with the old pavement as opposed to "throw and go" and "throw and roll" methods. The semi-permanent method is preferred during mild weather conditions. The repair starts by cutting and cleaning the failed pavement (Lavin, 2003) at a distance from the pothole 0.3 m approximately (Washington State Department of Transportation, 2017). The sides are squared to help the fill material to adhere to the existing layer of old asphalt. Then, the hole is filled with the patching material and compacted with small and manually controlled rollers or vibrating plates (Lavin, 2003; Thom 2008; Washington State Department of Transportation 2017). The patching material is either a dense graded or fine graded HMA (Lavin, 2003).

2.4.2 Permanent repair (patching)

The process of patching (or else patch repair) is similar to the semi-permanent repair method. However, in this method, if the failure of the pavement has reached the base or subgrade courses, then all the distressed portion of the pavement is removed and rebuilt. The patching material is dense or fine graded HMA to ensure adequate stiffness and repair durability in contrast with cold mix asphalt. A major difficulty when using HMA as a patching material is to complete compaction prior to the mixture reaching 75 ºC to 80 ºC (Delgadillo and Bahia, 2008; West et *al*., 2010). If this cannot be avoided, then, the result is low dense repair prone to premature failure. Figure 2.8 shows the repair of a large area. For smaller repairs, the steps described in Figure 2.8 are usually done with manually controlled equipment.

2.5   **Parameters causing failure to patch repair**

In traditional repair methods, the repair material is transported hot from the mixing plant to the repair site. Depending on the method of transport, distance to the site and climatic conditions, the temperature of the fill material when placed may be close to or below that required to form a durable repair. The reason is that thermal segregation is initiated (Lavin, 2003; Thom, 2008; McDaniel et *al*., 2014; Washington State Department of Transportation, 2017), which impacts on repair compaction quality (British Standards Institution, 2015a) and bonding of the repair with the host pavement. The geometry of the excavated pothole and the application or not of a tack coat at the faces of the excavation also affect the repair adhesion with the underlying asphalt (Thom, 2008). Thus, five parameters affecting patch repair durability emerge; all of these are shown in Figure 2.9 and further discussed in sections 2.5.1 – 2.5.5.

2.5.1 Effect of transportation

The transportation method of HMA for a repair operation or road construction is vital for securing the quality of the mixture. Usually, the asphalt material is prepared at the asphalt production plant and then by using an appropriate vehicle is transported to the paving site. It is during this stage where a great amount of aggregate and thermal segregation is detected in asphalt (Bode, 2012). There are three usual types of vehicle for transporting asphalt named as end dump, bottom dump or belly dump, and live bottom or flo-boy (Roberts et *al*., 1991; US Army Corps of Engineers, 2000). The design of the trucks is aimed to maintain asphalt temperature and properties from the time that is received at the production plant to its arrival at the repair site. Therefore, the way that the material is dropped in the transportation vehicle has a huge impact on the extent of aggregate segregation. Dropping the material onto the

vehicle in one batch is less preferred than in smaller masses. Further, the truck bed should be cleaned and lubricated to maintain the properties of the mixture and it should be insulated and covered to help maintain the asphalt temperature (Huerne, 2004).
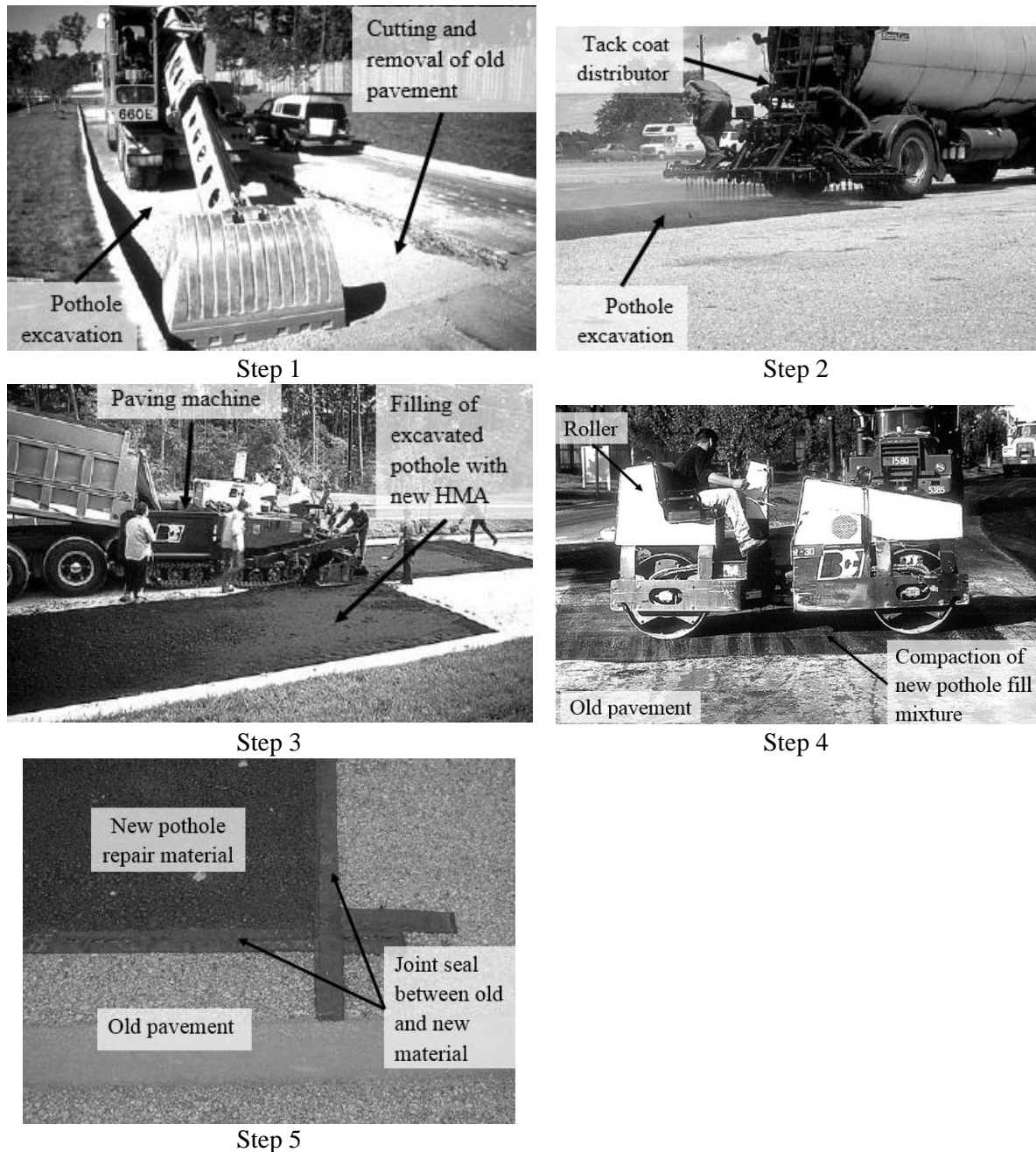
Figure 2.8 Permanent repair method (steps 1-4 from US Army Corps of Engineers (2000, p.123, 126, 123, 124 respectively) and step 5 from McDaniel et *al*. (2014, p.7), label added by author)
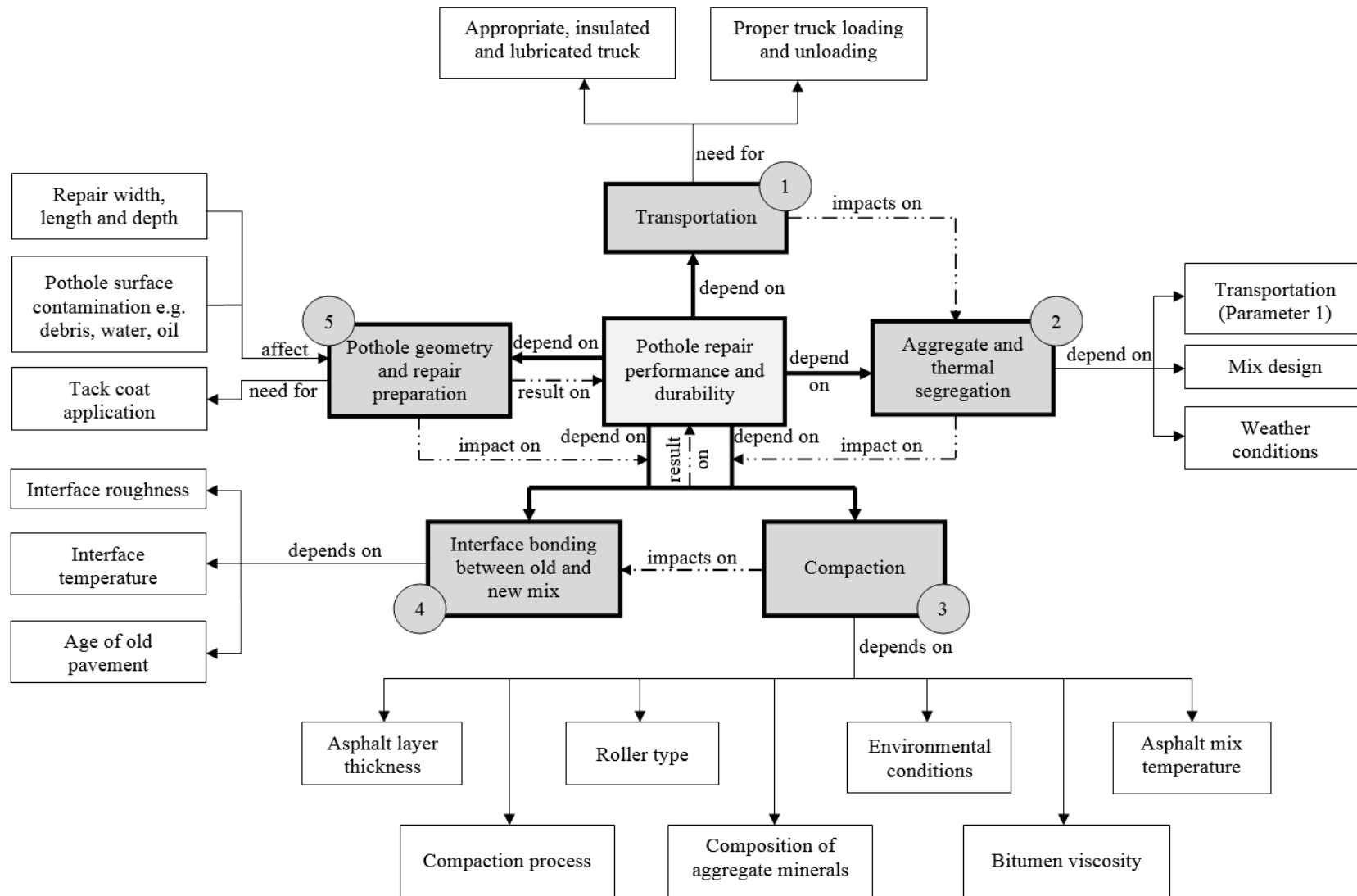
Figure 2.9 Parameters affecting patch repair performance due to repair process inadequacy

2.5.2 Effect of segregation

The term segregation includes both temperature segregation and gradation segregation. Stroup-Gardener and Brown (2000) refer to also a third type of segregation that mainly appears in stone matrix asphalt (SMA) mixes and is named as aggregate-asphalt segregation. Among gradation and thermal segregation, the first term is defined as non-uniform distribution of coarse and fine aggregates in the asphalt matrix whilst the second term is referred to as the existence of temperature differentiations or else known as cold spots in the asphalt mix surface (Stroup-Gardener and Brown, 2000).

Gradation segregation may be visually identified or by using sand patch testing (National Asphalt Pavement Association, American Association of State Highway and Transportation Officials, 1997) and nuclear density gauges (British Standards Institution, 1990). Thermal segregation can be identified using thermal imaging (Rahman et *al.*, 2013), ground-penetrating radar, nuclear or density gauges, laser surface texture measurements and the seismic pavement analyser (Stroup-Gardener and Brown, 2000).

Thermal segregation occurs throughout (a) HMA transportation between asphalt plant and repair sites, (b) placement of the material in the pothole void and (c) compaction of the placed material. The influence of thermal segregation during completion of these three steps is that inadequate compaction and weak interface bonding between new and old asphalt mix may occur (Byzyka, Rahman and Chamberlain, 2017b).

2.5.3 Effect of compaction

Compaction is the process of asphalt mix densification or change in volume. It is affected by previous stages in the patch repair process and constitutes a significant factor in achieving strong repairs in terms of surface smoothness (Huerne, 2004) and repair durability. Surface smoothness relates to achieving road users' satisfaction. Durability is linked to reducing the number of repetitions of completed repairs and reducing repair costs.

The process of compaction, thickness of asphalt layers, roller type, environmental conditions, composition of the aggregate minerals, viscosity of the bitumen, and the temperature of the asphalt mix highly affect compaction. The composition of the asphalt mix, on the other hand, is substantially related to the pavement traffic loading that the asphalt pavement structure is constructed for and the weather conditions that the asphalt mix is composed for. Proper

compaction offers high bonding between bitumen and aggregate, high friction between aggregate particles and therefore high density. A strong mix with the described characteristics reduces asphalt pavement deformation (Hartman, Gilchrist and Walsh, 2001; Commuri and Zaman, 2008; Kassem et *al*., 2015). Common compacting equipment for new asphalt pavement are light roller machines, static compaction and others. In pothole repair, suitable compaction equipment are tampers, manually controlled vibratory plates and rollers (Thom, 2008; Kloubert, 2009).

2.5.4 Effect of adhesion formation

Failure in interface bonding has been reported for patch repairs (Nazzal, Kim and Abbas, 2014). The temperature difference between the existing asphalt pavement and new repair materials is significant, possibly creating a low strength interface that can easily start to lose mix in a few months of operation. This allows water to penetrate and further develop the repair failure. Other aspects that strong interface bonding relies on are interface roughness and host pavement age. The latter is included as pavement age has a direct relationship with the heating regime applied by the pothole repair system. Addressing the interface issue is not only important from a repair cost point of view but also being able to offer adequate riding conditions for road users. An issue that has attracted a number of researchers such as Freeman and Epps (2012); Nazzal, Kim and Abbas (2014); and Uzarowski et *al*., (2011) is the use of pre-heating of the pothole surface.

2.5.5 Effect of pothole geometry and preparation

The geometry and preparation of the repair excavation impact on compaction and interface bonding between repair fill mixture and host pavement. A lack of well-defined excavation geometry coupled with absence of an interbonding tack coat is commonly accepted to lead to reduced repair performance (Thom, 2008; McDaniel et *al*., 2014).

2.6   Patch repair failures

As discussed above, pothole repairs may fail due to overall low-quality repair construction. Common failures are bleeding, dishing, debonding, raveling, pushing and shoving (Anderson et *al*., 1988, cited in Rosales-Herrera, Prozzi and Prozzi, 2007, p.7); all identified below:

- Bleeding is an excessive film of binder at the surface of the pavement
- Dishing is settling of asphalt repair mixture due to poor compaction
- Debonding is lack of adhesion of repair mixture with host pavement

- Raveling means loss of material from fill mixture
- Pushing and shoving cause distortion of asphalt surface course due to asphalt displacement

Debonding is the main failure mechanism that concerns this study. Assuming that the pothole excavation has been properly cut, cleaned from debris and water and tack coat has been applied in the pothole excavation, the repair mixture may still not adhere with the host pavement due to fast cooling at the edges of the repair. This happens due to cold underlying asphalt layer during placement of hot-fill material, low temperature of fill mixture due to inappropriate transportation of HMA from the production plant to the repair site and cold weather resulting in low density repair interfaces and weak points prone to premature failure (Thom, 2008). Several heating technologies have emerged to avoid debonding named infrared, microwave and induction heating.

2.7   Infrared, microwave and induction heating in asphalt repair

Anderson and Thomas (1984) evaluated Pennsylvania's pothole repair practices due to high annual maintenance costs triggered by such repairs, repetitions of patching, excessive number of potholes and increased public dissatisfaction due to roads being in a poor state. The authors underline the importance of doing the repair right the first time and explain that such procedure should include: marking of the distressed area to be removed; cutting; creation of vertical sides, cleaning and tacking to help the new HMA to adhere with the host pavement; filling; compaction; and edge sealing to stop water ingress at the repair interface (although edge sealing not proven to respond well to such protection). The authors also refer to the use of infrared or radiant heat in pothole repairs. They suggest that the technology is typically used for repairing overlays, smoothing and blending utility cuts, and levelling of old patches. However, they do not recommend the use of infrared heat for full-depth repair.

Blaha (1993) built an automated patching machine (Figure 2.10) to create high quality repairs in terms of patching lifetime (this meaning repair quality and durability the same as the host pavement), patching costs, traffic disruption time, effective patching process that allows repairs throughout the entire year and productive heating time (this meaning low heating time to keep repair time to a minimum). The machine was designed with an infrared heating system to heat the surface of the failed asphalt only to its softening point and ensure high bonding between the new fill mixture and host pavement.
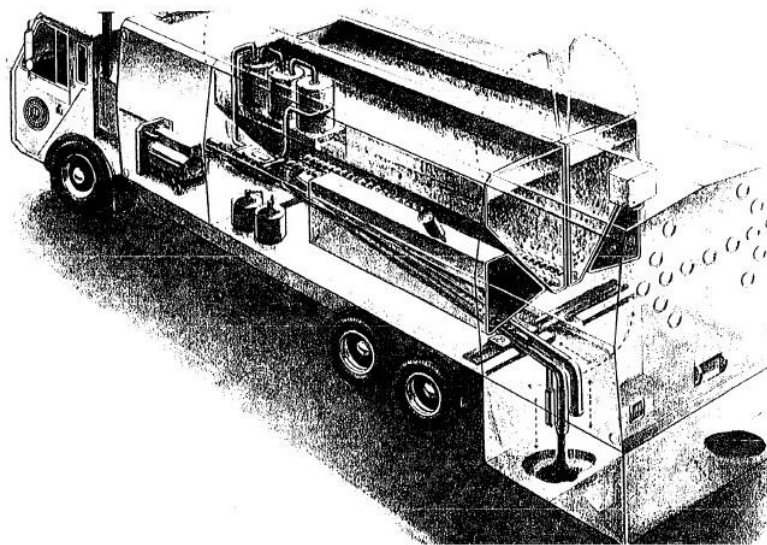
Patching machine component layout from front to back:

- Pavement cutter (hydraulic, joystick operated)
- Computer system in truck cab (dual processors, optical disk drive)
- Generator set (15 kW)
- Vacuum filtration system and waste hopper
- High volume, dual purpose blower
- Liquid propane gas tanks for heating system
- Dual hoppers for rock aggregate storage covered by doors
- Dual emulsion tanks for liquid asphalt emulsion storage
- Repair box enclosed area (doors unfold down to pavement level)
- Vision system cameras to view pavement (CCD and 3-D laser scanning)
- Robotic arm manipulator (moves the three tools below)
- Vacuum nozzle with extension to descend into hole
- **Hot air lance pavement heating system**
- Patching material dispensing nozzle

Figure 2.10 Pothole repair machine with a heating system built by Blaha (1993, p. 55 for the description of machine components and p.56 for machine image)

To integrate the heating system of the patching machine, the author needed to gather the following information: host pavement and air temperatures; asphalt thermal properties; asphalt heating time; and heater operating temperature to avoid overheating the asphalt. The author used thermocouples and a handheld infrared thermometer to monitor heat flow and external surface temperatures in asphalt samples respectively. However, the procedure of the experiments and the study of heat flow to determine productive use of the heating system in asphalt repair are unclear and roughly explained. The study jumps to the conclusion of 1 minute heating time for a surface asphalt softening point between 71 $^{\circ}$C and 82 $^{\circ}$C with the heater set to an extremely high heat power of 58 kW. To achieve such operation, microwave, electric heaters and air propane burners were examined.

Air propane burners had the advantage to heat a large area of asphalt by using multiple heating plates or moving the heater above the asphalt surface. However, the enclosure of such heaters prevented the author from measuring asphalt temperatures during heat application. A propane-fired lance was found to offer fast heating, controlled heating process and low operating and maintenance costs. The lance blast temperatures and its heat application on the asphalt surface were studied for 10 seconds and 14 seconds operating time respectively with the lance being

at an offset 450 mm from the asphalt. It was found that the temperatures at the centre area of the blast ranged from 49 ºC to 93 ºC and the asphalt temperatures were at 68 ºC.

Thom (2008) refers to the use of infrared heat (named as direct heating) for crack repair. For this kind of repair, the heater is put above the distressed area, then asphalt is heated to its softening point, scarified to blend with the new HMA and finally compacted. The author mentions the limitation of the system to heat asphalt up to 20 – 30 mm depth (this meaning possible treatment of surface course rutting, top-down cracking or ravelling but not deeper treatments) and that effective heating is achieved mainly when existing asphalt material is uniform.

Huang et *al*. (2010) and Williams (2011) investigated the use of infrared heat for decreasing longitudinal joint failures in asphalt pavement. The heater is shown in Figure 2.11. The longitudinal joint failure mechanism is similar to pothole repair interface failure. Joint failures happen due to high air void content in the joint, 5-10% higher than asphalt layers adjacent to the joint (Burati and Elzghbi, 1987; Khandal and Mallick, 1996 cited in Huang et *al*., 2010). High air voids mean easier penetration of water which accelerates bitumen oxidation and loss of volatiles and leads to premature failure of the longitudinal joint expressed as longitudinal cracking. This failure may happen within one year of pavement construction.

Figure 2.11 Heat Design Equipment, Inc. joint heater used in longitudinal joint adhesion by Huang et *al*. (2010) and Williams (2011) (images source Williams (2011, p.55), label added by author)

Huang et *al*. (2010) studied a field longitudinal joint project in Tennessee between lanes of HMA pavement with 12.5 mm aggregate size. The authors compared the effectiveness of the infrared heat method in terms of joint quality improvement against six longitudinal joint construction techniques prepared with joint adhesives and joint sealers. Air void content, permeability, indirect tensile strength tests, water absorption tests and x-ray scanning were employed to study the joint strength and air void joint distribution. The infrared heat method was done with a propane fired heater pre-heating the cold lane up to 121 ºC before placement of the hot lane.

The results showed that between the adjacent lanes to the joint, the first paved lane had higher air voids than the second paved lane due to unconfined state during compaction. If no joint technique was used then the air voids were the highest. Joint adhesives and sealers did not help in reducing air voids in the longitudinal joint area since they were used to increase the strength of the joint. However, the infrared joint method gave a denser joint, reduced the permeability coefficient along the joint and in nearby areas of asphalt and the indirect tensile strength was increased due to better compaction.

Further, the study gave a very interesting analysis of air void content along the depth of the longitudinal joint for infrared and control joint methods. High air voids were found for both methods near the surface. Between 5 mm and 20 mm depth in the joint area, the air voids for the infrared joint method decreased from 10% to 5% whereas, for the control joint method, air voids were found to range between 7% and 10%. At 23 mm depth, the air voids for the infrared joint method remained at 5% whereas for the control method they increased to approximately 11%.

Despite the extensive analysis of infrared joint construction method, the authors do not discuss the effect in the heating process of asphalt from air temperature, environmental conditions, asphalt thermal properties, heater offset from the asphalt, heater power operation, temperatures on heater plate, heating time and heat flow in the joint. With such analysis, effective heating procedures for longitudinal joint or general asphalt repair could be fundamentally characterised.

Williams (2011) studied longitudinal joint adhesiveness at three field sites with 12.5 mm Superpave asphalt surface mixes. The joints were tested in terms of their density, permeability

coefficient levels and water absorption resistance. The tests were done to establish appropriate assessments methods for quality assurance of joint construction methods and then use these tests to assess the quality of eight joint construction techniques including an infrared joint method for field projects. The infrared joint method was done with a propane powered infrared heater supplied by Heat Design Equipment, Inc (Figure 2.11). The repair method and adhesiveness quality were similar and comparable to that reported by Huang et *al*., (2010).

Clyne, Johnson and Worel (2010) used a 915 MHz microwave heater (Figure 2.12(a)) to repair potholes in the field. The method is described in detail in Johnson (2009). The patch material was 100% recycled asphalt pavement (RAP). The air and old pavement temperatures were 0 $^{\circ}$C and -2.5 $^{\circ}$C - 3 $^{\circ}$C respectively. The process was as follows: water and debris were removed from the pothole; heating was applied to pothole area for 10 minutes until portions of the hole reached 80 $^{\circ}$C to dry and warm the failed asphalt surface; the hole was filled with a first lift of RAP and heated for 20 minutes until the material reached 108 $^{\circ}$C to 114 $^{\circ}$C; the hole was filled with a second lift of RAP and heated for 10 minutes; the two lifts were blended and compacted with a hand-tamper and the wheel of a truck. After 3 months in service, more than 10% of the patch material was lost mainly along the sides of the patch.

Uzarowski et *al.* (2011) researched the use of infrared heating in cracked asphalt repairs. Their system, which had the ability to cover a large area, comprised a number of heaters (Figure 2.12(b)). The heating process included high and low heating of the cracked area for 3 to 5 minutes each with the high temperatures being applied first. The authors underline the importance of the repair area being heated to not greater than 190 $^{\circ}$C. The time to heat the area is noted to be dependent on weather conditions, asphalt mix type, clean repair area (water and debris removed) and asphalt starting temperature. Other parameters, however, to add that are not mentioned by Uzarowski et *al.* are asphalt thermal properties, ageing of asphalt pavement and heater configuration process e.g. heater offset from pavement, heater power, whether moving or stationary heater above the failed area. Results obtained from cores revealed appropriate densities and therefore effective compaction, with no degradation and strong bonding between the host and repair asphalt materials. The study concluded that infrared heating technology is efficient, cost-effective and can offer crack repairs that perform well for 13 or more years. However, to establish a detailed crack repair process with infrared heating that fully replaces conventional crack repair methods further research is necessary such as study of infrared heat application impact in asphalt oxidation.

Freeman and Epps (2012) repaired 83 longitudinal cracks in San Antonio, Texas with infrared heat. Heating was applied using a 45 kW HeatWurx heater (Figure 2.12(c)), at weather and pavement temperatures 15 ºC - 21 ºC and 19 ºC - 30 ºC respectively. 56 minutes of heat raised the asphalt temperature between 187 ºC and 332 ºC, this measured with an infrared camera. The repair included: heating of cracks and intermediate material to desired temperature; milling, sizing and mixing of the heated asphalt; application of rejuvenator to old asphalt to reinstate its properties; filling with new HMA and compaction with a small vibratory hand roller. The effectiveness of crack patch repairs by using infrared heating was defined by subjecting cores of the repaired and unrepaired areas to bulk and maximum theoretical density testing, resilient modulus and indirect tensile testing. All the repaired sites were visited 5 and 12 months after completion and it was revealed that some repairs performed well and others had started to fail mainly by shoving and settling. However, the investigation showed good repair bonding for cold weather patching.

Nazzal, Kim and Abbas (2014) evaluated winter pothole patching methods among which infrared patching was included. In total 60 repairs were studied and infrared patching was evaluated in terms of patch performance, productivity and cost-effectiveness. To undertake infrared patching, the researchers used an existing industrial infrared asphalt heater (Figure 2.12(d)). The average patching duration was 20 minutes with 3 to 10 minutes allocated for pre-heating. It is suggested, to pre-heat the old pavement until temperatures reach 135 ºC to 190 ºC levels. The authors suggest a heater offset from the pavement of 254 mm and that a lower offset would burn the asphalt surface.

In the described studies from Clyne, Johnson and Worel (2010), Uzarowski et *al*. (2011), Freeman and Epps (2012), Nazzal, Kim and Abbas (2014), only the surface temperature of the formed repairs was measured. The authors suggest a heating pattern and arrangement between heater and distressed area to soften the asphalt. However, the authors disregard the fact that asphalt low thermal conductivity and high specific heat capacity and repair interface thermal contact resistance make possible the coexistence of high surface temperatures and low repair interface and pavement internal temperatures respectively. There is no acknowledgement of the influences of repair geometry, climatic conditions heating pattern, compaction method, asphalt ageing and temperatures of fill hot asphalt and host pavement. Further, the interaction

between asphalt mixture and infrared heat has been studied mainly from on-site observations under diverse climatic conditions, not from controlled laboratory tests.
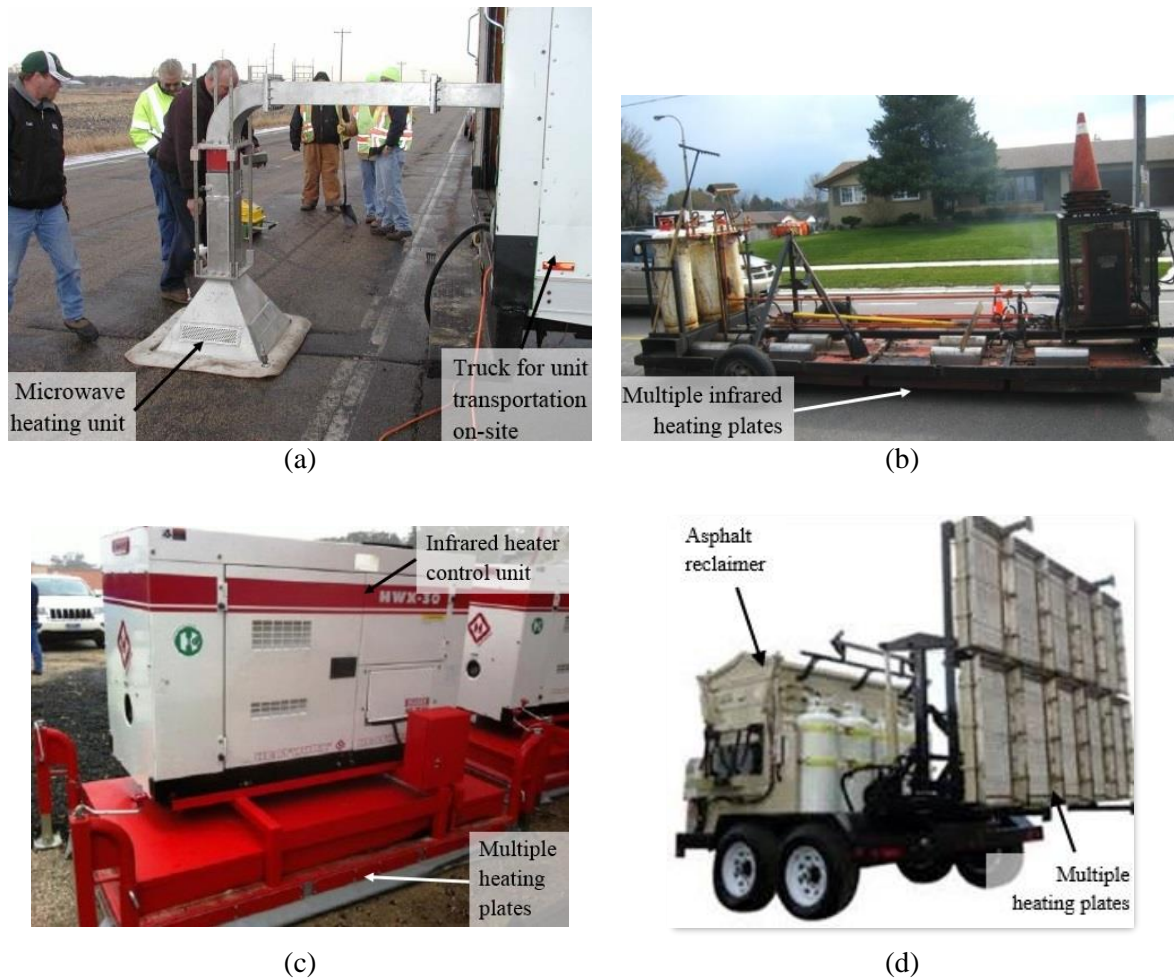
Figure 2.12 Microwave and infrared heating machines used in asphalt repair by: (a) Clyne, Johnson and Worel (2010, p.15); (b) Uzarowski et *al.* (2011, p.6); (c) Freeman and Epps (2012, p.6); (d) Nazzal, Kim and Abbas (2014, p.20) (label added by author)

Leininger (2015) evaluated patch repairs in the field. Thermocouples were set on the asphalt surface and at depths of 25 mm, 38 mm and 51 mm to measure temperatures for 15 minutes of heating time. Some patches were done with two heating-cooling cycles and not continuous heating. Intermittent heating made it difficult to measure temperatures of asphalt, however, the method allowed deeper heating of asphalt. The heater is shown in Figure 2.13. Patches were assessed for bulk density and indirect tensile strength at the repair joint. Further, both Finite Difference Method (FDM) and Finite Element Method (FEM) were used to simulate infrared heat in asphalt repair. The concept of the models was similar to the field projects for 15 minutes continuous heating at 677 $^\circ$C.

**Figure 2.13 Infrared heater used in a field asphalt pavement heating project by
Leininger (2015, p.25) (label added by author)**

Findings from the study relate to the effects of density, rejuvenator and heating methods in
asphalt repair. Regarding the infrared repair method, the author found that when heat is applied
in heating-cooling cycles the indirect tensile strength is increased due to deeper heat penetration
and higher bonding between new HMA and old pavement. The voids of the patches was found
to range from 3% to 10%. The surrounding pavement during infrared heated repairs was found
to stay intact without any change in strength. The FDM model performed better than the FEM
model. This happened due to poor representation of infrared heat application. The calculated
data from the FDM model were found to be in good agreement with the measured data. The
FDM model is suggested to be useful for finding heat depth.

The study could be seen as a preliminary research approach for defining the relationship
between infrared heat and asphalt pavement. However, the study was conducted for a field
project and the effect of parameters such as asphalt mixture type, asphalt ageing, surface
cleaning and preparation, weather conditions, pavement moisture, density, pavement
temperature and asphalt thermal properties could not be controlled.

Figure 2.14 shows a general infrared heated repair method in asphalt pavement as it emerges
from the literature review. Parameters such as heater power setting, heater offset from asphalt
pavement, heating time and heating set up are not mentioned in this method since they are

affected by many factors, i.e. environmental conditions, asphalt ageing, repair geometry and type etc. that differ between studies described in previous paragraphs.

1. Cleaning and marking

2. Setting-up of infrared heater

6. Pre-heating of old pavement

4. Scarification of old pavement

5. Application of rejuvenator to reinstate the properties of old asphalt mixture

6. Filling with new HMA

7. Mixing old and asphalt materials

8. Compaction of edges firstly and then inner part

Figure 2.14 General infrared heated pothole repair method (Nazzal, Kim and Abbas, 2014, p.26-27, image steps, font and label have been modified)

Another heated patch repair was recently suggested by Obaidi, Gomez-Meijide and Garcia (2017). The authors performed, analysed and evaluated in the laboratory pothole repairs using asphalt tiles bonded in the pothole cavity with induction heating and slight compaction. Heating time ranged from 1 second to 1 minute, this being decided by the time when test specimens started smoking. Induction heating was applied with a 6 kW induction heating generator at 50 mm offset from the asphalt pavement surface. The suggested pothole repair method included cutting; clearing; use of styrene-butadienestyrene (SBS) bonding layer; fill with prefabricated asphalt tile and finally welding of the tile to the road by induction heat (Figure 2.15).
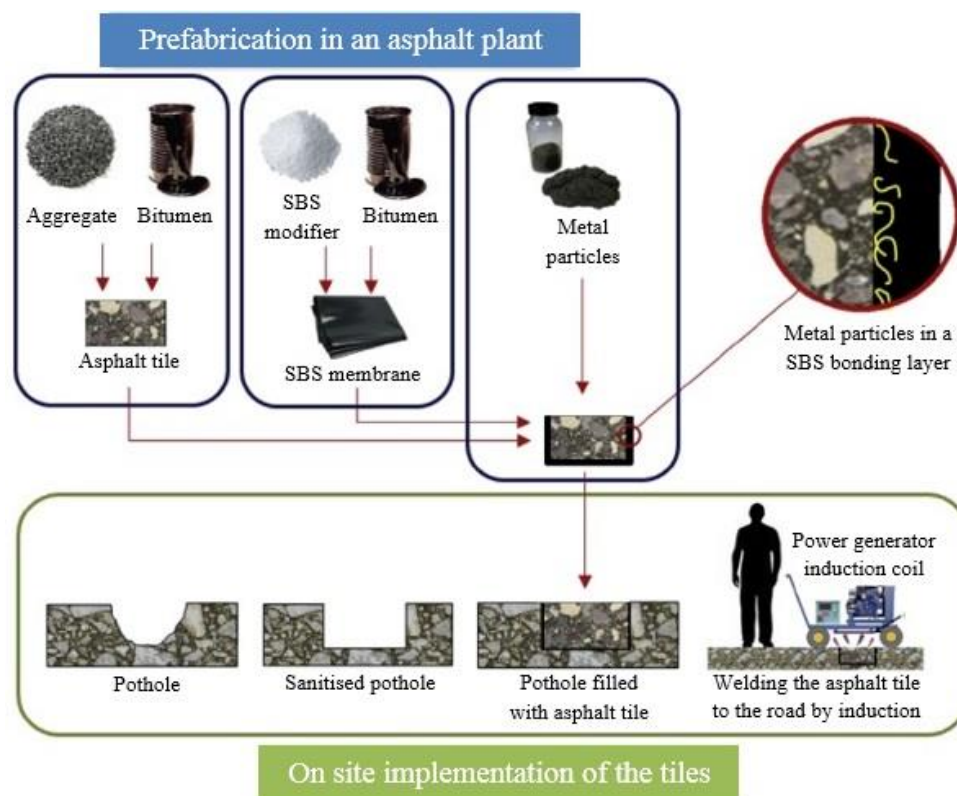
Figure 2.15 Pothole repair with induction heating and asphalt tiles suggested by Obaidi, Gomez-Meijide and Garcia (2017, p.593, image has been modified to standardised font)

Tensile bond tests (TBT's) and shear bond tests (SBT's) were used to evaluate the tensile adhesion strength and shear strength respectively of the repair interface. The authors found that depending on the number of bonding layers, percentage of open area of loose fibres and induction heating time, maximum TBT and SBT were 0.35 MPa and 0.2 MPa respectively. In the case of the repairs with chicken wire of 37% to 74% open area, the TBT ranged approximately from 0.1 to 0.37 MPa and the SBT ranged from 0.04 to 0.13 MPa.

Further, in the study of Obaidi, Gomez-Meijide and Garcia (2017), test samples repaired with tiles and cold mix and test samples without any repair (original test samples) were tested using the wheel track test. The results showed that test samples with asphalt tiles suffered 16.9% more rutting than the original test samples. Rutting in test samples with cold mix asphalt was approximately 40 times higher than in the original test samples. Therefore, tests samples with asphalt tiles outperformed repairs with cold mix. However, further research is suggested mainly when the excavated pothole contains loose stones or dirt between the tile and the old pavement or has uneven surfaces.

Finally, the use of microwave and induction heating with conductive materials has been extended in asphalt healing operations. These studies have been reported by Liu et *al.* (2010); Liu et *al.* (2011); Liu et *al.* (2012); Garcia et *al.* (2012); Gallego et *al.* (2013) and Norambuena-Contreras and Garcia (2016) and others. Figure 2.16 shows a common induction heating unit. No further discussion is done for these publications in this study since they extend their scope of study and overall analysis and results of asphalt outside the scope of this study. The effect however of microwave and induction heating application in bitumen and distribution of air voids of dense asphalt mixtures investigated by Norambuena-Contreras and Garcia (2016) is found relevant to thermal tests done in this research with infrared heat application in asphalt repair and will be referred again in later chapters.

Figure 2.16 Common induction heating coil (Liu et *al.*, 2010, p.1209)

2.8   Radiation heat transfer in asphalt pavement

Thermal radiation is emitted by any object with a temperature above 0 degrees Kelvin (-273 $^{\circ}$C). Typical transmission of radiation is by electromagnetic waves that are defined by their wavelength and frequency categorized by the electromagnetic spectrum. The infrared portion of the spectrum is from 0.7 microns (equal to a $7e^{-7}$ m) to 103 microns (equal to a $1e^{-3}$ m). The

energy transmitted by an infrared heater is proportional to its temperature. The higher the temperature, the shorter the wavelength and the higher the amount of energy radiated (Modest, 2013).

When the transmitted radiation energy of the heater hits the asphalt surface, then infrared heat transfer occurs. A portion of this radiation is absorbed and increases the temperature of the asphalt mixture by conduction, whereas other portions are transmitted or reflected to the surrounding area (Modest, 2013) (Figure 2.17). Therefore, in an infrared-heater-asphalt thermal efficient relationship, the effectiveness of radiant energy emittance of the heater (associated with the heater emissivity (ε)), the transmitted percentage of radiative energy by the heater that strikes the asphalt (associated with the view factor (F)) and the amount of this energy absorbed by the asphalt (associated with asphalt emissivity (ε)) are dominant.

Other parameters to add to this relationship are asphalt thermophysical properties. These properties affect heat transfer and storage inside the pavement initiated by the absorbed radiation energy of radiative heat application on the surface of the pavement. There are two distinct categories of these properties named transport and thermodynamic properties. The transport properties relate to energy transfer through asphalt and are absorptivity (*a*), albedo (*1-a*), emissivity (ε) and thermal conductivity (*k*). The thermodynamic properties relate to the equilibrium state of asphalt mixture and are density (ρ) and specific heat capacity (c_P) (Bergman et *al*., 2011). In heat transfer analysis, the ratio of thermal conductivity to the heat capacity of asphalt is thermal diffusivity (*a*), given by Eq. 2.1 (Chalbourn et *al*., 1996; Bergman et *al*., 2011). Specific heat capacity c_P is given by Eq. 2.2 (Hassn et *al*. 2016):

$$a = \frac{k}{\rho c_P} \tag{2.1}$$

where k = thermal conductivity, W/m K; ρ = density, kg/m^3; and c_P = specific heat capacity, J/kg K.

$$c_P = \frac{1}{m_{total}} \left[m_{aggregate} \times c_{aggregate} + m_{bitumen} \times c_{bitumen} \right] \tag{2.2}$$

where m = mass of each material, kg; and c = specific heat capacity of each constituent, J/kg K.
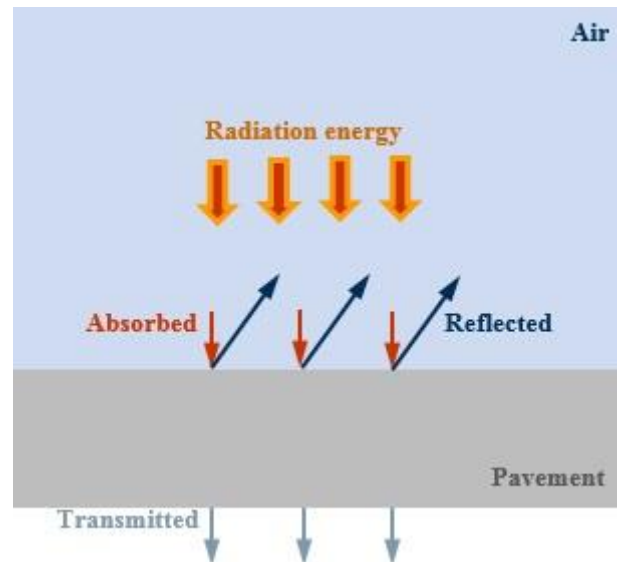
Figure 2.17 Radiation heat transfer in asphalt pavement

Thermal conductivity of asphalt is affected by the mixture type, aggregate type (Andersland and Ladanyi, 2004), aggregate gradation (Mirzanamadi, Johansson and Grammatikos, 2018) mixture density (Hassn et *al*., 2016), mixture temperature (Chadbourn et *al*., 1996) and presence of moisture in the mixture (Hassn et *al*., 2016; Mirzanamadi, Johansson and Grammatikos, 2018). For example, Hassn et *al*. (2016) found that as density increases thermal conductivity may increase too since the voids of air in the mixture decrease. In addition, moisture and freezing conditions may also increase asphalt thermal conductivity as reported by Mirzanamadi, Johansson and Grammatikos (2018). However, asphalt thermal conductivity may decrease at temperatures higher than 25 $^{\circ}$C reported by Chadbourn, Luoma and Newcomb (1996). Specific heat capacity and thermal diffusivity are both affected by thermal conductivity levels. For example, Hassn et *al*. (2016) found that when air voids increase, and thermal conductivity decreases then specific heat capacity and thermal diffusivity decrease too.

2.8.1 Measurement of thermal conductivity

There are two techniques to measure thermal conductivity: the steady state and the non-steady state. Investigation of thermal conductivity with the steady state technique implies that the measurement is done when the material has reached thermal equilibrium. Due to this requirement, the technique is time consuming. The non-steady state technique gives faster results since thermal conductivity is measured during the heating up of the material (Crompton, 2006). Tables 2.2 and 2.3 summarize steady state and transient techniques whose operation

methods are explained in the following paragraphs. In these tables, the references from the standards are not written as per Brunel Harvard referencing guide in order to fit them into the tables. The correct referencing format is written in Table 2.1.

Three commonly used steady state methods are the absolute techniques, the comparative techniques and the radial heat flow method. For the absolute technique, the sample test is put between a heat source and a heat sink and then is heated with a steady-state power input. When a steady-state temperature distribution along the length of the sample is reached, the temperature difference $\varDelta T$ is measured by two thermocouples with a known distance between them L. For a square plate, the thermocouples are put at a distance from the corners equal to one-fourth of the measuring length of the sample. For a round plate, the thermocouples are evenly spread out across the sample (American Society for Testing and Materials, 2004). Thermal conductivity k of the sample is calculated using Eq. 2.3 in Table 2.2.

The comparative technique is similar to the absolute technique. However, to calculate thermal conductivity of the test sample only the thermal conductivity of a standard material need to be known as well as its geometrical parameters. Therefore, there is no need to calculate heat flow Q. The test sample in the radial heat flow method is heated internally by a heat pipe which in turn should be uniformly heated by an internal electric heater. The sample is kept between the two heaters. The apparatus should also have thermocouples to control the temperatures of the pipe, insulation, ambient temperature and heater power. When a steady-state radial temperature distribution is reached, $\varDelta T$ is measured by two thermocouples with known radial coordinates r (Flynn, 1963). Thermal conductivity k for both methods is calculated using Eqs. 2.5 and 2.6 respectively in Table 2.2.

The non-steady state (transient) technique, consists of the hot wire and transient plane source (TPS) methods (Table 2.3). To measure thermal conductivity k with the hot wire method, the linear heat source is inserted at the centre of the sample. A thermocouple is also put at a known distance from the hot line source. The thermocouple captures the temperature difference $\varDelta T$ in the sample for a specific duration of time that heat flows from the hot wire. Then, k is calculated using Eq. 2.8 shown in Table 2.3. It is important to ensure that the test sample is put in a furnace to maintain its temperature during the testing (American Society for Testing and Materials, 2001). The needle probe method is similar in execution with the hot-wire method. The

difference between the methods is that the probe works as a heating element source and a sensor for the needle-probe method (American Society for Testing and Materials, 2000).

The TPS method uses a very thin insulated metal disk that works both as a heat source and a sensor. The metal disk is put between two similar pieces of sample with insulated external faces, a constant current is applied to the metal disk to heat up the sample and the temperature difference over time is captured (Bouguerra et *al*., 2001). Thermal conductivity is determined from Eq. 2.9 in Table 2.3.

Table 2.1 Referencing guide for standards included in Tables 2.2 and 2.3

Standard name	References
ASTM C177:2004	American Society for Testing and Materials, 2004
BS EN 12667:2001	British Standards Institution, 2001
ISO 8302:1991	International Organization for Standardization, 1991
ASTM E1225:2013	American Society for Testing and Materials, 2013b
ASTM C518:2017	American Society for Testing and Materials, 2017
ASTM E1530-11:2016	American Society for Testing and Materials, 2016b
ASTM C335:1995	American Society for Testing and Materials, 1995
BS EN ISO 8497:1997	British Standards Institution, 1997
ASTM C1113/C1113M-09:2013	American Society for Testing and Materials, 2013a
BS EN ISO 8894-1:2010	British Standards Institution, 2010
ASTM D5930:2001	American Society for Testing and Materials, 2001
ASTM D5334:2000	American Society for Testing and Materials, 2000
ASTM D7984:2016	American Society for Testing and Materials, 2016a
BS EN ISO 22007-2:2015	British Standards Institution, 2015b

Table 2.2 Steady state technique for measurement of thermal conductivity (Q= heat flow, L= distance between thermocouples, A= sample cross-sectional area, ΔT= temperature difference between thermocouples, p= heating power, Q_{loss}= heat losses due to radiation, conduction and convection, r= radial distance, H= height) (source Zhao et al., 2016 unless stated otherwise)
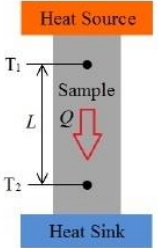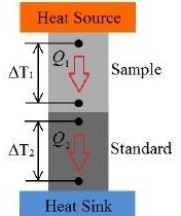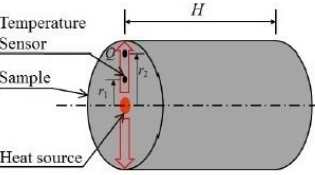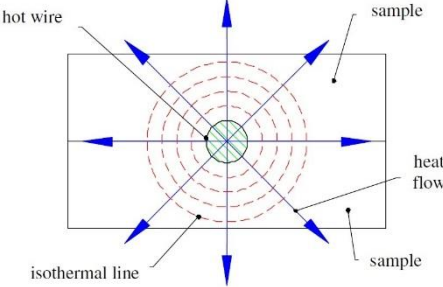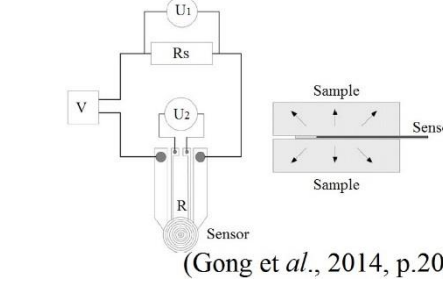
Techniques & methods	Schematic	Calculation of thermal conductivity	Standards & studies	Sample	Apparatus	Limitations
Absolute technique	(Zhao et al., 2016, p.7)	*Fourier's law of heat conduction:* $k = \frac{QL}{A\Delta T}$ (2.3) $Q = p - Q_{loss}$ (2.4)	*For test apparatus and procedure:* • ASTM C177:2004 • BS EN 12667:2001 • ISO 8302:1991	Rectangular or cylindrical shape	Guarded-hot-plate	• Difficulty to measure ΔT and determine heat flow rate Q with heat losses Q_{loss} being present • Thermocouples should be carefully chosen to minimise heat conduction through their wires • Large samples only can be tested • Long testing time
Comparative technique	(Zhao et al., 2016, p.7)	$k_1 = k_2 \frac{A_2 \Delta T_2 L_1}{A_1 \Delta T_1 L_2}$ (2.5) where elements with numbers *1* and *2* represent the test sample material and the standard material respectively	*For comparative cut-bar meter:* • ASTM E1225:2013 *For heat flow meter:* • ASTM C518:2017 • ASTM E1530-11:2016 • BS EN 12667:2001	Rectangular or cylindrical shape	Comparative cut-bar meter Heat flow meter (for low thermal conductivity materials)	• Heat flow needs to be controlled since it is neglected in the measurement • Best accuracy achieved when thermal conductivities of the test sample and standard material are at similar levels (Tritt, 2005)
Radial heat flow method	(Zhao et al., 2016, p.7)	*Fourier's law of heat conduction for cylindrical sample:* $k = \frac{Q ln(\frac{r_2}{r_1})}{2\pi H \Delta T}$ (2.6)	*For test apparatus and procedure:* • ASTM C335:1995 • BS EN ISO 8497:1997	Cylindrical shape	Radial heat flow meter	• Radial heat flow with no heat losses should be ensured • Long testing time (Presley and Christensen, 1997)

Table 2.3 Transient (time-domain) technique for measurement of thermal conductivity (ΔT= temperature difference, Q= heat flow, L= distance between thermocouples, p= heating power, $D(\varphi)$= a dimensionless theoretical expression of sensor time-dependent heat conduction, a= temperature coefficient of the resistivity, r= radial distance, H= height) (source Zhao et al., 2016 unless stated otherwise)

Techniques & methods	Schematic	Calculation of thermal conductivity	Standards & studies	Sample	Apparatus	Limitations
Hot-wire method	(Franco, 2007, p.2498)	$\Delta T = T(t_2) - T(t_1) = \frac{p}{4\pi k L}\ln(\frac{t_2}{t_1})$ (2.7) $k = \frac{p}{4\pi[T(t_2)-T(t_1)]L}\ln(\frac{t_2}{t_1})$ (2.8) (Franco, 2007)	*For test apparatus and procedure for the hot-wire method:* • ASTM C1113/C1113M-09:2013 • BS EN ISO 8894-1:2010 *For test apparatus and procedure for the needle method:* • ASTM D5930:2001 • ASTM D5334:2000	Rectangular shape	Hot wire method Needle-probe method	This method is used for low thermal conductivity materials. Typical range of thermal conductivity for the hot wire method is 0.08-2.0 W/m K (ASTM D5930:2001) and for the needle-probe method is 0.2-5 W/m K (ASTM D5334:2000)
Transient plane source (TPS) method	(Gong et al., 2014, p.20)	$\Delta T(\varphi) = \frac{Q}{\pi^{1.5}rk}D(\varphi)$ (2.9) $\varphi = \sqrt{\frac{ta}{r^2}}$ (2.10) (Bouguerra et al., 2001)	*For test apparatus and procedure:* • ASTM D7984:2016 • BS EN ISO 22007-2:2015	Rectangular or cylindrical shape	Hot disk instrument	Close contact between the two solid pieces of sample should be ensured. If the sample is not a solid i.e powder, it is difficult to achieve this contact between the upper and down layers of the sample

2.9   Simulation modelling of asphalt pavement and repair

Hermansson (2004) developed a simulation model to predict hourly asphalt pavement surface temperatures during summer and winter time. Parameters such as hourly values of solar radiation, air temperature and wind velocity data were input in the simulation. Long-wave and short-wave radiation and convection losses were considered in the simulation. Thinner elements were adopted for areas closer to the surface of the asphalt pavement and thicker for deeper levels. Each element is assigned an initial temperature which starts to change in accordance with heat conduction theory when the simulation is run. Heat flow depends on thermal conductivity, specific heat capacity and thermal diffusivity of the asphalt. The model was validated by in-situ temperature measurements on the surface and at 25 mm deep inside the pavement. It was found that between measured and calculated data, an average error of less than 2 °C existed. The model accurately simulated hourly asphalt pavement surface temperatures for both summer and winter conditions.

Minhoto et *al*. (2005) developed a three-dimensional (3D) finite element (FE) model to simulate the transient behaviour of asphalt pavement. The model consisted of a 3D asphalt pavement geometry of constant thickness; homogeneous, continuous and infinite in the horizontal direction and semi-infinite in the vertical direction. Heat transfer modes due to conduction, convection and radiation were adopted in the simulation. For asphalt surface convection and radiation, the film coefficient and emissivity were used. For internal heat flow, the asphalt thermophysical properties (thermal conductivity, specific heat capacity and density) were defined. Heat flux was applied on the surface of the pavement geometry to simulate solar radiation. For boundary conditions, null heat flux was applied at all other surfaces of the pavement. For the mesh, a finer mesh was adopted near the traffic loading and the reflective cracking caused by this. The final eight-node elements were 13,538 in number.

Parameters such as hourly values of solar radiation, air temperature and wind velocity data were input in the simulation. These parameters and internal pavement temperatures at seven different depths (0 mm, 27.5 mm, 55 mm, 125 mm, 165 mm, 220 mm, and 340 mm) were measured in-situ for 4 months. The internal pavement temperatures were captured using thermocouples. The different locations of temperature measurements in the pavement were chosen to cover distribution of temperatures along the depth of the asphalt pavement and were used to validate the simulation model. The results showed good correlation between measured and simulated date and a promising tool to simulate asphalt temperatures.

Yang and Liu (2007) developed an FE modelling using ANSYS software to simulate field temperature of asphalt pavement. The geometry of the model was designed with three asphalt layers of 40 mm, 50 mm and 60 mm depths, a cement treated base of 400 mm depth and a subgrade layer of 450 mm depth. All three modes of heat flow namely radiation, convection and conduction were incorporated in the model. Since the model was built to simulate temperature distribution and thermal stresses in asphalt pavement, the following parameters were defined: density, specific heat capacity, film coefficient, thermal conductivity, emissivity, stiffness modulus, resilient modulus and coefficient of thermal expansion. For the mesh, eight-node elements were chosen.

The results showed that air temperature greatly affects temperature profiles in all asphalt layers of a pavement but not temperatures within cement treated base and subgrade. This shows that thermal cracking in asphalt pavement is rarely influenced by non-asphalt layers. Looking at temperatures along the depth of an asphalt layer, temperatures on the surface are higher than at the bottom of the layer. This because of the influence of asphalt thermal properties in internal heat flow. The results also showed stiffness modulus and coefficient of thermal expansion have a great influence in the calculation of thermal stresses in the pavement.

Tang et *al*. (2008) studied microwave heating for maintenance of asphalt pavement. The authors simulated in the laboratory and using ANSYS software heat distribution in asphalt pavement for 2.45 GHz and 5.8 GHz magnetrons. The simulation model consisted of an asphalt geometry $150 \times 150 \times 150$ mm^3. The environment and pavement temperatures were set to 20 ºC. The simulation was run for 200 seconds heating time and temperatures were measured at 0 mm to 150 mm deep inside the pavement geometry. For the laboratory testing, an asphalt block $500 \times 500 \times 300$ mm^3 was built and 36 thermocouples were set in it. Temperatures were measured every minute for 10 minutes heating time duration.

No comparison between measured and simulated data was done by the authors. Nevertheless, the simulation showed at the end of 200 seconds heating time, temperatures at 0 mm to 135 mm depth ranged from 32.3 ºC to 23.8 ºC for the 2.45 GHz and from 66.7 ºC to 37.3 ºC for the 5.8 GHz magnetrons respectively. The experimental work showed temperature distribution from the surface of the asphalt to 210 mm depth from 70 ºC to 9 ºC and 125 ºC to 9 ºC at the end of 10 minutes heating for the 2.45 GHz and 5.8 GHz magnetrons respectively. The main

conclusion from the study was that the 5.8 GHz magnetron can heat asphalt to a depth of 70 mm - 80 mm which is sufficient for most depths of asphalt distress repaired in China.

However, the authors did not consider the impact of asphalt mixture type, volumetric and thermal properties of asphalt that significantly affect heat distribution in asphalt pavement. Initial air and pavement temperatures for the laboratory tests conducted are also not reported. Both parameters greatly affect temperatures in asphalt. Further, it seems that temperature measurements in the laboratory were done in only one asphalt sample which makes the authors argument, regarding the effectiveness of microwave heating, weak.

Zhu et *al.* (2009) developed a two dimensional (2D) mathematical heat transfer model of microwave heating application for recycling asphalt pavement. The model was evaluated with similar experimental work during which a compacted asphalt mixture was heated for 10 minutes and 15 minutes using a microwave heater with an output power of 0.65 kW. The offset of the microwave heater plate from the asphalt surface is not mentioned, however, the author suggests heating in heating-cooling cycles than heating continuously to achieve a more uniform temperature distribution. Further, for the experimental tests, the author suggests the use of a metal frame around the microwave heater for the safety of the operators. It would be interesting to see if such frame contributes to more effective heating of asphalt while eliminating the effect of wind in the heating pattern, however, no tests or discussion were done in this matter by the authors.

The results from the mathematical model and the laboratory tests showed higher concentration of temperatures in the middle of the asphalt sample and lower temperatures at the edges of the sample due to heat loss. The increase of temperature during heating was non-linear. The mathematical model showed that for 10 minutes of heating, temperatures increased from 18 °C to 86.2 °C and then within 5 minutes of heater operation reached 143.4 °C. The author suggests that this happened because the temperature increase rate is higher for mixtures with higher initial temperature. However, the author did not consider the effect of asphalt thermal properties in this result. Between the mathematical model and the laboratory tests, a 15 °C difference was found for the highest asphalt temperatures achieved at the end of heating. According to the author, this was due to energy reflected to the surrounding environment and energy lost from the steel frame of the microwave heater during the experimental heating work. These effects were not considered in the mathematical model.

Rahman et *al*. (2013) designed a 3D FE model to simulate temperatures in the pothole repair interface of an asphalt pavement. The model had two bonded geometries: the HMA repair of $300 \times 300 \times 100$ mm^3 and the host asphalt pavement of $1000 \times 1000 \times 300$ mm^3. An eight-node brick element was used for the model. The repair geometry was assigned with an initial temperature of 150 ^{o}C and the model was run for two different air temperatures, 22 ^{o}C and 5 ^{o}C. Further, thermal conductivity, specific heat capacity and density of asphalt mixtures were kept constant. For boundary conditions, convection was applied only at the surface of the pavement and repair. The model seems to have been simplified in terms of any moisture effect.

The simulation model demonstrated promising results. However, the authors did not define the bonding condition in the repair interface, the boundary conditions at the faces of the host pavement geometry (excluding the surface), the solar radiation at the surface of the pavement and repair that may affect the simulated repair temperatures. No mesh refinement is reported.

Huang et *al*. (2016) simulated heating effects of asphalt pavement during hot in-place recycling using the discrete element method. The authors managed to recreate for the simulation, the non-continuity of asphalt material nature by taking a digital image of an actual core and input that in the simulation. The geometrical model of the simulation comprised of three different asphalt mixtures and had a total depth 180 mm. The boundary conditions of the two lateral sides of the infinite horizontal direction of the model were neglected. Heat flow happens from the surface of the pavement where induction heating application was expressed in terms of heat flux at 175 ^{o}C. Surface and bottom pavement temperatures were considered constant at 20 ^{o}C and 10 ^{o}C respectively. Thermal conductivity and specific heat capacity of asphalt materials were measured in the laboratory and input into the simulation model. It is understood that the authors used thermal contact resistance to simulate heat flow within asphalt material; however, no other information is given or any discussion is done for this in the paper. Induction heating application for hot-in-place asphalt recycling was simulated for continuous heating and intermittent heating methods for a heating unit moving across the asphalt at 2 m/min and 6 m/min speed respectively.

From the simulation of continuous heating, temperatures showed a lowering trend from top to bottom. For example, between 10 mm and 40 mm depth from the pavement surface, temperatures were found to range from 100 ^{o}C to 51 ^{o}C. According to the authors this happened because of asphalt low thermal conductivity and therefore slow heat conduction and

temperature rise deep in the asphalt. However, the authors neglect to consider specific heat capacity that defines the time and energy needed to increase mixture temperature. Further, fluctuating temperatures were found nearer the surface of the pavement during induction heating application. This happened because of fluctuating applied heating the effect of which was lowered as heat flowed deeper in the pavement. It was also observed that heat continued to flow inside the pavement even when the heater was temporarily stopped.

From the simulation of intermittent heating, temperatures followed a similar trend as explained previously but higher temperatures. For example, between 10 mm and 40 mm depths from the pavement surface, temperatures were found to range from 161 $^{\circ}$C to 68 $^{\circ}$C respectively.

The simulation model was validated with laboratory work. During the induction heating experiments of asphalt material, temperatures were measured on the surface and at depths of 20 mm and 40 mm using thermocouples. The comparison between simulated and measured temperatures showed larger difference for temperature distribution in the upper part of the pavement but lower difference for the lower part of the pavement. Furthermore, it was seen that simulated temperatures were generally higher than measured temperatures. These happened because parameters such as wind speed and solar radiation were not considered in the simulation and heat loss is less for the lower part of the pavement. However, it was concluded that the simulation was a promising tool to analyse the heating effects of asphalt pavement during hot in-place recycling.

2.10 Performance evaluation of patch repair

As discussed in section 2.7, methods such as indirect tensile strength, shear bond and wheel tracking tests are used to measure the interface bond strength of asphalt pavement layers and to assess the resistance of such materials under the wheel loading. However, there are no tests that similarly evaluate the performance of pothole repairs. Therefore, in this study, shear bond and wheel tracking tests were adopted for such evaluation (similar action was taken in Obaidi, Gomez-Meijide and Garcia, 2017). Background information for these two methods is given in the following sections.

2.10.1 Shear bond test (SBT)

Interlayer bonding of asphalt pavement mixtures can be performed in accordance with BS EN 12697-48 (British Standards Institution, 2013). This standard describes the apparatus and

testing procedures for five methods: (a) torque bond test (TBT); (b) shear bond test (SBT); (c) tensile adhesion test (TAT); (d) compressed shear bond test (CSBT); and (e) cyclic compressed shear bond test (CCSBT).

This study chose SBT for laboratory testing of repair interfaces of HMA patch repairs. Typical apparatus for SBT of a cylindrical sample is shown in Figure 2.18. Based on the BS EN standard, to perform the test, the sample is conditioned for at least 5 hours in a controlled temperature cabinet at 20 (±1) °C; then it is fitted and tightened between the lower and upper shear rings of the apparatus with sample shear interface aligned between the two rings; the load frame is adjusted directly above the upper shear ring; and the test is performed with a loading rate of 50 (±2) mm per minute. At the end of the test, shear stress is calculated using Eq. 2.11. A simplified version of the SBT apparatus is presented in Raab and Partl (1999) cited in Raposeiras et *al*. (2013) (Figure 2.19) and was adopted to fit the dimensions of test samples of this study. The device and experimental work are shown in Chapter 8.

Key
1   base body
2   sample support
3   lower shear ring
4   upper shear ring
5   upper body
6   guiding bar
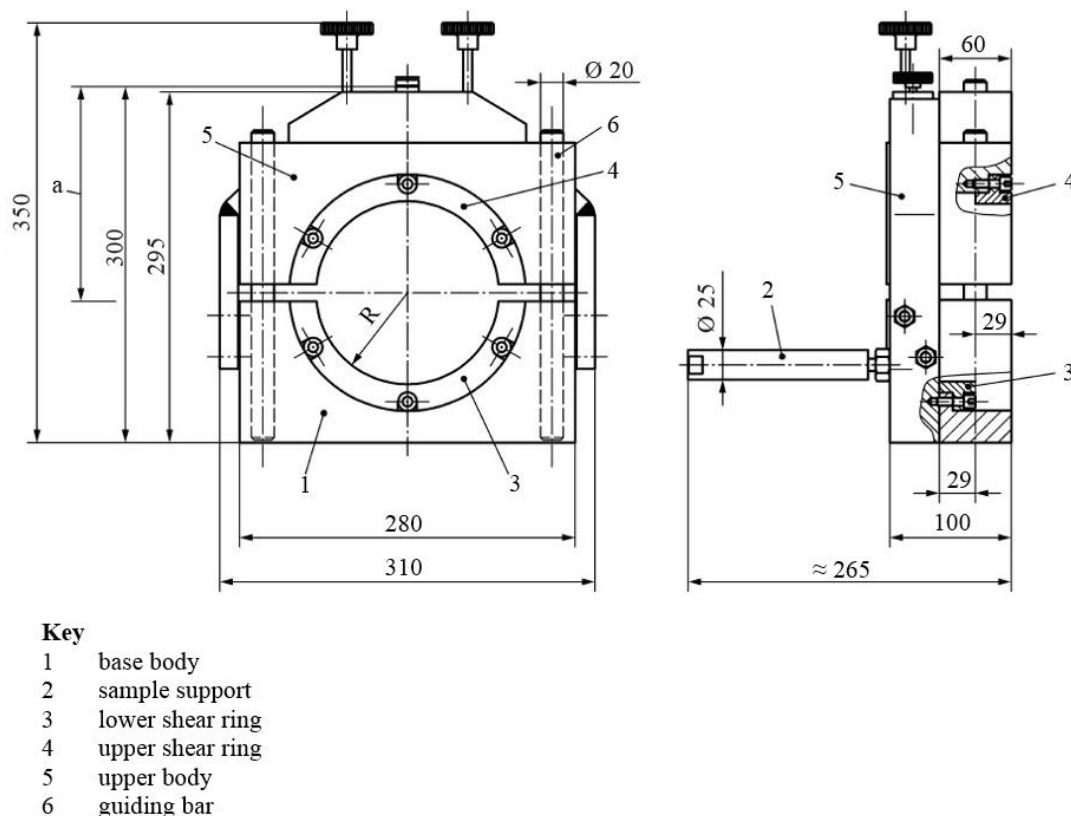
Figure 2.18 Typical SBT apparatus (all dimensions are in mm, British Standards Institution, 2013, p.13, image has been modified to standardised font)

$$\tau_{SBT} = \frac{4P_{SBT}}{\pi D^2} \qquad (2.11)$$

where τ_{SBT} = shear stress, kg/cm^2; P_{SBT} = vertical shear force, kg; D = initial diameter of specimen, cm.
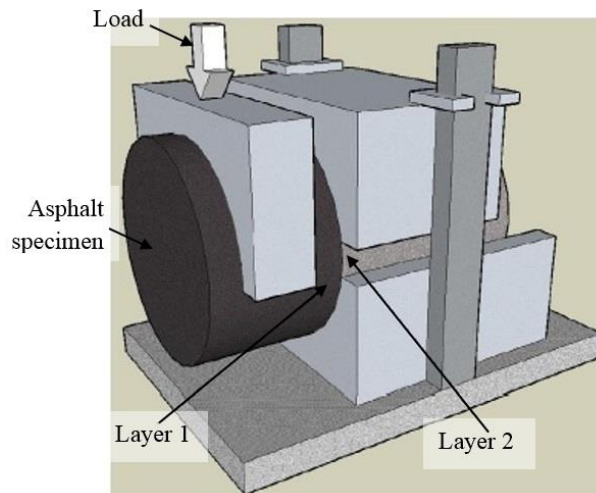
Figure 2.19 Simplified SBT apparatus (Raposeiras et *al*., 2013, label added by author)

2.10.2 *Wheel tracking test (WTT)*

The wheel tracking test (WTT) may be performed in accordance with BS EN 12697-22 (British Standards Institution, 2003) and AASHTO T324 (American Association of State Highway and Transportation Officials, 2004). Typically, a loaded rubber or stainless-steel wheel tracks the asphalt sample under a specified load, speed and temperature. During the test, the sample is submerged in water and rutting is measured automatically by the machine using calibrated linear variable displacement transducers (LVDT). The BS EN test uses water simply to heat the specimen up to a specified or investigated temperature by the researcher and maintain this temperature during the test. The AASHTO test uses water to control the sample temperature and to also initiate stripping after an initial phase of permanent deformation. For this reason, in this study, the WTT was performed in accordance with the AASHTO test procedure. The wheel tracking machine and experimental work of this study are shown in Chapter 8.

The AASHTO test is used for both laboratory compacted asphalt samples and field cores taken from a compacted asphalt pavement. Both slab specimens and cylinder samples may be tested. The asphalt mixture may be of the researcher's choice and in accordance with their scope of

work. The AASHTO standard suggests thorough mixing and a conditioning procedure in accordance with AASHTO R30 (American Association of State Highway and Transportation Officials, 2006). Laboratory rectangular samples should be compacted with a Linear Kneading Compactor and have dimensions $320 \times 260 \times (38 \text{ to } 100)$ mm^3 (Figure 2.20). Cylindrical samples should be compacted with a Superpave Gyratory Compactor (SGC) and should be 150 mm in diameter with varying thickness 38 mm - 100 mm (Figure 2.21). Field cores and slabs should be 250 mm in diameter and 38 mm in height and $320 \times 260 \times (38 \text{ to } 100)$ mm^3 in size respectively.

Figure 2.20 Demonstration of rectangular slab specimen and steel mould for wheel tracking test (Controls, 2018, p. n/a, label added by author)
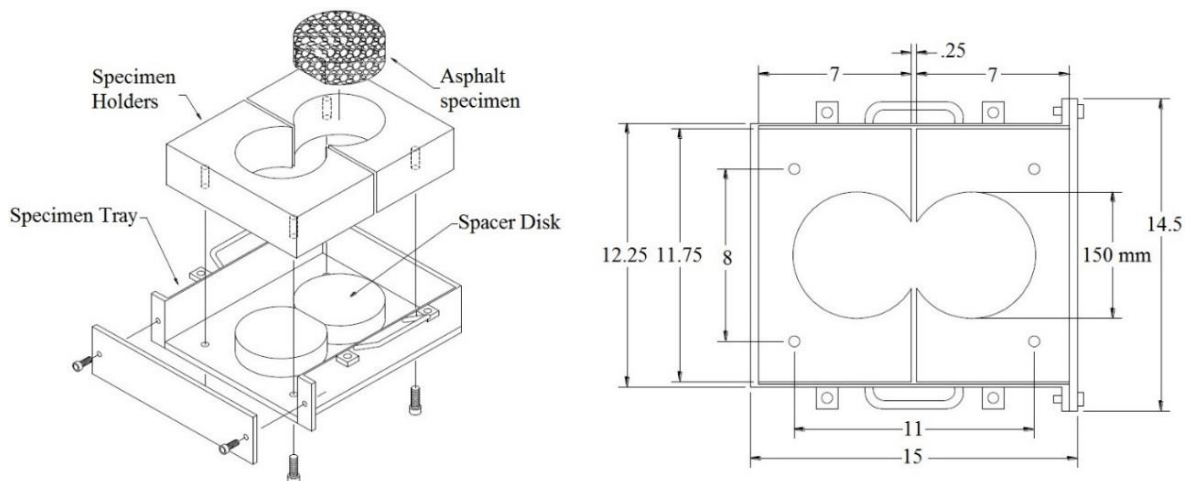
Figure 2.21 Typical cylindrical sample and high-density polyethylene (HDPE) mould used in wheel tracking test (Tsai et *al*., 2016, p.3, all dimensions are in cm unless stated otherwise and image has been modified to standardised font)

Further, the moving wheel of the wheel tracking machine is 203.2 mm in diameter and 47 mm wide. The wheel load is specified at 705 (±4.5) N and moves with a maximum speed of 0.305 m/s. The test temperature should be maintained at similar levels during sample conditioning and test duration and may be set between 25 °C and 70 °C. The test procedure is as follows: the compacted sample and its mould are initially put in the tank and submerged in water; LVDT's are inserted in the sample; the water temperature is adjusted, and the specimen conditioned to the specified test temperature; after this, the test starts after 30 minutes of final conditioning by lowering the wheels onto the specimen and pressing the start button. The test ends either after 20,000 passes have occurred or when 40.90 mm rutting depth has been reached (20.0 mm is commonly selected as maximum rutting depth by many researchers (i.e. see Tsai et *al*., 2016; Obaidi, Gomez-Meijide and Garcia, 2017). A typical wheel tracking test curve is shown in Figure 2.22. The stripping inflection point is calculated using Eq. 2.12.
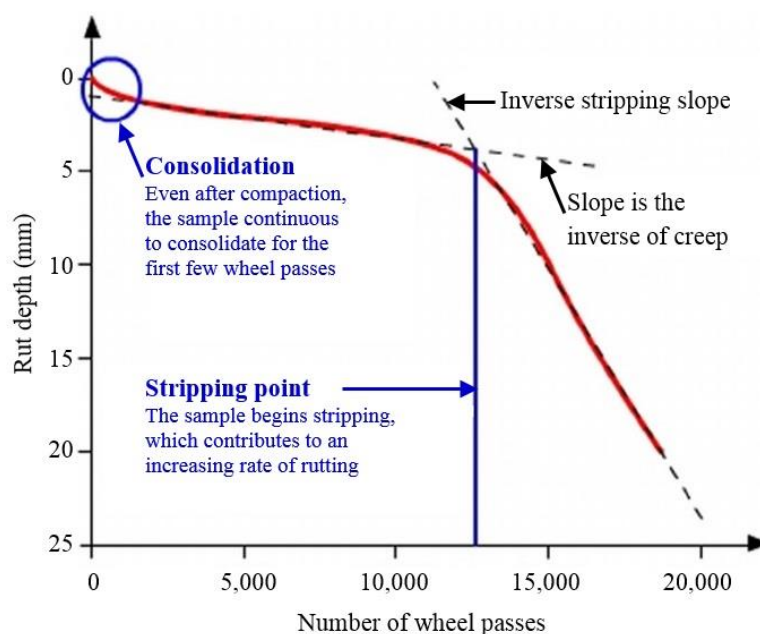
Figure 2.22 Typical wheel tracking test curve (Chaturabong and Bahia, 2017, p.341, image has been modified to standardised font)

$$Stripping\ Inflection\ point\ (SIP) = \frac{Intercept\ (second\ portion) - Intercept\ (first\ portion)}{Slope\ (first\ portion) - Slope\ (second\ portion)} \quad (2.12)$$

2.11 Research motivation

As established from the previous sections, one of the major distresses modes in asphalt pavement is potholes. They can be locally developed and are created due to base or subgrade

failure, poor drainage and poor workmanship during construction (Lavin, 2003, Washington State Department of Transportation, 2017). The main objective of permanently repairing a pothole is to a create high quality repair in terms of (a) patching lifetime (this meaning quality and durability the same as the existing pavement), (b) low patching costs (caused by labor, equipment and traffic control (McDaniel et *al*., 2014)), (c) minimum traffic disruption time ((c) and (d) can be achieved by less repetitions of patching), and (d) effective patching process (this referring to patching done in any weather conditions) (Blaha, 1993).

However, compaction of hot fill mix for patching operations has been always a struggle since there is not sufficient time available to compact the mix with temperatures rapidly reaching cessation levels (Thom 2008). Wind velocity and environmental conditions at the time of the repair affect this rapid decrease in temperature. As a result, fast cooling is mainly observed in the edges of the repair due to the cold underlying asphalt layer creating low density interfaces, poor repair adhesion with host pavement and weak repair interfaces prone to premature failure (Thom 2008, Uzarowski et *al*., 2011, Dong, Huang and Zhao, 2014).

Reflecting the above, in section 2.9 it was discussed how heating the underlying layer, prior to pothole filling and compaction enhances the bonding between the cold host pavement and the new hot-fill mix and decreases early edge disintegration and repair failure. Infrared, microwave and induction heating technologies have been previously investigated for this purpose. Some researchers state that the infrared repair method is not as efficient as microwave and induction heating repair methods. However, it seems that this conclusion is taken due to lack of fundamental experimental, theoretical and numerical simulation research work in the use of infrared heat in pavement construction and repair. To address this, the author has concluded that the effect of the following parameters in the infrared repair operation should be investigated and fully understood: pothole geometry and depth; ambient temperature; host pavement temperature; fill mixture temperature; host pavement and fill mixture thermophysical properties; infrared heater properties; infrared heating time; infrared heat offset and position; temperature distribution in host pavement external faces and heat flow inside the host pavement during infrared heat application and repair work. This study works along these parameters to assess the use of infrared heat in asphalt repair and set a scientifically based foundation for infrared heated repairs. Below is described the status of each parameter set for this study:

- Pothole geometry: constant

- Pothole excavation depth: variable

- Host pavement thermophysical properties: investigated

- Fill mixture thermophysical properties: investigated

- Infrared heater properties: assumed constant (same infrared heater was used for all experiments but with different operating power)

- Infrared heating time: variable

- Infrared heater offset from host pavement surface: variable

- Infrared heater position: variable

- Temperature distribution in host pavement external faces: investigated

- Heat flow inside the host pavement: investigated

2.12 Summary

The foregoing sections investigated asphalt pavement failures, pothole development, methods to repair potholes and methods to evaluate the performance of HMA patch repairs in the laboratory. Heat transfer in asphalt pavement was explored and simulation modelling of asphalt pavement and repair temperatures were discussed. It was seen that the performance of patch repair is greatly reduced due to faster loss of temperature and inferior compaction at the interface. To avoid a cool repair interface, previously investigated studies suggest pre-heating of the host pavement prior to repair using infrared, microwave or induction heating methods. It was found that infrared heated pothole repair is under-explored and fundamental parameters in an infrared-heater-asphalt thermal relationship ignored or not explored. It was also found that radiation heat transfer in asphalt repair based on theory and simulation modelling were also not reported. The next chapter presents the experimental infrared heating equipment used in this study in patch repairs.

Chapter 3

Experimental infrared heating equipment

The chapter describes the experimental infrared heater used in this research to perform dynamically heated repairs. The heater has the capability to control the temperature of its heating element plates and apply static and dynamic heating. The chapter also presents the experiments conducted to establish temperature distribution on and below the heating element plate of the heater when operating between 20% and 100% gas feed rates, the results from these experiments and the calculation of the heater heat power for all gas feed rates. The reported investigation was necessary because (a) no previous study has quantified the performance of a heater and the exact output of the heater; (b) it helped to optimise the heater heating operation, heating power, heating time and heating process itself; and (c) the temperatures of the heater plate were used to calibrate the finite element (FE) thermal simulations of Chapter 7. The chapter forms part of the second objective of the research which is fully addressed in Chapter 4.

3.1 Heater operation

This study used an experimental infrared heater that had been developed and patented by Chamberlain (2014), however, not previously used in asphalt research or commercial asphalt pavement processes. The main advances of the presented heater are: (a) multiple heating elements that configure to accommodate different sizes and shapes of pothole repairs; (b) independent precise temperature control of individual heater elements; (c) precise motion-controlled passage of the heating elements over the repair surface; (d) short message service (SMS) messaging on system activity, including temperature and time base; and (e) global positioning system (GPS).   The heater and its central control unit are presented in Figure 3.1 and its operation process in Figure 3.2.

(a)

(b)

(c)
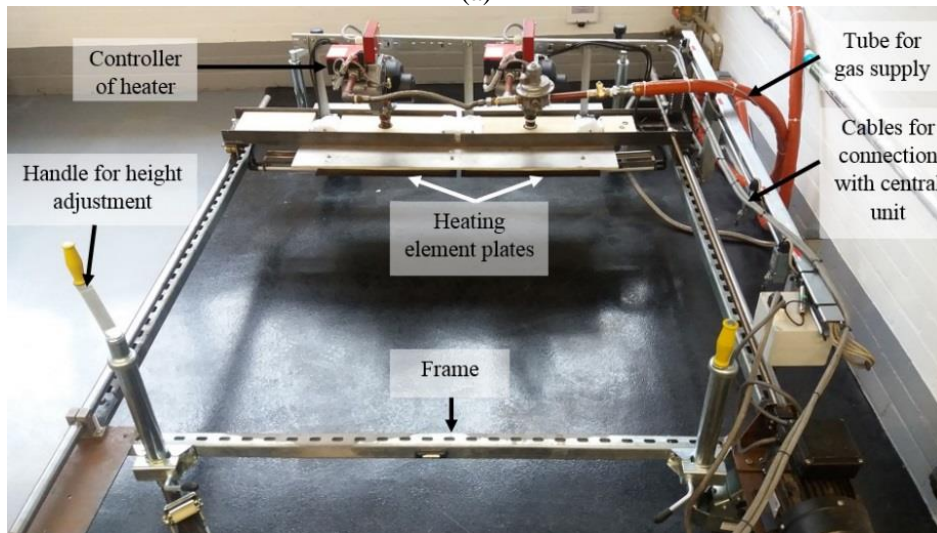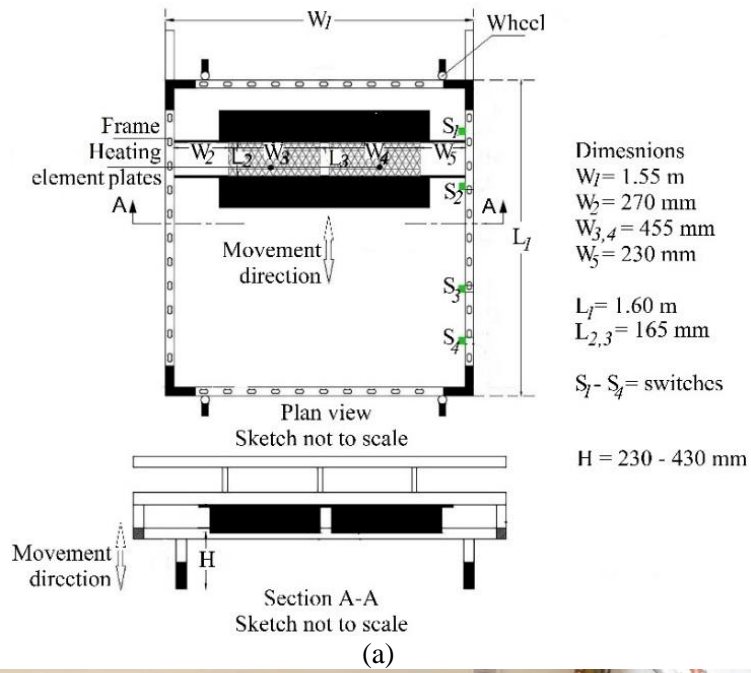
Figure 3.1 Experimental infrared heater: (a) plan and section views; (b) prototype; and (c) central control unit

```
                    Preparing patch heater for operation


                         Is extraction unit        No
                           turned on?                      Turn on extraction unit          Patch heater is ready for operation
                                                                                                         Yes
                              Yes
                                                                                       Is corresponding        No    Consult patch heater
                          Is heat energy          No                                   heater 1 and/or 2             manual for errors
                        detector operational?            Reset to main                     lamp on

                              Yes
                                                                                        Switch heater 1 and/or 2 on
                            Is test area           No
                             clear of                    Clear hazards
                            hazards?                                                                Select Manual
                                                                           Select area of   Auto   or Auto       Manual
                              Yes                                           heater operation        operation

                        Move test sample into the
                             test area                                                   Set heater in home position

                        Move system over the test                                       Release emergency stop
                             sample                                                      button and press Reset

                        Connect heat energy and                                                    Yes
                         electricity supply
                                                                                         Is the Man-Off-     No   Turn switch to off
                        Select operation of one or                                       Auto switch in          position
                             two heaters                                                  off position?

                              Yes
```

Figure 3.2 Operation process of the heater

In the current research, not all the described functions of the heater were utilised or analysed in-depth. The experiments were performed in a laboratory environment and there was no need to move the heater to different construction sites or control the use of it remotely. One or two heating elements were used depending on the scope of the study's performed experiments. Each heating element operates with a propane gas feed rate of 20% to 100% which is controlled by the control unit (Figure 3.1(c)). The equivalent kW rating against percentage gas rate is presented in section 3.5.

The ignition of the heating element occurs behind its surface which in turn emits infrared heat that directly penetrates an asphalt surface beneath it as discussed in Chapter 2, section 2.8. To understand how the heating element heats the asphalt surface, investigations described in sections 3.2 – 3.3 were executed.

3.2   Temperature distribution on heating element plate

This cycle of experiments dealt with temperature measurements on the heating element plate when operating between 20% and 100% gas feed rates. The temperatures were captured using, initially, a handheld infrared thermometer (Omega, 2016a) and, later, for more precise measurements, a 1.5 m long insulated thermocouple probe (Omega, 2016c) connected to a data logger (Omega, 2016b). Temperatures measured with the handheld infrared thermometer served as a guide for the secondary analysis. They were gathered by pointing on the plate at five points along its 455 mm length for gas feed levels between 20% and 100% (Figure 3.3(a)).

The preliminary results (Figure 3.3(b)-3.3(f)) showed a continuous increase of temperatures reaching after 350 seconds of heater operation an average of 840 ºC, 858 ºC, 904 ºC, 946 ºC and 983 ºC (accuracy ±2 ºC) for 20%, 40%, 60%, 80%, and 100% gas feed rate respectively. Maximum temperatures were observed in the middle area of the plate, mainly for 80% and 100% gas feed rates. This preliminary study is published in the author's paper Byzyka, Chamberlain and Rahman (2017a).
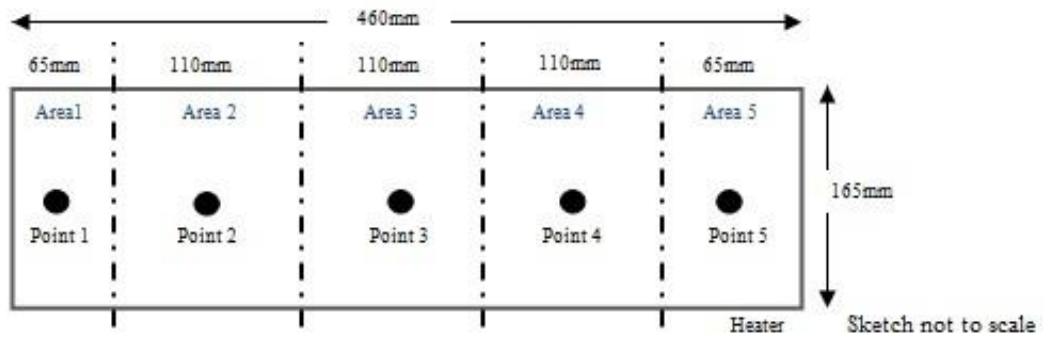
(a)
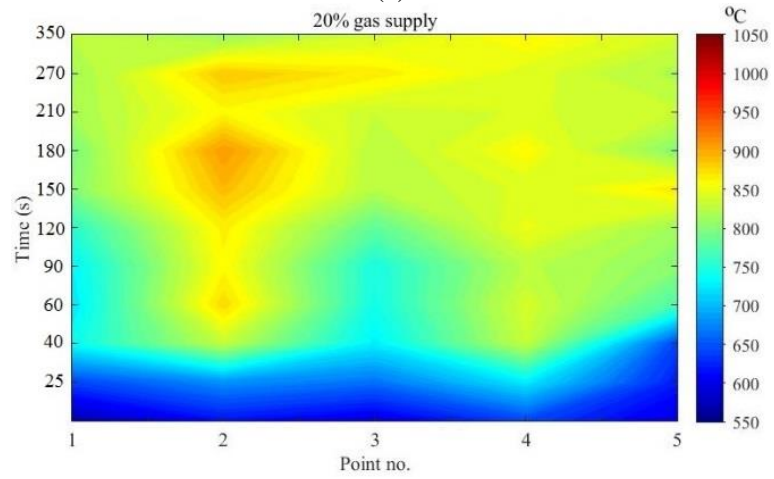
(b)
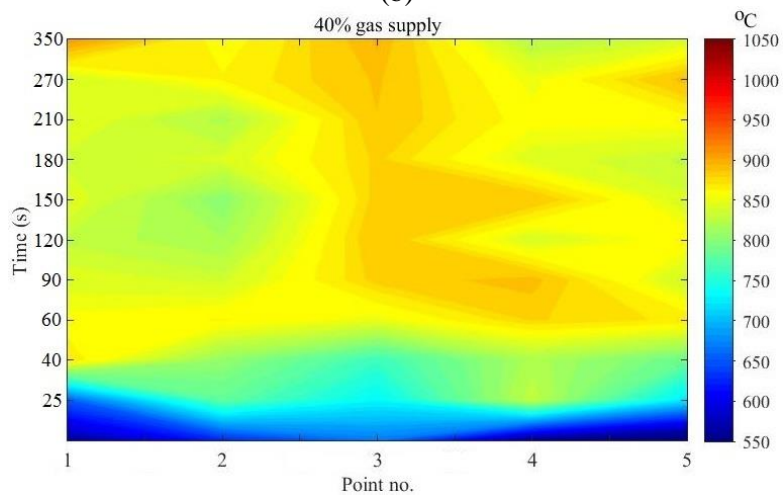
(c)

Figure 3.3 (figure continues on the next page)

(d)

(e)

(f)
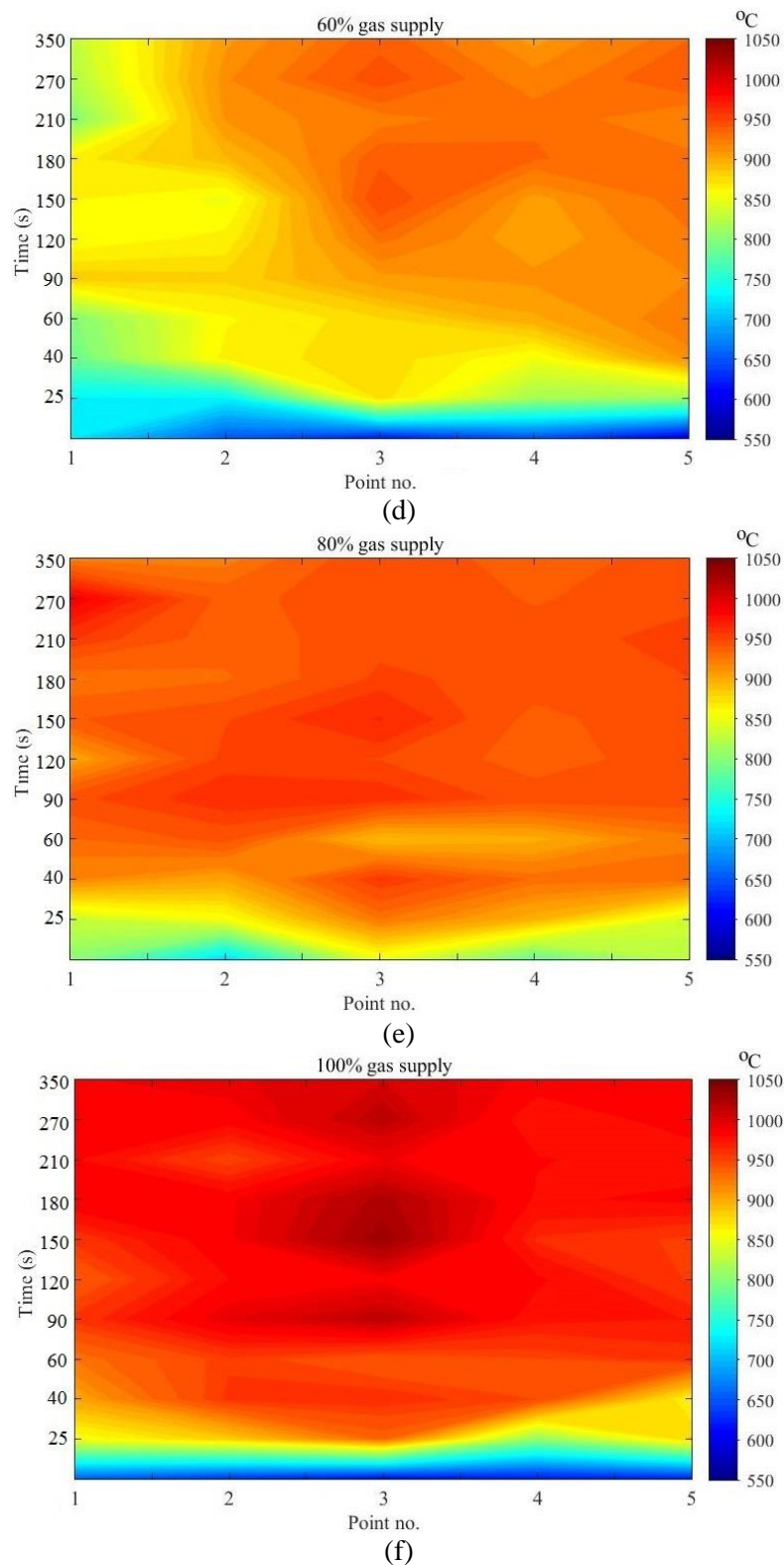
Figure 3.3 (a) Point measurement sketch for temperature measurement with a handheld infrared thermometer; and infrared detected temperature distribution after 300 seconds on heater plate when operating at (b) 20%, (c) 40%, (d) 60%, (e) 80%, and (f) 100% gas feed rates

Therefore, for the secondary measurements, the plate was divided into fifty-two zones, giving thirty-six temperature sampling point measurements on its surface (Figure 3.4(a)); twelve points along the length of the plate and three points along its width numbered as 1-12 and a-c respectively in Figure 3.4(b).

(a)

(b)
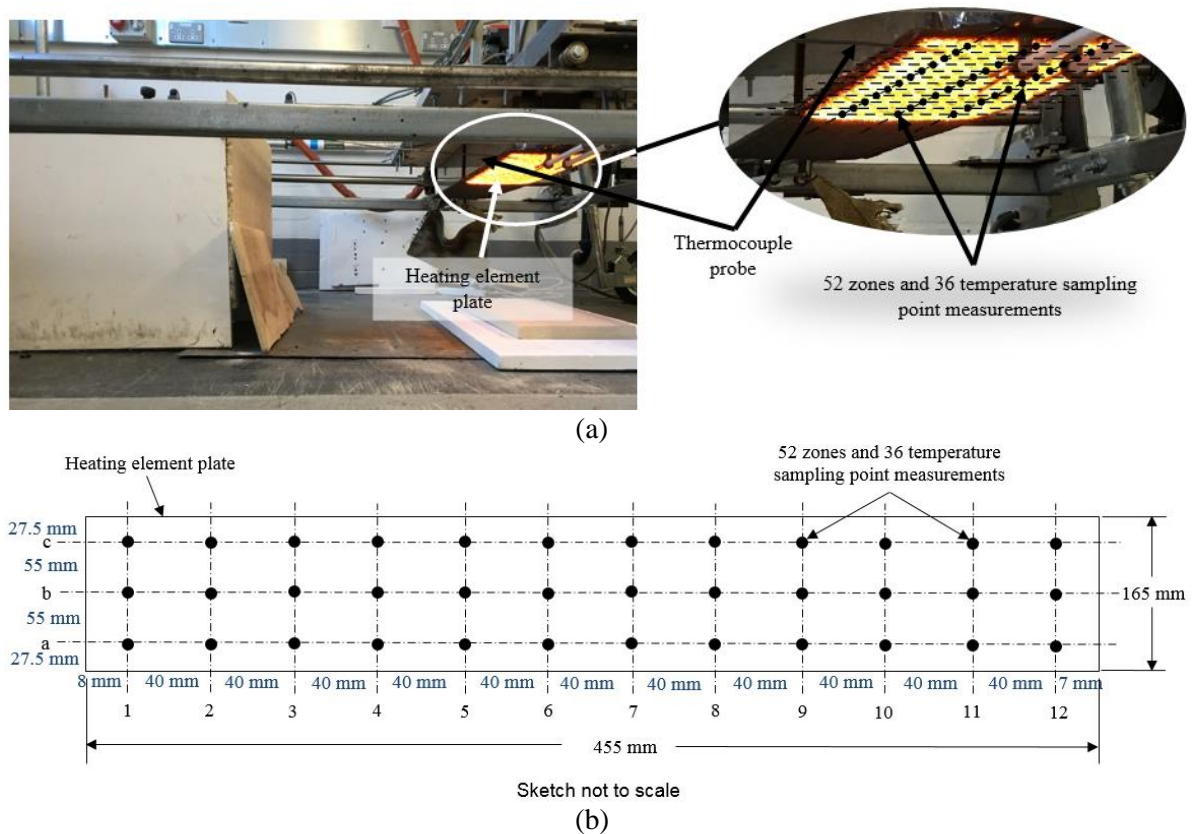
Figure 3.4 Experimental set-up to measure temperatures on heating element plate: (a) temperature sampling areas; (b) sketch of point temperature measurement grid

The probe is capable of measuring temperatures up to 1335 °C (accuracy ±1.1 °C). The probe's connector (or plug) was set at 1.5 m distance from the plate and the end of the probe directly below the plate. The plug was put on top of a wooden frame that consists of an insulating sheet (Ebay, 2016) in the front of it. The sheet withstands temperatures up to 1000 °C. Twelve holes were drilled through the insulating sheet to accommodate the previously described temperature sampling points. The test setup is presented in Figure 3.5.

(a)

1: Wooden frame
2: Insulating sheets
3: Data logger
4: 1.5 m thermocouple probe
5: Heating element plate
6: Laptop for data collection

(b)

7: 3 parallel lines on the top surface of the wooden frame that represent the positions of points a, b, and c along the width of the plate (Figure 3.4(b))
8: 12 holes drilled in the insulating sheet to represent the positions of points 1 – 12 along the length of the plate (Figure3.4(b))
9: Infrared patch heater controller

Figure 3.5 Experimental set-up to: (a) measure temperatures at points 1c - 12c of Figure 3.4; (b) measure temperatures at points 1a-12a and 1b-12b of Figure 3.4

Temperatures at points 1c - 12c were measured from the left-hand side of the heater (Figure 3.5(a)) and temperatures at points 1a, 1b - 12a, 12b on the right-hand side of the heater (Figure 3.5(b)) for the probe to properly touch the heater plate. Any gap between the probe and the plate affects the accuracy of the temperature measurements, which could not be completely avoided. In total, 180 temperature point measurements were completed. The ambient temperature during the experiments was 20 ($\pm$2) $^{\circ}$C. The heating element ignites after 23 seconds to 26 seconds and its temperature is stabilised after approximately 90 seconds for all gas feed rates. Thus, the temperatures were measured for 180 seconds. The results are shown in Figure 3.6 with illustrated temperatures being the average of points a-c for temperature sampling points 1-12 in Figure 3.4(b). The *x*-axes and *y*-axes of the contours in Figure 3.6 show points of temperature sampling related also to Figure 3.4(b) at corresponding experimental times.

(a)

(b)

(c)
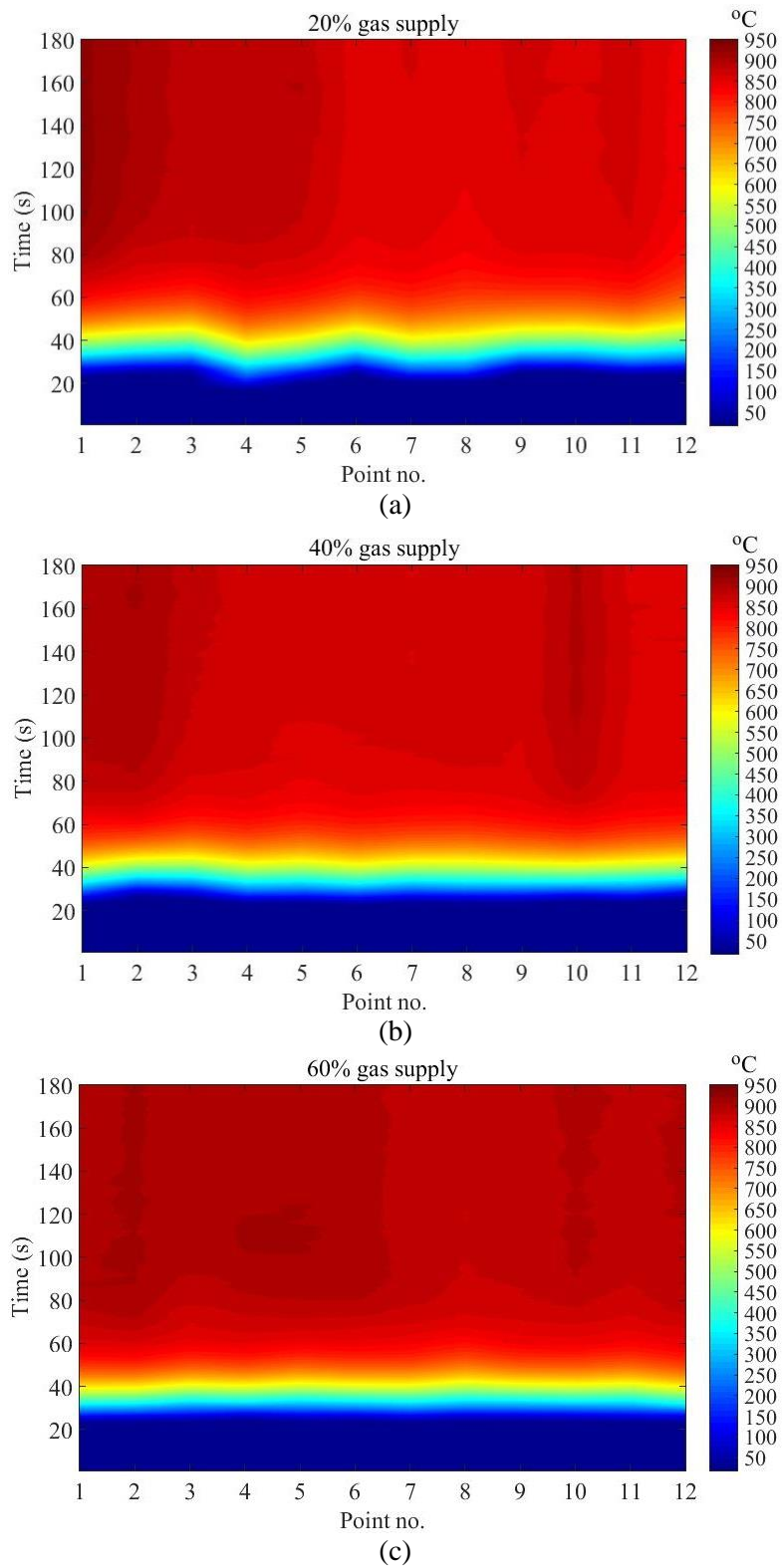
Figure 3.6 (figure continues on the next page)

(d)

(e)
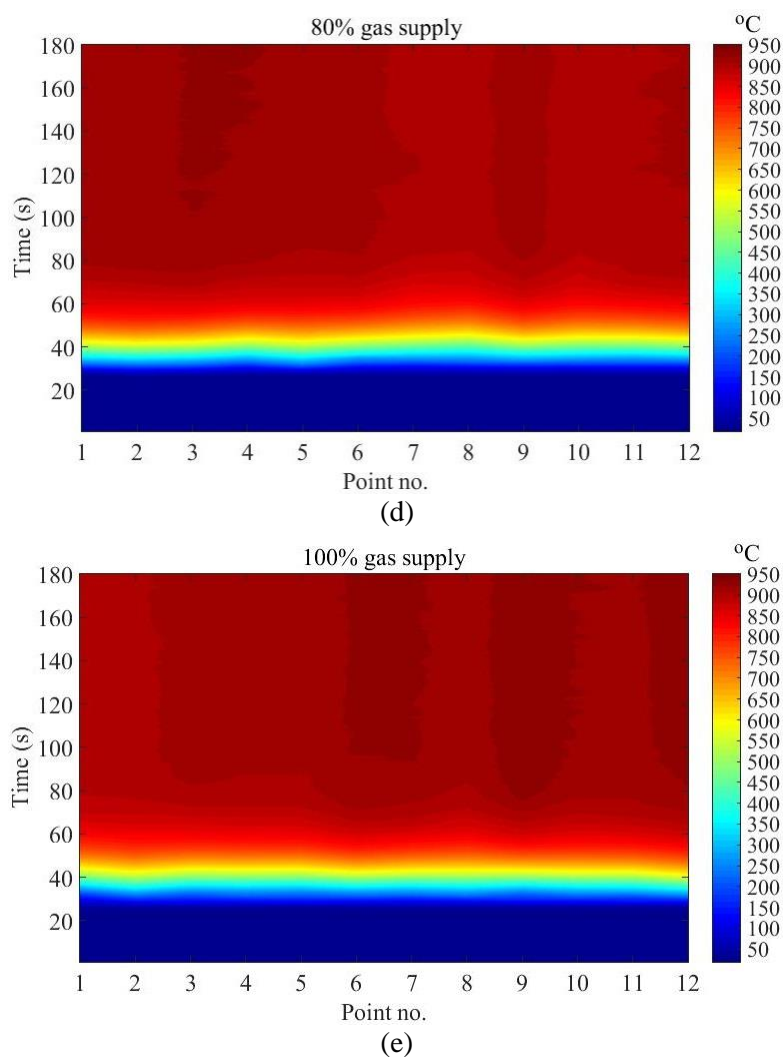
Figure 3.6 Temperature distribution on heating element plate for: (a) 20%; (b) 40%; (c) 60%; (d) 80%; and (e) 100% gas feed rates

To ensure that plate temperature was reproduced by the heater, temperature measurements at points 1b, 6b and 12b shown in Figure 3.4(b) were repeated four times performing heating-cooling cycles. This type of heater operation is from now on called "dynamic heating". For the experiment of this section, for the heating part of the cycle the heating element plate was turned on for 180 seconds and for the cooling part it was turned off for 60 seconds. The test was repeated at the same points for gas feed rates between 20% and 100%. The experiment set-up was as previously described. The ambient temperature during the tests was 16 (±2) °C. The results are presented in Figure 3.7.
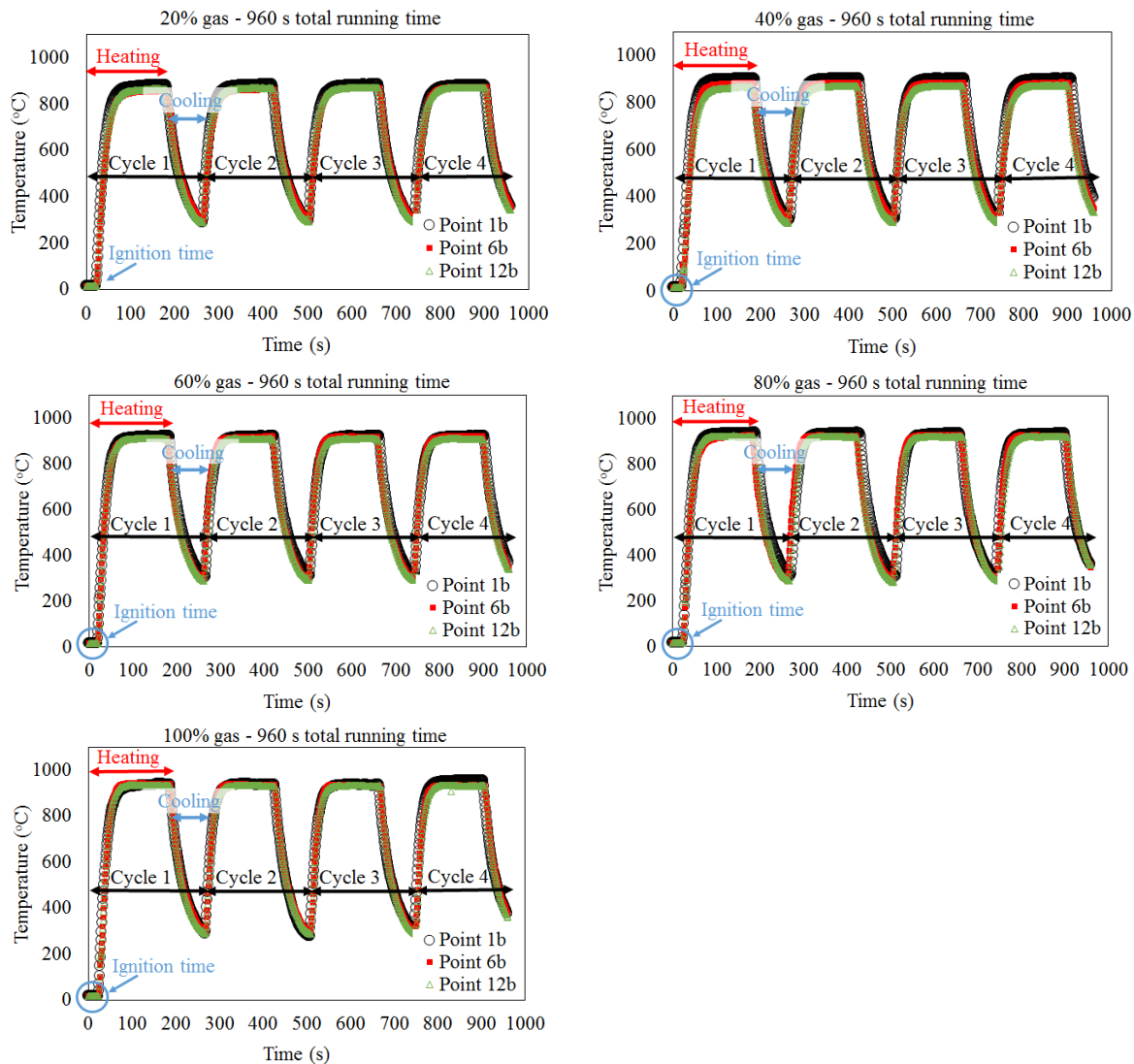
Figure 3.7 Temperatures on heating element plate during dynamic heating measured at points 1b, 6b and 12b of Figure 3.4(b)

3.3   Temperature distribution below heater plate

A non-reflective, thermal insulation board was marked out (Figure 3.8(b)) as per the matrix design shown in Figure 3.8(a); this was positioned below the heater at an offset of 300 mm below the heater plate. T-type thermocouples (Omega, 2016d) were located on the indicated 49 positions of the matrix design. A series of five temperature measurements each of 5 minutes in duration was completed; these captured the temperature distribution developed by the heating element plate when operated at 20% to 100% gas feed rates. The ambient temperature during the experiments was 29 ($\pm$4) ^{o}C. Real-time temperatures were captured using thermocouples connected to a multi-channel data logger. The thermocouples measure temperatures up to 250 ^{o}C (accuracy $\pm$ 0.5 ^{o}C). The outcomes are presented in Figure 3.9. This

experimental work is published in the author's paper Byzyka, Chamberlain and Rahman (2017a).
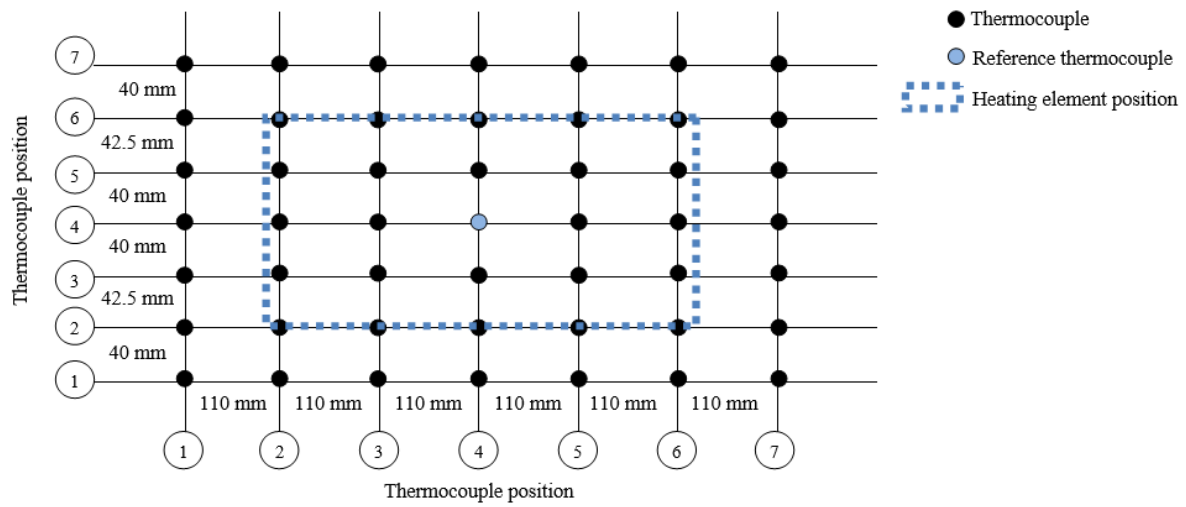
(a)
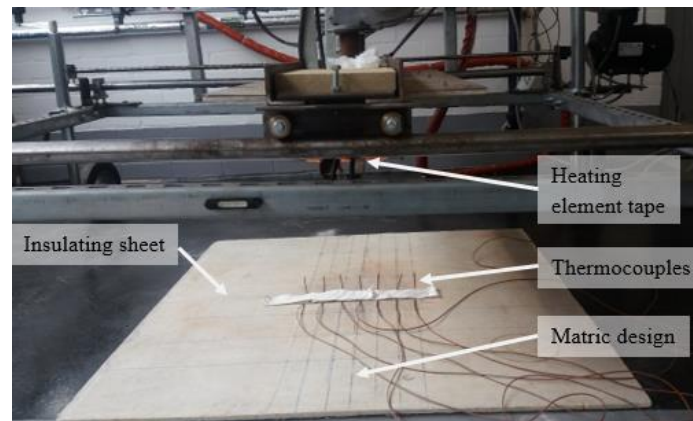
(b)

Figure 3.8 Experimental set-up to measure temperatures below the heater: (a) matrix design; (b) physical implementation of matrix

(a)

(b)

(c)
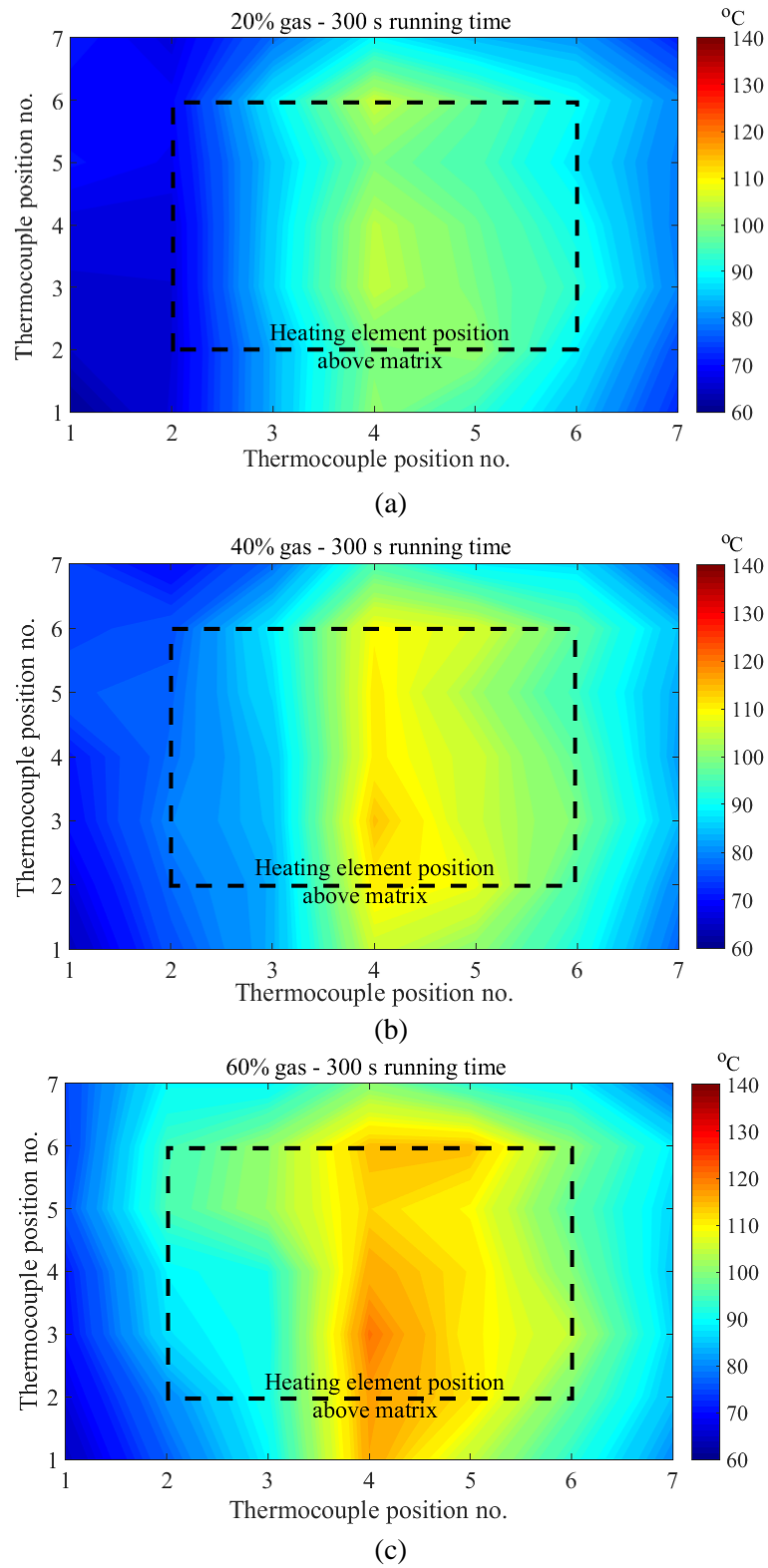
Figure 3.9 (figure continues on the next page)

(d)

(e)
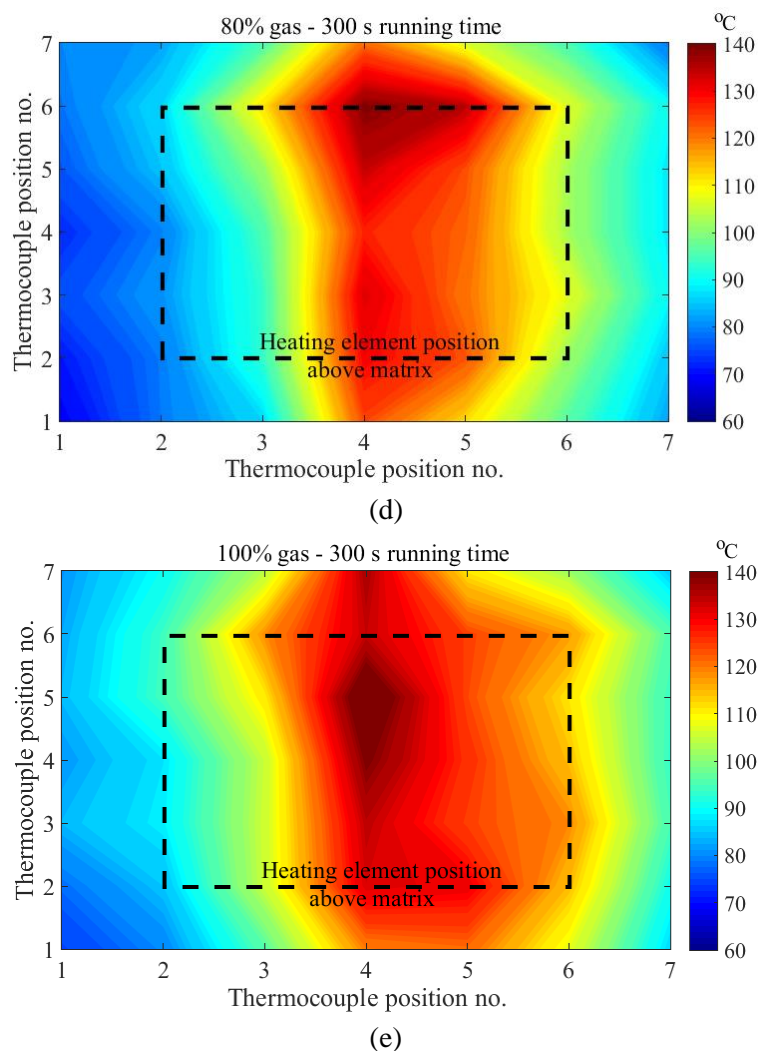
Figure 3.9 Temperature distribution below heating element plate for: (a) 20%; (b) 40%; (c) 60%; (d) 80%; and (e) 100% gas feed rates

3.4   Heater cover

To defend against the effects of extended air movement, an insulating shield was built around the heating elements. Initially, the cover was built of a high heat resistant tape (Figure 3.10(a)) (Textile Technologies Ltd, 2016) which later was replaced by thermal insulation sheets (Figure 3.10(b)) that allowed vertical movement of the cover for the different height operating capabilities of the heater. The cover also ensured safe operation of the heater by the user.
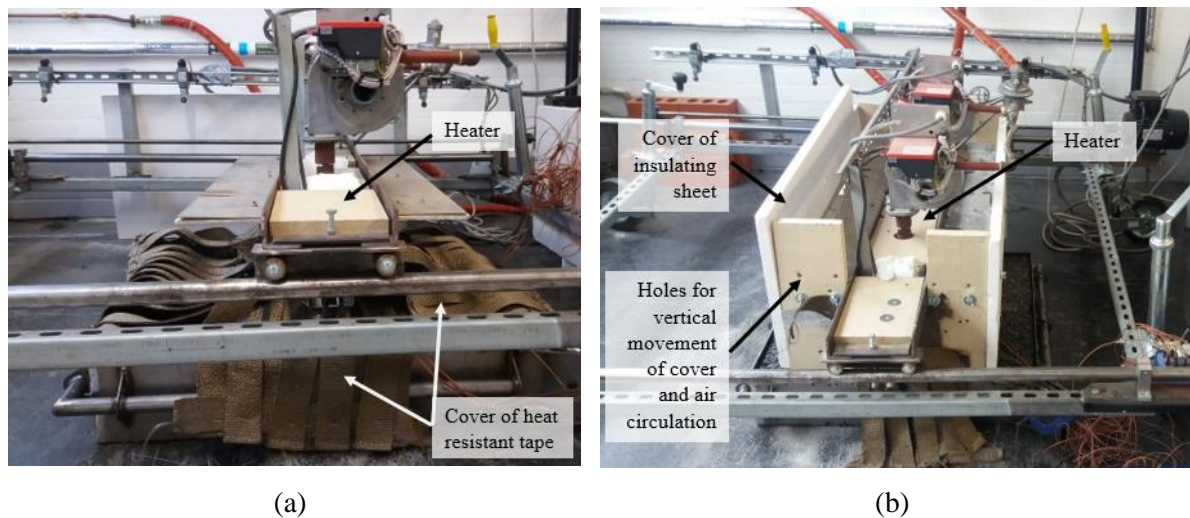
Figure 3.10 Infrared heater cover: (a) initial approach; (b) final design

3.5   Calculation of heater heat power

Heat power was calculated using the Stefan Boltzmann Law formula (Eq. 3.1):

$$P = \epsilon\, \sigma T^4 A \qquad\qquad (3.1)$$

where P = radiation energy, W; σ = Stefan-Boltzmann Constant 5.67×10^{-8} W/m^2 K^4; T = absolute temperature, K; ε = emissivity of the material; and A = area of the emitting body, m^2.

For the absolute temperature, temperatures measured on the heating element plate as described in section 3.2 and presented in Figure 3.6 were used. Since the temperatures of the plate stabilised at their respective level of radiative heat for each gas feed rate (20% - 100%) after approximately 1 minute 30 seconds of running time, only temperatures at the end of 2 minutes of the heater overall operating time were used in the calculations. The emissivity of the heater is 0.9 (Hermansson, 2001). The area of the heater is 0.075075 m^2. The average heat power of twelve temperature sampling points per gas feed rate is shown in Table 3.1. Appendix A shows in detail the values used for all the parameters of Eq. 1.

Table 3.1 Heater heat power

Gas feed rate	Heat Power (W)	Heat Power (kW)
20%	6635.33	6.6
40%	6712.24	6.7
60%	7146.72	7.1
80%	7539.39	7.5
100%	7697.47	7.7

3.6   Summary

This chapter introduced the experimental infrared heater used in the study and described experimental work done by the author to correlate heater gas feed rates with corresponding heater plate output temperatures and heat power. The next chapter utilizes the infrared heater to study temperature distribution in shallow and deep HMA pothole excavations when infrared heat is applied, correlate face excavations' temperatures with corresponding infrared heat power and find the optimum infrared heat method for shallow and deep potholes.

Chapter 4

Patch repair pre-heating method using dynamic heating

In hot mix asphalt patch repair, inadequate temperature at the interfaces is one of the influencing factors for inferior compaction and poor interface bonding. To enhance repair performance, a precisely controlled infrared pre-heating method for patch repair has been investigated and presented in this chapter. HMA slabs with 45 mm, 75 mm and 100 mm deep pothole excavations were subjected to dynamic heating. Dynamic heating was applied with the experimental infrared heater presented in Chapter 3, section 3.1. For the thermal tests of this chapter, the heater was operating at 6.6 kW - 7.7 kW heat powers. In addition, the heater was kept either stationary or moving slowly across the excavations at 130 mm and 230 mm offsets. The tests included evaluating temperature increase throughout the excavations and inside the slab and effective heating time to warm up the asphalt mixture of the slabs without burning the asphalt. The results were analysed to find the optimum pre-heating method for 45 mm, 75 mm and 100 mm deep pothole excavations in order to improve patch repair interface strength and increase repair durability. The chapter aims to address the second objective of the research.

4.1   Experiments

4.1.1 Materials

The selection of the constituent materials of an asphalt mixture for the construction of a pavement in a particular area depends mostly on traffic, climate and layer thickness. For pavement structures designed to facilitate high traffic loading, a 40/60 penetration grade bitumen binder is suitable for both base and binder courses, whereas the use of a harder bitumen such as 30/45 penetration grade bitumen binder is suitable for surface courses. In the case of a pavement structure designed for lower traffic loading, a softer bitumen type can be used for all courses. Therefore, for base and binder courses the binder can be 70/100 penetration grade bitumen and for surface course it can be either 70/100 or 100/150 penetration grade bitumen. Further, for very high trafficked roads, modified bitumens may also be considered for surface course. The choice of aggregates for all pavement courses depends on the demand in

traffic for the specific area for which the pavement is being designed and the in-place conditions where the pavement is going to be constructed (British Standards Institution, 2005). Therefore, since the choice of bitumen and aggregates depends on the factors explained above and the number of asphalt mixtures that results from the above is considerable, this study used one type of dense asphalt mixture to conduct the research.

Thus, asphalt slabs were manufactured with 20 mm dense bitumen macadam (DBM). The mix comprised of granite coarse and fine aggregate and limestone filler. The design of the mixture conforms to BS EN 13108, part 1 (British Standards Institution, 2016b) (see Table 4.1). The mixture gradation curve is shown in Figure 4.1. The binder used was 100/150 penetration grade bitumen. The binder content (equal to 4.6%) complies with BS EN 13108, part 1 (British Standards Institution, 2016b). The binder type complies with the Manual of contract documents for Highway works, Volume 1, Specification for highway works (Department for Transport, 2008).

4.1.2 Preparation of HMA and construction of HMA slabs

To construct the slabs, the asphalt mixture was first prepared. The preparation of the aggregate, filler and bitumen prior to mixing, the asphalt mixing and the procedure followed to control the mix temperature conform with BS EN 12697, part 35 (British Standards Institution, 2016a) and is shown in Figure 4.2. The slabs were constructed in batches of 7.6 kg. Twelve, seventeen and eighteen asphalt batches were used to build slabs S1 - S4, S5 - S8 and S9 - S12 respectively. The batches for each slab were all made at once and then they were used to build the slab.

The construction parameters of the HMA slabs are shown in Table 4.2. In total twelve slabs of 695 ($\pm$5) mm $\times$ 695 ($\pm$5) mm were built. Each slab was designed with one pothole excavation of 305 ($\pm$2) mm $\times$ 165 ($\pm$2) mm located in the middle of it. The depths of the excavations were 45 ($\pm$2) mm, 75 ($\pm$2) mm and 100 ($\pm$2) mm with respective slab heights 100 ($\pm$5) mm and 140 ($\pm$5) mm. The size of the slabs was selected: (a) to fulfil the purpose of the experimental work for this chapter and Chapters 6 and 8 where repair interface temperatures and strength are discussed respectively; (b) to accommodate shallow and deep pothole excavations; (c) to help limit heat losses during the thermal tests of this chapter and Chapter 6; and (d) build each slab within the opening times of the laboratory with the only available 10 lt capacity asphalt mixer.

Table 4.1 20 mm size DBM in accordance with BS EN 13108, part 1 (British Standards Institution, 2016b)

Sieve size: mm	% by mass passing	% passing selected
31.5	100	100
20	99-100	99.52
10	61-63	63.15
6.3	47	48.60
2	27-33	30.93
0.25	11-15	13.26
0.063	6	6.12
Pan	0	0
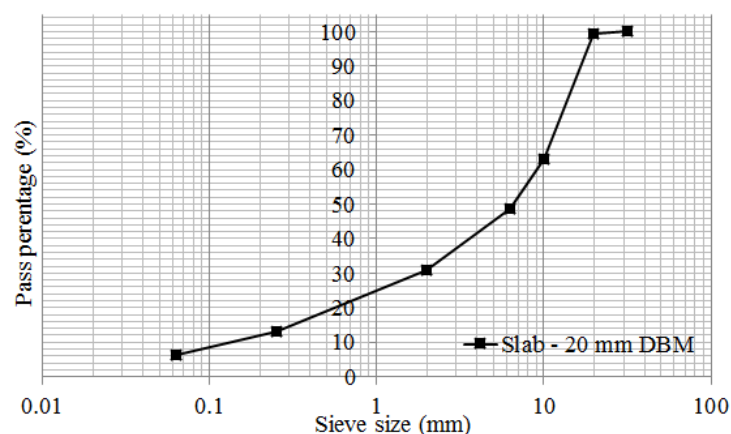
Figure 4.1 Composition of slab asphalt mixture

The depths of the potholes were chosen to represent shallow and deep potholes considering pothole depth range studied and stated by the following authors. Rahman and Thom (2012) repaired potholes with 25 mm – 50 mm depths. Miller and Bellinger (2014) note that potholes may be deeper than 50 mm. Dong, Huang and Zhao (2014) completed patches with an average depth range of 25 mm to 75 mm. McDaniel et *al*. (2014) state that patch depth may range from 38 mm to 152 mm. In addition, the area of the pothole excavations was chosen to be close to the size of the heating element plate of the experimental infrared heater used in this study and represent sizes of potholes that may be found in field projects. For example, Dong, Huang and Zhao (2014) note that they repaired potholes in field projects with surface areas ranging from 0.01 m^2 to 4.5 m^2.

(a)

(b)

(c)

(d)

(e)

(f)

Figure 4.2 Preparation of HMA batches: (a) sieving; (b) manual mixing of aggregates; (c) drying and heating of aggregates and filler for (24 + 3) hours at 110 (±5) ⁰C to a ventilated oven; (d) heating of binder and mixer bawl for 3 hours and 1 hour respectively at 140 (±5) ⁰C to a ventilated oven; (e) mixing at 140 (±5) ⁰C; (f) HMA

batches put into the ventilated oven at 140 (±5) ºC until all mixes were ready for building the slab

Table 4.2 Asphalt slabs construction parameters

Slab no.	Mixture	Slab size: (L) × (W) × (H) (mm³)	Pothole excavation size: (L) × (W) × (H) (mm³)	Construction layers	Construction layers depth (mm)
S1	20 mm DBM	695 × 695 × 100	305 × 165 × 45	2	50, 50
S2					
S3					
S4					
S5	20 mm DBM	695 × 695 × 140	305 × 165 × 75	3	50, 50, 40
S6					
S7					
S8					
S9	20 mm DBM	695 × 695 × 140	305 × 165 × 100	3	50, 50, 40
S10					
S11					
S12					

The construction process for the first and the second lifts of the 45 mm deep pothole excavations is shown in Figures 4.3 and 4.4 respectively. For the 75 mm and 100 mm deep excavations a similar construction method was followed and is shown in Appendix B, but with a larger number of batches and a larger number of aluminium tubes. The aluminium tubes (Metals4u, 2018) were embedded between the batches of the slabs to help measure temperatures during the thermal tests. This is described in more detail in section 4.1.3.

One slab could be constructed per day considering laboratory opening times. Each slab was constructed upside down. Slabs S1 - S4 were compacted in two lifts, whereas slabs S5 - S12 were compacted in three lifts. Each lift was approximately 50 mm deep and was compacted for 7 minutes using a vibratory plate compactor as described in Standard Code of Practice, New Roads and Street Works Act 1991, Specification for the Reinstatement of Openings in Highways (Department of Transportation, 2010). The lifts were bonded together by pre-heating each compacted lift for 3 minutes with infrared heat to an average surface temperature 110 (±10) ºC. This was done because the surface mixture temperature of each lift prior to compaction was on average 110 (±10) ºC. The surface temperature was measured using an infrared camera Flir C2 (Flir, 2018).

The slabs were demoulded 19 hours after their construction. The pothole moulds were removed using infrared heat. To do this, the heater was put above the pothole mould at 230 mm offset. The mould was then heated two or three times for 45 seconds with 1 minute cooling time between the heating times. This was done to allow heat to be conducted from the pothole mould to the excavation wall and warm up the asphalt. The mould was then removed by manually pulling it out. There was not any destruction observed in the excavations with the conducted demoulding process.
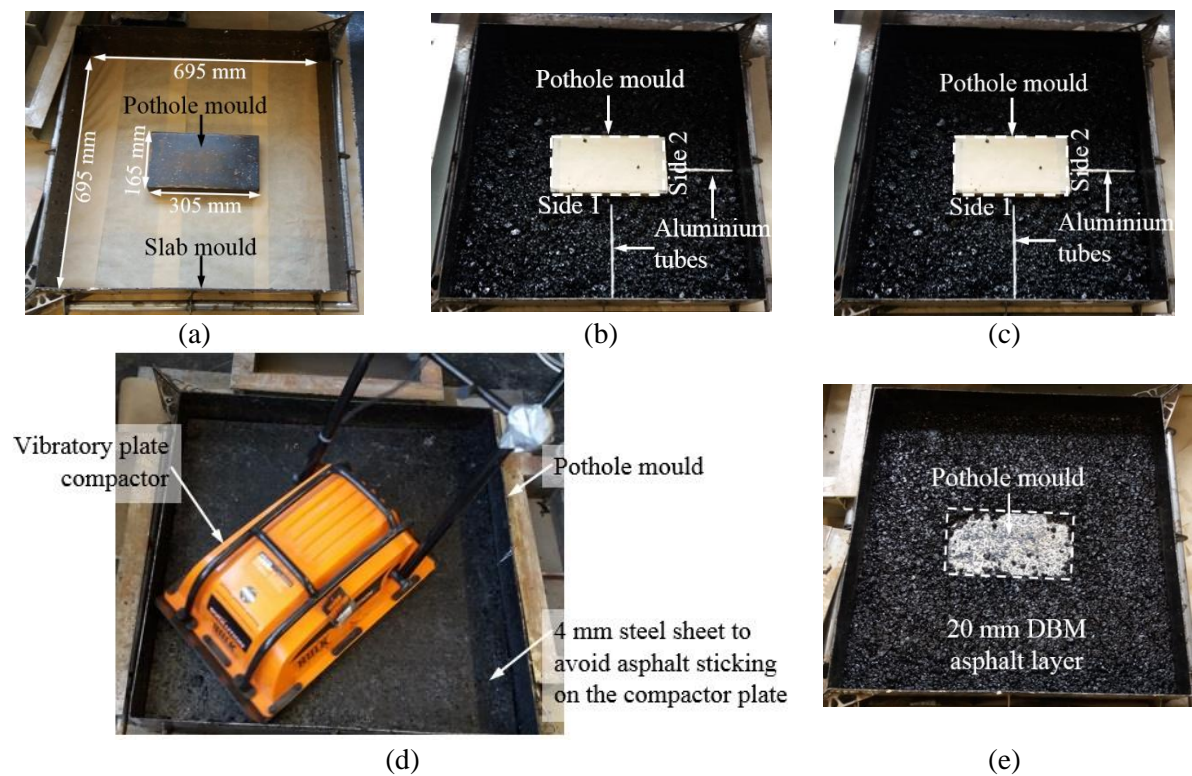
Figure 4.3 Slab with 45 mm deep pothole excavation and embedded aluminium tubes to accommodate thermocouples for thermal tests – Preparation and compaction of first lift: (a) moulds set up; (b) and (c) 4 aluminium tubes put between six asphalt batches of first lift; (d) compaction of first lift; (e) end of compaction
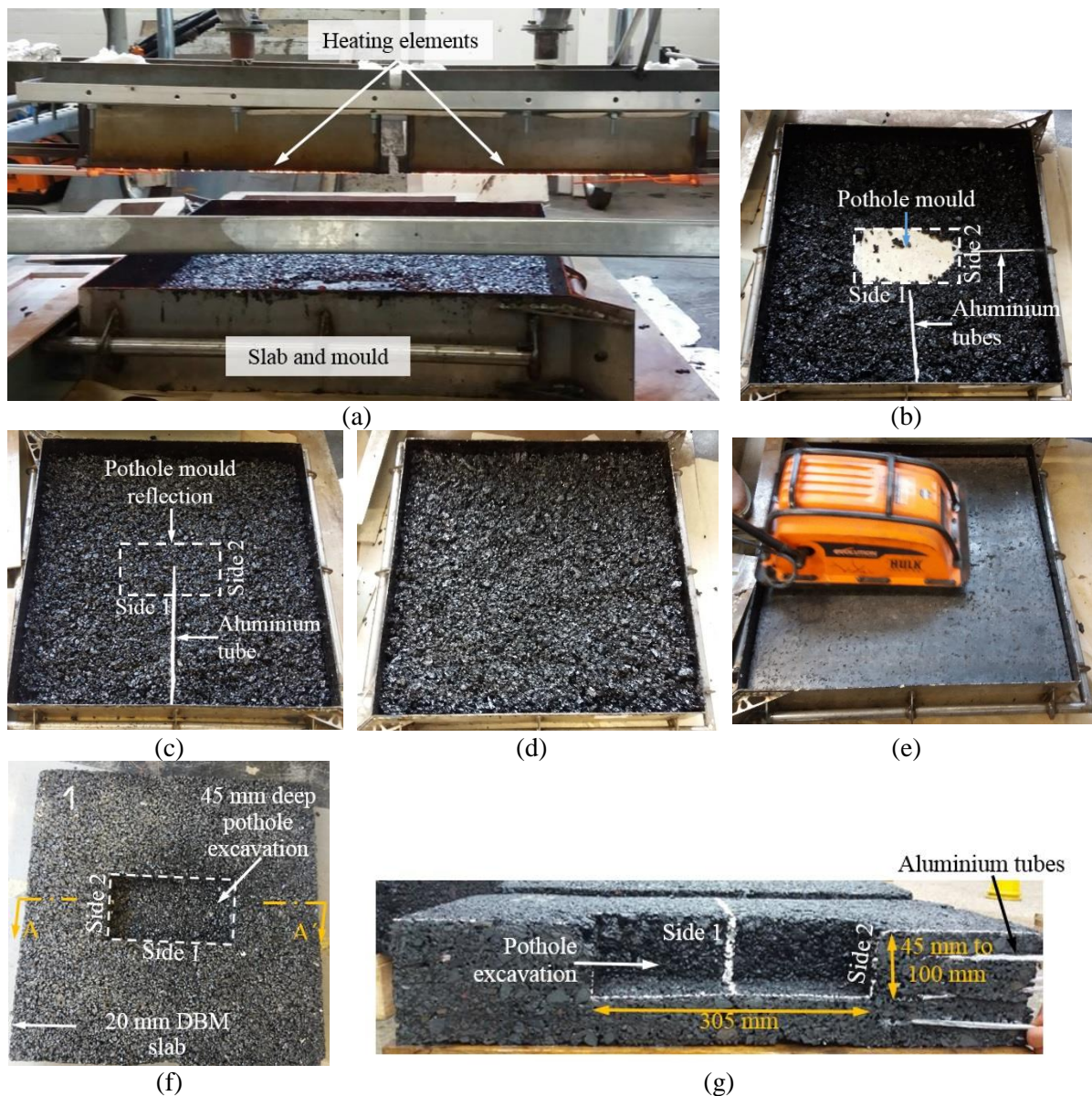
Figure 4.4 Slab with 45 mm deep pothole excavation and embedded aluminium tubes to accommodate thermocouples for thermal tests – Preparation and compaction of second lift: (a) pre-heating of compacted first lift shown in Figure 4.3(e); (b) and (c) 3 aluminium tubes between six asphalt batches of second lift; (d) final batch poured and lift ready for compaction; (e) compaction; (f) constructed slab turned upside down and pothole mould removed after 19 h of construction; (g) slab section A-A'

4.1.3 Method for measuring temperatures within the pothole excavation under dynamic heating

T-type thermocouples (accuracy of 0.5 °C) (Omega, 2016d) were used to measure real-time temperatures inside the slabs under dynamic infrared heating. The positions of the thermocouples are described in Tables 4.3 and 4.4 and shown in Figure 4.5. Hollow aluminium tubes, 4 mm in diameter, were put into the slabs during their construction. The tubes were used to put thermocouples inside the slabs (Figure 4.5(d)) and measure internal mixture temperatures during the application of infrared heat in the pothole excavations. For a 45 mm deep pothole excavation, 4 slabs (S1-S4) were built in total and 7 aluminium tubes of lengths L1, L2 and L3 (Table 4.4) were put at varying depths inside each slab. Six tubes were fixed perpendicular to sides 1 and 2 shown in Figures 4.3(b), 4.3(c) and 4.4(b) and one tube was positioned below and near the bottom face of the excavation (Figure 4.4(c)). Although the positioning of the tubes for all slabs was done similarly, the tubes moved during the construction of the slabs. This is expected to have happened mainly during the compaction of the slab mixture. For example, Tables 4.3 and 4.4 show that thermocouple T1 measured temperature at a depth from the slab surface of 22 ($\pm$5) mm and a distance from the slab external faces of L2 = 243 ($\pm$5) mm (Figure 4.5). This means that temperature at T1 may have been measured at a depth of 17 mm - 27 mm and at a distance of 238 mm - 248 mm. Similarly, nine aluminium tubes were set inside the slabs for the 75 mm and 100 mm deep excavations.

Table 4.3 Position of thermocouples laying inside the slabs

Slab no.	Slab depth (mm)	Pothole exc. depth	Thermocouple (T) no.		Depth (d) (mm)
			Side 1	Side 2	
S1 – S4	100	45 mm	T1	T5	22 ($\pm$5)
			T2	T6	42 ($\pm$8)
			T3	T7	66 ($\pm$6)
			T4	-	80 ($\pm$3)
S5 – S8	140	75 mm	T8	T13	40 ($\pm$5)
			T9	T14	65 ($\pm$5)
			T10	T15	80 ($\pm$10)
			T11	T16	102 ($\pm$6)
			T12	-	118 ($\pm$4)
S9 – S12	140	100 mm	T17	T22	25 ($\pm$5)
			T18	T23	50 ($\pm$10)
			T19	T24	75 ($\pm$10)
			T20	T25	90 ($\pm$10)
			T21	-	120 ($\pm$5)

Table 4.4 Length of thermocouples inside the slabs from slab external faces

Lengths (mm)								
L1	L2	L3	L4	L5	L6	L7	L8	L9
165 (±13)	243 (±5)	355 (±1)	165 (±15)	243 (±15)	360 (±10)	165 (±15)	243 (±150)	360 (±5)
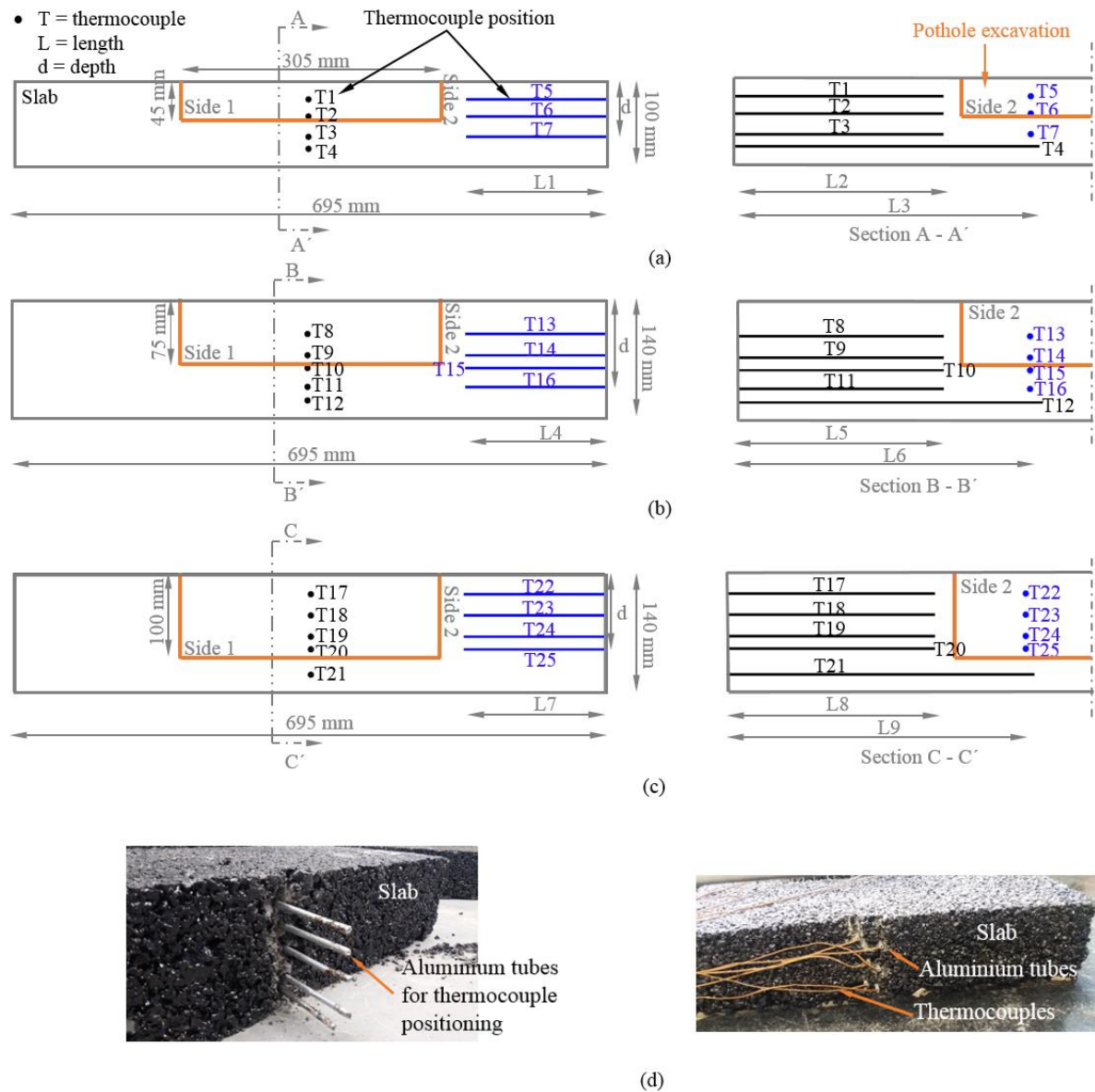
Figure 4.5 Demonstration of thermocouple positions and lengths laying inside the slabs for: (a) 45 mm; (b) 75 mm; (c) 100 mm deep pothole excavations. The physical implementation of the previous sketches is shown in (d)

T-type thermocouples (Omega, 2016d) were also used to measure temperatures at eight points within the pothole excavations. A thin steel mesh was used to keep the thermocouples in place

during the application of dynamic heat. The mesh helped also to retain the shape of the excavations. Two thermocouples were placed at the bottom corner and mid-area of the excavation respectively, four thermocouples were placed in the middle of the excavation vertical sides, and two thermocouples in the mid-top periphery of the excavation (Figure 4.6 and Table 4.5).

(a)   (b)
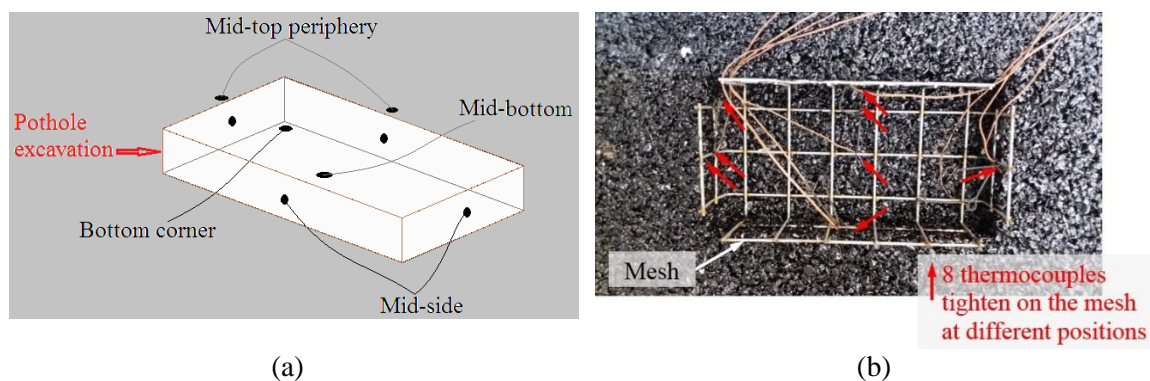
Figure 4.6 Thermocouples in the pothole excavation: (a) sketch; (b) physical implementation

Table 4.5 Characterisation of thermocouples in the pothole excavation

Slab no.	Pothole depth	Mid-bottom	Bottom-corner	Mid-side				Mid-top	
S1 – S4	45 mm	T26	T27	T28	T29	T30	T31	T32	T33
S5 – S8	75 mm	T34	T35	T36	T37	T38	T39	T40	T41
S9 – S12	100 mm	T42	T43	T44	T45	T46	T47	T48	T49

4.1.4 Description of dynamic heating method for thermal tests

The parameters of the thermal tests are summarised in Table 4.6. Dynamic heating was applied in the pothole excavations using the experimental infrared heater described in Chapter 3, section 3.1. The excavations were heated in heating-cooling cycles, referred to as "dynamic heating". For the heating part of the cycle, the heater was operating at heat powers 6.6 kW, 6.7 kW, 7.1 kW, 7.5 kW and 7.7 kW. The excavations were heated until the thermocouples closest to the heating element plate (see T32, T33, T40, T41, T48 and T49 in Figure 4.6 and Table 4.5) measured asphalt temperatures between 140 ℃ and 160 ℃. This was done to avoid burning the asphalt. Similar asphalt heating levels are also suggested by previous studies. Uzarowski et *al*. (2011) suggest heating the repair area to a temperature not greater than 190 ℃. Nazzal, Kim and Abbas (2014) suggest to pre-heat the old pavement until temperatures reach 135 ℃ to 190

ºC levels. In addition, Huang, Xu and Jiang (2016) note that heating asphalt between 137 ºC and 226 ºC reduces ageing or charring of asphalt binder. Asphalt ageing happens due to volatilisation, oxidation, and other chemical processes. Asphalt oxidation should be avoided because it leads to pavement failure due to asphalt binder hardening, change in viscosity, asphalt separation, asphalt embrittlement, loss of bitumen cohesion and bitumen-aggregate adhesion (Mill et *al*., 1992). For the cooling part of the cycle, the heater was simply turned off and no heating was applied until temperatures of T32, T33, T40, T41, T48 and T49 reached temperatures between 70 ºC and 80 ºC. Cooling was done to allow heat to be conducted within the slab and warm up the asphalt mixture around the pothole excavations.

Further, the tests were conducted with heating applied at 130 mm and 230 mm offsets from the surface of the slab. The heating elements were stationary above the excavations or moving across the excavations. The moving distance within the heater steel frame was 1 m. This distance could be automatically set to be covered by the heating elements in which case they would be moving forward and backwards repetitively within the heater steel frame.

Table 4.6 Thermal test parameters

Slab no.	Heat Power (kW)	Heater offset from slab top surface: 130 mm		Heater offset from slab top surface: 230 mm	
		Stationary heater	Moving heater	Stationary heater	Moving heater
S1	6.6, 6.7, 7.1, 7.5 and 7.7	✓			
S2			✓		
S3				✓	
S4					✓
S5	6.6, 6.7, 7.1, 7.5 and 7.7	✓			
S6			✓		
S7				✓	
S8					✓
S9	6.6, 6.7, 7.1, 7.5 and 7.7	✓			
S10			✓		
S11				✓	
S12					✓

4.1.5 Thermal tests set up

Dynamically heating the pothole excavation is intended to improve common pothole repair practices with or without pre-heating to ultimately increase interface bonding and therefore pothole repair durability. The pothole pre-heating method discussed in this chapter would be

expected to follow after the failed asphalt mixture of the pavement is removed and the excavation is cleaned from debris and water. Since the pothole excavations studied in the research were artificially created, these steps were not included in the described pre-heating processes.

The thermal test set up is shown in Figure 4.7. It consists of the infrared heater with its frame discussed in Chapter 3, section 3.1, the asphalt slab with its mould that helps to keep the slab confined during the thermal tests, the thermocouples for real-time temperature measurement, the data loggers and a laptop for real-time collection of temperatures. Sixty thermal tests were completed in total (20 tests per pothole excavation depth). Temperatures were measured for a duration of approximately 30 minutes. The tests were performed 30 days after the construction of the slabs and measurement of thermal conductivity. As the sample size was big, this timeframe was necessary to optimise laboratory resources during sample preparation and production and carry out additional test (like thermal conductivity) on the whole sample. The ambient temperature during the tests was approximately 21 (±1) °C.
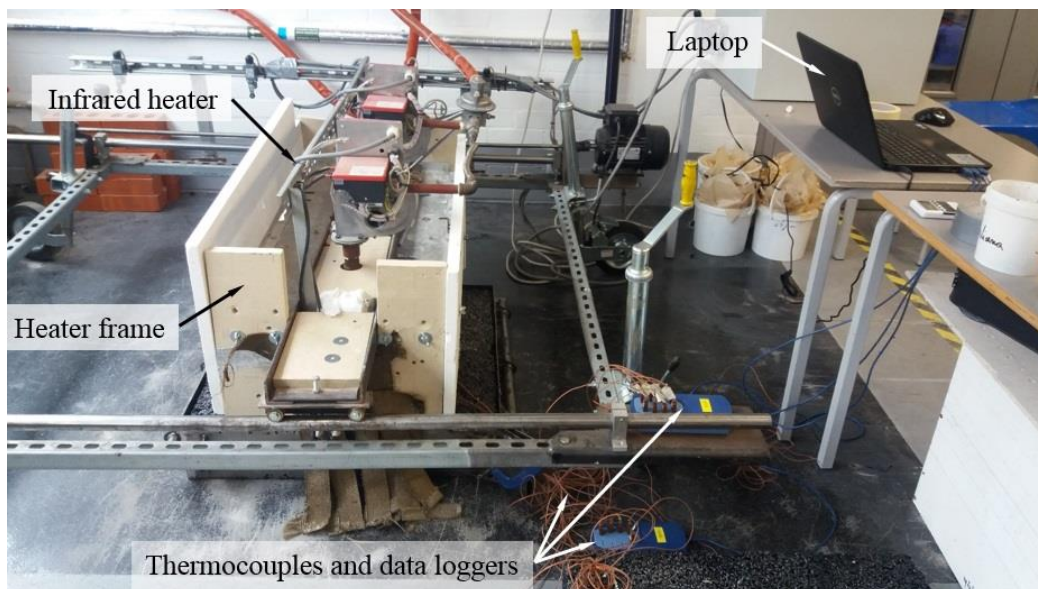
Figure 4.7 Thermal test setup for stationary and moving heater

4.2   Asphalt thermal properties

4.2.1 Thermal conductivity (k)

For this study, thermal conductivity was measured at eleven points per slab (Figure 4.8(a)) prior to commencing the thermal tests. During the measurement of thermal conductivity, the

ambient temperature was approximately 20 ($\pm$2) $^{\circ}$C. At the same time, the temperature of the slabs was approximately 21 ($\pm$1) $^{\circ}$C. Thermal conductivity was measured with the transient line source (TLS) (Thermtest, 2018) shown in Figure 4.8(b). The temperature of the slabs was also measured using the TLS. This method of thermal conductivity measurement was discovered in the literature and was described in Chapter 2, section 2.8.1.

(a)
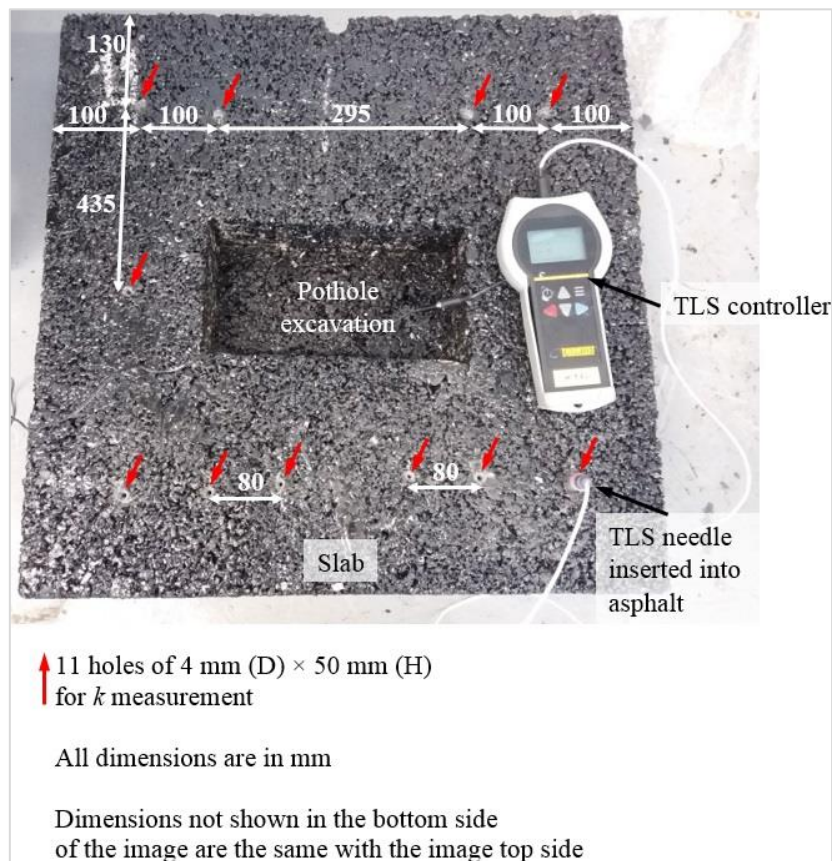
(b)

Figure 4.8 Measurement of thermal conductivity in asphalt slabs: (a) TLS 50 mm needle with thermal paste; (b) TLS-50 mm instrument and sampling points for *k* measurement

The TLS includes the TLS controller and a 50 mm needle designed for testing samples that are tough to drill such as rock, concrete or asphalt samples. The TLS has an accuracy of 5% and reproducibility of 2%. The TLS method follows ASTM D5334 (American Society for Testing and Materials, 2000) and has been previously used in investigations of thermal conductivity by Chadbourn et *al.*, (1996), Blázquez et *al.* (2018) and Lu et *al.* (2018). To measure thermal conductivity with the TLS-50 first 4 mm (D) $\times$ 50 mm (H) holes were drilled in the asphalt slab (Figure 4.8(b)). Then, the excess powder in the holes created from drilling was blown out with compressed air. The needle was covered with a thermal paste called Arctic Alumina (Overlockers, 2018) (Figure 4.8(a)) before inserting it completely into the slab. The thermal paste helps to fill any air gaps in the hole and promote good thermal contact between the slab mixture and the needle. Thermal conductivity was calculated by the TLS using Eq. 4.1:

$$k = \frac{q}{4\pi a} \tag{4.1}$$

where k = thermal conductivity, W/m K; q = heating power, W; a = slope. The slope comes from a plot of temperature rise in the sample when heated by the TLS versus the logarithm of time (Thermtest, 2018).

4.2.2 Thermal diffusivity (a) and specific heat capacity (c_P)

Thermal diffusivity (a) and specific heat capacity (c_P) were calculated using Eq. 2.1 and Eq. 2.2 respectively described in Chapter 2, section 2.8.

4.3   Air voids content

The air voids content of the compacted asphalt slabs was calculated based on the calculation of the maximum specific gravity and the maximum theoretical specific gravity of asphalt mixture from cores extracted from the slabs. The bulk specific gravity (G_{mb}) was determined through the AASHTO T166, method A (American Association of State Highway and Transportation Officials, 2007) and the maximum theoretical specific gravity (G_{mm}) was calculated with Eq. 4.2 (Roberts et *al.*, 1991). In this equation, the effective specific gravity of aggregate (G_{se}) was taken as 2.65 and the specific gravity of bitumen (G_b) as 1.01 (measured at 25 ºC). The specific gravities were provided by the companies from where the materials were purchased. Thereafter, the percentage of air voids in the mixture was calculated with Eq. 4.3.

$$G_{mm} = \frac{W_T}{\frac{W_{agg}}{G_{se}} + \frac{W_{AC}}{G_b}} \tag{4.2}$$

where W_T = total eight of asphalt mixture, gr; Wagg = weight of aggregate, gr; W_{AC} = weight of total asphalt binder, gr.

$$VTM = \left(1 - \frac{G_{mb}}{G_{mm}}\right) \times 100\% \tag{4.3}$$

where VTM = voids in total mix, %.

Figure 4.9 shows the coring rig (JKS UK LTD, 2018) used in this study and the locations from where the cores were in general obtained from each slab. The cores were extracted throughout the whole sample in order to test overall air voids distribution. Further, the cores were extracted from the slabs at the end of the thermal tests conducted per slab. After the coring, the slabs were not used in any testing.

                                  (a)   (b)
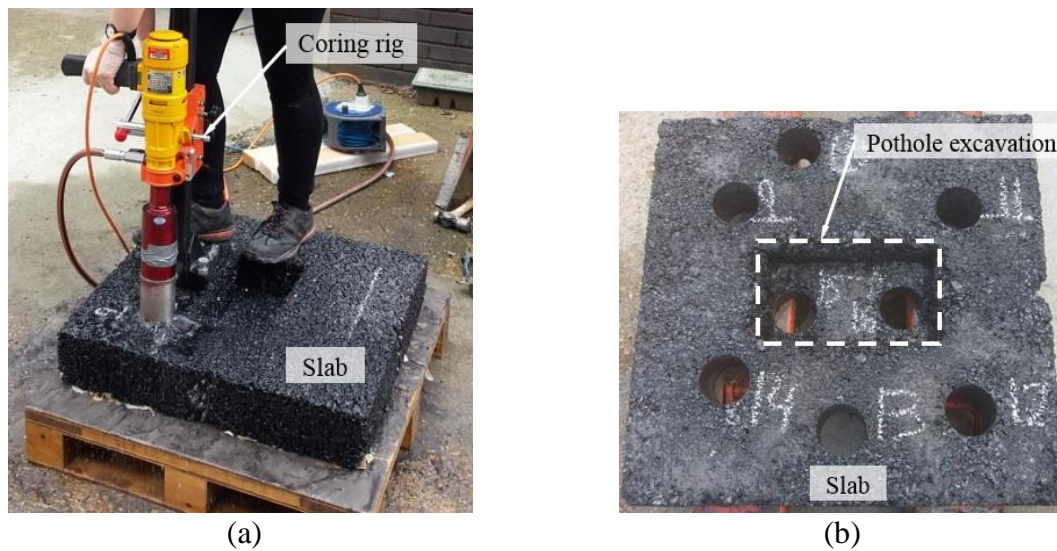
Figure 4.9 Coring: (a) slab and coring rig; (b) locations of cores

4.4   Results and discussion

4.4.1 Thermophysical properties

Table 4.7 shows air voids, thermal conductivity, calculated specific heat capacity and thermal diffusivity of the compacted asphalt slabs. The table shows values from the average of five

cores per slab for slabs S1 and S2 and from the average of eight cores per slab for slabs S3 to S12. The number of cores depended only on how many cores could be taken from the constructed slabs. Slabs S1 and S2 where cored first and it was then seen that even more than five cores could be taken. Appendix C presents in detail the thermophysical properties of slabs S1-S12.

Table 4.7 Calculated average thermophysical properties of asphalt mixture and standard deviation (SD) of results

Slab no.	Core diameter (mm)	Core height (mm)	Air voids content (%)	SD of air voids content (%)	Thermal conductivity (W/m K)	SD of thermal conductivity (W/m K)	Specific heat capacity (J/kg K)	Thermal diffusivity ($\times 10^{-7}$) (m²/s)	SD of thermal diffusivity ($\times 10^{-7}$) (m²/s)
S1	72	1 core of 55 & 4 cores of 100 per slab	10.04	0.43	1.12	0.12	865.44	5.84	0.63
S2	72		10.51	0.71	1.05	0.12	865.44	5.52	0.63
S3	72	1 core of 55 & 7 cores of 100 per slab	11.99	0.32	0.98	0.06	865.44	5.20	0.34
S4	72		11.18	0.52	1.10	0.05	865.44	5.78	0.29
S5	72	2 cores of 65 & 6 cores of 140 per slab	13.08	1.39	1.24	0.15	865.44	6.72	0.88
S6	72		11.52	2.23	1.11	0.17	865.44	5.86	0.89
S7	72		12.25	0.82	1.09	0.22	865.44	5.80	1.18
S8	72		10.88	1.22	1.22	0.25	865.44	6.39	1.22
S9	72	1 core of 40 & 7 cores of 140 per slab	10.74	0.32	1.00	0.08	865.44	5.26	0.46
S10	72		10.79	0.52	1.16	0.06	865.44	6.08	0.31
S11	72		11.10	1.39	1.18	0.15	865.44	6.18	0.88
S12	72		10.47	2.23	1.22	0.17	865.44	6.36	0.89

The results show that air voids content ranged from 10% to 13%. The effect of asphalt pre-heating on air voids has not been investigated in this study due to lack of laboratory equipment and no other study for infrared heated patch repair was found to mention it. However, the author acknowledges that in some areas of the slabs, air voids may have been reduced, while in other areas they may have been increased. This happens because when the temperature increases bitumen tends to flow as a consequence of gravity. As a result, the internal structure of the mixture can be redistributed and the air voids can be restructured. The areas affected by the pre-heating would probably be those closer to the heated pothole excavation, near the heater

where some cores were also taken or in the areas where heat was conducted due to excavation pre-heating. The effect of asphalt heating in asphalt mixture air voids has been noted by Norambuena-Contreras and Garcia (2016) in their study for self-healing of asphalt mixture by microwave and induction heating.

Table 4.7 demonstrates that thermal conductivity of the asphalt slabs ranged from 0.98 W/m K to 1.24 W/m K. The results show that thermal conductivity is significantly affected by the high percentage of air voids in the slabs. This happened because air has much lower thermal conductivity (0.025 W/m K (Eppelbaum, Kutasov and Pilchin, 2014) compared to the thermal conductivity of granite aggregate (2.68 W/m K (Eppelbaum, Kutasov and Pilchin, 2014)) and limestone filler (2.92 W/m K (Pan et *al*., 2017)) used in this study and binder (0.39 W/m K (Pan et *al*., 2014)). High air voids also means lower interlocking between the aggregates of the mixture, less thermal conductance paths into the asphalt mixture and therefore lower thermal conductivity. This effect of air voids in asphalt thermal conductivity has also been reported by Mirzanamadi, Johansson and Grammatikos (2018) and Hassn et *al*. (2016).

Further, in this study, thermal conductivity was measured with the TLS method. The TLS needle was inserted into holes drilled throughout the slabs and thermal conductivity was calculated by the TLS controller using the heat conduction equation. This means that the measurement of thermal conductivity was affected by the distribution of mineral materials around the drilled hole, the cleanliness of the hole and the thermal contact between the asphalt mixture and the needle. In addition, specific heat capacity was found equal to 865.44 J/kg K. Specific heat capacity is considerably affected by the temperature and mass of the asphalt mixture. In this study, both parameters remained at similar levels for all slabs. Finally, thermal diffusivity had been found to range between 5.20×10^{-7} m^2/s and 6.72×10^{-7} m^2/s. These values were affected by the range of the thermal conductivity and volumetric heat capacity. The discussed effect is also noted by Mirzanamadi, Johansson and Grammatikos (2018) and Hassn et *al*. (2016).

In addition, Table 4.7 shows the standard deviation (SD) of air voids content, thermal conductivity and thermal diffusivity results per slab. The SDs of air voids content were found to range from 0.32% to 0.71% for S1-S4, from 0.82% to 2.23% for S5-S8 and from 0.32% to 2.23% for S9-S12. The SDs of thermal conductivity were found to range from 0.05 W/m K to 0.12 W/m K for S1-S4, from 0.15 W/m K to 0.25 W/m K for S5-S8 and from 0.08 W/m K to

0.17 W/m K for S9-S12. The SDs of thermal diffusivity were found to range from 0.29 ($\times 10^{-7}$) m^2/s to 0.63 ($\times 10^{-7}$) m^2/s for S1-S4, from 0.88 ($\times 10^{-7}$) m^2/s to 1.22 ($\times 10^{-7}$) m^2/s for S5-S8 and from 0.31 ($\times 10^{-7}$) m^2/s to 0.89 ($\times 10^{-7}$) m^2/s for S9-S12. Generally, it seems that the SDs of all calculated thermophysical properties of asphalt mixture were higher for slabs S5-S12 which were constructed with three lifts and had a post compaction height of 140 mm, whereas slabs S1-S4, those with lowers SDs, were constructed with 2 lifts and had a post-compaction height of 100 mm. Overall, the resulting deviations are considered acceptable for a non-homogeneous material like asphalt.

4.4.2 Temperature distribution in pothole excavation and inside the slabs under dynamic heating

The temperatures captured in the 45 mm, 75 mm and 100 mm deep excavation walls and inside the slabs are presented in Figures 4.10 to 4.15. Figures 4.10, 4.12 and 4.14 show temperature profiles for a stationary heater above the excavations, whereas, Figures 4.11, 4.13 and 4.15 show temperature profiles for a heater moving across the excavation. Each figure contains ten graphs and demonstrates temperatures per thermocouple position at the end of approximately 10 minutes, 20 minutes and 30 minutes dynamic heating. Temperatures are reported for operation of heater with 6.6 kW, 6.7 kW, 7.1 kW, 7.5 kW and 7.7 kW heat powers and for 130 mm and 230 mm heater offsets. The slab number used to perform the thermal tests and the number of heating-cooling cycles for each dynamic heating time are also reported. All thermal tests finished with the heating part of the cycles (or half cycle) and therefore the heating-cooling cycles are reported with numbers such as 3.5, 6.5, 8.5 etc. For example, in Figure 4.10, for 10 minutes dynamic heating and the heater operating at 6.6 kW heat power at 130 mm offset, three and a half cycles were done. For the three whole cycles, the heater was on and off repeatedly. For the half-cycle, the heater was on for some time and then removed from the pothole pre-heating procedure. The heating-cooling cycle procedure was also described in section 4.1.4.

Overall, the results show higher temperatures in the faces of the pothole excavation than inside the slabs. This happened because the temperatures in the excavation increase due to radiation, whereas, the percentage of the heater radiative energy that reaches the slab and is absorbed by it will increase the temperature of the asphalt mixture inside the slab. The absorptivity of asphalt mixture depends on the colour of the mixture, as light colour asphalt surfaces have higher reflectance (Kyriakodis and Santamouris, 2018), and the surface roughness (Stephens and Cody,1977). Hassn et *al*. (2016) showed that asphalt pavements with high percentage of

air voids, like the slabs in this study, have higher reflectance than pavements with lower percentage of air voids. This happens because the illumination surfaces and angles are higher for high air void content mixtures (Stephens and Cody,1977). Once the heater energy is absorbed by the asphalt, the increase of mixture temperature inside the slabs depends on initial slab temperature and heat transfer mainly due to conduction which is dependent on the thermal properties of the mixture.

4.4.2.1   Slabs with 45 mm deep pothole excavation

The heating effects of dynamic heating are shown in Figures 4.10 and 4.11. It is observed that temperatures in the pothole excavation and inside the slab were increased non-uniformly. The temperature increase rate inside the slab was higher for the first 10 minutes of heating than between 10 minutes and 30 minutes of heating. This happened because thermal conductivity decreases as mixture temperature increases. The effect of temperature in thermal conductivity of asphalt mixture will be shown in Chapter 5. It has been also previously noted by Chadbourn et *al*. (1996) for temperatures between 25 ^{o}C and 75 ^{o}C and by Pan et *al*. (2017) for temperatures between -20 ^{o}C and 60 ^{o}C. Further, Pan et *al*. (2017) suggest that the decrease of thermal conductivity at higher mixture temperatures is mainly affected by the thermal conductivity of aggregates, as they account for more than 90% of the mixture than the thermal conductivity of the binder.

Overall, temperatures measured in the mid-bottom of the pothole excavation (T26) exhibited the highest increase in temperature and reached 140 ^{o}C to 160 ^{o}C. High temperatures but lower than T26, mainly in the region of 120 ^{o}C to 140 ^{o}C, were observed in the mid-top periphery of the pothole excavation (T32 and T33). There were two reasons that T26 had higher temperatures than T32 and T33. Firstly, the uneven distribution of temperatures on the heating element plate as shown in Chapter 3, section 3.2. Secondly, T32 and T33 were located at the top of the excavation periphery and it seems that the heat loss was higher at those points than at the bottom of the excavation. This also shows that the effect of the external environment was higher for T32 and T33 than T26. In addition, the lowest temperatures were observed in the sides (T28-T31) and the corner (T27) of the pothole excavation. This shows that the heater had a larger view of the points located in the horizontal faces of the pothole excavation than the points located in the vertical faces of the excavation. To this extent, temperatures for T28-T31 and T27 ranged from 80 ^{o}C to 120 ^{o}C.

Overall, temperatures in the pothole excavation were higher for 7.7 kW than for 6.6 kW. However, no increasing or decreasing trend was observed for temperatures resulting from heater heat powers in between the 6.6 kW-7.7 kW range. This means that temperatures in the pothole excavation may either increase or decrease without depending on the heater heat power between the heat power range noted above Similar reaction was also observed when excavation temperatures were compared (a) between 130 mm and 230 mm heater offsets for stationary and moving heater for each heater operating heat power and (b) between stationary and moving heater for 130 mm and 230 mm heater offsets for each heater operating heat power.

Heat inside the slabs was transferred from top to bottom. Temperatures tend to increase during the heating-cooling cycles but had a lowering trend from the top to the bottom of the slabs. The latter is mainly attributed to the slow heat transfer due to low thermal conductivity and volumetric specific heat capacity of the asphalt mixture of this study. Overall, thermocouples T1 and T5 located closer to the top surface of the slabs captured temperatures between 40 $^{\circ}$C and 80 $^{\circ}$C. Below T1 and T5, temperatures for T2-T4, T6 and T7 ranged from 20 $^{\circ}$C to 70 $^{\circ}$C. A similar pattern of temperature increase between temperatures in pothole excavation and inside the slabs was observed for the three different durations of dynamic heating with heater being either stationary or in motion.
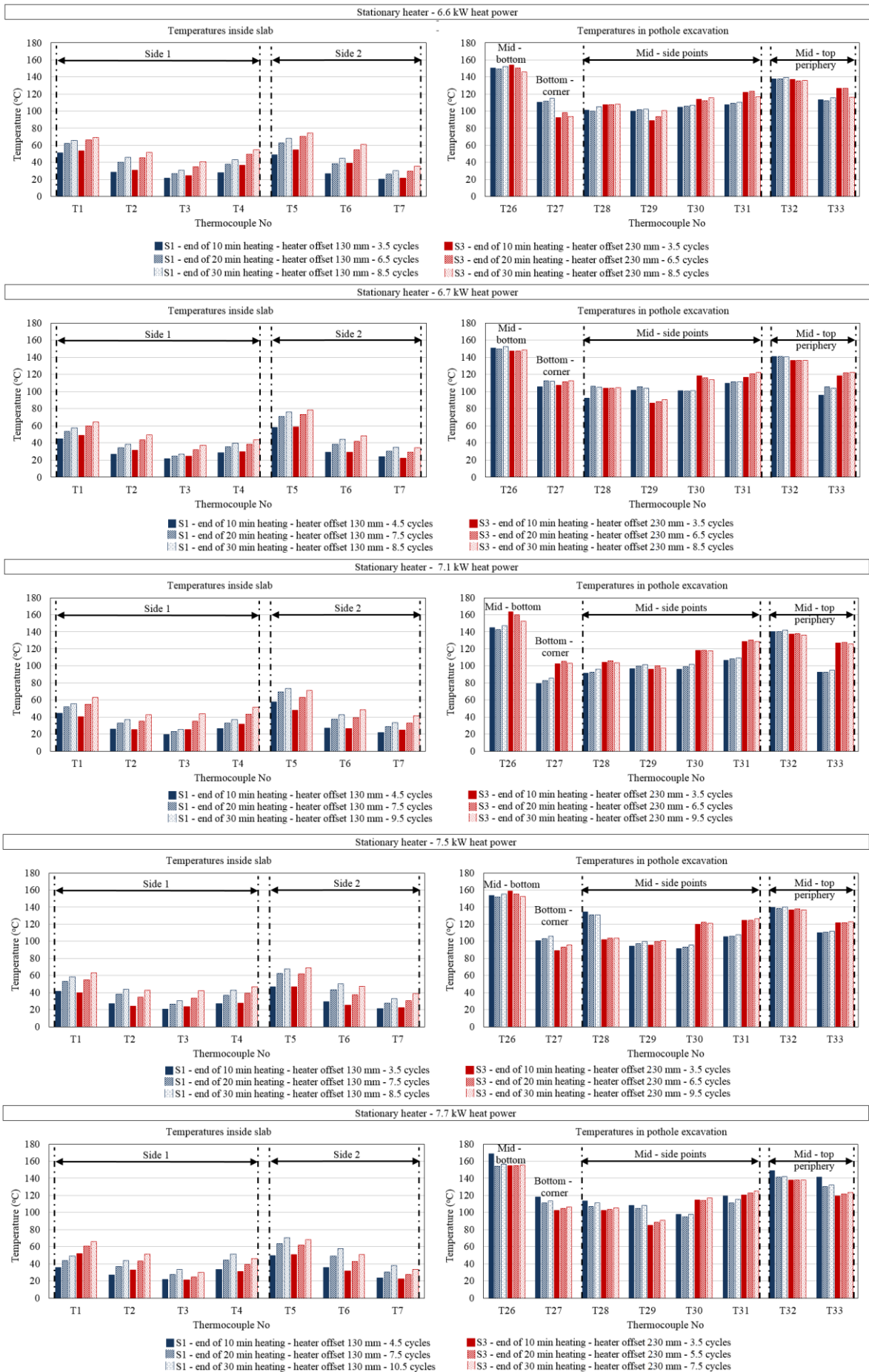
Figure 4.10 Temperature profile in 45 mm deep pothole excavation and stationary heater
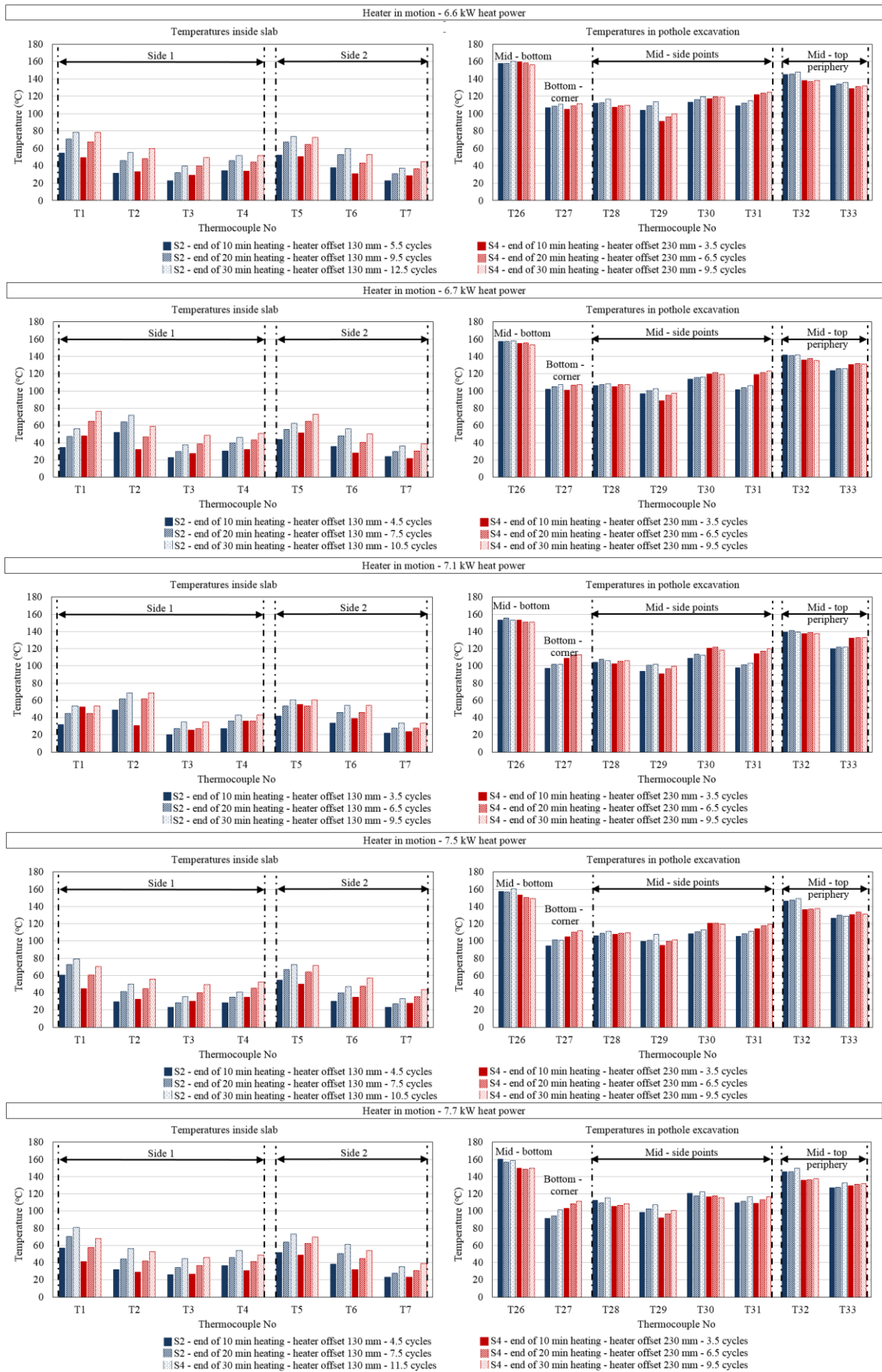
Figure 4.11 Temperature profile in 45 mm deep pothole excavation and moving heater

4.4.2.2 Slabs with 75 mm deep pothole excavation

The temperature profile under dynamic heating is shown in Figures 4.12 and 4.13. Similarly, with the 45 mm deep pothole excavation, temperatures inside the slab were lower than in the excavations as a result of the thermal properties of the mixture. Temperatures inside the slabs also showed a lowering trend from top to bottom. The effect of dynamic heating in the temperatures of the excavation faces was larger for 230 mm heater offset than 130 mm offset. This happened for all heat powers with the stationary heater above the excavation and for heat powers between 6.7 kW and 7.5 kW for the moving heater. However, the temperature was at similar levels in the pothole excavation for moving heater with 6.6 kW and 7.7 kW and 230 mm heater offset. The overall temperature distribution in the 75 mm deep pothole excavation was more uniform than in the 45 mm deep pothole excavation for the stationary heater. T39 located in one of the vertical faces of the excavation was the only thermocouple that had lower temperatures than the rest of the excavation. This may have happened because the thermocouple moved or was mistakenly covered by a wire of the steel mesh that was holding the thermocouples in place during the thermal tests.

From Figure 4.13, it is also observed that for the moving heater thermocouple T41 had significantly lower temperatures than T40 although both thermocouples were located at the top of the excavation. This happened because the heater was moving across the excavation and perpendicular to the long sides of the pothole where T41 was located in the middle of it. The air circulation due to the moving heater seems to have significantly affected and cooled down the temperatures of T41 compared to T40.

Reflecting the above, between 10 minutes and 30 minutes heating for the stationary heater at 130 mm offset, temperatures for T34-T38 were 94 ºC – 130 ºC; for T39 were 76 ºC – 91 ºC; for T40 were 143 ºC – 150 ºC; and for T41 were 106 ºC – 136 ºC. Meanwhile, at a heater offset of 230 mm, temperatures for T34-T38 were 103 ºC – 164 ºC; for T39 were 89 ºC – 129 ºC; for T40 were 135 ºC - 146 ºC; and for T41 were 90 ºC – 134 ºC (Figure 4.12). For the moving heater at 130 mm offset temperatures for T34-T38 were 84 ºC – 117 ºC; for T39 were 51 ºC – 74 ºC; for T40 were 146 ºC – 158 ºC; and for T41 were 94 ºC – 127 ºC. Meanwhile, at a heater offset of 230 mm, temperatures for T34-T38 were 96 ºC – 140 ºC; for T39 were 83 ºC – 110 ºC; for T40 were 140 ºC – 156 ºC; and for T41 were 90 ºC – 137 ºC (Figure 4.13).
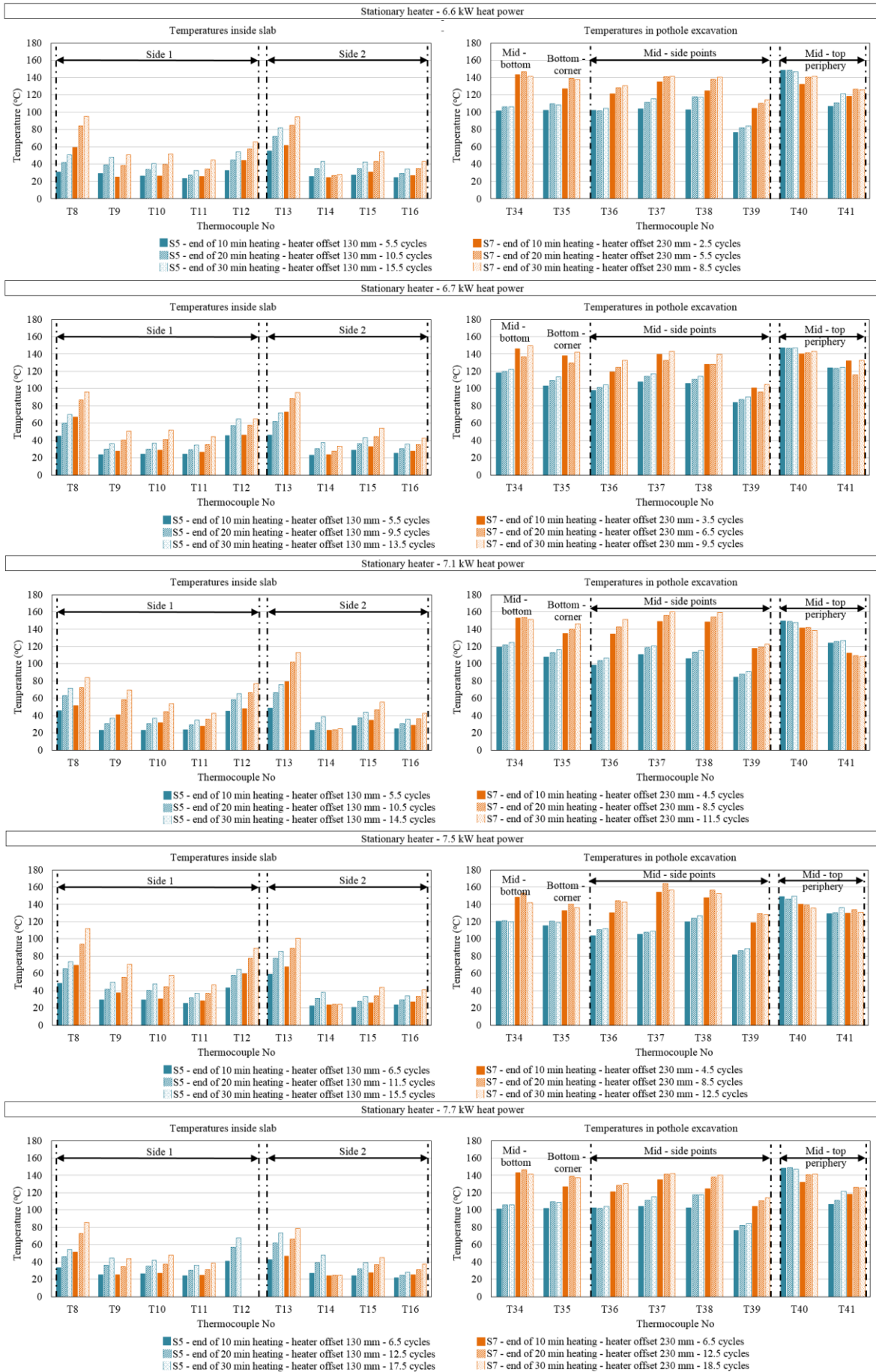
Figure 4.12 Temperature profile in 75 mm deep pothole excavation and stationary heater
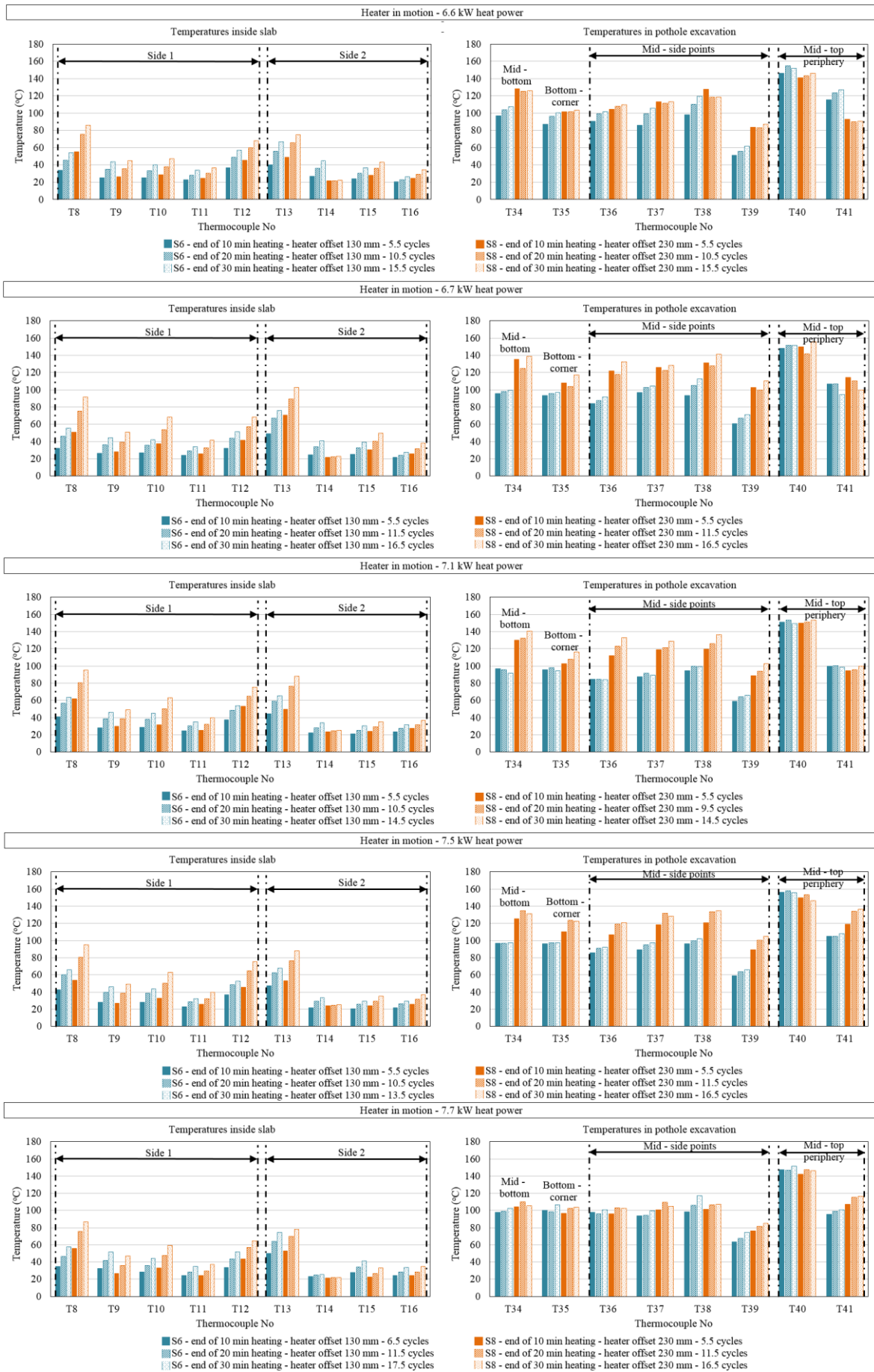
Figure 4.13 Temperature profile in 75 mm deep pothole excavation and moving heater

For internal slab temperatures, for both the stationary heater and heater in motion at 130 mm offset, temperatures were fluctuating from 30 ℃ to 70 ℃ for T8. This sensor was located closer to the top surface of the slab. Below T8, temperatures ranged between 25 ℃ and 50 ℃ (T9-T11 and T14-T16). Similar temperatures to T8 were captured from thermocouple T12 located below the bottom surface of the pothole excavation. For 230 mm offset, the temperature profile inside the slab did not change significantly. Specifically, T8 captured temperatures between 50 ℃ and 90 ℃ and temperatures for T9-T11 and T14-T16 ranged from 25 ℃ to 75 ℃ and 20 ℃ to 55 ℃ respectively. T12 measured temperatures between 40 ℃ and 75 ℃. T13 showed temperatures between 50 ℃ and 110 ℃ (Figures 4.12 and 4.13).

4.4.2.3　*Slabs with 100 mm deep pothole excavation*

The heating effects of dynamic heating are shown in Figures 4.14 and 4.15. Higher temperatures were seen between the excavation and inside the slab. Temperatures inside the slab were higher in the upper part of the slab and lower near the bottom of the slab. Both temperature trends were seen for the 45 mm and 75 mm deep excavations. However, temperatures measured in the 100 mm deep excavation were even more uniform than the 45 mm and 75 mm deep excavations. This may have happened because the deeper the excavation, the smaller the effect of the surrounding environment in the cooling of the temperatures in the excavation. Overall, temperatures for thermocouples T42 to T46 located within the excavation ranged between 80 ℃ and 110 ℃. The lowest temperatures in the excavation were seen for T47. For this sensor, for the stationary heater and heater in motion at 130 mm offset, temperatures were from 50 ℃ to 65 ℃. For 230 mm offset, temperatures ranged from 65 ℃ to 85 ℃. The highest temperatures were observed in the top of the excavation. These temperatures were captured by T48 and T49 and ranged between 110 ℃ and 160 ℃. The effect of cooling at T48 due to the heater moving across the excavation was mainly observed at heater heat powers between 6.7 kW and 7.7 kW.

Inside the slab mixture, the temperature for points closer to the top surface of the slab ranged from 30 ℃ to 70 ℃ (T17) and from 45 ℃ to 85 ℃ (T22). At lower depths, temperatures were between 20 ℃ and 55 ℃. These temperatures were measured by T18-T20 and T23-T25 and were affected by the thermal properties of the mixture as already discussed. Finally, temperatures between 30 ℃ and 55 ℃ were captured from thermocouple T21 located below the bottom surface of the pothole excavation.
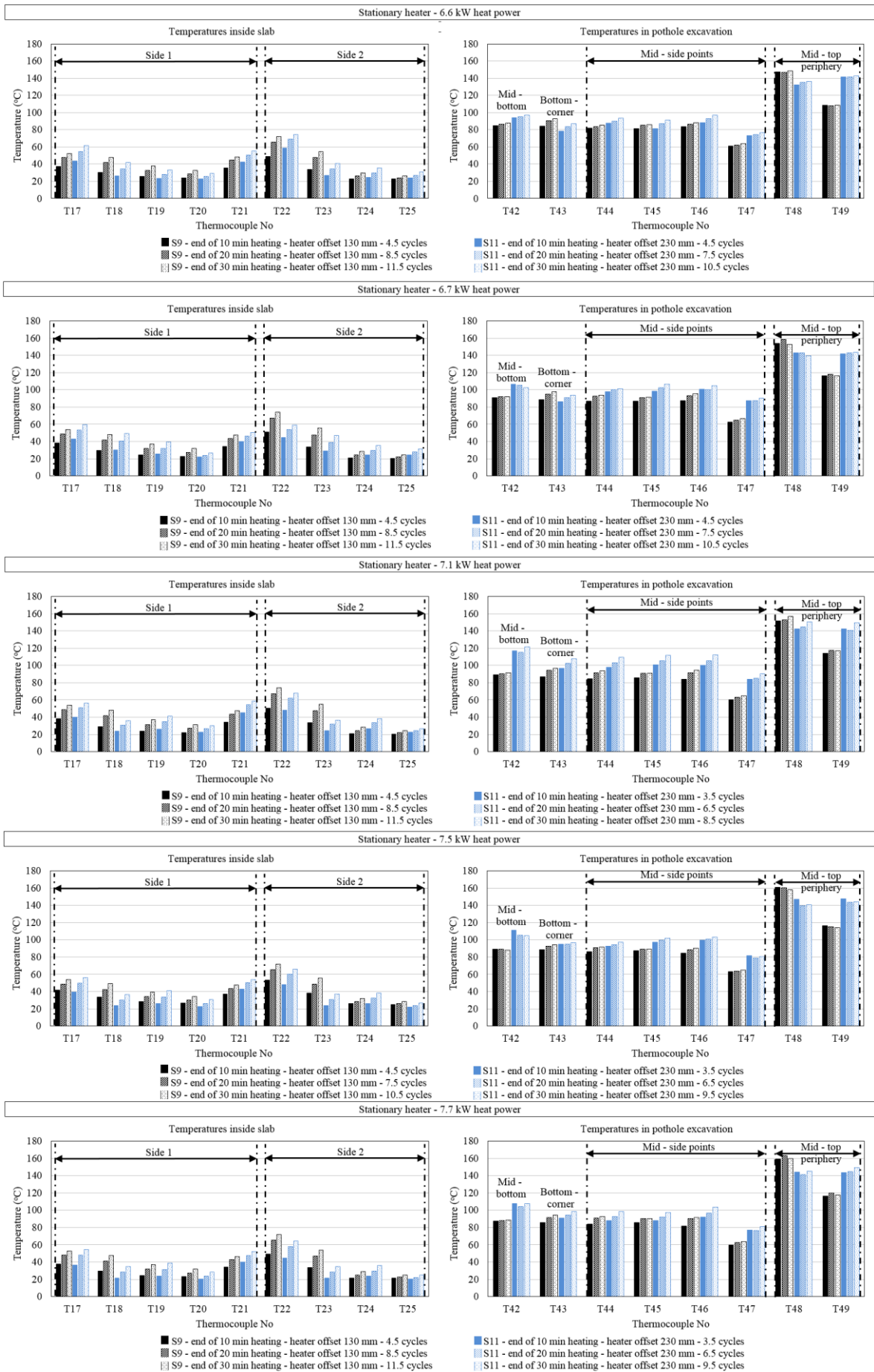
Figure 4.14 Temperature profile in 100 mm deep pothole excavation and stationary heater
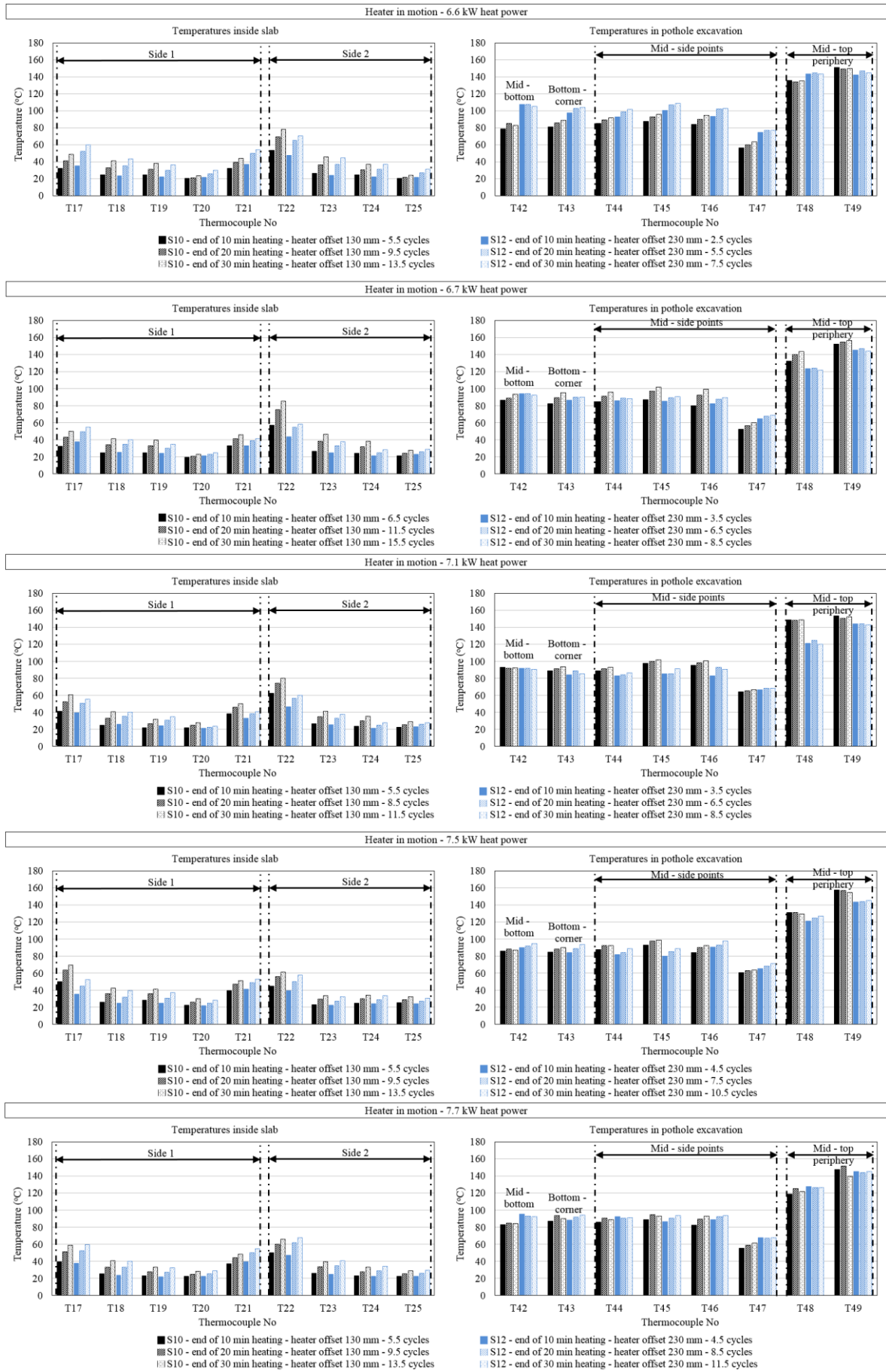
Figure 4.15 Temperature profile in 100 mm deep pothole excavation and moving heater

4.4.2.4 Optimum dynamic heating methods for 45 mm, 75 mm and 100 mm deep pothole excavations

For each temperature sampling point, the effect of heater power, offset and state above the excavations was analysed. This is discussed in sections 5.2.1 to 5.2.3. The optimum methods were chosen after finding the method that offered the highest increase of temperature per thermocouple, performed with a lower number of heating-cooling cycles, and low heat power was used for the heating part of the cycles. To find the method with the described characteristics, only the temperatures inside the slabs were examined for approximately 10 minutes of heating. The temperatures in the pothole excavation were not considered because the results showed that same temperature levels were achieved with each heating-cooling cycle. However, more heating time was needed to warm up the mixture of the slabs.

Further, the temperatures inside the slab were studied for 10 minutes of heating because the results showed that the temperature increase rate was higher for the first 10 minutes of heating than between 10 minutes and 30 minutes of heating. Secondly, because for pre-heating above 10 minutes of heating time, it was noticed that the faces of the pothole excavation became too loose showing evidence of overheating the asphalt although no smoking of bitumen was observed. If this happens in a field patch repair then the construction team would probably need to remove much more asphalt mixture into the sound pavement than should be necessary.

Initially, the five best heating methods were chosen among the twenty thermal tests conducted per pothole excavation. Figures 4.16, 4.17 and 4.18 present the selected five methods. In these figures, the temperature increase per thermocouple location is compared against each method. Then, the optimum pre-heating method for 45 mm, 75 mm and 100 mm deep excavation was determined and shown in Figure 4.19, after eliminating the heating methods that did not meet the criteria discussed in the previous paragraph.
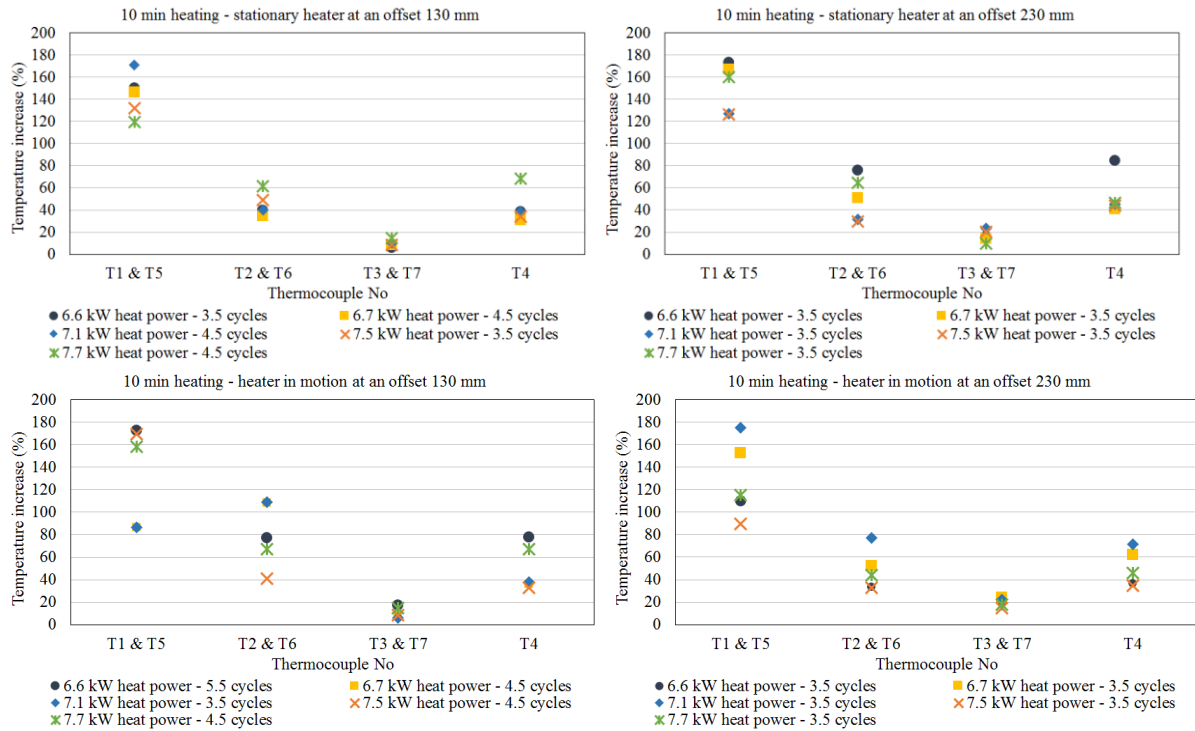
Figure 4.16 Temperature increase percentage per thermocouple for approximately 10 minutes heating in 45 mm deep pothole excavation
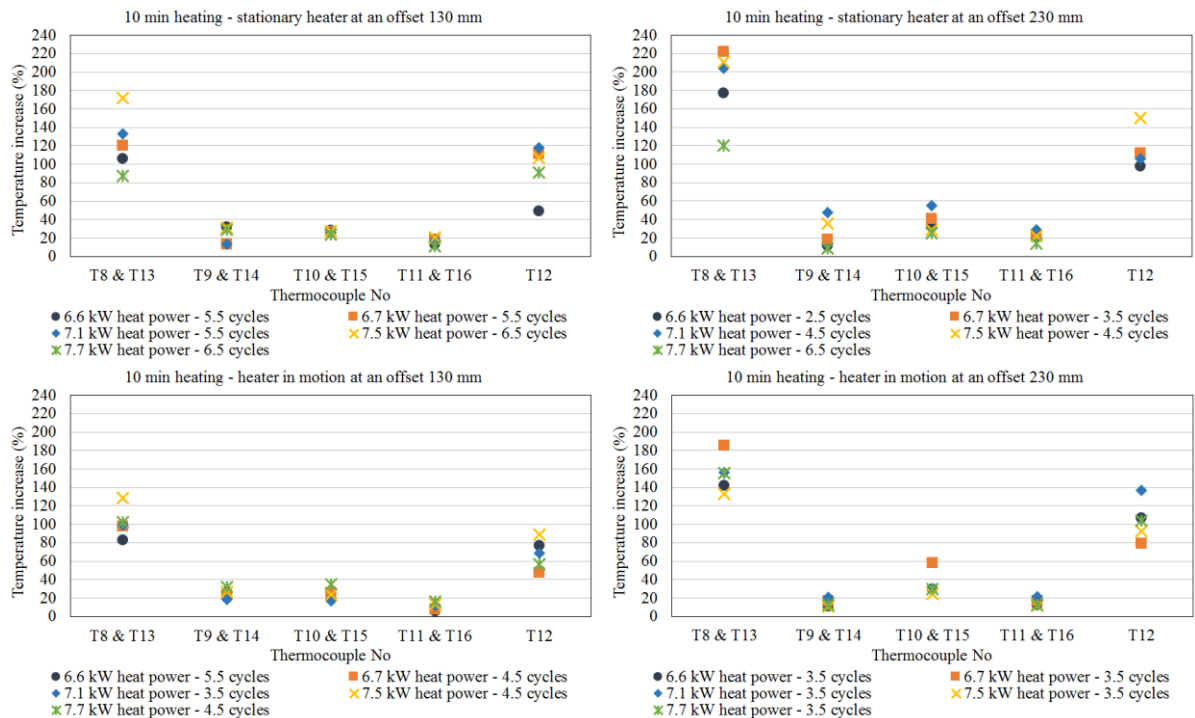
Figure 4.17 Temperature increase percentage per thermocouple for approximately 10 minutes heating in 75 mm deep pothole excavation
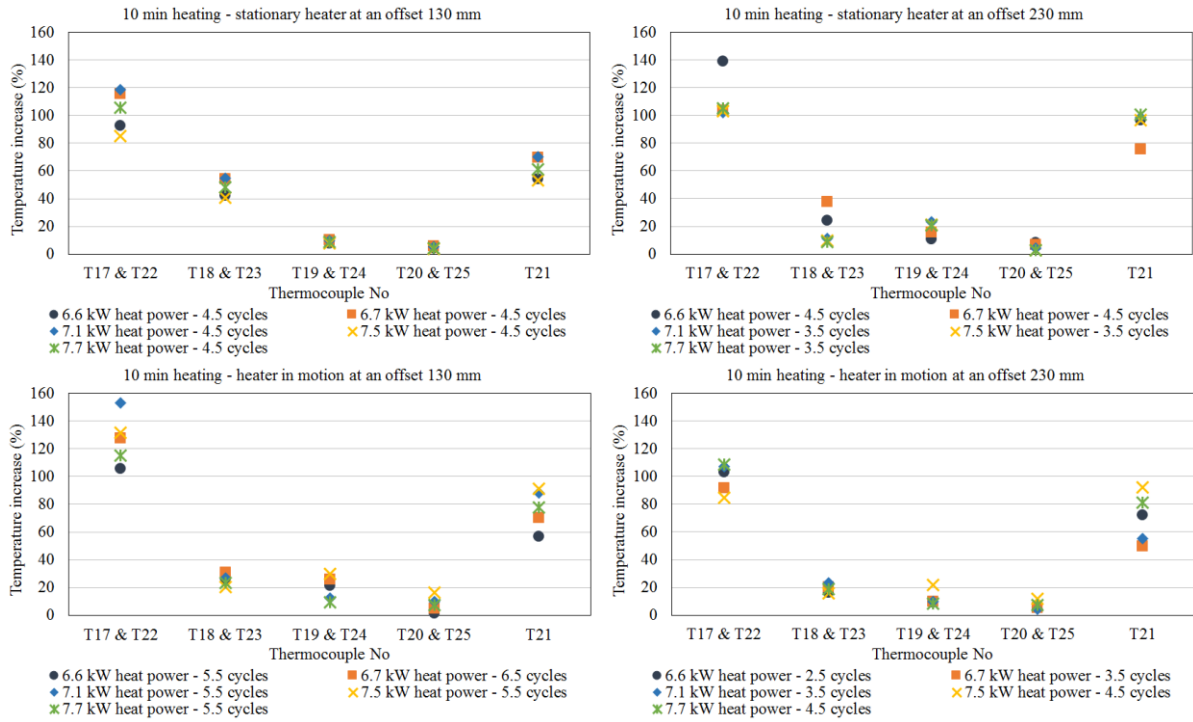
Figure 4.18 Temperature increase percentage per thermocouple for approximately 10 minutes heating in 100 mm deep pothole excavation
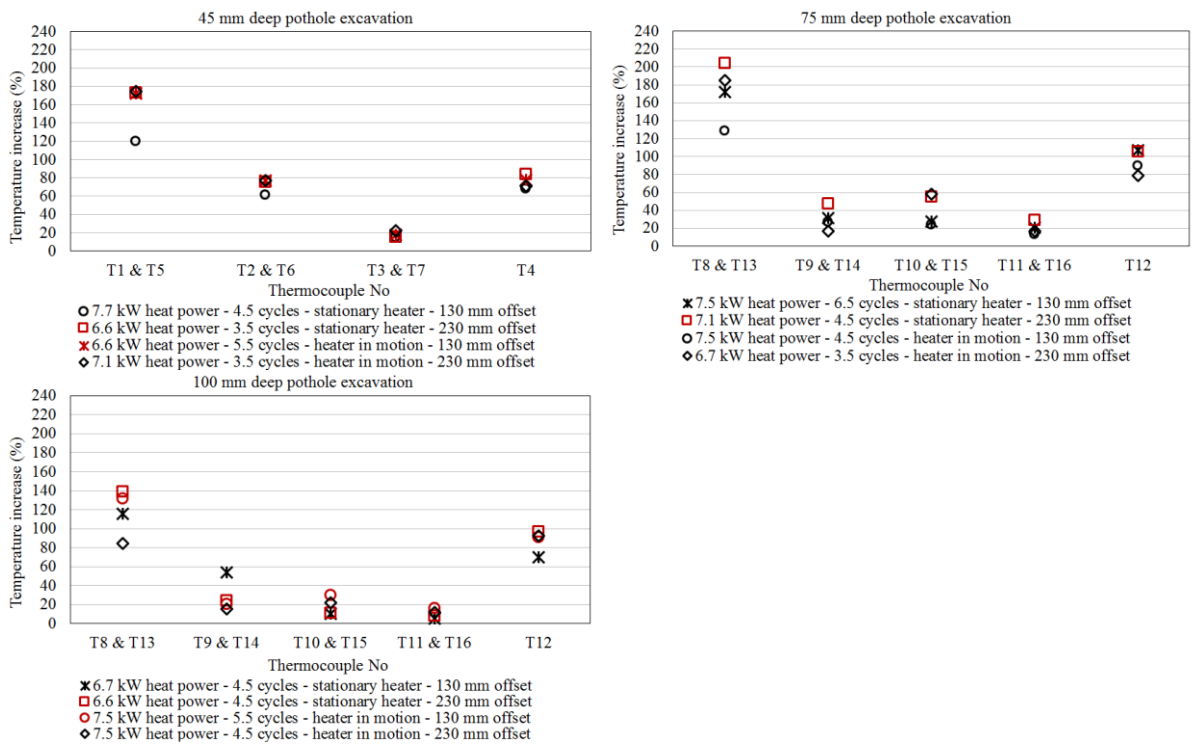
Figure 4.19 Optimum dynamic heating methods for 45 mm, 75 mm and 100 mm deep pothole excavations (optimum methods marked in red)

The time frames of heating-cooling cycles for optimum dynamic heating methods for all excavations are presented in Figure 4.20. For 45 mm and 100 mm deep pothole excavations, optimum heating methods with stationary heater and heater in motion are suggested. However, to avoid heating a large area around a pothole excavation with an area of 305×165 mm^2, the stationary heater is preferable. In this study, for the thermal tests with the moving heater, it was much more difficult to control the heated area around the pothole excavation because of the heater settings with regard to heater moving distance in its steel frame of 1.55 m $\times$ 1.60 m.
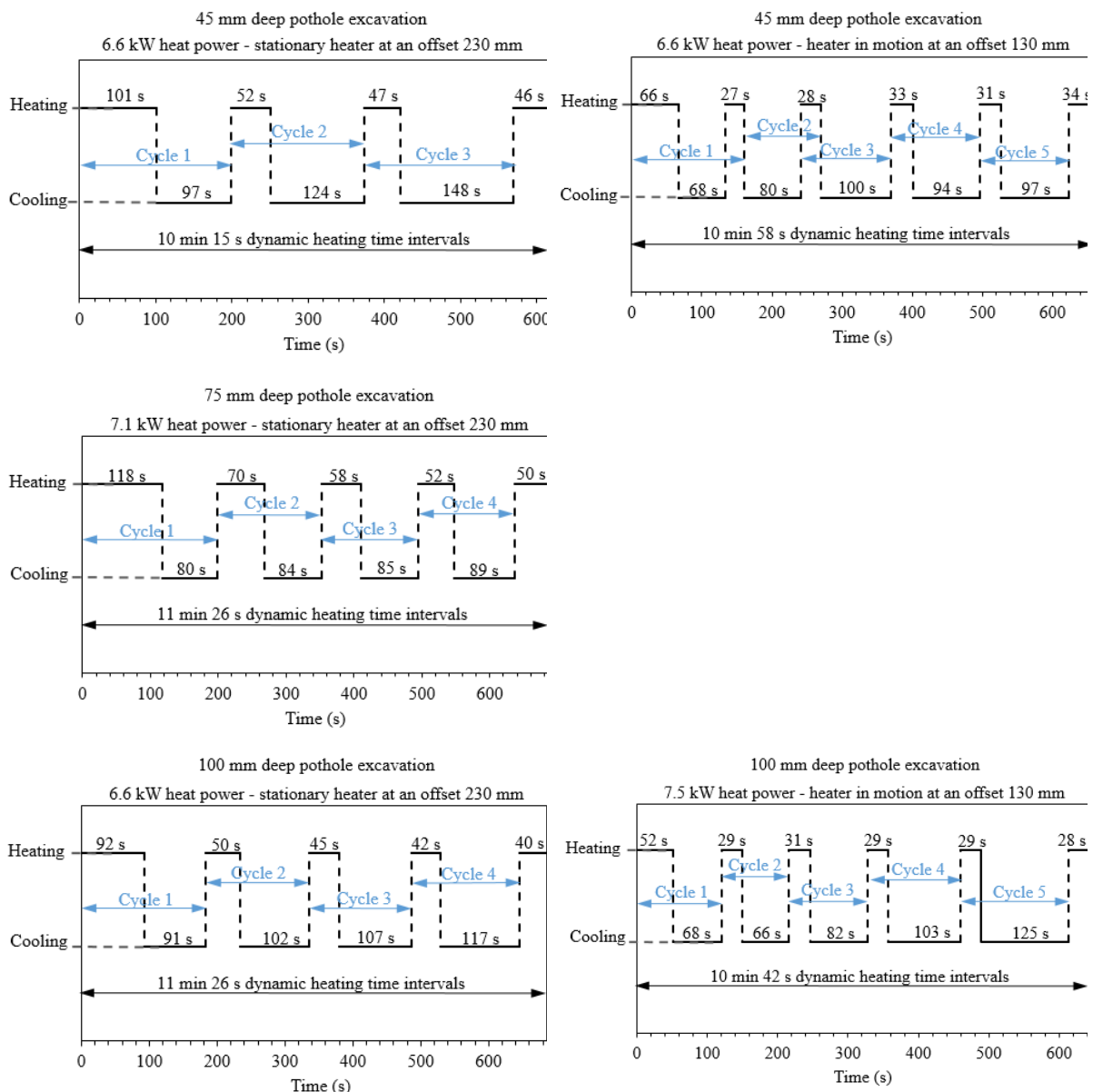
Figure 4.20 Heating – cooling cycle times for optimum dynamic heating methods for 45 mm, 75 mm and 100 mm deep pothole excavations

4.5   Summary

This chapter experimentally investigated the temperature profile in asphalt slabs and various depths of pothole excavations during dynamic infrared heat application. Temperatures were studied for various slab-heater configurations. These were 130 mm and 230 mm heater offsets and operating heat powers from 6.6 kW to 7.7 kW for stationary and moving heaters. For each temperature sampling point, the effect of heater power, offset and state above the excavations was analysed. Air voids content and thermal properties of the asphalt mixture were also determined and used to explain temperature profiles in the pothole excavations and inside the slabs when dynamic infrared heat was applied. The chapter ended by finding the optimum infrared pre-heating methods for 45 mm, 75 mm and 100 mm deep pothole excavations. The next chapter studies the effect of temperature, aggregate size, mixture composition and mixture ageing on the thermal properties of three different hot asphalt mixtures. This was done to further understand what effect the thermal properties may have in asphalt heat flow under infrared heat and to calibrate the finite element simulations of Chapter 7.

Chapter 5

Thermal properties of asphalt mixtures

In this chapter, thermal properties of specimens constructed with 20 mm DBM, asphalt concrete (AC) 14 and AC 6 asphalt mixtures are presented. Density and air voids of the compacted specimens are also shown. Thermal conductivity was measured in the laboratory for non-aged, short-term aged and long-term aged asphalt mixtures at three different temperatures 19 ($\pm$1) ^oC, 65 ($\pm$5) ^oC and 80 ($\pm$5) ^oC. Specific heat capacity and thermal diffusivity were calculated from equations derived from the literature. Heat penetration depth was also calculated and shows the heat from the thermal conductivity instrument heat source that dissipates into the asphalt specimens. The results were analysed to determine the effect of air voids content, transient line source (TLS) method, temperature and aggregate size in thermal conductivity and the effect of ageing on the thermal properties of the asphalt mixtures studied. The results of density, thermal conductivity and specific heat capacity presented in this chapter were used to calibrate the simulation models to be described in Chapter 7. The chapter aims to address the fourth objective of the research.

5.1 Experiments

5.1.1 Materials and experimental program

Three dense graded asphalt mixtures were studied called 20 mm DBM, AC 14 and AC 6 covering mixtures that are normally used for binder and surface courses in asphalt pavement. The mixtures comprised of granite coarse and fine aggregate and limestone filler. The binder used was 100/150 penetration grade bitumen. The same aggregate, filler and binder were used for specimens of Chapter 4, section 4.1.1 and those to be described in Chapter 6. The design of the mixture and the binder content comply with BS EN 13108, part 1 (British Standards Institution, 2016b). According to this standard, the binder content for 20 mm DBM, AC 14 and AC 6 asphalt mixtures should be 4.6%, 5.1% and 5.2% respectively. However, to construct specimens with air voids close to 5%, different sets of filler and binder contents were performed for trial samples. The filler content in the trial mixtures was changed at 5 gr increments and ranged from 145 gr to 160 gr for 20 mm DBM asphalt mixture, from 195 gr to 207 gr for AC

14 asphalt mixture and from 190 gr to 210 gr for AC 6 asphalt mixture. The binder content in the trial mixtures was changed at 0.5% increments and ranged from 53 gr to 67 gr for 20 mm DBM asphalt mixture, from 59 gr to 71 gr for AC 14 asphalt mixture and from 77 gr to 82 gr for AC 6 asphalt mixture. The final gradation and gradation curves of the mixtures resulting from the trials are shown in Tables 5.1-5.3 and Figure 5.1 respectively.

Table 5.1 20 mm size DBM in accordance with BS EN 13108, part 1 (British Standards Institution, 2016b) for 1035 gr of total aggregate

Sieve size: mm	% by mass passing	% passing selected
31.5	100	100
20	99-100	99.51
10	61-63	63.14
6.3	47	48.59
2	27-33	30.92
0.250	11-15	14.29
0.063	6	6.12
Pan	0	0

Table 5.2 AC 14 in accordance with BS EN 13108, part 1 (British Standards Institution, 2016b) for 1035 gr of total aggregate

Sieve size: mm	% by mass passing	% passing selected
20	100	100
14	100	100
10	77-83	80.36
6.3	52-58	55.82
2	25-31	28.65
1	14-26	20.23
0.063	6	5.50
Pan	0	0

Table 5.3 AC 6 in accordance with BS EN 13108, part 1 (British Standards Institution, 2016b) for 1035 gr of total aggregate

Sieve size: mm	% by mass passing	% passing selected
10	100	100
6.3	98	98
2	42-56	49
1	24-46	35
0.250	11-19	19.32
0.063	4-8	7.73
Pan	0	0

Table 5.4 shows the executed experimental program and the materials used for the study. Forty-five cylindrical specimens were built in total, fifteen per asphalt mixture type comprising five non-aged, five short-term aged and five long-term aged specimens. All specimens were used to measure thermal conductivity (k) in the laboratory at three different temperatures 19 ($\pm$1) ºC, 65 ($\pm$5) ºC and 80 ($\pm$5) ºC.
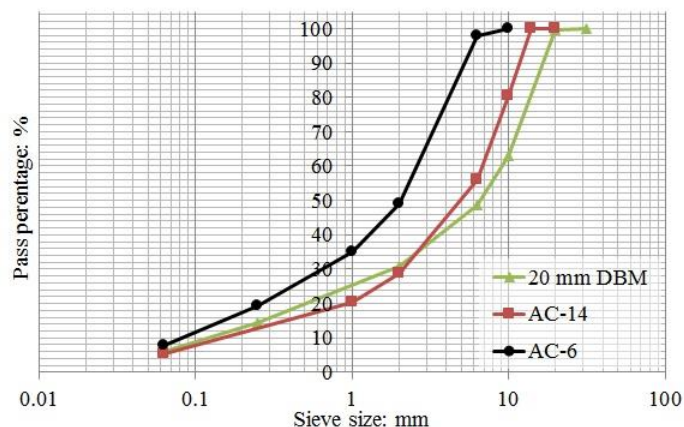
Figure 5.1 Composition of slab asphalt mixture

Table 5.4 Materials and experimental program

Specimen no.	Asphalt mixture type	Asphalt mixture condition	Temperatures for thermal conductivity k measurements		
			19 ($\pm$1) ºC	65 ($\pm$5) ºC	80 ($\pm$5) ºC
C1-C5	20 mm DBM	Non-aged	✓	✓	✓
C6-C10		Short-term aged	✓	✓	✓
C11-C15		Long-term aged	✓	✓	✓
C16-C20	AC 14	Non-aged	✓	✓	✓
C21-C25		Short-term aged	✓	✓	✓
C26-C30		Long-term aged	✓	✓	✓
C31-C35	AC 6	Non-aged	✓	✓	✓
C36-C40		Short-term aged	✓	✓	✓
C41-C45		Long-term aged	✓	✓	✓

5.1.2   Preparation of test specimens

5.1.2.1   Non-aged asphalt mixtures

Figure 5.2 shows the steps for specimen preparation. Prior to sieving (Figure 5.2(a)), the aggregates were dried for 24 hours at 110 ($\pm$5) ºC in a ventilated oven. The preparation of the aggregate, filler and binder prior to mixing, the asphalt mixing and the procedure followed to control the mix temperature conform with BS EN 12697, part 35 (British Standards Institution,

2016a). The preparation of the Marshall compaction hammer and the mould prior to compacting the specimens and the number of blows per specimen side for compacting the specimen conform to BS EN 12697, part 30 (British Standards Institution, 2012). Fifty compaction blows were chosen for this study per specimen side.

(a)   (b)   (c)

(d)   (e)   (f)

(g)   (h)   (i)   (j)

Figure 5.2 Preperation of test specimens: (a) sieving (example for 20 mm DBM mixture); (b) heating of aggregates and filler for 3 hours at 110 (±5) ºC to a ventilated oven; (c) heating of binder and mixer bawl for 3 hours and 1 hour respectively at 140

(±5) °C to a ventilated oven prior to asphalt mixing; (d) heating of foot and impact hammer and mould for 10 minutes at 140 (±3) °C to a ventilated oven prior to mixture compaction; (e) the last 4 minutes of step (d) mixing of asphalt was done at 140 (±3) °C; (f) pre-heated mould put onto the compaction pedestal and a thin disk was put on the mould base prior to filling; (g) filling with asphalt mixture which was evenly distributed with a heated spatula and the surface leveled; (h) cover of mixture with a second filter disc; (i) compaction with the pre-heated foot and impact hammer of Marshall compactor; (j) extruding of specimen from the mould with an extruding device after 3 hours of cooling

A trial specimen for each asphalt mixture type was first prepared prior to making the batches for all specimens. The compacted specimen diameters and heights were 101.3 (±0.2) mm and 62.0 (±0.7) mm respectively. The amount of asphalt mixture for a specimen was 1,100 gr. The mixture for each specimen was prepared separately and compacted immediately after mixing. The mixture temperature prior to compaction was 110 (±5) °C which differs from the one suggested in BS EN 12697, part 35 (British Standards Institution, 2016a). The temperature was monitored using an infrared camera (Flir, 2018). At the end of compaction, the specimens were allowed to cool down for 3 hours and then they were de-moulded with the extruding device shown in Figure 5.2(j). The specimens were stored in a hermetically closed container at 19 (±1) °C (Figure 5.3) until testing.

Figure 5.3 Specimen storing after extracting them from their moulds

5.1.2.2 *Short-term aged asphalt mixtures*

Short-term aged asphalt mixtures were prepared as described in section 5.1.2.1 but prior to compaction and immediately after mixing, the loose mixture was placed in a pan, evenly spread

out and put for 4 hours at 135 (±3) ºC to a ventilated oven (Figure 5.4) to achieve short-term ageing. The mixture was stirred every 60 minutes to maintain uniform conditioning. The described method of short-term ageing asphalt mixtures complies with AASHTO R30 (American Association of State Highway and Transportation Officials, 2006). The mixtures were compacted immediately after conditioning. The compaction method, cooling time after compaction, extraction from the mould and storing of specimens after extraction was done as described in the previous section.

Figure 5.4 Conditioning of loose mixture for 4 hours at 135 (±3) ºC to a ventilated oven for short-term ageing

5.1.2.3   Long-term aged asphalt mixtures

The specimens for this section were prepared as described in section 5.1.2.1. After the specimens were extracted from the moulds, they were stored for 16 hours in a hermetically closed container at 19 (±1) ºC (Figure 5.3). Then, they were covered with a steel mesh and put for conditioning for 5 days at 85 (±3) ºC into a ventilated oven for long-term ageing (Figure 5.5). The steel mesh was used to protect the specimens from expanding during conditioning. At the end of conditioning, the oven was turned off and the specimens were allowed to cool at room temperature for 16 hours. The described method of long-term ageing asphalt mixtures complies with AASHTO R30 (American Association of State Highway and Transportation Officials, 2006). In the end, the specimens were removed from the oven and stored inside the hermetically closed container shown in Figure 5.3.

Figure 5.5 Conditioning of compacted specimen for 5 days at 85 (±3) ᵒC to a ventilated oven for long-term ageing

5.2   Air voids content

The air voids content of the compacted cylindrical specimens was calculated as described in Chapter 4, section 4.3. This was done after cooling the specimens for 16 ($\pm$1) hours at 19 ($\pm$1) ᵒC after their extraction from the compaction mould (American Association of State Highway and Transportation Officials, 2006).

5.3   Asphalt thermal properties and heat penetration depth

5.3.1 Thermal conductivity (k)

Thermal conductivity was measured with the transient line source (TLS) instrument presented in Chapter 4, section 4.2.1. These measurements were conducted after the air voids of the specimens were determined. Therefore, prior to measuring thermal conductivity, the specimens were dried at 40 ᵒC to constant mass in a ventilated oven. This was adopted after Islam and Tarefder (2014) study and it took approximately 24 hours to complete. After drying, the specimens were allowed to cool in a room at 19 ($\pm$1) ᵒC for 24 hours. After cooling, thermal conductivity was measured.

As described in Chapter 4, section 4.2.1 to measure thermal conductivity, first a hole 4 mm (D) $\times$ 50 mm (H) was drilled in the middle of the specimen. Second, the hole was cleaned from excess powder with compressed air. Lastly, the needle was covered with thermal paste called Arctic Alumina (Overlockers, 2018) and inserted completely into the specimen. In addition, the specimens were covered with an insulating sheet which was held in place with a steel mesh to ensure no loss of heat during the measurements. However, the manufacturing company of

the TLS equipment assured that the insulating sheet was not needed. This could probably be justified by the results of the heat penetration depth to be shown in section 5.4 which demonstrate that the heat applied by the TLS penetrates the mixture does not reach the boundaries of the specimen outer diameter.

Figure 5.6(a) and 5.6(b) show the test set-up for measuring thermal conductivity at 19 (±1) °C and at 65 (±5) °C and 80 (±5) °C respectively. For the tests shown in Figure 5.6(b), the specimens were put for 24 hours in a ventilated oven at 65 (±5) °C. Then, thermal conductivity was measured inside the oven. After this, the specimens were let for another 24 hours in the oven at 80 (±5) °C and thermal conductivity measured at the end of conditioning.

5.3.2 Thermal diffusivity (a) and specific heat capacity (c_P)

Thermal diffusivity (a) and specific heat capacity (c_P) were calculated using Eq. 2.1 and Eq. 2.2 respectively described in Chapter 2, section 2.8.

(a)

(b)
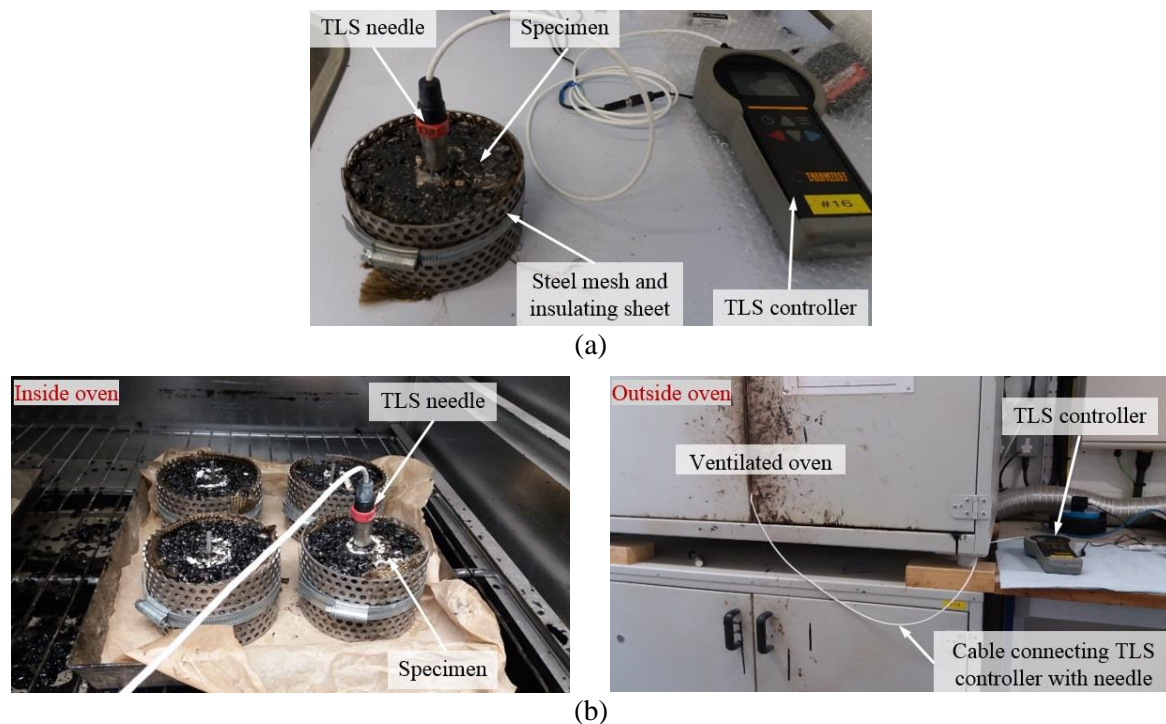
Figure 5.6 Measurement of thermal conductivity (k) at: (a) 19 (±1) °C; (b) 65 (±5) °C and 80 (±5) °C (temperatures achieved with a ventilated oven)

5.3.3 Heat penetration depth (d)

Heat penetration depth was calculated using Eq. 5.1 (British Standards Institution, 2015b). It measures the depth a heat wave travels inside the asphalt mixture in the direction of heat flow. In this study, the calculation of the heat penetration depth helps in understanding the volume of mixture that participates and may affect the measurements of thermal conductivity.

$$d = \kappa\sqrt{at_{tot}} \qquad\qquad (5.1)$$

where d = heat penetration depth, mm; $\kappa = 2$, temperature recording sensitivity constant of the TLS method used in this study; a = thermal diffusivity, (mm^2/s); t_{tot} = 150 seconds, total time of TLS to measure thermal conductivity.

5.4　Results and discussion

Tables 5.5-5.7 show density, air voids, thermal conductivity, calculated specific heat capacity, thermal diffusivity and heat penetration depth for all the asphalt mixtures studied. For each specimen, thermal conductivity was measured three times. Thus, the results show the average of the three readings. Appendix D presents all thermal conductivity readings.

Table 5.5 Main parameters of the 20 mm DBM asphalt mixture specimens studied

No.	Density (kg/m^3)	Air voids content (%)	Thermal conductivity (W/m K)			Specific heat capacity (J/kg K)	Thermal diffusivity (×10^{-7}) (m^2/s)	Heat penetration depth (mm)
			Non-aged asphalt mixture					
		25 ºC	19 ºC	65 ºC	80 ºC		19 ºC	
C1	2,297	4.98	1.455	1.062	0.873	883.96	7.17	20.74
C2	2,296	4.99	1.330	1.183	0.853	884.17	6.55	19.82
C3	2,290	5.25	1.906	1.464	1.053	884.64	9.41	23.76
C4	2,289	5.28	1.727	1.161	0.922	884.04	8.53	22.63
C5	2,280	5.55	1.907	1.142	0.928	885.29	9.45	23.81
			Short-term aged asphalt mixture					
		25 ºC	19 ºC	65 ºC	80 ºC		19 ºC	
C6	2,287	5.30	1.624	0.915	0.753	884.94	8.02	21.94
C7	2,287	5.35	1.697	0.997	0.884	884.46	8.39	22.44
C8	2,285	5.48	1.411	0.699	0.631	884.03	6.99	20.47
C9	2,274	5.83	1.920	0.927	0.753	884.95	9.54	23.92
C10	2,266	6.08	1.788	0.808	0.611	886.06	8.90	23.11
			Long-term aged asphalt mixture					
		25 ºC	19 ºC	65 ºC	80 ºC		19 ºC	
C11	2,297	4.99	1.761	1.016	0.595	884.07	8.67	22.81
C12	2,289	5.23	1.561	0.831	0.365	884.73	7.71	21.50
C13	2,280	5.57	1.564	0.829	0.517	885.19	7.87	21.73
C14	2,265	6.17	1.626	0.822	0.436	885.40	8.11	22.05
C15	2,261	6.37	1.582	0.873	0.392	884.99	7.90	21.78

Table 5.6 Main parameters of the AC 14 asphalt mixture specimens studied

No.	Density (kg/m³)	Air voids content (%)	Thermal conductivity (W/m K)			Specific heat capacity (J/kg K)	Thermal diffusivity (×10⁻⁷) (m²/s)	Heat penetration depth (mm)
		25 ºC	19 ºC	65 ºC	80 ºC		19 ºC	
Non-aged asphalt mixture								
C16	2,320	4.67	1.427	1.339	0.996	885.32	6.95	20.42
C17	2,318	4.73	1.409	1.287	0.821	885.56	6.86	20.29
C18	2,317	4.75	1.748	1.284	0.944	886.06	8.51	22.60
C19	2,301	5.37	1.135	0.699	0.559	886.40	5.56	18.27
C20	2,295	5.65	1.184	1.041	0.835	886.27	5.82	18.69
Short-term aged asphalt mixture								
C21	2,316	4.80	1.971	1.074	0.865	886.20	9.61	24.01
C22	2,311	5.04	1.820	1.121	0.914	885.60	8.89	23.10
C23	2,298	5.40	1.751	1.076	0.898	887.59	8.58	22.69
C24	2,293	5.65	1.871	0.875	0.975	887.31	9.20	23.49
C25	2,287	6.01	1.886	0.812	0.722	885.88	9.31	23.64
Long-term aged asphalt mixture								
C26	2,294	5.76	1.681	1.055	0.829	885.38	8.28	22.29
C27	2,287	5.94	1.857	1.175	0.816	886.36	9.16	23.44
C28	2,284	6.09	1.738	1.041	0.858	886.34	8.59	22.70
C29	2,282	6.18	1.832	0.985	0.703	886.15	9.06	23.32
C30	2,278	6.43	1.970	1.140	0.840	885.14	9.77	24.21

Table 5.7 Main parameters of the AC 6 asphalt mixture specimens studied

No.	Density (kg/m³)	Air voids content (%)	Thermal conductivity (W/m K)			Specific heat capacity (J/kg K)	Thermal diffusivity (×10⁻⁷) (m²/s)	Heat penetration depth (mm)
		25 ºC	19 ºC	65 ºC	80 ºC		19 ºC	
Non-aged asphalt mixture								
C31	2,272	4.55	1.472	1.241	1.033	872.68	7.42	21.11
C32	2,270	4.61	1.346	1.121	0.896	872.79	6.79	20.19
C33	2,265	4.78	1.351	1.111	0.836	873.17	6.83	20.24
C34	2,263	5.04	1.625	1.296	0.963	871.70	8.24	22.23
C35	2,256	5.22	1.503	1.255	0.937	872.85	7.63	21.40
Short-term aged asphalt mixture								
C36	2,279	4.20	1.670	0.779	0.855	873.31	8.39	22.44
C37	2,270	4.40	1.883	1.061	0.826	874.57	9.48	23.85
C38	2,257	5.09	1.741	0.744	0.732	873.42	8.83	23.02
C39	2,254	5.09	1.664	0.788	0.816	874.52	8.44	22.51
C40	2,248	5.42	1.741	0.798	0.817	873.74	8.86	23.06
Long-term aged asphalt mixture								
C41	2,265	4.77	1.521	0.901	0.629	873.30	7.69	21.48
C42	2,265	4.81	1.673	0.981	0.712	873.04	8.46	22.53
C43	2,262	4.92	1.587	0.963	0.720	873.14	8.04	21.96
C44	2,249	5.39	1.731	1.037	0.729	873.60	8.81	22.99
C45	2,240	5.73	1.631	0.929	0.680	873.94	8.33	22.36

The results show thermal conductivity measured at three different temperatures. However, the calculations of the other parameters demonstrated in Tables 5.5-5.7 were done based on values measured at 25 ($\pm$1) °C in the case of density and air voids content and at 19 ($\pm$1) °C in the case of specific heat capacity, thermal diffusivity and heat penetration depth.

5.4.1 Density and air voids content

The air voids content obtained for all specimens ranged from 4.98% to 6.37% for 20 mm DBM, from 4.67% to 6.43% for AC 14 and from 4.20% to 5.73% for AC 6 asphalt mixture. However, the target air voids content was 5%. The variation of air voids from the target air voids content happened because when using an impact compactor it is difficult to prepare the samples with a specific air voids content. An impact compactor is a static compression method of compaction that needs high pressures to apply to the mix to achieve the required density. The method lacks a kneading action to re-orientate the aggregates and fails to optimize the distribution of aggregates, binder and air voids content (Hartman, Gilchrist and Walsh, 2001). This affected the density of the mixture which for this study for all specimens ranged from 2,261 kg/m^3 to 2,297 kg/m^3 for 20 mm DBM, from 2,278 kg/m^3 to 2,320 kg/m^3 for AC 14 and from 2,240 kg/m^3 to 2,279 kg/m^3 for AC 6 asphalt mixture.

5.4.2 Effect of air voids content and TLS method in thermal conductivity (k)

As is seen from the results in Tables 5.5-5.7, thermal conductivity measured at 19 °C for 20 mm DBM asphalt mixture ranged: from 1.33 W/m K to 1.907 W/m K for non-aged specimens; from 1.411 W/m K to 1.788 W/m K for short-term aged specimens; and from 1.561 W/m K to 1.761 W/m K for long term-aged specimens. At the same test temperature, thermal conductivity of specimens constructed with AC 14 mixture ranged: from 1.135 W/m K to 1.748 W/m K for non-aged specimens; from 1.751 W/m K to 1.971 W/m K for short-term aged specimens; and from 1.681 W/m K to 1.970 W/m K for long-term aged specimens. For specimens with AC 6 mixture, thermal conductivity ranged: from 1.346 W/m K to 1.625 W/m K for non-aged specimens; from 1.664 W/m K to 1.883 W/m K for short-term aged specimens; and from 1.521 W/m K to 1.731 W/m K for long-term aged specimens.

The results showed that thermal conductivity did not depend on the level of air voids in the mixture. This means that thermal conductivity did not follow an increasing or decreasing trend when air voids were increasing or decreasing too. This probably shows that the variation of air voids found in this study is too small to signify a directed change in thermal conductivity. For

example, Hassn et *al*. (2016) and Mirzanamadi, Johansson and Grammatikos (2018) found that for a large variation of air voids content (from 5.0% to 25.3% for the study of Hassn et *al*. (2016) and from 2.0% to 10.0% for the study of Mirzanamadi, Johansson and Grammatikos (2018)) thermal conductivity decreases when air voids increase. Hassn et *al*. (2016) used 20 mm maximum limestone aggregate size and 60/40 penetration grade bitumen, whereas, Mirzanamadi, Johansson and Grammatikos (2018) used three types of asphalt mixture named ABT11, ABS11 and AG22 which are classified as dense graded mixtures with 11 mm and 22 mm maximum aggregate sizes respectively. Further, the authors used 70/100 penetration grade bitumen for ABT11and ABS11 and 100/150 penetration grade bitumen for AG22.

Nevertheless, excluding a direct effect of air voids in thermal conductivity, there is still a variation in the thermal conductivity of specimens for each asphalt mixture type and conditioning. This happened because, as previously noted, compaction with an impact compactor affects the uniformity of air voids in the mix. This means that the area used by the TLS instrument to measure thermal conductivity may have different distribution of air voids, aggregate, filler and binder. The amount of exposure of these parameters also after drilling a hole in the middle of the specimens to measure thermal conductivity and their properties will affect thermal conductivity.

Thus, when thermal conductivity is measured with the TLS (or else the needle method) only a part of the sample is used. This can be seen by the heat penetration depth results shown in Tables 5.5-5.7 which for 20 mm DBM, AC 14 and AC 6 mixtures ranged from 19.82 mm to 23.92 mm, from 18.27 mm to 24.21 mm and from 20.19 mm to 23.85 mm respectively. The specimens of this study consisted of coarse and fine granite with an average thermal conductivity of 2.68 W/m K (this is affected by the porosity of the stone water content, local characteristics, sampling dependence and mineralogical composition with granite depending considerably on its quartz and albite content, Eppelbaum, Kutasov and Pilchin, 2014), limestone filler of 2.92 W/m K (Pan et *al*., 2017), binder without additives of 0.39 W/m K (Pan et *al*., 2014), air of 0.025 W/m K (Eppelbaum, Kutasov and Pilchin, 2014) and water of 0.565-0.615 W/m K (depending on the test temperature).

The thermal contact between the needle and asphalt mixture surface may also affect thermal conductivity measurements. This contact may be disturbed by entrapped air or remains of granite and limestone dust from the drilling of the hole in the sample. It can also be affected by

the non-uniformity of heat that moves away from the needle during the thermal conductivity measurement.

5.4.3 Effect of temperature in thermal conductivity (k)

For all asphalt mixtures studied, thermal conductivity was considerably decreased between test temperatures 19 °C and 80 °C (Figures 5.8-5.9). The average decrements of thermal conductivity between those test temperatures are shown in Figure 5.7 and for 20 mm DBM mixture were 43.7% (non-aged mix), 56.7% (short-term aged mix), 71.6% (long-term aged mix); for AC 14 mixture were 39.6% (non-aged mix), 52.8% (short-term aged mix), 55.3% (long-term aged mix); and for AC 6 mixture were 36.0% (non-aged mix), 53.4% (short-term aged mix), 57.4% (long-term aged mix). The results also show that the effect of temperature in thermal conductivity was larger for aged asphalt mixtures and for specimens designed with large aggregate size, those with 20 mm DBM mixture.

The evolution of thermal conductivity of asphalt at temperatures from 19 °C to 80 °C does not depend on the thermal conductivity of asphalt binder at high temperatures but on the thermal properties and proportion of aggregate and filler that account for more than 90% of asphalt. A previous study conducted by Pan et *al.* (2017) for AH-70 (penetration 73 dmm), AH-90 (penetration 87 dmm) and SBS modified asphalt binder (penetration 48.1 dmm) showed a minimal reduction of thermal conductivity of binder for temperatures between -20 °C and 60 °C of 8.9%, 7.1% and 7.5% respectively. Maqsood, Gul and Anis-ur-Rehman (2004) in their study about thermal properties of granite showed that thermal conductivity decreased with temperature increase (from -20 °C to 60 °C). The authors note that the effect of aggregates in thermal conductivity depends on the chemical composition, density, porosity and specific gravity of aggregate. The decreasing trend of thermal conductivity of asphalt mixtures with the rise in temperature has been also reported by Chadbourn et *al.* (1996). The authors studied asphalt mixtures of dense graded (DG) and 15.9 mm maximum size (SMA) granite and river gravel mixed with 120/150 penetration grade binder. For DG with 1970 kg/m^3 density, thermal conductivity decreased from approximately 1.5 W/m K to 1.2 W/m K for test temperatures from 25 °C to 75 °C. For SMA with 1880 kg/m^3, thermal conductivity decreased from approximately 2.5 W/m K to 2.2 W/m K for test temperatures from 25 °C to 75 °C.
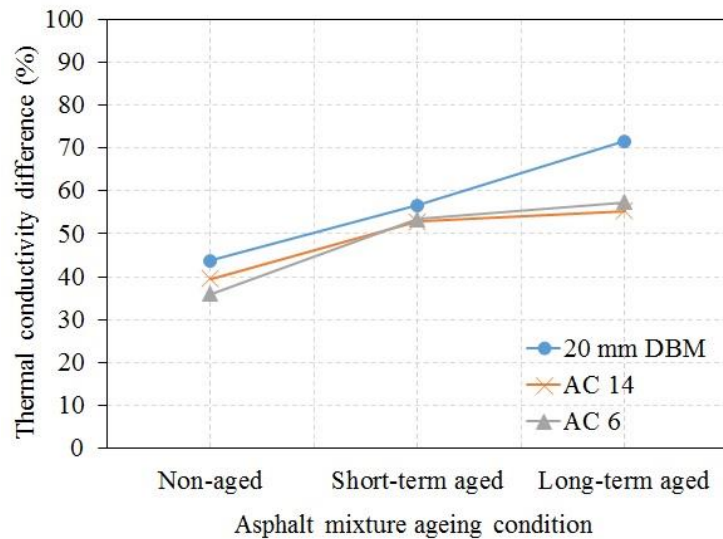
Figure 5.7 Average decrements of thermal conductivity for 20 mm DBM, AC 14 and AC 6 between 19 ^{o}C and 80 ^{o}C test temperatures
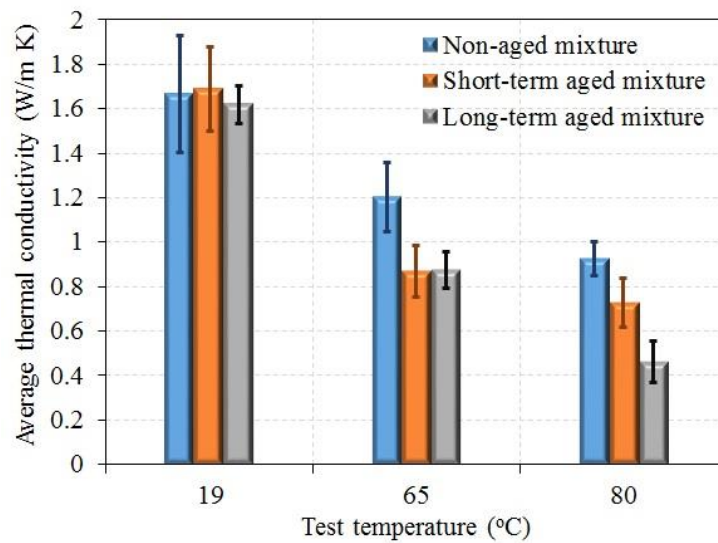
Figure 5.8 Effect of temperature in thermal conductivity of 20 mm DBM asphalt mixture (the error bars show the standard deviation (SD) of each value)
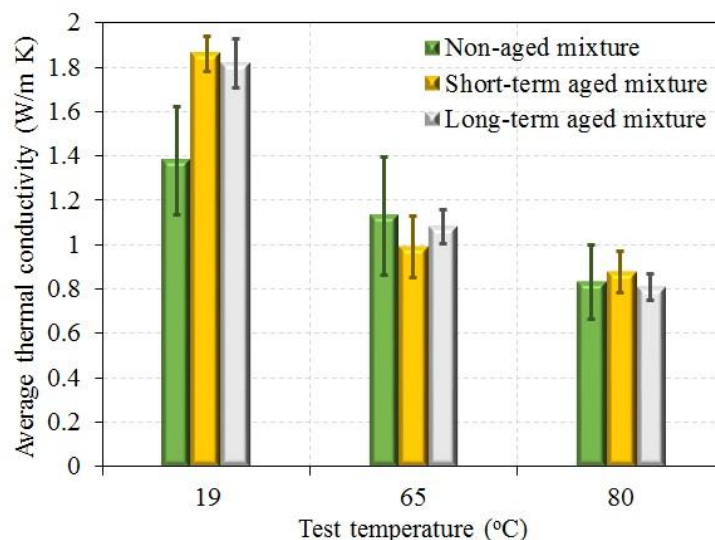
Figure 5.9 Effect of temperature in thermal conductivity of AC 14 asphalt mixture (the error bars show the SD of each value)
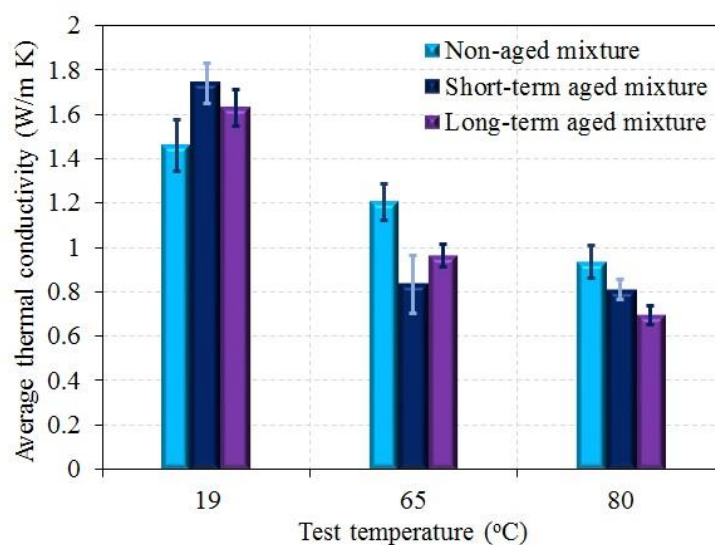
Figure 5.10 Effect of temperature in thermal conductivity of AC 6 asphalt mixture (the error bars show the SD of each value)

5.4.4 Effect of aggregate size in thermal conductivity (k)

The effect of aggregate size on thermal conductivity of the three asphalt mixtures was also studied. The results are shown in Figures 5.11-5.13 and result from the measurements presented in Tables 5.5-5.7. As is observed from the figures, for all mixtures, there is a higher difference of thermal conductivity between 20 mm DBM and AC 14 than between 20 mm DBM and AC 6 for all ageing conditions and test temperatures studied. For example, for non-aged mixtures

(Figure 5.11), at 19 ºC, thermal conductivity between 20 mm DBM and AC 14 changes by 18.65% and between 20 mm DBM and AC 6 thermal conductivity changes by 13.19%. For short-term aged mixtures (Figure 5.12), at 19 ºC, thermal conductivity between 20 mm DBM and AC 14 changes by 9.70% and between 20 mm DBM and AC 6 thermal conductivity changes by 3.03%. Further, for long-term aged mixtures (Figure 5.13), at 19 ºC, thermal conductivity between 20 mm DBM and AC 14 changes by 11.47% and between 20 mm DBM and AC 6 thermal conductivity changes by 0.62%. It seems that between 20 mm DBM and AC 6 the heat from the needle of the TLS is conducted in a similar way. This means that for AC 6 mixtures, the closer contacts of small aggregates improve heat conduction during the measurement of thermal conductivity. However, no specific conclusion could be made as to why thermal conductivity between 20 mm DBM and AC 14 had the highest difference for all ageing conditions and test temperatures. Therefore, further work is suggested in this matter as well as in the overall effect of aggregate size in thermal conductivity.

The results also showed that between 20 mm DBM and AC 14 or AC 6 aged mixtures, thermal conductivity changed the most for measurements done at 80 ºC test temperature. For example, for short-term aged mixtures (Figure 5.12), between 20 mm DBM and AC 14, thermal conductivity at 19 ºC changed by 9.70% whereas at 80 ºC thermal conductivity changed by 18.61%. For the same ageing conditions, between 20 mm DBM and AC 6, thermal conductivity at 19 ºC changed by 3.03% whereas at 80 ºC thermal conductivity changed by 10.81%. For long-term aged mixtures (Figure 5.13), between 20 mm DBM and AC 14, thermal conductivity at 19 ºC changed by 11.47% whereas at 80 ºC thermal conductivity changed by 54.80%. For the same ageing conditions, between 20 mm DBM and AC 6, thermal conductivity at 19 ºC changed by 0.62% whereas at 80 ºC thermal conductivity changed by 40.35%. However, it is not apparent if this change happens due to ageing or due to the effect of temperature in thermal conductivity. Nevertheless, in section 5.4.3 above it was observed that temperature dramatically affects thermal conductivity. Meanwhile, section 5.4.4 below shows that ageing doesn't necessarily change thermal conductivity if the effect of air voids, method of measurement, and thermal properties of binder into it are excluded.
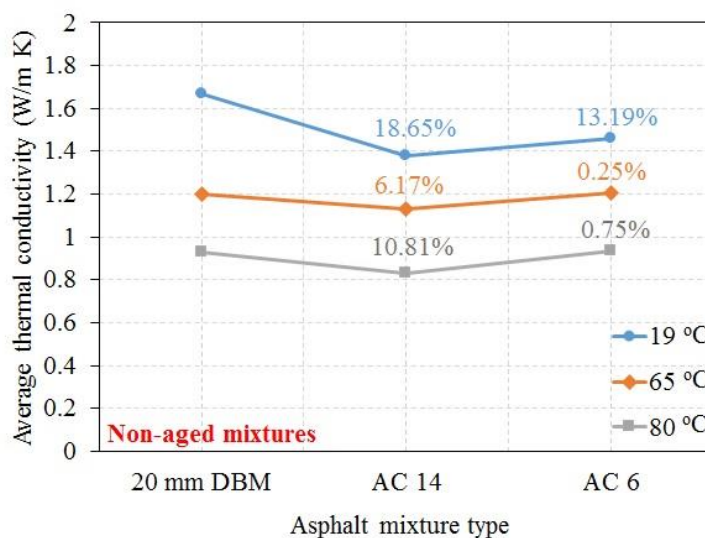
Figure 5.11 Effect of aggregate size in thermal conductivity of non-aged mixtures (the percentage values represent the thermal conductivity change between 20 mm DBM and the other two mixtures displayed in the figure)
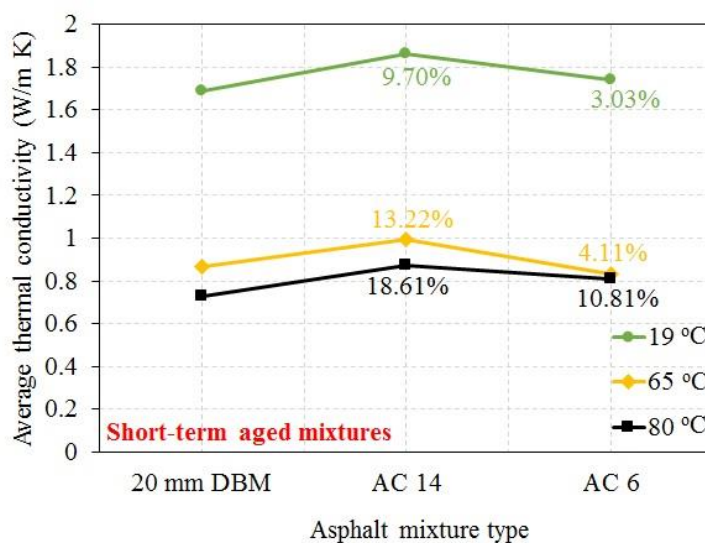
Figure 5.12 Effect of aggregate size in thermal conductivity of short-term aged mixtures (the percentage values represent the thermal conductivity change between 20 mm DBM and the other two mixtures displayed in the figure)
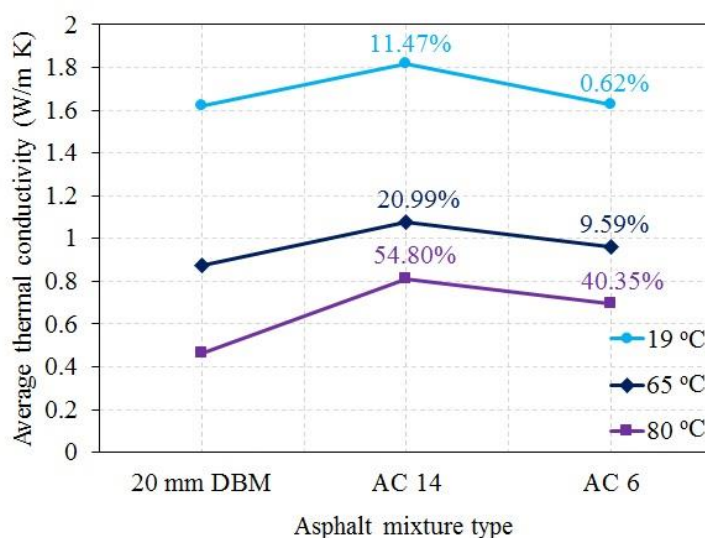
Figure 5.13 Effect of aggregate size in thermal conductivity of long-term aged mixtures (the percentage values represent the thermal conductivity change between 20 mm DBM and the other two mixtures displayed in the figure)

5.4.5 Effect of ageing in thermal conductivity (k), specific heat capacity (c_P) and thermal diffusivity (a)

The increase of the proportion of the colloid and asphaltene and the decrease of the proportion of saturates and aromatics of binder due to ageing changes the thermal properties of asphalt mixture. However, the effect of ageing in thermal properties of aggregate and filler is minimal (Pan et *al.*, 2017). Therefore, the effect of ageing on thermal conductivity of 20 mm DBM, AC 14 and AC 6 asphalt mixtures is expected to be minimal. The results are demonstrated in Tables 5.5-5.7.

The results demonstrate that for 20 mm DBM mixture the differences in thermal conductivity, specific heat capacity and thermal diffusivity at 19 $^{\circ}$C were less than 3% between non-aged specimens and short-term or long-term aged specimens. The lowest difference, less than 0.1%, was observed for specific heat capacity between the different ageing conditions. For the same mix, thermal conductivity measured at 65 $^{\circ}$C decreased by 27.7% between non-aged and short-term aged specimens and by 27.3% between non-aged and long-term aged specimens. For measurements done at 80 $^{\circ}$C, thermal conductivity decreased by 21.5% between non-aged and short-term aged specimens and by 50.2% between non-aged and long-term aged specimens.

For specimens with AC 14 and AC 6 asphalt mixtures the figure for most thermal parameters changed differently from that of 20 mm DBM asphalt mixture. However, the differences in specific heat capacity remained lower than 0.2% between non-aged specimens and short-term or long-term aged specimens.

For AC 14 mixture specimens and measurements done at 19 $^{\circ}$C, the differences in thermal conductivity and thermal diffusivity were from 30% to 35% between non-aged specimens and shot-term or long-term aged specimens. For thermal conductivity measured at 65 $^{\circ}$C, the differences were 12.2% between non-aged and short-term aged specimens and 4.5% between non-aged and long-term aged specimens. For thermal conductivity measured at 80 $^{\circ}$C, the differences were less than 5.5% between non-aged specimens and short-term aged or long-term aged specimens.

For AC 6 mixture specimens and measurements done at 19 $^{\circ}$C, the differences in thermal conductivity and thermal diffusivity were 19.2% between non-aged and short-term aged specimens and from 11% to 12% between non-aged and long-term aged specimens. For thermal conductivity measured at 65 $^{\circ}$C, the differences were 30.8% and 20.1% between non-aged specimens and short-term aged and long-term aged specimens respectively. For thermal conductivity measured at 80 $^{\circ}$C, the differences were 13.3% and 25.6% between non-aged specimens and short-term aged and long-term aged specimens respectively.

5.5   Summary

The effect of mixture air voids content, temperature and ageing in thermal properties of 20 mm DBM, AC 14 and AC 6 asphalt mixtures were experimentally investigated in this chapter. Thermal conductivity was measured with the TLS method, also discussed for the experimental work of Chapter 4, and the effects of this method in thermal conductivity measurements were also examined. The next chapter presents experimental work that has utilized the experimental infrared heater presented in Chapter 3 and the optimum dynamic heating method for shallow pothole excavation described in Chapter 4 to perform non-heated and infrared heated pothole repairs and characterise the thermal influence in those repairs.

Chapter 6

Temperature distribution at the interfaces of shallow patch repairs

The performance of HMA patch repairs is greatly reduced by repair edge disintegration. This is caused by low interface temperatures which result in poor repair bonding between fill material and old pavement. The advantage of controlled pre-heating of excavated asphalt surface prior to patch repair, referred as "dynamic repair", is presented in this chapter. The heating effects are compared against traditional non-heated HMA repair, referred as "static repair". In Chapter 4, the application of dynamic infrared heating was investigated for 45 mm, 75 mm and 100 mm deep pothole excavations. This chapter concentrates on measuring repair interface temperatures for 45 mm deep repairs and not for 75 mm and 100 mm deep repairs. This was done to limit the parameters that may affect the temperatures in patch repairs such as the depth of the repair. This is also the reason that the area of the pothole excavations was kept the same for Chapter 4, this chapter and the following Chapters 7 and 8.

Reflecting the above, twenty-four patch repairs, 45 mm in depth, comprising twelve static and twelve dynamic repairs heated for 10 minutes 15 seconds and 21 minutes 49 seconds respectively have been investigated. Controlled pre-heating methods used in this chapter were the optimum dynamic pre-heating methods found in Chapter 4 and section 4.4.2.4 for 45 mm deep pothole excavation. Temperatures were measured during the pouring and compaction of the fill mix at eleven locations in the repair interfaces. Physical and thermal properties of the asphalt mixtures were also investigated for calibration purposes of the repair simulation models to be presented in Chapter 7. The chapter aims to address the third objective of the research.

6.1 Experiments

6.1.1 Experimental program

Table 6.1 shows the executed experimental program. Twelve slabs named as S13-S22 were built, and twenty-four potholes were repaired: twelve static repairs and twelve dynamic repairs. In dynamic repairs, the pothole excavation was pre-heated for 10 minutes 15 seconds and 21 minutes 49 seconds for different repairs using the experimental infrared heater described in Chapter 3. In Chapter 4, section 4.4.2.4 it was recommended to use optimum pre-heating times of 10 minutes 15 seconds and of 21 minutes 49 seconds. However, by studying an extended heating time it ensures a comprehensive investigation of infrared heat application in patch repair. The tests were conducted in order to develop an accurate temperature distribution profile at the interfaces of static and dynamic repairs. Six repetitions were performed for measurement of temperatures at mid-depth points in the vertical interfaces of static repairs. For the same type of repairs, six repetitions were also performed for measurement of temperatures at points located at the bottom corners of the repair and at the middle of the bottom repair interface, Whereas, for a similar scope of tests, for the dynamic repairs, three repetitions were done per pre-heating time (Table 6.1).

Table 6.1 Experimental program

Pothole size	Scope of test	Slab no.	Pothole A - static repairs	Pothole B – dynamic repairs	
				10 min 15 sec pre-heating	21 min 49 sec pre-heating
300 mm × 160 mm × 45 mm	Measurement of temperatures at the corners and vertical repair interfaces	S13	✓	✓	
		S14	✓	✓	
		S15	✓	✓	
		S16	✓		✓
		S17	✓		✓
		S18	✓		✓
	Measurement of temperatures at the corners and bottom repair interfaces	S19	✓	✓	
		S20	✓	✓	
		S21	✓	✓	
		S22	✓		✓
		S23	✓		✓
		S24	✓		✓

6.1.2 Materials

The slabs of this chapter were constructed with the same 20 mm DBM asphalt mixture presented in Chapter 4, section 4.1.1. The simulated potholes were repaired with 6 mm dense graded mixture (AC 6) described in Chapter 5, section 5.1.1. Therefore, the slabs and repairs

comprised of granite coarse and fine aggregate and limestone filler. The bitumen used was 100/150 penetration grade bitumen. The gradation curves of the mixtures were also shown in the previously noted respective chapters and sections for each mixture.

6.1.3 Preparation of HMA and construction of HMA slabs

The slabs were built upside down with twelve asphalt batches of 7.6 kg each and compacted in two lifts of approximately 50 mm deep using a vibratory plate compactor in accordance with Standard Code of Practice, New Roads and Street Works Act 1991, Specification for the Reinstatement of Openings in Highways (Department of Transportation, 2010). The preparation of asphalt mixture for the slabs and the bonding of the slab lifts were similarly done as described in Chapter 4, section 4.1.2.

The construction of the slab's first and second lift is shown in Figures 6.1 and 6.2 respectively. The size of the slabs was 695 ($\pm$5) mm $\times$ 695 ($\pm$5) mm $\times$ 100 ($\pm$5) mm. Two pothole excavations were designed per slab. The size of the excavations was 305 ($\pm$2) mm $\times$ 165 ($\pm$2) mm $\times$ 45 ($\pm$2) mm. They were created by putting two steel pothole moulds inside the slab mould prior to filling it with asphalt mixture. The pothole moulds are marked as A and B in Figure 6.1(a) and indicate potholes for static and dynamic repairs respectively. The pothole moulds were removed from the slab using the infrared heater after 19 hours of the construction of the slab as described in Chapter 4, section 4.1.2.

During the construction of the slabs, aluminium tubes of 4 mm in diameter (Metals4u, 2018) were put at varying locations inside the slabs. The tubes were used later to accommodate thermocouples for measurement of interface temperatures during the pothole repair operations. To measure temperatures in locations along the vertical repair interfaces, the tubes were put in between the asphalt batches of the first lift of the slab (Figure 6.1(b)). This was performed for slabs S13-S18 of Table 6.1. Their positions were targeted to be in the middle of the respective interfaces, whereas, to measure temperatures at the bottom of the repair, the tubes were placed at the top of the compacted first lift of the slab (Figure 6.3). This was performed for slabs S19-S24 of Table 6.1.
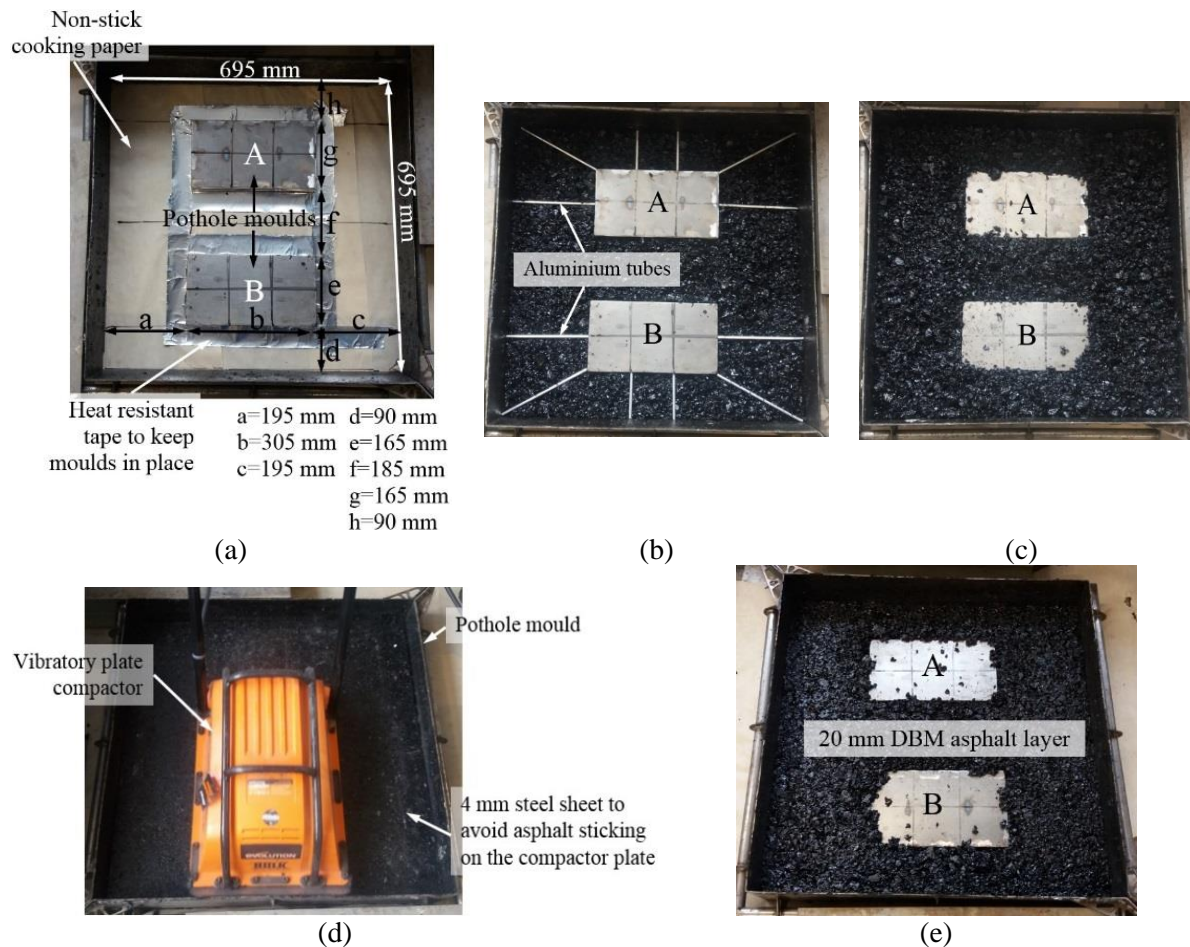
Figure 6.1 Construction of first lift of slabs S13-S18 with embedded aluminium tubes to accommodate thermocouples for measurement of temperatures at the vertical faces of the pothole repairs: (a) moulds set up; (b) 6 aluminium tubes per pothole above 3 asphalt batches of first lift; (c) following 3 batches poured; (d) compaction of 6 batches; (e) compacted first lift

6.1.4 Static pothole repairs

Twelve static repairs were performed for this set of tests. Real-time temperatures were captured using eleven T-type thermocouples of 0.5 °C accuracy (Omega, 2016d), four located at the corners, four at the vertical repair interfaces and three at the bottom of the repair (Figure 6.4). The thermocouples were inserted in the aluminium tubes (shown in Figures 6.1(b) and 6.3) prior to commencing the repair of the potholes. Temperatures were measured during the pouring and the compaction of the fill mix. The ambient temperature was 20 (±3) °C and the starting temperature of the slabs, prior to patching, ranged from 17 °C to 26 °C.
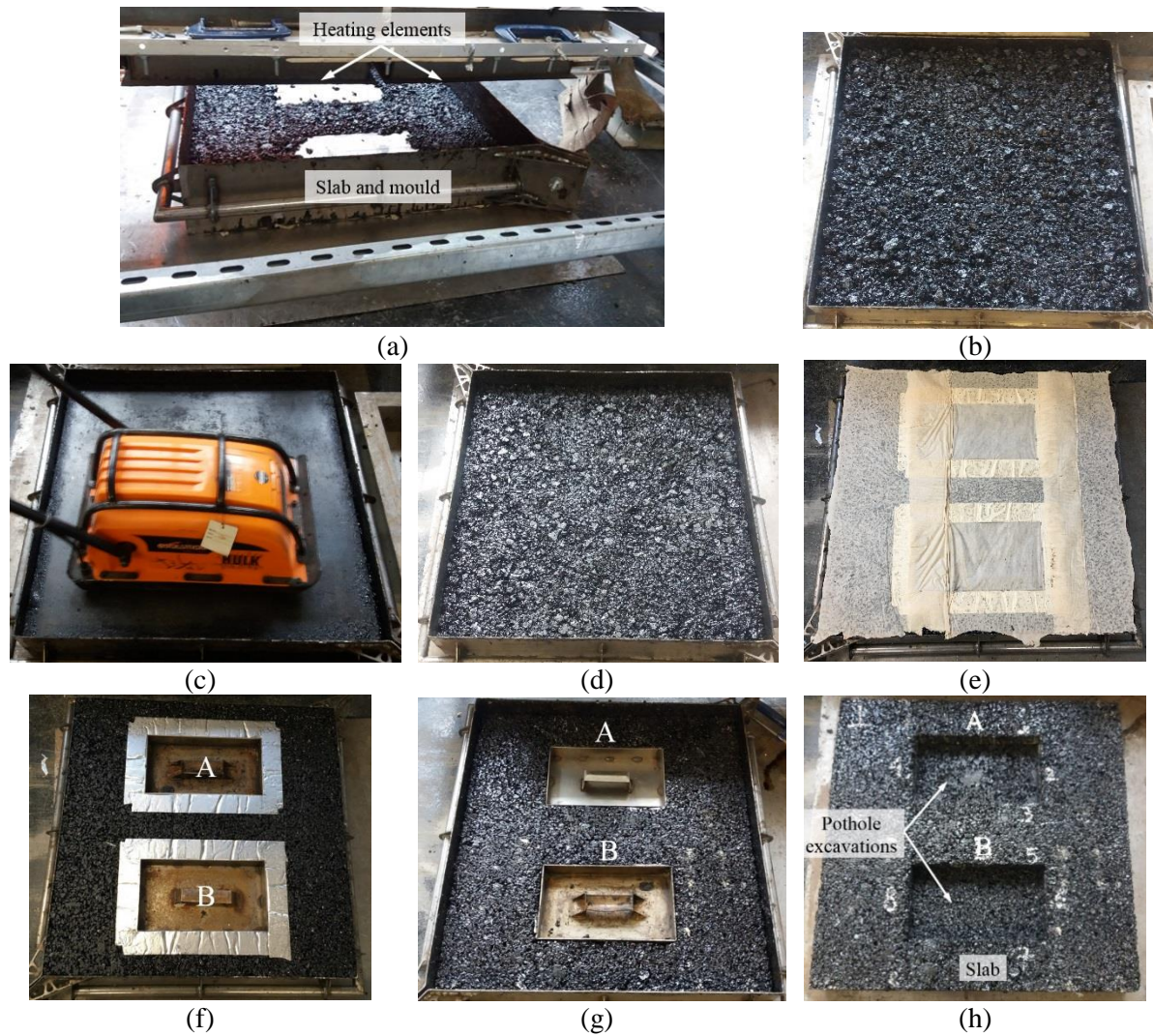
Figure 6.2 Construction of second lift of slabs S13-S18: (a) pre-heating of compacted first lift shown in Figure 6.1(e); (b) final 6 asphalt batches poured; (c) compaction of 6 batches; (d) compacted second lift; (e), (f) and (g) constructed slab turned upside down after 19 h of construction for demoulding; (h) final slab ready for pothole repair
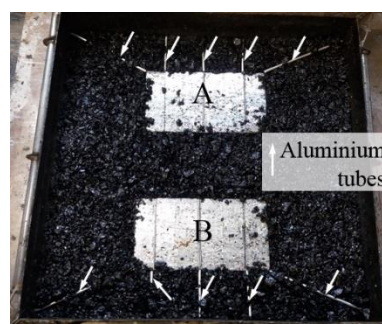
Figure 6.3 Aluminium tubes on the compacted first lift of slabs S19-S22 for measurement of temperatures at the bottom of the pothole repairs

(a)

Sides 1 and 4   Sides 2 and 5   Sides 3 and 6

(b)

Side 2 – pothole A   Side 5 – pothole B

(c)

Sides 1 and 6   Sides 2 and 5   Sides 3 and 4

(d)

Figure 6.4 Thermocouples in static and dynamic repairs completed for pothole A and B respectively: (a) slab and coordinate system for Table 6.2; (b) thermocouples T1-T6 for measurement of temperatures in the vertical interfaces of the pothole repairs; (c) thermocouples T7-T11 for measurement of temperatures in the bottom of the pothole repairs; (d) thermocouple routes from pothole excavations to data loggers

To capture the temperatures at the vertical repair interfaces and corners, only the end of the thermocouples was exposed in the pothole excavation (thermocouples T1-T6, Figure 6.4(b)), whereas, to capture the temperatures at the bottom of the repair, the thermocouples were extended in the pothole excavation by 85 mm (thermocouples T7-T11, Figure 6.4(c)). Six repetitions were executed for each temperature point measurement. The post-compaction coordinates of the tubes and thus the corresponding thermocouple locations during the thermal tests are given in Table 6.2. In this table, the sign "±" for each location indicates the inclusive range of temperature point measurements between slabs S13-S18 or slabs S19-S22. The coordinate system for the thermocouple locations is shown in Figure 6.4(a) and 6.4(d) and in Figure 6.5. The origin of the coordinate system is put on the top left corner of the slab. The x-axis and z-axis are set to be the length (695 mm) and width (695 mm) of the slab respectively, whereas the y-axis is put along the depth of the slab (100 mm). Appendix E, Table E.1 shows the locations of the thermocouples per slab for slabs S13-S22 from which Table 6.2 results.
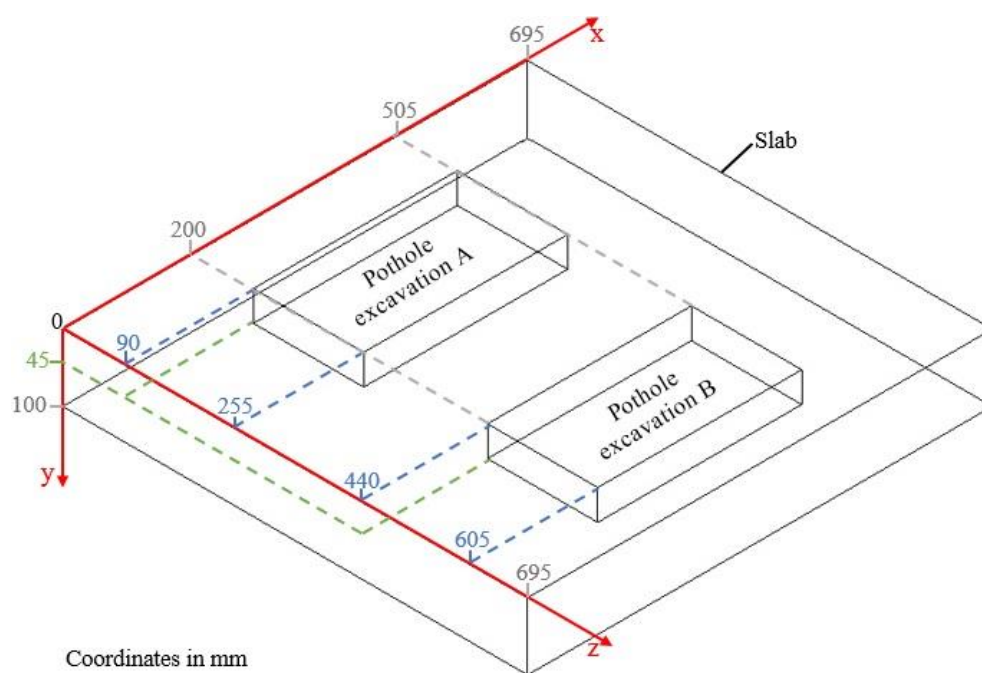
Figure 6.5 Sketch of the coordinate system for thermocouple locations given in Tables 6.2 and 6.3

The construction process of the static pothole repair is shown in Figure 6.7 and was done as follows. Tack coat was applied in the pothole cavity 14 minutes prior to pothole filling to simulate tack coat application of real time pothole repair. Then, hot mix asphalt was poured

and evenly laid out. The mix was compacted for 6 minutes using a vibratory plate compactor. For the tack coat, a thin layer and rapid setting solution of bitumen in solvent was used. The temperatures of the fill mixes were monitored using an infrared camera Flir C2 (Flir, 2018). These temperatures are presented in Figure 6.6. The figure shows also mixture temperatures for dynamic repairs to be discussed in the next section. Temperatures for slabs S13 and S14 not reported in Figure 6.6 are due to error of the infrared camera during the measurements.

Table 6.2 Post-compaction thermocouple locations in the pothole excavation of static repairs in accordance with the origin of the coordinate system shown in Figure 6.4(a) and 6.4(d)

Thermocouple no.	Slab no.	Coordinates (mm)	
		S13-S18	S19-S24
T1	x	200.0 (±1.0)	-
	y	28.5 (±3.5)	-
	z	177.5 (±2.5)	-
T2	x	205.0 (±5.0)	-
	y	25.5 (±4.5)	-
	z	90.0 (±1.0)	-
T3	x	307.5 (±2.5)	-
	y	29.5 (±3.5)	-
	z	90.0 (±1.0)	-
T4	x	405.0 (±5.0)	-
	y	28.5 (±2.5)	-
	z	90.0 (±1.0)	-
T5	x	505.0 (±1.0)	-
	y	26.5 (±3.5)	-
	z	90.0 (±1.0)	-
T6	x	505.0 (±1.0)	-
	y	25.0 (±2.0)	-
	z	175.5 (±4.5)	-
T7	x	-	200.0 (±1.0)
	y	-	28.5 (±3.5)
	z	-	90.0 (±1.0)
T8	x	-	247.5 (±7.5)
	y	-	28.5 (±3.5)
	z	-	175.0 (±1.0)
T9	x	-	332.5 (±22.5)
	y	-	28.5 (±3.5)
	z	-	175.0 (±1.0)
T10	x	-	456.5 (±6.5)
	y	-	28.5 (±3.5)
	z	-	175.0 (±1.0)
T11	x	-	505.0 (±1.0)
	y	-	28.5 (±3.5)
	z	-	90.0 (±1.0)
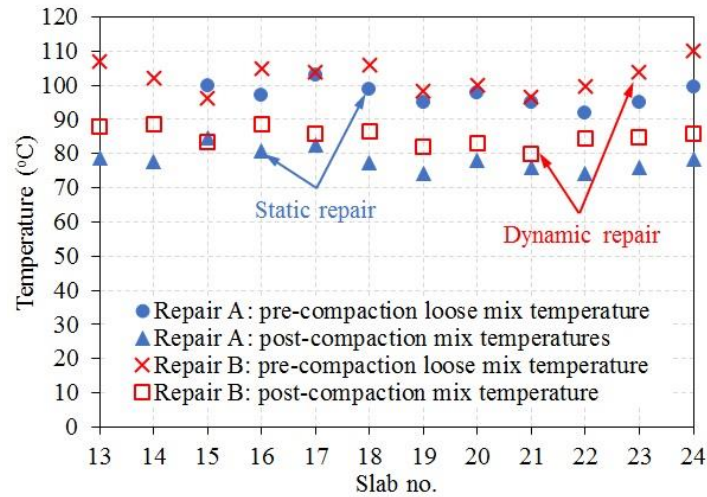
Figure 6.6 Pre- and post-compaction temperatures of pothole fill mixtures for static repair (repair A) and dynamic repair (repair B)
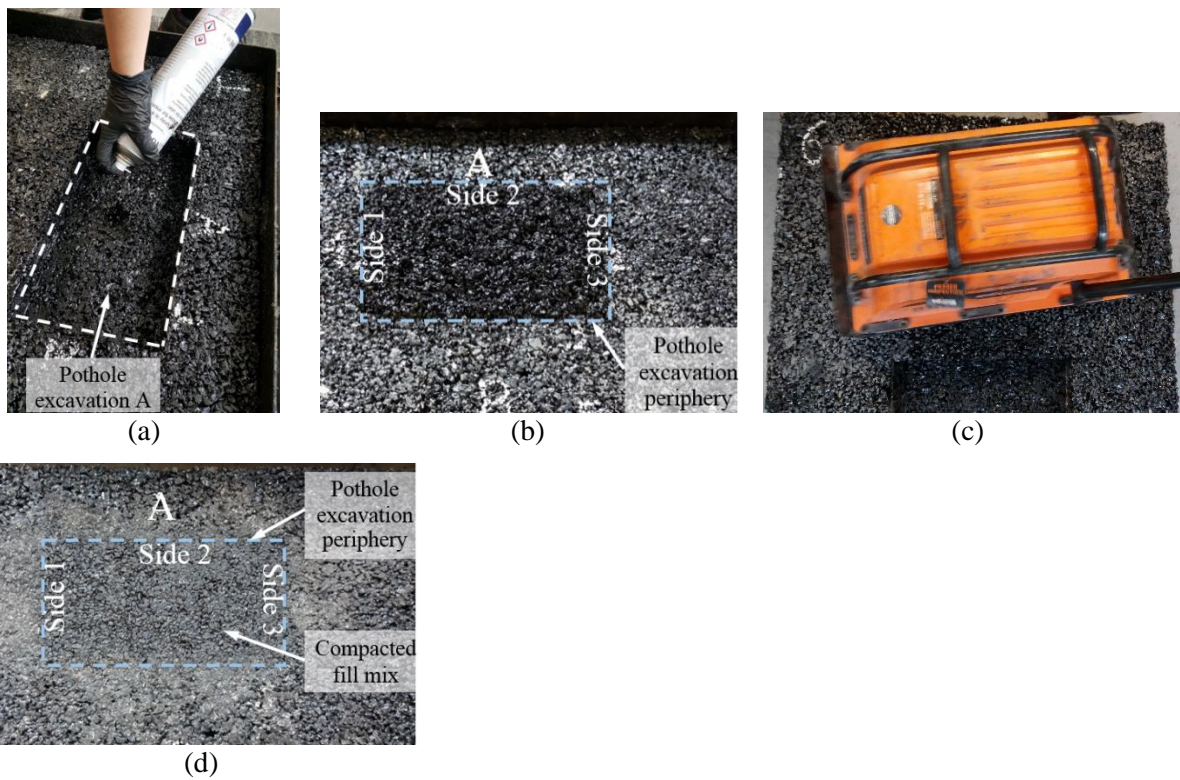
Figure 6.7 Static pothole repair: (a) tack coat application at all faces of the pothole excavation; (b) hot mix asphalt poured after 14 minutes of tack coat application; (c) compaction of fill mix for 6 minutes; (d) final repair (sides 1, 2 and 3 are the same sides with those shown in Figure 6.4)

6.1.5 Dynamic pothole repairs using the experimental infrared heater

Twelve dynamic repairs were constructed. The dynamic heating of the repairs was done using the optimum pre-heating method found in Chapter 4, section 4.4.2.4. According to this method, dynamic heating is applied in heating-cooling cycles with the infrared heater operating stationary above the pothole excavation with 6.6 kW heat power. The six repairs completed in slabs S13-S15 and S19-S21 were pre-heated for 10 minutes 15 seconds. The other six repairs completed in slabs S16-S18 and S22-S24 were pre-heated for 21 minutes 49 seconds. The duration of each heating and cooling time is shown in Figure 6.8.
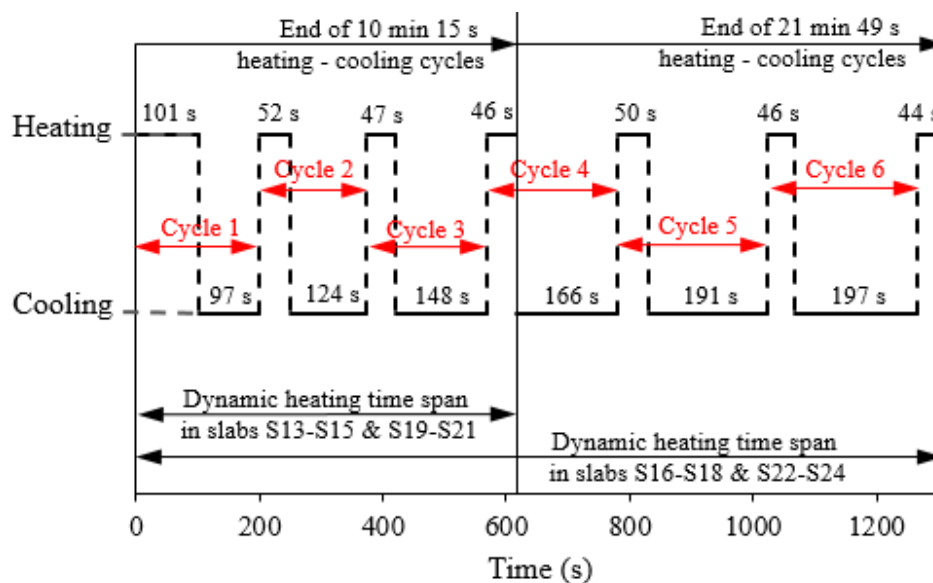
Figure 6.8 Dynamic heating cycle times for 10 minutes 15 seconds and 21 minutes and 49 seconds heating times

The interface temperatures were captured using the same T-type thermocouples as in the static repairs. This is shown in Figure 6.4. The preparation of the thermocouples, the ambient temperature during the repairs and the slab temperatures prior to repair were the same with the static repairs previously described. The ambient and slab temperatures were the same because the static and dynamic repairs for each slab were performed the same day. In addition, the post-compaction coordinates of the tubes and thus the corresponding thermocouple locations for dynamic repairs are given in Table 6.3. The origin of the coordinate system is the same with that of the static repairs shown in Figure 6.4(a), 6.4(d) and Figure 6.5. Appendix E, Table E.2 shows the locations of the thermocouples per slab for slabs S13-S24 from which Table 6.3 results.

Table 6.3 Post-compaction thermocouple locations in the pothole excavation of dynamic repairs in accordance with the origin of the coordinate system shown in Figure 6.4(a) and 6.4(d)

Thermocouple no.	Slab no.	Coordinates (mm)	
		S13-S18	S19-S24
T1	x	505.0 (±1.0)	-
	y	25.5 (±6.5)	-
	z	519.0 (±4.0)	-
T2	x	505.0 (±1.0)	-
	y	27.5 (±2.5)	-
	z	605.0 (±1.0)	-
T3	x	402.5 (±2.5)	-
	y	33.0 (±4.0)	-
	z	605.0 (±1.0)	-
T4	x	302.5 (±7.5)	-
	y	28.5 (±3.5)	-
	z	605.0 (±1.0)	-
T5	x	200.0 (±1.0)	-
	y	27.5 (±7.5)	-
	z	605.0 (±1.0)	-
T6	x	200.0 (±1.0)	-
	y	24.5 (±5.5)	-
	z	517.0 (±3.0)	-
T7	x	-	505.0 (±1.0)
	y	-	45.0 (±1.0)
	z	-	605.0 (±1.0)
T8	x	-	452.5 (±7.5)
	y	-	45.0 (±1.0)
	z	-	520.0 (±1.0)
T9	x	-	350.0 (±5.0)
	y	-	45.0 (±1.0)
	z	-	520.0 (±1.0)
T10	x	-	250.0 (±5.0)
	y	-	45.0 (±1.0)
	z	-	520.0 (±1.0)
T11	x	-	200.0 (±1.0)
	y	-	45.0 (±1.0)
	z	-	605.0 (±1.0)

The construction process of the dynamic pothole repairs is shown in Figure 6.9 and was done as follows. The infrared heater was put above the pothole excavation at an offset of 230 mm. Then, dynamic heating was applied. Immediately after pre-heating, the fill material was poured into the pothole excavation and compacted for 6 minutes. No tack coat was used during these repairs. The mixture temperatures are shown in Figure 6.6. The temperatures captured in the pothole excavation at the end of the two different time spans of dynamic heating were shown in Chapter 4, section 4.4.2.1, Figure 4.10 (the figure refers to results for 45 mm deep pothole

excavation, stationary heater, 6.6 kW heat power for heating for approximately 10 minutes and 20 minutes pre-heating).
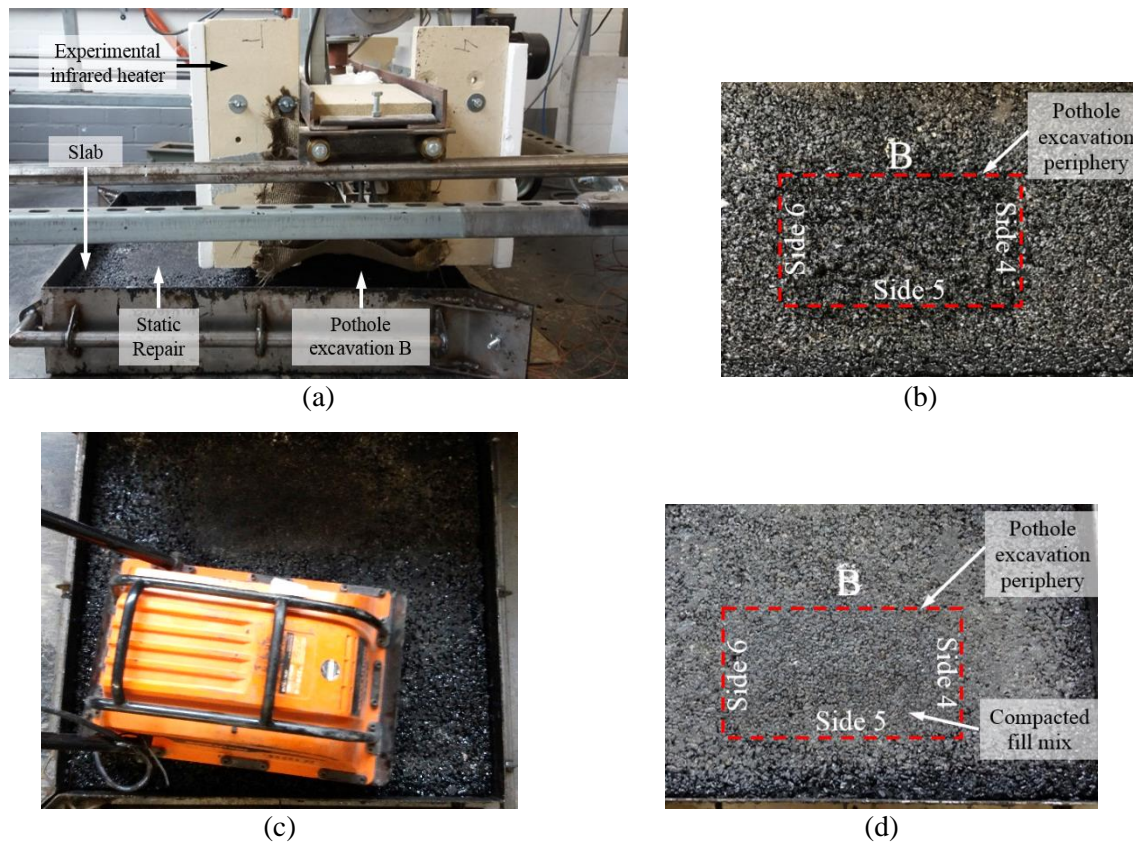
Figure 6.9 Dynamic pothole repair: (a) dynamic heating application; (b) hot mix asphalt poured immediately after pre-heating; (c) compaction of fill mix for 6 minutes; (d) final repair (sides 4, 5 and 6 are the same sides with those shown in Figure 6.4)

6.2 Asphalt thermal properties

6.2.1 Thermal conductivity (k)

Thermal conductivity of the slabs was measured 48 hours after their construction. Thermal conductivity of the repairs was measured 24 hours after their completion. Results were collected at six points throughout the asphalt slab and at two points per pothole repair (Figure 6.10). The measurements were conducted in the laboratory with air temperature at approximately 20 ($\pm$2) $^{\circ}$C and slab temperature at approximately 17.5 ($\pm$2.5) $^{\circ}$C. Thermal conductivity was measured with the TLS method described in Chapter 4, section 4.2.1.

6.2.2 Thermal diffusivity (a) and specific heat capacity (c$_P$)

Thermal diffusivity (a) and specific heat capacity (c$_P$) were calculated using Eq. 2.1 and Eq. 2.2 respectively described in Chapter 2, section 2.8.
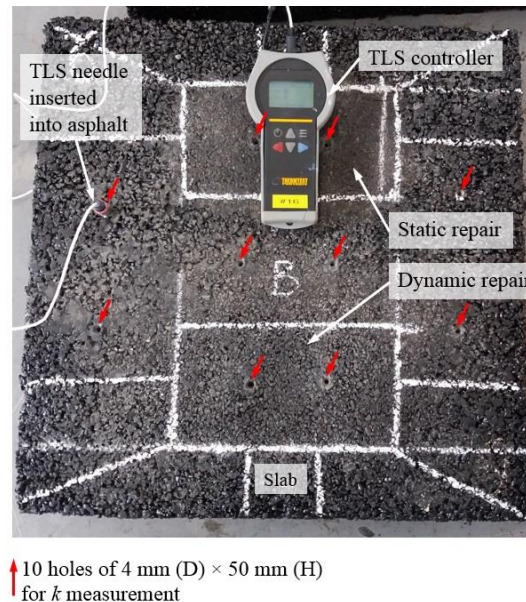
Figure 6.10 Measurement of thermal conductivity in slabs and pothole repairs

6.3   Air voids content

The air voids content of the compacted slabs and repairs were calculated as described in Chapter 4, section 4.3. For this chapter, slabs S13-S18 and their static and dynamic repairs were cored to determine the bulk specific gravity, maximum theoretical specific gravity and air voids content in the total mix. Nine cores were obtained per slab and three cores per pothole repair as shown in Figure 6.11. Slabs S19-S24 could not be cored to determine air voids content of slab and repairs. This was decided due to extensive cutting done on these slabs to examine the shear strength at the vertical repair interfaces to be described in Chapter 8.
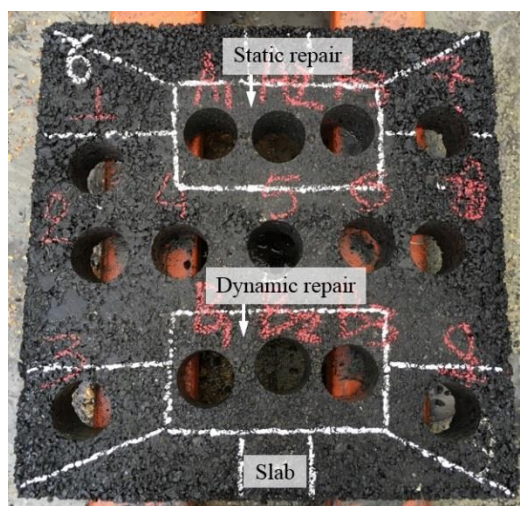
Figure 6.11 Locations of cores in slabs S13-S18 and their repairs

6.4   Results and discussion

6.4.1 Air voids content

Figure 6.12 presents the air voids content of the compacted slabs S13-S18 and of the static and dynamic pothole repairs built in them. The figure shows values from the average of nine cores per slab for all slabs and three cores per repair for all executed repairs. The number of cores depended only on how many cores could be taken from the constructed slabs and repairs. Appendix F presents the air voids of all cores taken from slabs S13-S18 and their corresponding repairs.
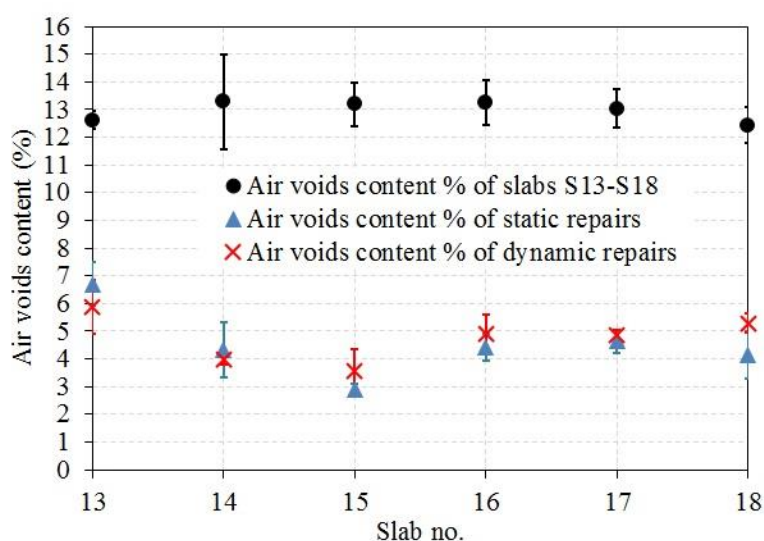
Figure 6.12 Average air voids content of slabs S13-S18 and their corresponding repairs (the error bars show the standard deviation (SD) of each value)

The results show that the air voids content of the slabs ranged from 12.43 % to 13.28 % showing no significant variation. Standard deviations (SD's) of mixture air voids are presented in Figure 6.12. The SD of slab air voids content was found equal to 0.33%, 1.72%, 0.80%, 0.81%, 0.70% and 0.64% for slabs S13, S14, S15, S16, S17 and S18 respectively. Lower air voids contents were observed for the executed repairs. Air voids in static repairs (2.91% - 6.70%) showed higher variation than in dynamic repairs (3.56% - 5.86%) although pre-compaction mix temperatures for static and dynamic repairs were measured to be at similar levels (97.8 $^{\circ}$C and 100.6 $^{\circ}$C in average respectively) and compaction time was also the same for all repairs. The SDs of the air voids content of the six static repairs built in slabs S13-S18 were found equal to 0.78%, 1.00%, 0.18%, 0.50%, 0.42% and 0.86%. The SDs of the air voids content of the six dynamic repairs built in slabs S13-S18 were found equal to 0.97%, 0.20%, 0.79%, 0.72%, 0.16% and 0.35%. Finally, as mentioned also in Chapter 4, section 4.4.1, the effect of pothole pre-heating on the air voids of slabs and dynamic repairs was not investigated in this study and will be included in the recommendations for future research in Chapter 9 since the issue was acknowledged by Norambuena-Contreras and Garcia (2016) in their study of the effect of microwave and induction heating in asphalt mixture air voids.

6.4.2 Thermal conductivity (k), specific heat capacity (c_P) and thermal diffusivity (a)

Figure 6.13 presents the thermal conductivities of slabs and their constituent repairs. The figure shows in (a) thermal conductivities from the average of six measurements per slab and two measurements per repair and in (b) and (c) specific heat capacities and thermal diffusivities respectively from the average of nine calculated values per slab and three values per repair. Appendix F presents in detail the thermophysical properties for all slabs. Specific heat capacity was found only for slabs S13-S18 and their repairs since it was calculated as the sum of the heat capacities of the asphalt constituent parts multiplied by their weight in the mixture per core for all nine cores taken per slab and the three cores taken per repair. Similarly, thermal diffusivity was found only for slabs S13-S18 and their repairs since it was calculated as the ratio of thermal conductivity over the volumetric heat capacity.

(a)

(b)

(c)
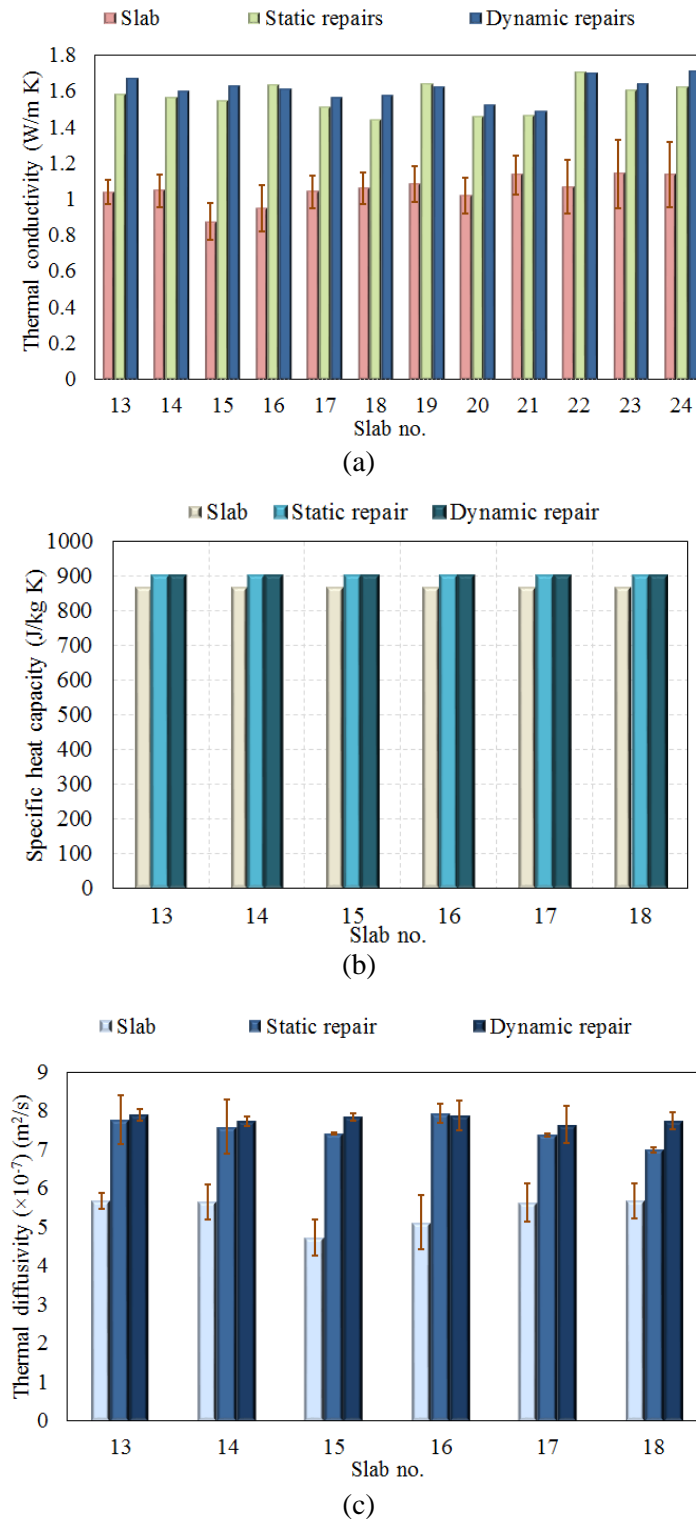
Figure 6.13 (a) Thermal conductivity (k); (b) specific heat capacity (c_P) and (c) thermal diffusivity (a) of slabs and repairs (the error bars in the sub-figures show the SD of each value)

As can be seen from Figure 6.13(a), thermal conductivity is significantly affected by the air voids of the asphalt mixture. This comparison is mainly done for slabs S13-S18 for which air voids of slabs and repairs were measured. Thus, asphalt slabs with high air voids from 12.43% to 13.28% had thermal conductivity ranging from 0.876 W/m K to 1.060 W/m K, whereas, static repairs with air voids from 2.91% to 6.70% had thermal conductivity ranging from 1.442 W/m K to 1.635 W/m K and dynamic repairs with air voids from 3.56% to 5.86% had thermal conductivity ranging from 1.565 W/m K to 1.671 W/m K.

For slabs S19-S24, although air voids were not measured for both slab and repair mixtures, thermal conductivity of the slab mixture was lower than that of the repairs as happened with slabs S13-S18 and their repairs. Thermal conductivity of slabs was found to range from 1.021 W/m K to 1.141 W/m K, of static repairs ranged from 1.460 W/m K to 1.704 W/m K and of dynamic repairs ranged from 1.485 W/m K to 1.711 W/m K.

Overall, no specific increasing or decreasing trend was found when comparing thermal conductivity with air voids content between slabs, static repairs and dynamic repairs separately. This may have happened because the range of air voids is too small to show a specific relationship between air voids and thermal conductivity. Therefore, since thermal conductivity was measured with the needle method (TLS) (explained in Chapter 4, section 4.2), it may have been mainly affected by the distribution of mineral materials around the drilled hole, the cleanliness of the hole and the thermal contact between the asphalt mixture and the needle.

The results of specific heat capacity of slabs and repairs are shown in Figure 6.13(b). The calculations of specific heat capacity showed no variation between the test slabs. This applies also to the specific heat capacities of the static and dynamic repairs. However, comparing specific heat capacities of repairs and slabs, it was found that repairs exhibit a specific heat capacity of 899.46 J/kg K, which is higher than the specific heat capacity of slabs 865.44 J/kg K. This shows that asphalt mixtures with lower air voids content, such as the repair mixture, have higher specific heat capacity than asphalt mixtures with higher air voids content, such as that of slab mixture.

Thermal diffusivity of slabs S13-S18 and their repairs are shown in Figure 6.13(c). Thermal diffusivities of repairs were found to be higher than those of the slabs. However, no significant variation was seen between thermal diffusivities of static and dynamic repairs. The thermal

diffusivity of slabs ranged from 4.73 ($\times$ 10^{-7}) m^2/s to 5.68 ($\times$ 10^{-7}) m^2/s. For the static and dynamic repairs, thermal diffusivities ranged from 7.00 ($\times$ 10^{-7}) m^2/s to 7.95 ($\times$ 10^{-7}) m^2/s and from 7.65 ($\times$ 10^{-7}) m^2/s to 7.88 ($\times$ 10^{-7}) m^2/s respectively. Therefore, overall asphalt mixtures with low air voids content demonstrated high thermal conductivity, low specific heat capacity and low thermal diffusivity. Similar results are reported by Chadbourn et *al*. (1996), Luca and Mrawira, (2005); Hassn et *al*. (2016); Zhang and Wang (2017); and Mirzanamadi, Johansson, and Grammatikos (2018).

Finally, since thermal conductivity, specific heat capacity and thermal diffusivity results presented in Figure 6.13 were obtained from a set of data values presented in Appendix F, standard deviation was also calculated and included in Figure 6.13. The SDs of thermal conductivity of slabs S13-S24 were found to range from 0.07 W/m K to 0.19 W/m K and the SDs of specific heat capacity of slabs ranged from 0.21 ($\times 10^{-7}$) m^2/s to 0.7 ($\times 10^{-7}$) m^2/s. Further, the SDs of specific heat capacity of static repairs built in slabs S13-S18 ranged from 0.03 ($\times 10^{-7}$) m^2/s to 0.64 ($\times 10^{-7}$) m^2/s. The SDs of specific heat capacity of dynamic repairs built in slabs S13-S18 ranged from 0.1 ($\times 10^{-7}$) m^2/s to 0.47 ($\times 10^{-7}$) m^2/s. No SDs were calculated for thermal conductivity of the repairs because only two measurements for this thermal property were possible to collect from the repairs. The resulted deviations are considered acceptable for a non-homogeneous material like asphalt.

6.4.3 Temperatures at the repair interfaces of static and dynamic repairs

The temperatures recorded at the repair interfaces are presented in Figures 6.14 and 6.15. The results present temperature profile over time and are divided into eleven graphs; one graph per thermocouple with positions given in Tables 6.2 and 6.3. For each thermocouple, the temperatures at the interfaces of static repairs are reported together with temperatures for dynamic repairs. Signal noise of thermocouples captured during the tests is also presented. This was observed mainly during the compaction of dynamic repairs and for thermocouples located in corners and vertical sides of the repairs. The disturbance of the thermocouples is attributed mainly to the softening of the asphalt during pothole pre-heating and secondary to the aggregate reorientation and forces applied during compaction.
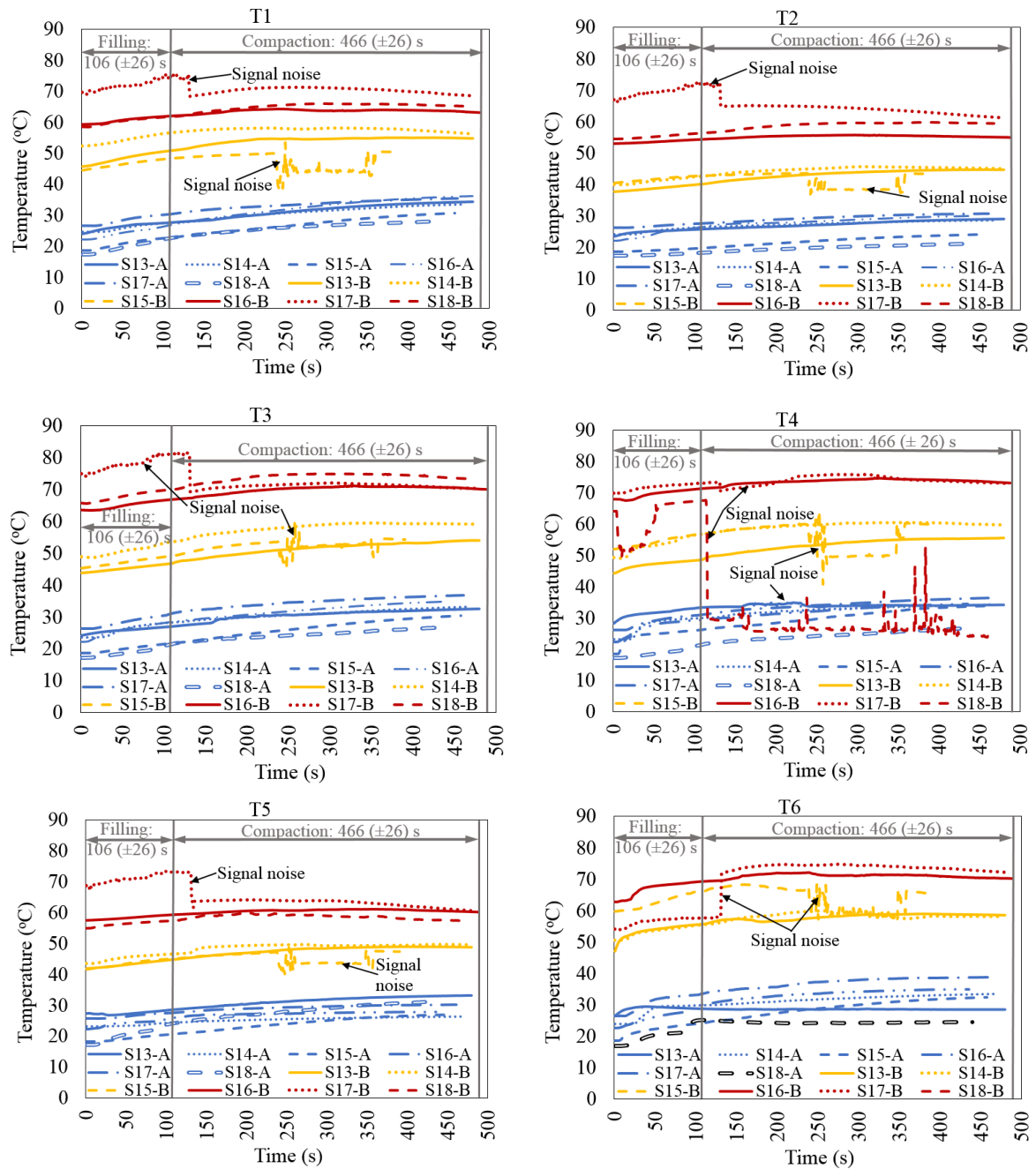
Ti: thermocouple number
Si: slab number
A: repair of pothole A
B: repair of pothole B
S13-A to S18-A: static repairs
S13-B to S15-B: dynamic repairs with 10 minutes 15 seconds pre-heating time
S16-B to S18-B: dynamic repairs with 21 minutes 49 seconds pre-heating time

Figure 6.14 Temperature over time at mid-depth points at the corners and vertical interfaces of static and dynamic repairs during mix pouring and compaction

Figure 6.15 Temperature over time at points at the bottom-corner and mid-bottom interface of static and dynamic repairs during mix pouring and compaction

Between static and dynamic repairs with 10 minutes 15 seconds and 21 minutes 46 seconds pre-heating time, post-compaction temperatures in the vertical interfaces averaged 33.35 ºC, 57.11 ºC and 69.85 ºC respectively (see T1, T3, T4 and T6 in Figure 6.14), whereas, at the bottom of the repair (See T8-T10 in Figure 6.15) temperatures averaged 62.89 ºC for static

repairs, 81.04 °C for dynamic repairs with 10 minutes 15 seconds pre-heating time and 85.26 °C for dynamic repairs with 21 minutes 46 seconds pre-heating time.

The lowest temperatures were observed at the corners of all executed repairs. Points located at the bottom corner of the repairs (T7 and T11 in Figure 6.15) averaged 22.57 °C for static repairs, 30.91 °C for dynamic repairs with 10 minutes 15 seconds pre-heating time and 48.06 °C for dynamic repairs with 21 minutes 46 seconds pre-heating time. There was a small increase in corner temperatures at higher points along the vertical side of the repairs, increasing from bottom to top. An average temperature 27.61 °C was measured for static repairs, 46.41 °C for dynamic repairs with 10 minutes 15 seconds pre-heating time and 58.86 °C for dynamic repairs with 21 minutes 46 seconds pre-heating time.

As was seen from the results, temperatures measured at points located at the vertical repair interfaces of the static repairs were lower than that of dynamic repairs. This happened because of the following. When two solid bodies of different temperatures are in thermal contact, energy is transferred from the hotter to the cooler body. At the interface of these bodies, there is a temperature drop which is caused by surface roughness and non-flatness. In areas where there is a contact between the two surfaces, heat is transferred by conduction. In the void spaces of this interface, heat is transferred by convection and radiation (Figure 6.16). Thus, the actual contact area is significantly smaller than the apparent contact area. This contact limitation at the interface creates a thermal contact resistance (Janna, 1999).
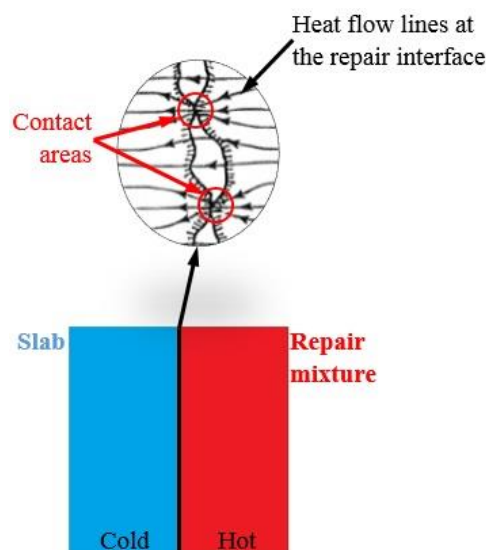
Figure 6.16 Heat flow at the repair interface

Thus, the thermal contact resistance in asphalt repair is the resistance to heat flow through the pothole repair interface due to limited interface contacts. The thermal interface resistance will happen in both cases of non-heated and pre-heated pothole repairs. However, the magnitude of the thermal resistance between non-heated and pre-heated repairs may differ because the characteristics of the two surfaces in contact of the repairs may differ as explained below.

The inverse of thermal contact resistance is thermal contact conductance. Thermal contact conductance can be calculated by the ratio of the conductivity of the material over its thickness and it is expressed in W/m^2 K. The higher the thermal conductance, the lower the thermal resistance at the interface. Thermal conductance is influenced by the characteristics of the two surfaces in contact (such as surface deformation, surface cleanliness, surface roughness, waviness and flatness (Gilmore, 2002), the contact pressure between the two bodies and any conducting fluid (fluids or gases) in the voids spaces of the bodies' interface (Cooper, Mikic and Yovanovich, 1969).

As was seen in the literature review chapter, in non-heated repairs such as the case of static repairs built it this study, low density interfaces are created due to cold underlying layer pavement during placement of hot-fill material (Thom, 2008). However, in pre-heated repairs such as the case of dynamic repairs investigated in this study, the air voids at the repair interfaces are decreased due to the pre-heating taking place prior to filling of the pothole excavation with the hot-fill material. Although this was not evaluated in this study, past studies discussed in the literature review chapter (Chapter 2, section 2.7) and conducted by Huang et *al*. (2010) and Williams (2011) confirm this.

Therefore, between static and dynamic repairs, higher air voids at the interface of static repairs means less contact areas exist between the slab and the fill material and the repair interface temperatures are lower than in dynamic repairs as shown from the experimental results (Figures 6.14 and 6.15). The opposite happens in dynamic repairs where due to pre-heating, the air voids decrease, the contact areas increase and the repair interface temperatures increase too.

The results also showed that temperatures at the bottom of the repair for both static and dynamic repairs were higher than temperatures at the vertical sides of the repair. This is expected to have happened because when compaction force is applied during the repair, the pressure at the vertical interfaces of the repair is expected to be less than at the bottom of the repair. This

increases the thermal resistance at the vertical interfaces which consequently affects the temperatures and creates cooler vertical repair boundaries than the bottom of the repair.

Interpreting the above mechanism in the interaction of in-situ cold old surface pavement and hot asphalt fill mixture, depending on how much pre-heating of the cold surface is done it is expected that the contact areas of the repair interface to change. Thus, depending on the heating time, the temperature of the cold surface is increased, the contact areas are also increased and better heat transfer occurs at the repair interface. Thus, during cold months more heating will probably be better for higher heat transfer but less heating will probably be needed for summer months to achieve similar levels of heat transfer at the repair interface.

The results indicate that controlled pre-heating of the cold surface is fundamental so maximum heat transfer can happen. Increasing heat transfer due to conduction at the repair interface means higher repair bonding is achieved which is proven in the assessment of the repairs in Chapter 8.

6.5   Summary

This chapter experimentally investigated the temperatures at the boundaries of static and dynamic repairs. Non-heated potholes were repaired using a conventional repair method whereas the experimental infrared heater presented in Chapter 3, section 3.1 with capability of precisely controlling heat application, was used to pre-heat pothole excavations of dynamic repairs prior to filling and compaction. Temperatures were measured during the laying and compaction of the fill mixes at eleven locations of the repair interfaces, using extractable thermocouples. Air voids content and thermal properties of the asphalt mixtures were also determined. The chapter ended by quantifying the repair interface temperatures in static and dynamic repairs and by defining the parameters that create a cool boundary in static repairs but much higher boundary temperatures in dynamic repairs. These parameters include air voids levels and contact areas at the repair interfaces which create a thermal contact resistance at the interface. However, the distribution of air voids at the repair interfaces was not investigated in this study. They were assumed higher for static repairs and lower for dynamic repairs following the existing literature. The next chapter simulates the repair interface temperatures using the above assumption by defining thermal contact conductance.

Chapter 7

Finite Element simulation of transient heat distribution in shallow patch repairs

As discussed in the literature review (Chapter 2), sufficiently high temperatures at repair interfaces in hot mix asphalt (HMA) pothole repair are necessary to achieve durable bonding of the repair mix to the surrounding host pavement. Current hot mix repair methods tend to suffer from inadequate net interface heating because the combined effect of placing hot mix in an ambient temperature pothole gives inadequate net temperature levels. The outcome of this is low durability and limited life. In contrast, the outcomes of placing hot mix in a strategically pre-heated excavation is high failure stress capacity on interface boundaries and substantially increased working life.

In this Thesis, Chapter 4 discussed the investigation of a precisely controlled infrared pre-heating method for shallow and deep pothole excavations and presented optimum pre-heating methods for the potholes. In Chapter 6, the optimum pre-heating method was used in the repair activity of shallow potholes to evaluate the temperatures at the interfaces of non-heated and infrared heated repairs. Heat transfer Finite Element models have been run for this chapter for the cases of (i) HMA placed in an ambient temperature pothole (experimentally investigated in Chapter 6, section 6.1.4) (ii) the heated pothole excavation (experimentally investigated in Chapter 4) and (iii) HMA placed in the pre-heated pothole excavation (experimentally investigated in Chapter 6, section 6.1.5).

The reported models were necessary because (a) there is currently no such simulation that investigates heat flow in asphalt pothole repairs that could help to overcome the issue of cool repair boundary; (b) the models could be used in the future for calibrating infrared heaters and help to optimise the heaters' use in asphalt repair under a variety of environmental conditions, repair conditions,

repair geometry and asphalt properties; (c) the initial development of the static repair model followed by the dynamically heated pothole excavation model helped in building and concluding the dynamically heated repair model.

The air-pavement-heater system model comprises a host pavement with two pothole repairs or one empty pothole excavation in the case of the second thermal model and an infrared heating element plate. For calibration purpose, experimental work from Chapter 3 and 5 was used. The air-pavement-heater system set-up follows the optimum pothole pre-heating method determined in Chapter 6. The thermal models were validated with experimental work presented in Chapters 4 and 6. The chapter aims to address the fifth objective of the research.

7.1   The presented models

Static and dynamic repair models and a dynamically heated pothole excavation model are presented in this chapter. The models simulate temperature distribution in the repair interfaces and on the faces of a pothole excavation under the application of dynamic heating. These simulations were developed using ANSYS software. A preliminary version of the dynamically heated pothole excavation is published in author's paper Byzyka, Rahman and Chamberlain (2017a) but has since undergone significant alterations and improvements. This is why only the final version of this model is presented in this chapter. The discussed improvements were used to integrate all models. Specifically, the thermal and physical properties of the asphalt mixtures were measured in the laboratory as shown in Chapters 4-6 and were used to calibrate the models. The thermal contact in the repair activities was simulated using thermal contact conductance (TCC) discussed in Chapter 6, section 6.4.3 and to be calculated in the following sections of this chapter. In addition, the presented models were validated by a total of thirty-seven temperature point measurements. These measurements were described in Chapter 4, section 4.4.2.1 and Chapter 6, section 6.4.3.

7.2   Simulated materials

Three geometries were designed for the simulations: a host asphalt pavement, a pothole fill and a heating element plate of the experimental infrared heater presented in Chapter 3, section 3.1. The simulated asphalt mixtures were 20 mm Dense Bitumen Macadam (DBM) and 6 mm dense graded asphalt (AC 6) for the host pavement and repairs respectively discussed in Chapter 6.

The simulated mixture of the infrared heating element plate was Fecralloy. The properties of all simulated materials are shown in the respective models' sections.

7.3   Static repair model

7.3.1 Model generation

The static repair models for simulating temperatures at the vertical and bottom repair interfaces represent the repair for pothole A of slabs S13 and S19 respectively shown in the experiments of Chapter 6, section 6.1.4. Therefore, each model comprises a host pavement 695 mm × 695 mm × 100 mm with two pothole excavations 305 mm × 165 mm × 45 mm and a pothole fill of similar dimensions with the pothole excavation (Figure 7.1). The geometry of the pavement represents the two top layers of a multi-layered asphalt pavement named as surface and binder courses. This two-layered asphalt pavement was idealized in the simulation as a homogeneous, continuous and semi-infinite in the horizontal and vertical directions.
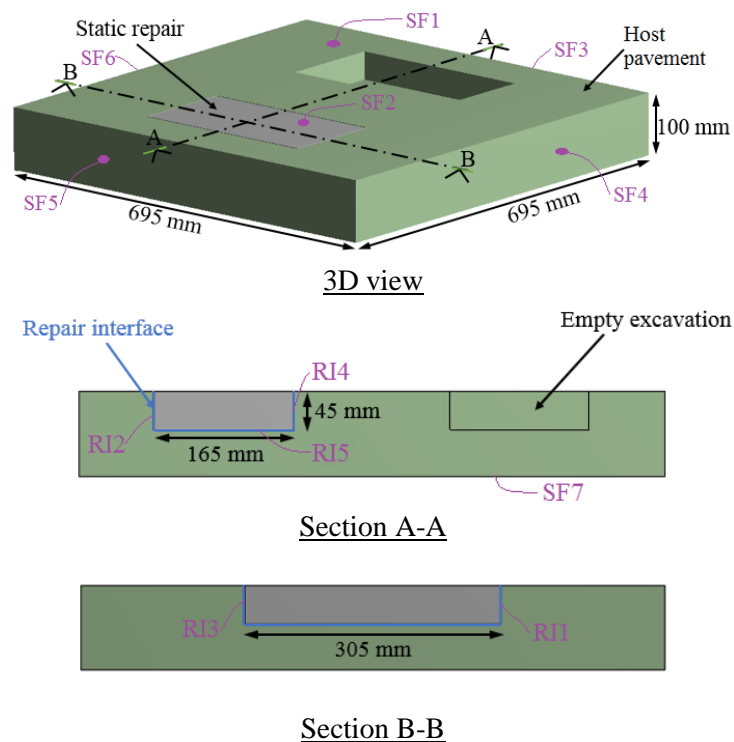
Figure 7.1 Static repair three-dimensional geometrical modelling (SF = surface, RI = repair interface)

7.3.2 Material properties

Densities of the host pavement and repair geometries were set at 2150 kg/m^3 and 2230 kg/m^3 respectively. Specific heat capacities of the host pavement and repair geometries were set at

865.44 J/kg K and 899.46 J/kg K respectively. The same values were used for both static repair models. Thermal conductivity of the host pavement was initially set at 1.040 W/m K and 1.090 W/m K. These values were measured in the laboratory for slabs S13 and S19 respectively and shown in Chapter 6, section 6.4.2. However, during the convergence study to be described in section 7.3.4 below it was found that defining thermal conductivity at different temperatures helps to more accurately simulate the repair. Therefore, thermal conductivity measurements at three different temperatures of a 20 mm DBM mixture presented in Chapter 5, section 5.4 were used to calibrate this model. Thus, thermal conductivity of the pavement was changed to 1.330 W/m K (at 19 ^{o}C), 1.183 W/m K (at 65 ^{o}C) and 0.853 W/m K (at 85 ^{o}C) and of the repair to 1.503 W/m K (at 19 ^{o}C), 1.255 W/m K (at 65 ^{o}C) and 0.937 W/m K (at 85 ^{o}C).

7.3.3 Formation of thermal analysis

Steady-state thermal analysis was used to apply body temperatures and initial air temperature followed by transient thermal analysis to simulate the thermal relationship between the pavement and the pothole repair. Heat energy and radiation exchange between the air and the pavement in the simulation model were defined by applying convection at surfaces SF1-SF7 and radiation at surfaces SF1 and SF2 respectively (Figure 7.1).

The heat conduction at the bonded repair interfaces (R11-R15 (Figure 7.1)) was defined by the TCC. TCC is the reciprocal of thermal contact resistance (TCR) and therefore, determines the resistance to pavement/repair thermal conduction per unit area at the repair interface (Thompson and Thompson, 2007). TCC in the repair activity is influenced by many factors such as contact pressure, interface temperature, heat flow direction, surface oxidation, compaction load cycling, surface cleanliness, surface roughness, surface contact spots and interstitial zones (Somé, Delaunay and Gaudefroy, 2013; Dou et *al*., 2016; Frekers et *al*., 2017). Therefore, TCC plays a significant role in simulating the heat flow and bonding in the repair interfaces.

In this study, the TCC for the vertical repair interfaces was calculated as explained by Straube (2000-2003) for an enclosure assembly. Firstly, the TCC of each asphalt layer of the pavement-repair assembly was calculated using Eq. 7.1. Then, the TCR of each layer was calculated using Eq. 7.2. After this, the sum of the individual TCR's was found and used in Eq. 7.3 to calculate the individual TCC of the four repair interfaces (R11-R14) of the assembly.

$$TCC = \frac{k}{t} \tag{7.1}$$

where TCC is expressed in W/m^2 K; k = thermal conductivity, W/m K; t = thickness, m.

$$TCR = \frac{1}{TCC} \tag{7.2}$$

$$TCC = \frac{1}{TCR} \tag{7.3}$$

In addition, the TCC for the bottom repair interface was not calculated but altered until the simulated interlayer temperatures showed no change. This was done because during the compaction of the pothole repair it is expected that the contact pressure at the bottom of the repair will be higher than at the sides of the repair. High contact pressure at the interface, means high contact conductance but low contact resistance. Table 7.1 shows the individual TCC of the repair interfaces for all cases of the convergence study presented in the following section. Table 7.2 and Figure 7.2 present the thicknesses used in the calculation of the TCC.

Table 7.1 TCC of the pavement-repair assembly at the repair interfaces

Repair interface no.	Thermal conductivity of pavement geometry ($k_{pav.}$) (W/m K)	Thermal conductivity of repair geometry (k_{repair}) (W/m K)	TCCpav. from Eq. 7.1 (W/m^2 K)	TCCrepair from Eq. 7.1 (W/m^2 K)	TCRpav. from Eq. 7.2 (m^2 K/W)	TCRrepair from Eq. 7.2 (m^2 K/W)	TCRassembly (m^2 K/W)	TCCassembly from Eq. 7.3 (W/m^2 K)
R11	1.330	1.503	6.82	4.93	0.15	0.20	0.35	2.86
R12	1.330	1.503	14.78	9.11	0.07	0.11	0.18	5.64
R13	1.330	1.503	6.82	4.93	0.15	0.20	0.35	2.86
R14	1.330	1.503	7.19	9.11	0.14	0.11	0.25	4.02

Table 7.2 Thicknesses used in the calculation of TCC in Table 7.1

No.	Thickness (t) (m)
t_1	0.195
t_2	0.090
t_3	0.195
t_4	0.185
t_5	0.305
t_6	0.165
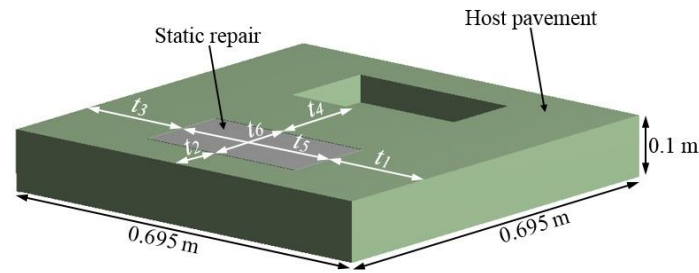
Figure 7.2 Demonstration of thicknesses (*t*)

7.3.4 Convergence study

To ensure a representative model, a mesh convergence test was performed. Six different cases were run, all shown in Table 7.3. The convergence study was combined with testing also the most appropriate values of thermal conductivity. Except for case 1 for which no TCC values were applied at the repair interfaces, for cases 2-6 the TCC assembly values from Table 7.1 were used. This was done to explore the influence of TCC in the simulated repair temperatures. Further, for cases 1-3, thermal conductivities measured at room temperature and shown in Chapter 6, section 6.4.2 were used. However, for cases 4-6, thermal conductivities measured at three different temperatures and shown in Chapter 5, section 5.4 were used. This was done to understand if thermal conductivity influences the simulation results. It should be noted that only the thermal conductivity from the results of Chapter 5 was adopted for the models. The air voids, densities and specific heat capacities of the samples simulated in this section were kept the same as those found in Chapter 6, sections 6.4.1 and 6.4.2.

In addition, for cases 1-5, convection was applied at surfaces SF1-SF7 and radiation was applied at surfaces SF1 and SF2 as described in section 7.3.3. No radiation was used for these cases at the repair interfaces (R11-R15 (Figure 7.1)). However, for case 6, convection and radiation were applied at the same surfaces as cases 1-5 but radiation was also applied at the repair interfaces. This was done because there was a temperature difference between the pavement and the hot pothole fill material and heat exchange by radiation may occur across the air voids in the repair interfaces. This phenomenon is also noted by Frekers et *al*. (2017). During the convergence tests the simulated temperatures were compared with the measured temperatures until close correlation was achieved. The final simulation case concluded from the convergence study was case 6.

Table 7.3 Cases for convergence study

Cases	Thermal conductivity of pavement geometry (W/m K)	Thermal conductivity of repair geometry (W/m K)	TCC assembly	Mesh method for pavement geometry	Mesh method for repair geometry	Pavement geometry sizing (mm)	Repair geometry sizing (mm)	Pothole excavation faces sizing (mm)	Repair geometry faces sizing (mm)
1	19 ºC: 1.04	19 ºC: 1.584	Not used	Tetrahedrons/ Patch conforming/ Element mid-side nodes: not kept	Tetrahedrons/ Patch conforming/ Element mid-side nodes: not kept	20	15	-	-
2	19 ºC: 1.04	19 ºC: 1.584	As shown in Table 7.2	Tetrahedrons/ Patch conforming/ Element mid-side nodes: kept	Tetrahedrons/ Patch conforming/ Element mid-side nodes: kept	20	15	-	-
3	19 ºC: 1.04	19 ºC: 1.584				15	10	-	-
4	19 ºC: 1.330 65 ºC: 1.183 80 ºC: 0.853	19 ºC: 1.506 65 ºC: 1.255 80 ºC: 0.937				15	10	-	-
5	19 ºC: 1.330 65 ºC: 1.183 80 ºC: 0.853	19 ºC: 1.506 65 ºC: 1.255 80 ºC: 0.937				15	10	2	2
6	19 ºC: 1.330 65 ºC: 1.183 80 ºC: 0.853	19 ºC: 1.506 65 ºC: 1.255 80 ºC: 0.937				15	10	-	-

7.3.5 *Final simulation parameters*

The final parameters of the simulations are presented in Table 7.4. The air and pavement temperatures and pre-compaction mixture temperatures were those measured in the laboratory when completing static repairs in slabs S13 and S19 shown in Chapter 6, section 6.1.4, Figure 6.6. The convection film coefficient was imported from ANSYS software and represent the simplified case of stagnant air. This was done because the model represents experimental work completed in the laboratory where there was no significant movement of air. The TCC shown in Table 7.4 was discussed in the previous section. The final mesh elements for the models is 134,487 in number. The simulations were run for 480 seconds and 445 seconds of heat transfer. This was the time taken in the laboratory to place the asphalt mixture in the pothole excavation, evenly spreading and compacting it.

Table 7.4 Static repair model final parameters

Parameters	Model for prediction of temperatures at the vertical repair interfaces for repair made in S13	Model for prediction of temperatures at the bottom repair interface for repair made in S19
Air temperature	21.5 ºC	20.05 ºC
Pavement temperature prior to repair	25.54 ºC	20.48 ºC
Pre-compaction repair mix temperature	99.73 ºC	95.70 ºC
Density of pavement geometry	2150 kg/m³	2150 kg/m³
Thermal conductivity of pavement geometry	19 ºC: 1.330 W/m K 65 ºC: 1.183 W/m K 80 ºC: 0.853 W/m K	19 ºC: 1.330 W/m K 65 ºC: 1.183 W/m K 80 ºC: 0.853 W/m K
Specific heat capacity of pavement geometry	865.44 J/kg K	865.44 J/kg K
Density of repair geometry	2230 kg/m³	2230 kg/m³
Thermal conductivity of repair geometry	19 ºC: 1.506 W/m K 65 ºC: 1.255 W/m K 80 ºC: 0.937 W/m K	19 ºC: 1.625 W/m K 65 ºC: 1.296 W/m K 80 ºC: 0.963 W/m K
Specific heat capacity of repair geometry	899.46 J/kg K	899.46 J/kg K
Convection film coefficient at surfaces SF1-SF7	5 W/m²	5 W/m²
Asphalt emissivity (Hermansson, 2001)	0.9	0.9
Air-pavement-repair heat flow	Convection applied at SF1-SF7. Radiation applied at SF1 and SF2 (Figure 7.1)	
Pavement repair heat flow	Radiation applied at RI1-RI5 (Figure 7.1)	
TCC	RI1: 2.86 W/m² K; RI2: 5.64 W/m² K; RI3: 2.86 W/m² K; RI4: 4.02 W/m² K; RI5: 300 W/m² K	
Mesh	Tetrahedrons with midside elements nodes	
Total elements no.	134,487	134,487
Analysis time	480 seconds	445 seconds

7.4 Dynamically heated pothole excavation

This simulation model represents slab S3 of Chapter 4 and the optimum dynamic heating method for a 45 mm deep pothole excavation also described in Chapter 4, section 4.4.2.4.

7.4.1 Model generation

The model consists of a host pavement 695 mm × 695 mm × 100 mm with a pothole excavation 305 mm × 165 mm × 45 mm and a heating element plate 455 mm × 165 mm × 10 mm (Figure 7.3). According to the optimum pre-heating method, the heater is stationary above the pothole excavation at 230 mm offset, heat is applied in heating-cooling cycles and the heater operates

with 6.6 kW heating power for the heating part of the cycles. This dynamic heating is applied for 615 seconds.

To simulate the operation of the heater, the heating element plate geometry was designed with twelve bonded three-dimensional sections (Figure 7.3). Temperatures measured in the laboratory from each section and shown in Chapter 3, section 3.2 were input at the bottom surface of the heater simulation geometries. The heating element plate of the actual heater is a continuous plate. However, the division of it in the simulation model helped to better correlate the temperature non-linearity and unevenness between the twelve sections when operating at 6.6 kW heat power.

7.4.2 Material properties

Density and specific heat capacity of the pavement were set at 2170 kg/m^3 and 865.44 J/kg K. Thermal conductivity of the host pavement was initially set at 1.002 W/m K. All given values were measured in the laboratory for slab S3. However, as discussed in section 7.3.2 above, to develop a more accurate model, the initial thermal conductivity of the pavement was changed to 1.330 W/m K (at 19 ^{o}C), 1.183 W/m K (at 65 ^{o}C) and 0.853 W/m K (at 85 ^{o}C). The change of thermal conductivities is shown in the different cases of convergence test of section 7.4.4 below. Density, thermal conductivity and specific heat capacity of the heater element plate were set at 7220 kg/m^3, 16 W/m K (at 20 ^{o}C) and 460 J/kg K respectively (Resistalloy, 2016).

7.4.3 Formation of thermal analysis

Steady-state and transient analysis was used to build this model with convected air temperature 22.3 ^{o}C applied at surfaces SF8-SF13. To simulate the application of infrared heat from the heater to the pothole excavation, radiation was applied at the faces of the excavation, the pavement top surface and on the heating element plate bottom faces. Convection at air temperatures of 120 ^{o}C, 160 ^{o}C and 180 ^{o}C were applied at the bottom of the pothole excavation (SF18) and at faces SF15-SF17 and SF14-SF16, respectively (Figure 7.3). This was done to provide close correlation between simulated and measured temperatures under infrared heat and was concluded from the convergence study described in the section below. The main issue is that the vertical faces of the excavation are not as exposed to the heater plate as the bottom face. This means that the temperatures calculated by the simulation in the vertical faces may be lower than the measured temperatures in the laboratory executed repairs. This may happen because the surface to surface radiation algorithm of ANSYS software incorporates view factor

calculations, which will take into account how much radiative heat can be transmitted to the surfaces defined within an enclosure. Further, in practice, due to the presence of convection, it is likely that the vertical surfaces of the pothole will be heated due to their proximity to the base of the excavation and the heat being convected from that surface. This was not taken into consideration automatically by the software.

Figure 7.3 Three-dimensional geometrical modeling (SF = surface, RI = repair interface)

7.4.4 Convergence study

Five different cases were run, all shown in Table 7.5. These cases were run to understand the influence of the parameters shown in the table on the simulated excavation temperatures when infrared heat is applied and find good correlation between measured and simulated temperatures. The simulations were run for 615 seconds according to the optimum laboratory heating method. Initially, a mesh sizing of 15 mm was used for both pavement and plate geometries. For this case (case 1), only thermal conductivity measured at 19.51 $^{\circ}$C was used and convection applied at 22.3 $^{\circ}$C air temperature. The same parameters were kept for case 2 except thermal conductivity which ranged from 1.330 W/m K to 0.853 W/m K for temperatures from 19 $^{\circ}$C to 80 $^{\circ}$C. For case 3, the mesh sizes of the excavation and heating element plate

faces were added in the simulation in comparison with cases 1 and 2 and set at 6 mm and 8 mm respectively. Cases 4 and 5 were based on case 3 with the added values of different air temperatures for convection applied at the pothole excavation faces.

Table 7.5 Cases for convergence study

Cases	**Parameters**									
	Thermal conductivity of pavement geometry (W/m K)	**Mesh method for pavement and heating element plate geometries**	**Pavement geometry sizing (mm)**	**Pothole excavation faces sizing (mm)**	**Heating element plate geometry sizing (mm)**	**Heating element plate geometry bottom face sizing (mm)**	**Convection at pavement top surface SF8 (W/m²)**	**Convection at pothole excavation faces SF15 and SF17**	**Convection at pothole excavation faces SF14 and SF16**	**Convection at pothole excavation bottom face SF18**
1	19.51 ºC: 1.002	Tetrahedrons/ Patch conforming/ Element mid-side nodes: kept	15	-	15	-	22.3 ºC: 5[a]	-	-	-
2	19 ºC: 1.330 65 ºC: 1.183 80 ºC: 0.853		15	-	15	-	22.3 ºC: 5[a]	-	-	-
3	19 ºC: 1.330 65 ºC: 1.183 80 ºC: 0.853		10	6	15	8	22.3 ºC: 5[a]	-	-	-
4	19 ºC: 1.330 65 ºC: 1.183 80 ºC: 0.853		10	6	15	8	22.3 ºC: 5[a]	160 ºC: 5[a]	160 ºC: 5[a]	120 ºC: 5[a]
5	19 ºC: 1.330 65 ºC: 1.183 80 ºC: 0.853		10	6	15	8	22.3 ºC: 5[a]	160 ºC: 5[a]	180 ºC: 5[a]	120 ºC: 5[a]

Note:
[a] The temperature level refer to air temperature that convection of 5 W/m² was applied.

The final simulation case concluded from the convergence study was case 5. For this case for the mesh, a finer element size was adopted for the faces of the pothole excavation in the pavement geometry and on the heating element plate bottom faces. The final mesh elements are 52,967 in number.

7.4.5 Final simulation parameters

The final parameters of the simulation are presented in Table 7.6. The air and pavement temperatures were those measured in the laboratory when testing a 45 mm deep pothole excavation under the application of infrared heat for slab S3 shown in Chapter 4. Similarly with the static repair model, the convection film coefficient was imported from ANSYS

software and represent the simplified case of stagnant air. The properties of the pavement and heater plate emerge from the previous sections.

Table 7.6 Model parameters for dynamically heated pothole excavation

Air temperature	22.3 ºC
Pavement temperature prior to heating	19.86 ºC
Heating element plate temperature prior to heater operation:	18.89 ºC
Density of pavement geometry	2150 kg/m³
Thermal conductivity of pavement geometry	19 ºC: 1.330 W/m K 65 ºC: 1.183 W/m K 80 ºC: 0.853 W/m K
Specific heat capacity of pavement geometry	865.44 J/kg K
Density of heating element plate[a]	7220 kg/m³
Thermal conductivity of heating element plate[a]	20 ºC: 16
Specific heat capacity of heating element plate[a]	460 J/kg K
Convection film coefficient at SF8-SF18	5 W/m²
Asphalt emissivity (Hermansson, 2001)	0.9
Heating element plate emissivity[b]	0.9
Air-pavement-heater heat flow	Convection at 22.3 ºC applied at SF8-SF13. Radiation applied at SF8
Pothole excavation heat flow	Convection at 120 ºC applied at SF18 Convection at 160 ºC applied at SF15 and SF17 Convection at 180 ºC applied at SF14 and SF16 Radiation applied at SF14-SF18
Mesh	Tetrahedrons with midside elements nodes
Total elements no.	52,967
Analysis time	615 seconds
Note: [a] From Resistalloy (2016). [b] The emissivity of the heating element plate was provided by the Heat Design equipment Inc company after personal communication with the manager of the company.	

7.5 Dynamic repair model

This model was built combining the static repair and the dynamically heated pothole excavation models (Figure 7.4). Therefore, the design of the geometries, the position of the heater above the pavement, the material properties and the simulation model parameters are identical. The difference is in the repair mixture temperature and simulation time. The simulation built to validate temperatures at the vertical repair interfaces was run for a total of 1095 seconds (615 seconds pre-heating of pothole excavation + 480 seconds dynamic repair simulation time). The simulation built to validate temperatures at the bottom repair interface was run for 1054 seconds (615 seconds pre-heating of pothole excavation + 439 seconds dynamic repair simulation time). In the simulations, the elements of the dynamic pothole repair geometry were set to an extremely soft stiffness for 615 seconds to allow excavation pre-heating time to

happen without any interaction with the repair geometry. The stiffness was then restored at the end of the heating time for 480 seconds or 439 seconds depending on the simulation run at the time. The initial temperatures of the repair mixtures for these simulations were set at 107 $^{\circ}$C and 98.3 $^{\circ}$C respectively. The final mesh elements are 432,382 in number.
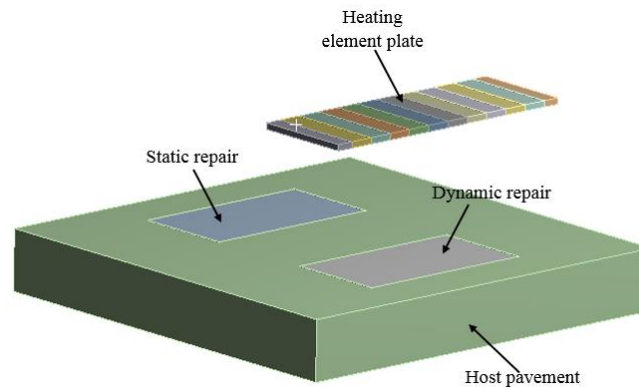
Figure 7.4 Dynamic repair three-dimensional geometrical modelling

7.6   Results

7.6.1 Static repair model

Figure 7.5 shows temperature profile over time at eleven sampling points at the interfaces of a 45 mm deep static repair. Simulated temperatures are compared against temperatures measured in laboratory experiments. Thermocouples T1-T6 show temperatures in the vertical sides mid-depth of the repair for a simulated and experimental repair time of 480 seconds. Thermocouples T7-T11 show temperatures at the corners and bottom of the repair for a simulated and experimental repair time of 445 seconds. The exact positions of the thermocouples were shown previously. The data used to validate the static repair model were taken from one laboratory repair work for each thermocouple group although six repetitions were performed in the laboratory for each temperature sampling point. However, this was done because in the experimental study it was concluded that temperatures were similarly increased for repairs constructed when air and host pavement temperatures ranged from 17 $^{\circ}$C to 22 $^{\circ}$C and from 17 $^{\circ}$C to 26 $^{\circ}$C respectively. The same air and pavement temperatures were used in the simulation.

The results showed that for T1-T6 there was in average 94.53%, 95.52%, 95.62%, 91.83%, 95.52% and 95.07% agreement respectively between measured and simulated temperatures. The highest temperature difference was observed at T7 and T11 located at two corners at the

bottom of the repair. In these locations, 67.50% and 75.97% agreement were seen between simulated and test data. The prediction of temperatures improved for T8-T10 located at mid-bottom areas of the repair interface where simulated temperatures agreed in average with the test temperatures by 86.51%, 86.23% and 83.00% respectively. For the first 10 seconds of simulating time, for thermocouple positions T8-T10 temperatures increased rapidly from approximately 21 ^{o}C to 55 ^{o}C, whereas, at the same locations, temperatures measured in the laboratory increased from approximately 20 ^{o}C to 27 ^{o}C. Theoretically the analysis is correct but due to thermal contact resistance at the repair interface, the laboratory measurements stand as accurate. For this reason, no correlation of data is included in Figure 7.5 for T8-T10 for the first 10 s of simulation time.
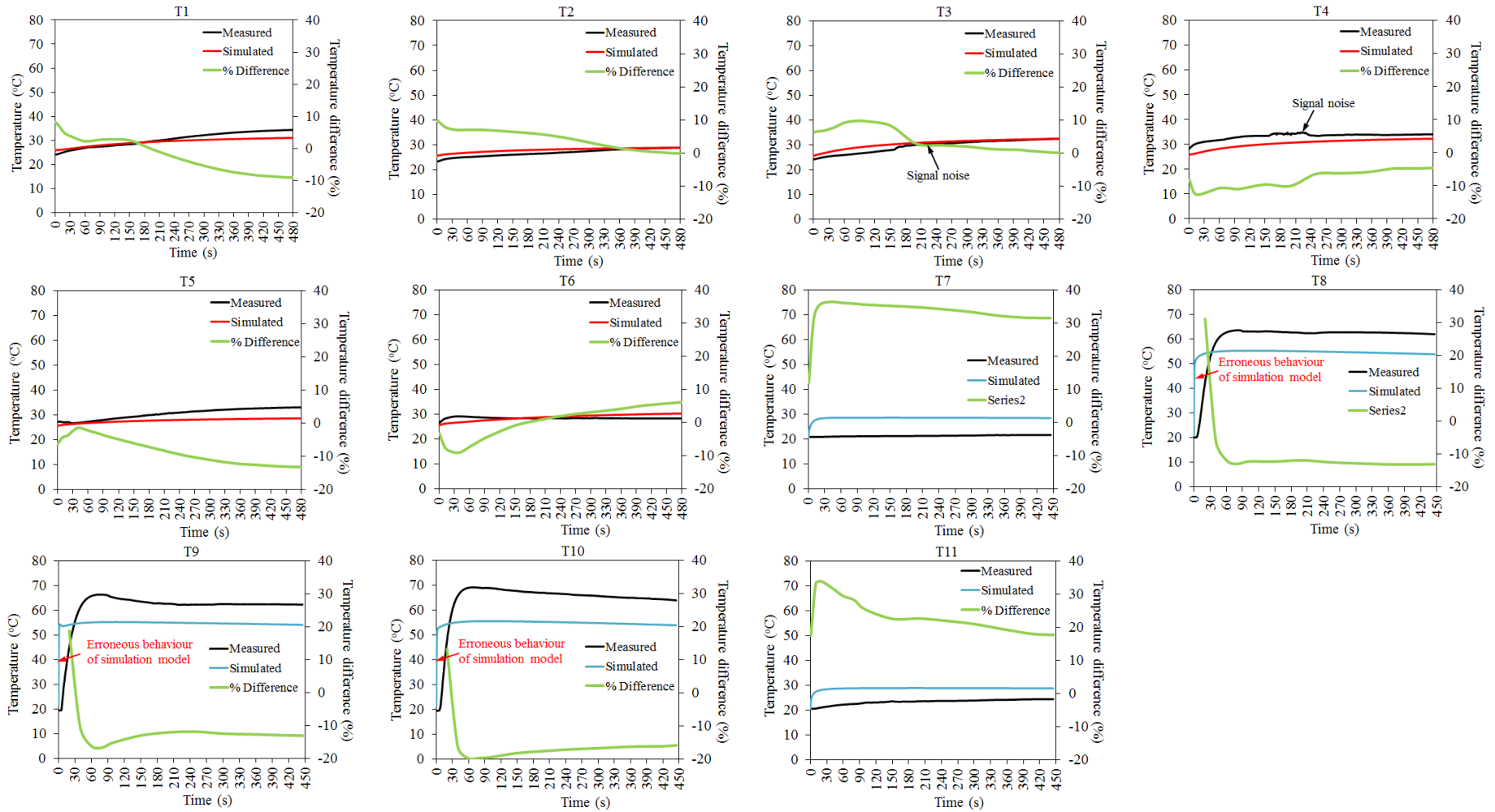
Figure 7.5 Comparison of simulated and measured temperatures at the interfaces of static repair (Ti = thermocouple number as per experimental thermocouple numbering of Chapter 6, Table 6.2)

7.6.2 Dynamically heated pothole excavation model

The results and validation of this model are presented in Figures 7.6 and 7.7. In these figures, the characterisation and locations of the thermocouples follow that of the experimental work. In Figure 7.6, estimated temperatures at eight locations in the pothole excavation are compared against laboratory measurements. Considering the three-dimensional view of the model in Figure 7.3, T26 and T27 are located at the mid-bottom and bottom-corner of the cavity respectively. Thermocouples T28-T31 are located at the middle of each vertical excavation face and T32, T33 are located at mid-top points of the cavity. In Figure 7.7, seven more sampling points are presented. They were used to validate simulated temperatures at points located inside and across the depth of the host pavement at a distance from the excavation long and short faces 20 (±5) mm and 30 (±13) mm respectively.

Simulated temperatures at T26 and T28-T33 reached an average agreement with the measured temperatures 83.29%, 86.51%, 77.53%, 87.71%, 75.85%, 81.93% and 80.52% respectively. Lower correlation was observed for T27 with simulated temperatures matching test data on average by only 59.63%. The figure improves for temperatures predicted at locations inside the host pavement during the dynamic heating of the pothole excavation. Specifically, on average, at T1, T3-T7 a correlation 89.59%, 97.15%, 88.40%, 91.45%, 99.15% and 91.88% respectively was observed. The lowest agreement (69.60%) between simulation and experimental work was seen at T2.

7.6.3 Dynamic repair model

This model simulates temperatures over time at the interfaces of a 45 mm deep repair that has been dynamically heated prior to fill and compaction. The results are shown in Figure 7.8. Thermocouples T1-T6 show temperatures at the vertical sides mid-depth of the repair for a simulated and experimental repair time of 1095 seconds. Thermocouples T7-T11 show temperatures at the corners and bottom of the repair for a simulated and experimental repair time of 1054 seconds. There is a low correlation between simulated and measured temperatures for this model when compared with the static repair model since the simulated temperatures at the repair interfaces are to a degree affected by the temperatures achieved during the pre-heating of the excavation. Therefore, for T1-T6 for the first 30 seconds of repair time, there was an overall average agreement 40.77%. This figure increased for repair time between 40 seconds and 480 seconds and was equal to 64.92%. However, bottom temperatures T8-T10 had a high correlation 95.70%, 91.36% and 94.34%. The model fails to accurately simulate

bottom corner temperatures where for T7 and T11 an agreement 34.65% and 44.96% respectively were seen.
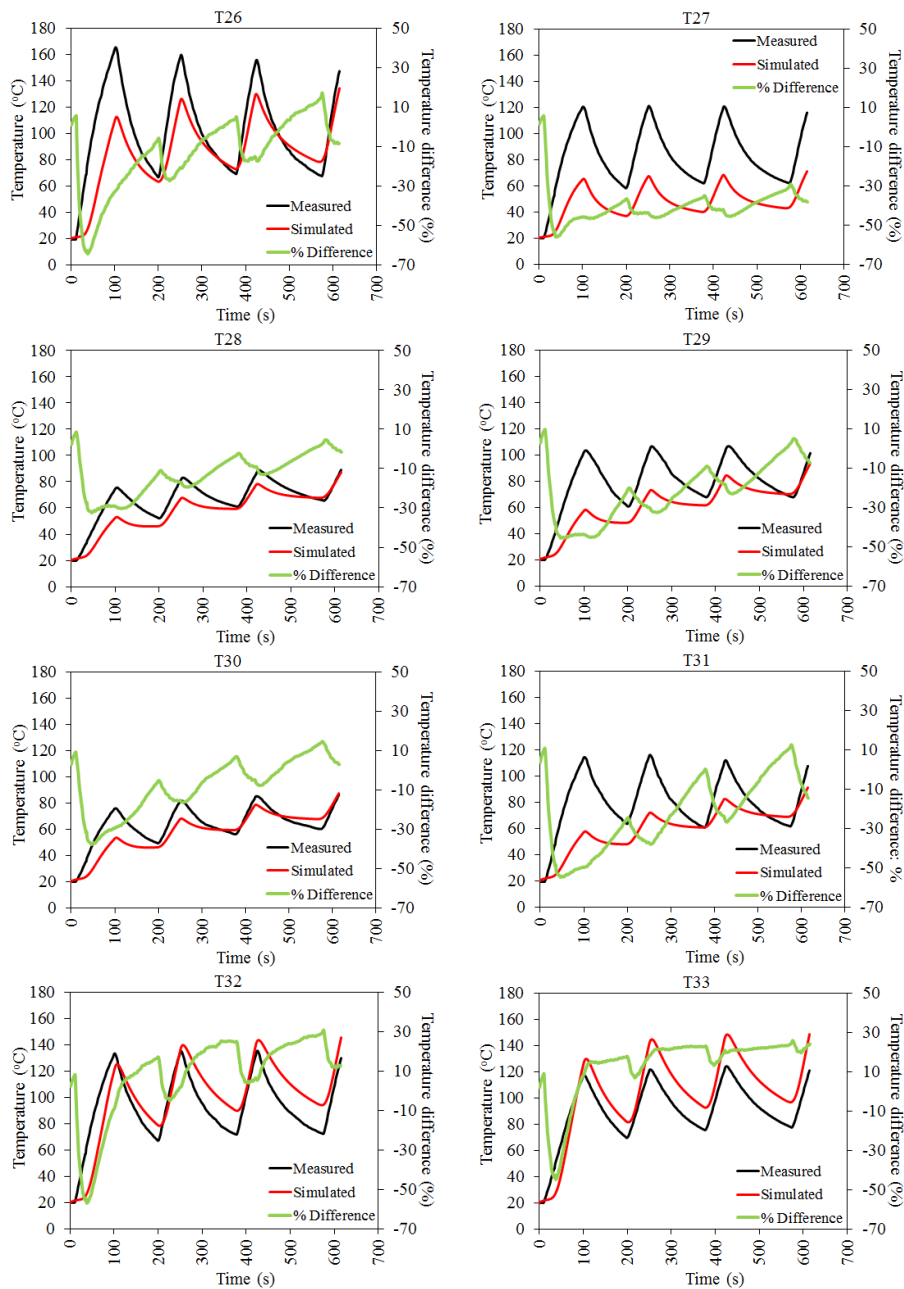
Figure 7.6 Comparison of simulated and measured temperatures at the faces of dynamically heated pothole excavation (Ti = thermocouple number as per experimental thermocouple numbering of Chapter 4, Table 4.5)
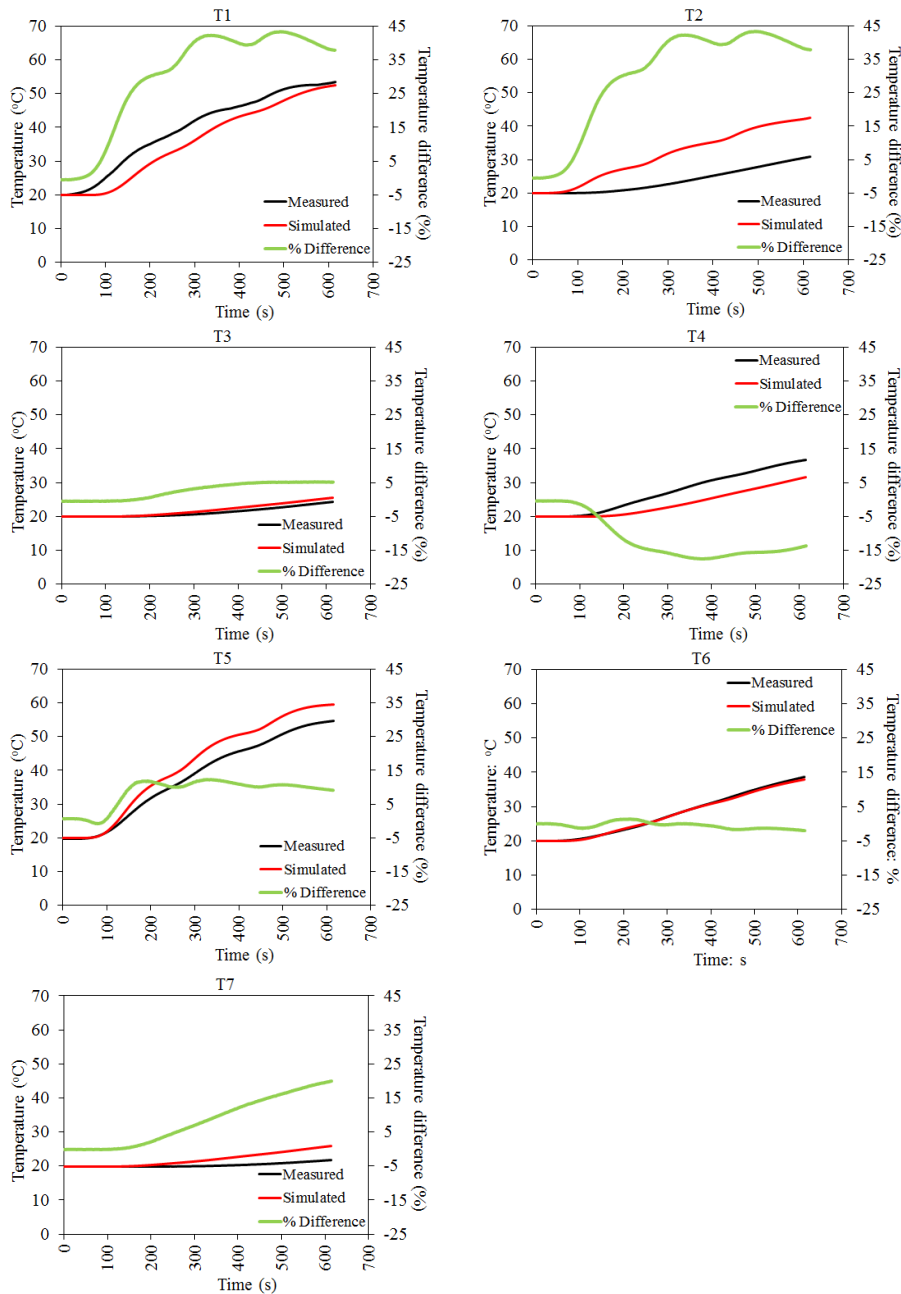
Figure 7.7 Comparison of simulated and measured temperatures inside the host pavement of dynamically heated pothole excavation (Ti = thermocouple number as per experimental thermocouple numbering of Chapter 4, Table 4.3)
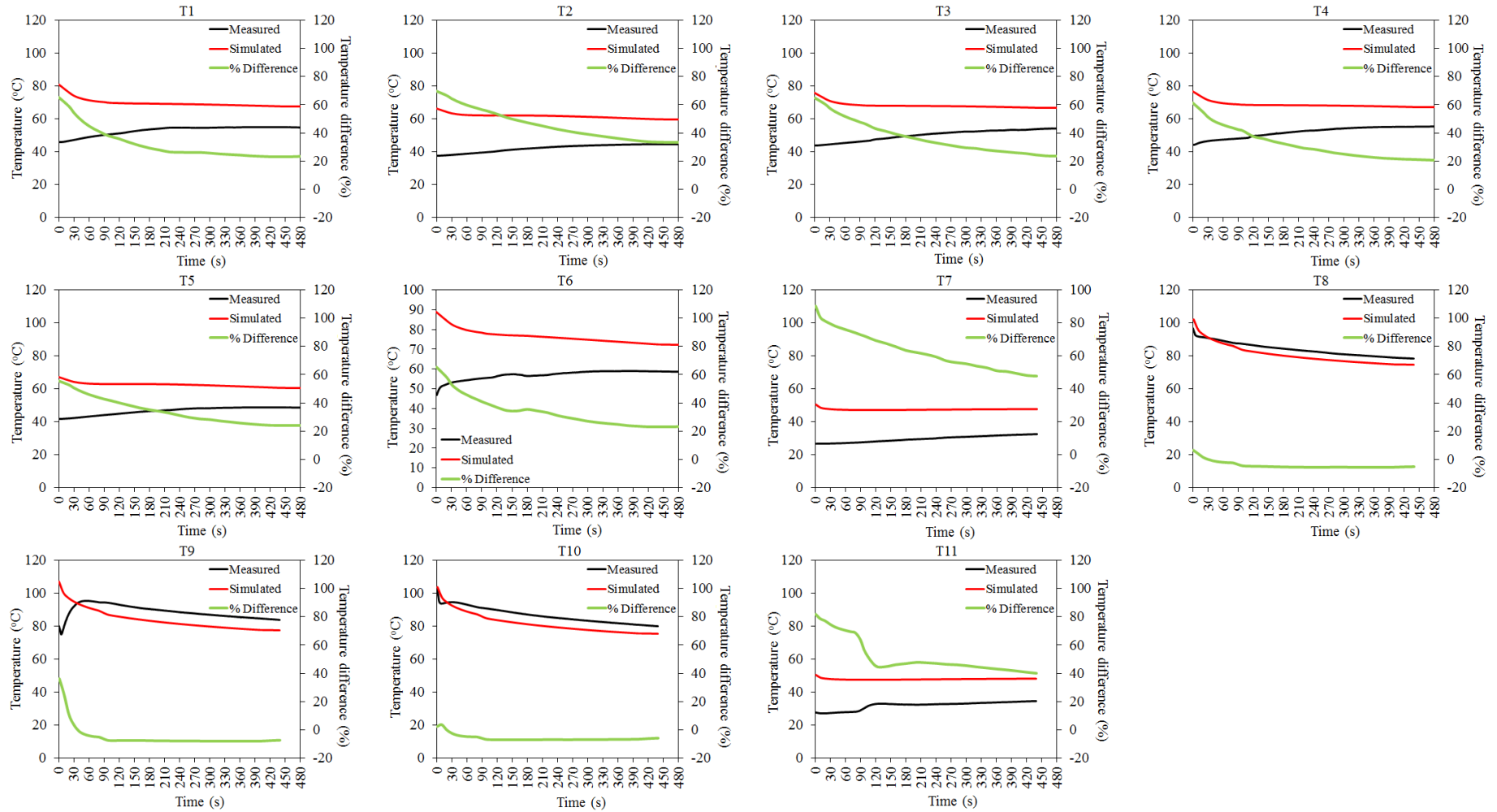
Figure 7.8 Comparison of simulated and measured temperatures at the interfaces of dynamic repair (Ti = thermocouple number as per experimental thermocouple numbering of Chapter 6, Table 6.2)

7.7   Summary

In this chapter, a 45 mm deep static repair, dynamically heated pothole excavation and dynamic repair were simulated and individually validated with experimental work driven from Chapters 4 and 6 for the dynamically heated pothole excavation and pothole repair simulations respectively. The validation of the excavation was done at temperature sampling points located at all surfaces and two corners of it. Meanwhile, the validation of the repair models was mainly concentrated at the interfaces of the actual repair where low in temperature interfaces during the fill and compaction of the pothole mixture affect the bonding of the repair with the old pavement and therefore the repair life duration. The next chapter presents the experimental validation of the strength and rutting resistance of static and dynamically heated pothole repairs that were extensively studied in this chapter and Chapter 6.

Chapter 8

Performance evaluation of shallow patch repairs

The advantage of controlled pre-heating in dynamic repair against static repair is presented in this chapter. Shear bond tests and immersion wheel tracking tests were performed to asses the quality of both types of repair. The twelve slabs described in Chapter 6 were cored and used to perform the shear bond tests. However, six new slabs with static and dynamic repairs were built for the wheel tracking tests. Therefore, the description of materials and construction of slabs and pothole repairs included in this chapter refer only to test samples for wheel tracking tests. The chapter aims to address the sixth objective of the research.

8.1 Materials and experimental methods

8.1.1 Experimental program

The experimental program and test parameters are presented in Table 8.1. Eighteen slabs were used to investigate repair interface bonding and rutting performance of static and dynamic repairs. For shear bond tests, the twelve slabs described in Chapter 6 were used. Therefore, two dynamic heating times (10 minutes 15 seconds and 21 minutes 49 seconds) were tested for the dynamic repairs. The shear bond tests were performed at 20 (±3) ^{o}C. For wheel tracking tests, six new slabs were built. Two pothole excavations were designed per slab for simultaneous testing of static and dynamic repairs. Dynamic repairs with 10 minutes 15 seconds pre-heating time were only tested. The wheel tracking tests were performed at two testing temperatures 25 (±1) ^{o}C and 4 (±1) ^{o}C.

8.1.2 Materials

The same materials as Chapters 4 and 6 were used to build the slabs and repairs for wheel tracking tests. The slabs were built with 20 mm DBM comprising coarse and fine granite aggregate and limestone filler. The bitumen used was 100/150 pen. The pothole excavations were repaired with 6 mm dense graded mixture (AC 6). The gradation curves of the slab and repair mixtures were shown in Chapter 4, section 4.1.1 and Chapter 5, section 5.1.1 respectively.

Table 8.1 Experimental program

Slab no.	Slab size: mm	Pothole size: mm	Pothole A: static repair at room temperature 20 (±3) °C	Pothole B: dynamic repair with 10 min 15 s heating time at room temperature 20 (±3) °C	Pothole B: dynamic repair with 21 min 49 s heating time at room temperature 20 (±3) °C	Shear bond test in vertical repair interfaces at 20 (±3) °C	Shear bond test in bottom repair interfaces at 20 (±3) °C	Wheel track test at 25 (±1) °C	Wheel track test at 4 (±1) °C
S13	695 × 695 × 100	305 × 165 × 45	✓	✓			✓		
S14			✓	✓			✓		
S15			✓	✓			✓		
S16			✓		✓		✓		
S17			✓		✓		✓		
S18			✓		✓		✓		
S19			✓	✓		✓			
S20			✓	✓		✓			
S21			✓	✓		✓			
S22			✓		✓	✓			
S23			✓		✓	✓			
S24			✓		✓	✓			
S25			✓	✓				✓	
S26			✓	✓				✓	
S27			✓	✓				✓	
S28			✓	✓					✓
S29			✓	✓					✓
S30			✓	✓					✓

8.1.3 Preparation of HMA and construction of HMA slabs

The preparation of asphalt mixture and the construction of the slabs were done as described in Chapter 6, section 6.1.3. The size of the slabs was 695 (±5) mm × 695 (±5) mm × 100 (±5) mm and of the two pothole excavations was 305 (±2) mm × 165 (±2) mm × 45 (±2) mm. The first difference between the slabs for shear bond tests and those for wheel tracking tests was the arrangement of the pothole excavations within the slab. The pothole excavations for the wheel track tests were arranged so a repair interface fell directly below the wheel load path. This is shown in Figure 8.1. The second difference was that no aluminium tubes were included in the construction of the slabs. The aluminium tubes were not necessary because temperatures were not measured during the repairs since the temperature profile at the repair interfaces was already established by the tests described in Chapter 6. Further, the author wanted to avoid creating gaps inside the slabs that may affect the results of the wheel tracking tests.
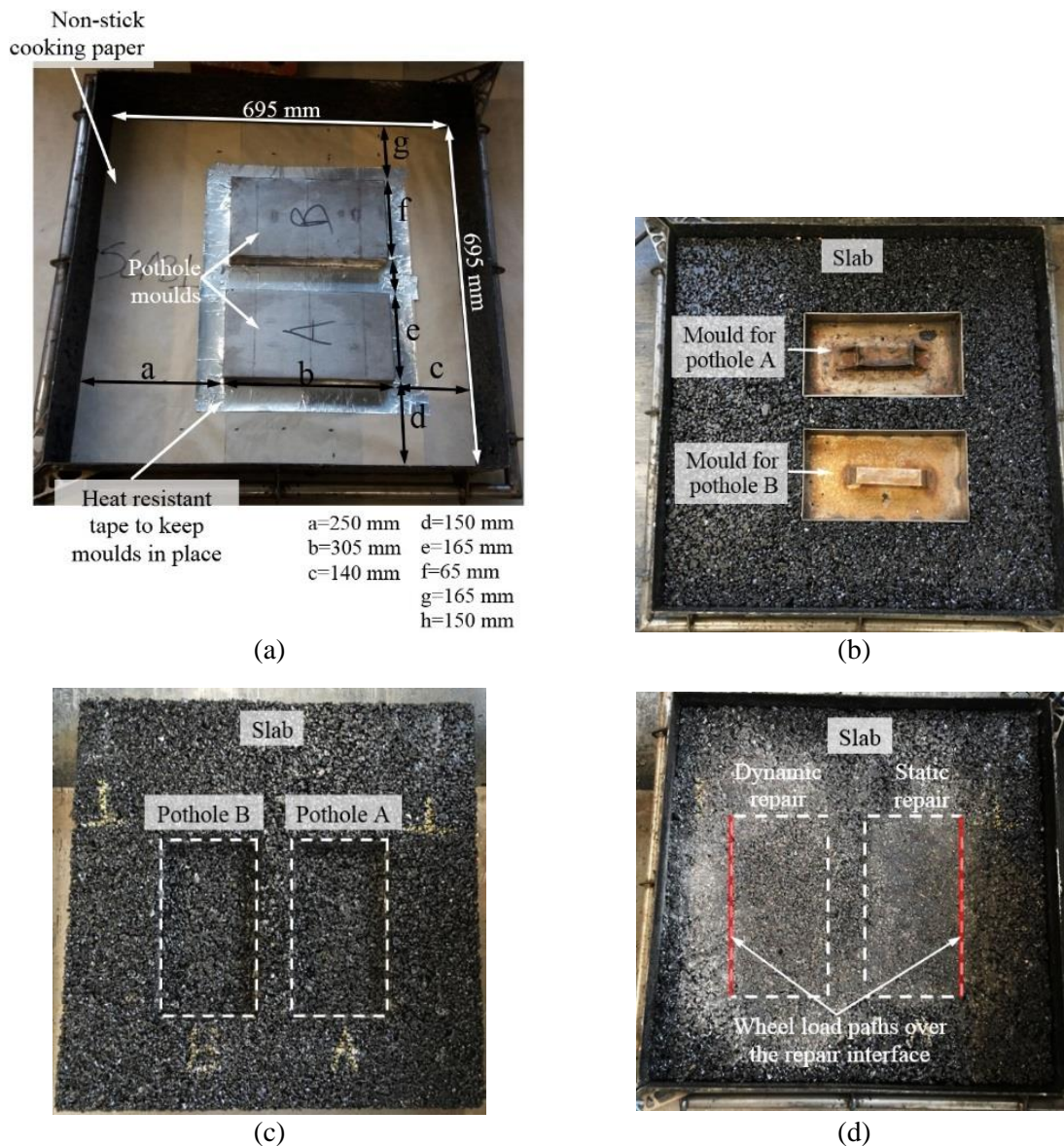
Figure 8.1 Slabs for wheel tracking tests: (a) moulds; (b) constructed slab with pothole moulds; (e) demoulded slab; (f) repaired slab and demonstration of wheel load path at the repair interface

8.1.4 Static pothole repairs

Static repairs were completed as shown in Chapter 6, section 6.1.4. Pre- and post-compaction repair mixture temperatures are shown in Figure 8.2.

8.1.5 Dynamic pothole repairs

Dynamic repairs were completed as shown in Chapter 6, section 6.1.5. Pre- and post-compaction repair mixture temperatures are shown in Figure 8.2.
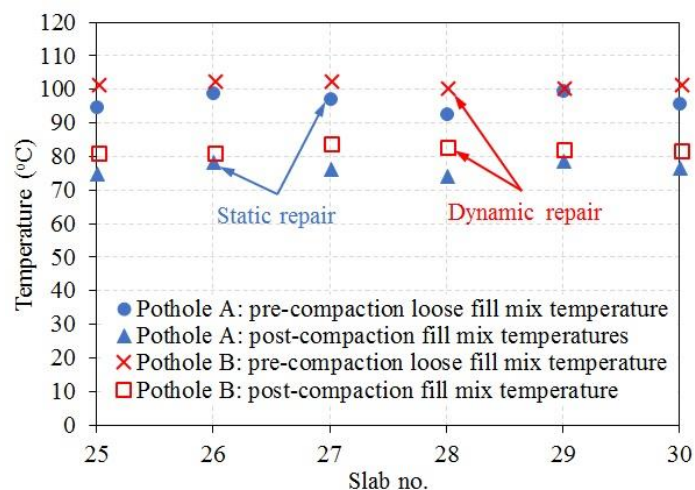
Figure 8.2 Pre- and post-compaction temperatures of pothole fill mixtures for static and dynamic repairs in slabs S25-S30

8.1.6 Air voids content of slabs and repairs

The air voids content for slabs and repairs used for shear bond tests was presented in Chapter 6, sections 6.3 and 6.4.1. It was not possible to measure air voids content for test samples constructed for wheel tracking tests. However, a similar level of air voids was expected to have been achieved for these samples due to the consistent construction method for slabs and repairs followed by the author. The consistency in measured air voids of samples for shear bond tests also supports this assumption.

8.1.7 Shear bond tests (SBT's)

Shear bond tests (SBT's) were performed to evaluate the bonding at the interfaces of both static and dynamic repairs built in slabs S13-S24. To determine the bonding at the bottom interface of the repairs, the repairs of slabs S13-S18 were cored as shown in Figure 8.3. For vertical repair interfaces, the slabs were first cut by a wet saw into smaller blocks and then cored. The coring direction was perpendicular to the repair interface. A notch was created in the cores to concentrate loading on the repair interface (Figure 8.4). At the end of coring and after conditioning test cores at a room temperature 20 ($\pm$3) $^{\circ}$C for 24 hours, they were sheared to failure.

Background information on the SBT was given in the literature review chapter (Chapter 2) in section 2.10.1. For this study, the SBT's were conducted using an Instron hydraulic machine together with a shearing rig specifically designed for this study (Figure 8.5). The design of the

shearing rig was done in accordance with Raposeiras et *al.* (2013) for a 70 mm diameter extracted core. The shear displacement rate was 20 mm/min following Obaidi, Gomez-Meijide, and Garcia (2017). The gap between the shearing platens was 5 mm and the tests were conducted at a room temperature 20 (±3) °C. The maximum shear stress was calculated using Eq. 2.11 in Chapter 2, section 2.10.1.

(a)

(b)

(c)

(d)
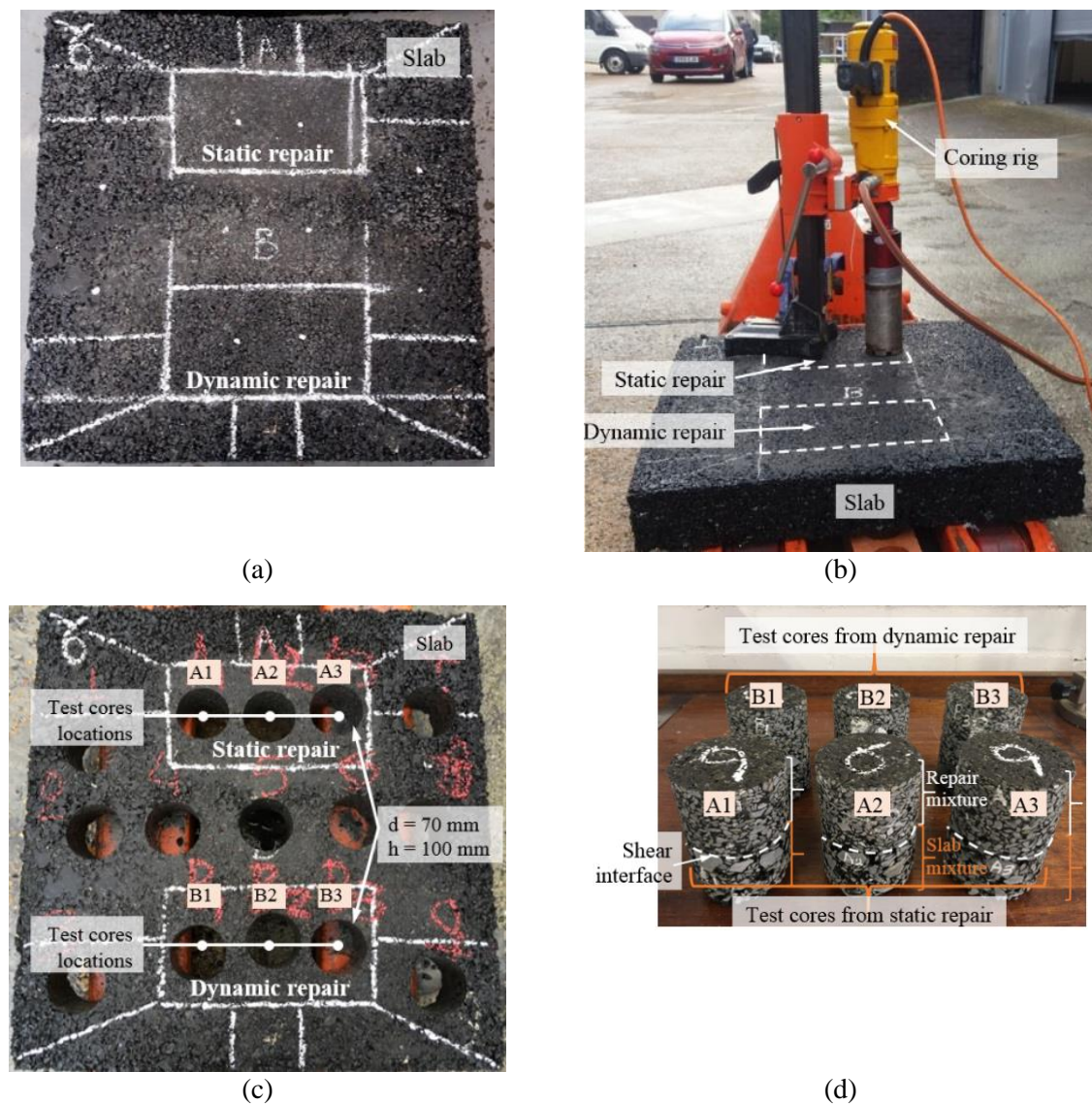
Figure 8.3 Coring of slabs S13-S18 to obtain test cores for SBT's of bottom repair interface: (a) marking; (b) coring; (c) coring locations; (d) test cores

(a)

(b)

(c)

(d)

(e)
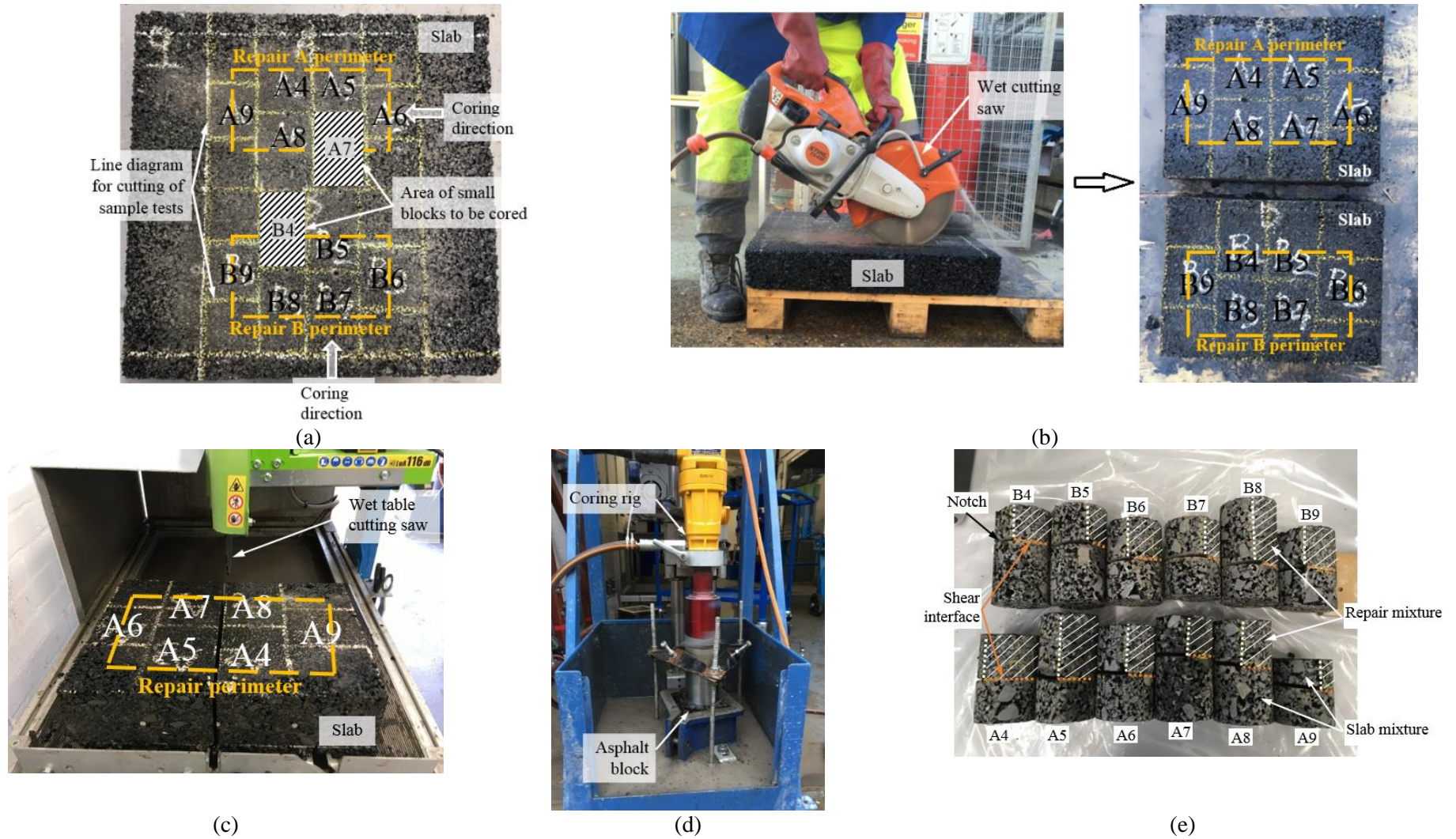
Figure 8.4 Coring of slabs S19-S24 to obtain test cores for SBT's of vertical repair interfaces: (a) marking; (b) cutting of slabs to blocks; (c) cutting of blocks to smaller blocks; (d) coring of small blocks; (e) test cores

Key
1   Upper ring for sample support
2   Lower ring for sample support
3   Shear ring
4   4 bolts for holding upper and lower rings
5   Support for lower ring to keep it stable
6   Aluminium block to separate load head from shear ring
7   Load from Instron hydraulic machine
8   Asphalt sample test

Figure 8.5 SBT apparatus designed for this study

8.1.8 Wheel tracking tests (WTT's)

Figure 8.6 shows the test samples for wheel tracking tests. The tests at 25 ($\pm$1) $^\circ$C were conducted using a Hamburg wheel tracking device in accordance with AASHTO T324 (American Association of State Highway and Transportation Officials, 2004) with test tank and moulds specifically designed for this study. Tests performed at 4 ($\pm$1) $^\circ$C are non- standard, nevertheless, a similar procedure was followed. The 4 ($\pm$1) $^\circ$C temperature was controlled with a K1 chiller integrated with the wheel tracking device. Static and dynamic repairs were simultaneously tested. 20,000 cycles were applied to each repair, as shown in Figure 8.7. Rutting depth was measured at 4 mm spacing along 96 mm of repair interface. The tests were conducted 24 hours after the completion of the repairs.

(a)   (b)
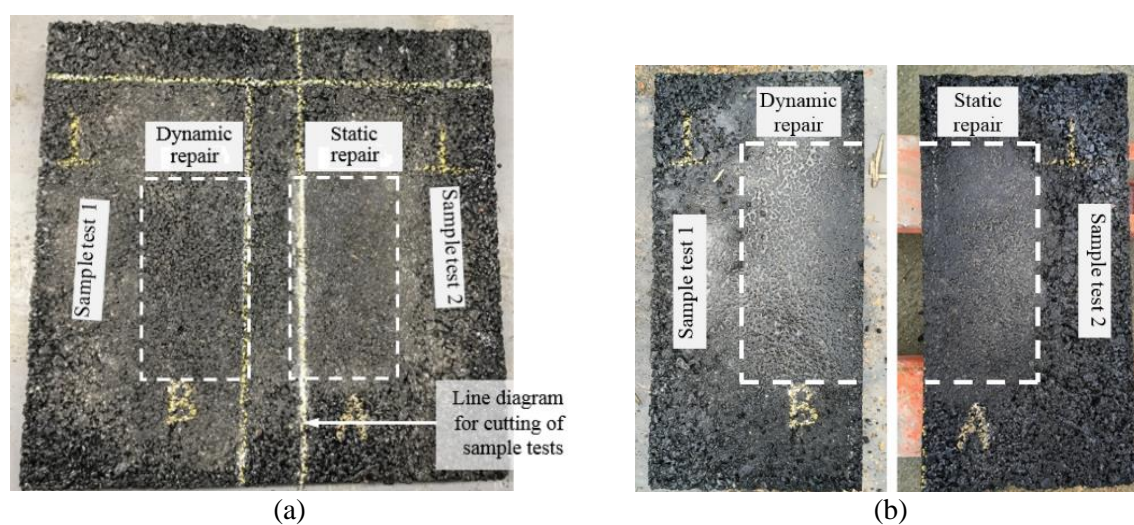
Figure 8.6 Samples for wheel tracking test: (a) initial slab; (b) sample blocks ready for wheel tracking tests (slab cut with a wet saw cut)

(a)

(b)
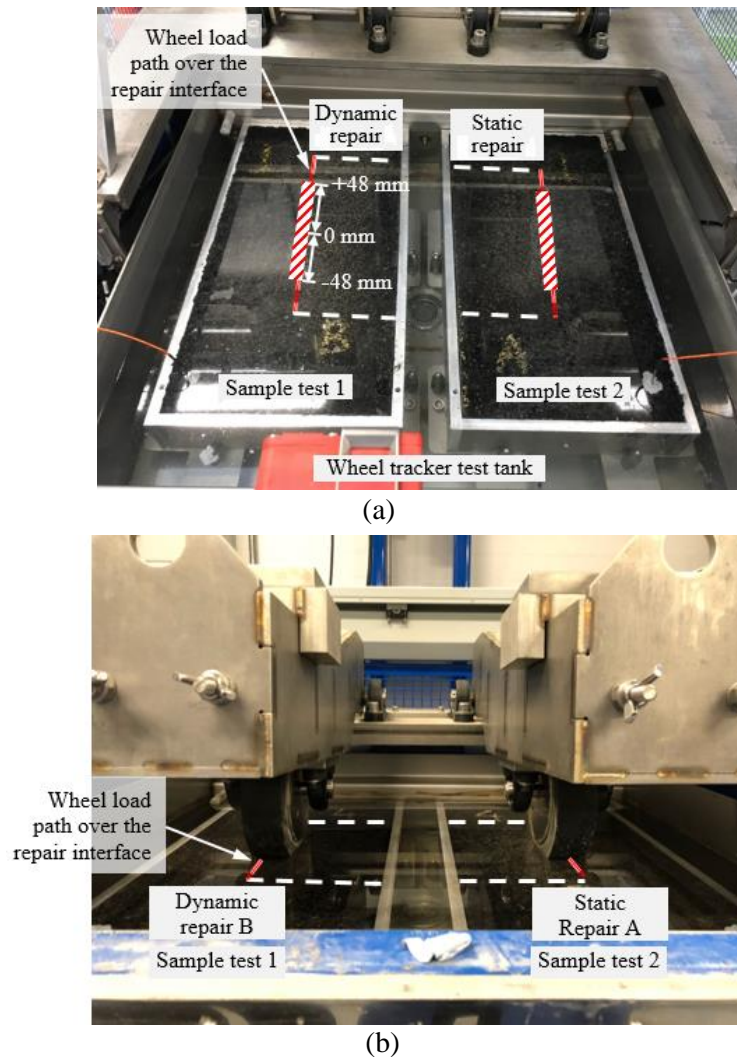
Figure 8.7 Simulation of wheel load at the interface of static and dynamic repairs: (a) samples; (b) wheel loading

8.2   Results and discussion

8.2.1 SBT's

Figure 8.8 shows the average interface shear strength for static (A samples) and dynamic (B samples) repair methods with 10 minutes 15 seconds and 21 minutes 49 seconds heating duration. Appendix G shows the shear strength of all test cores. Eighteen test cores were used to investigate the shear strength at the bottom repair interface of static repairs. A set of nine cores were tested for both heating durations of dynamic repairs. Thirty-six cores were used to investigate the shear strength on the vertical repair interfaces of static repairs and eighteen cores per heating time for similar testing of dynamic repairs. All testing produced failure on the bonding interface. Four cores taken from the vertical interface of static repairs failed as soon

as they were put on the shearing rig. These failures are included in Figure 8.8. Four further tests were aborted due to equipment failure.
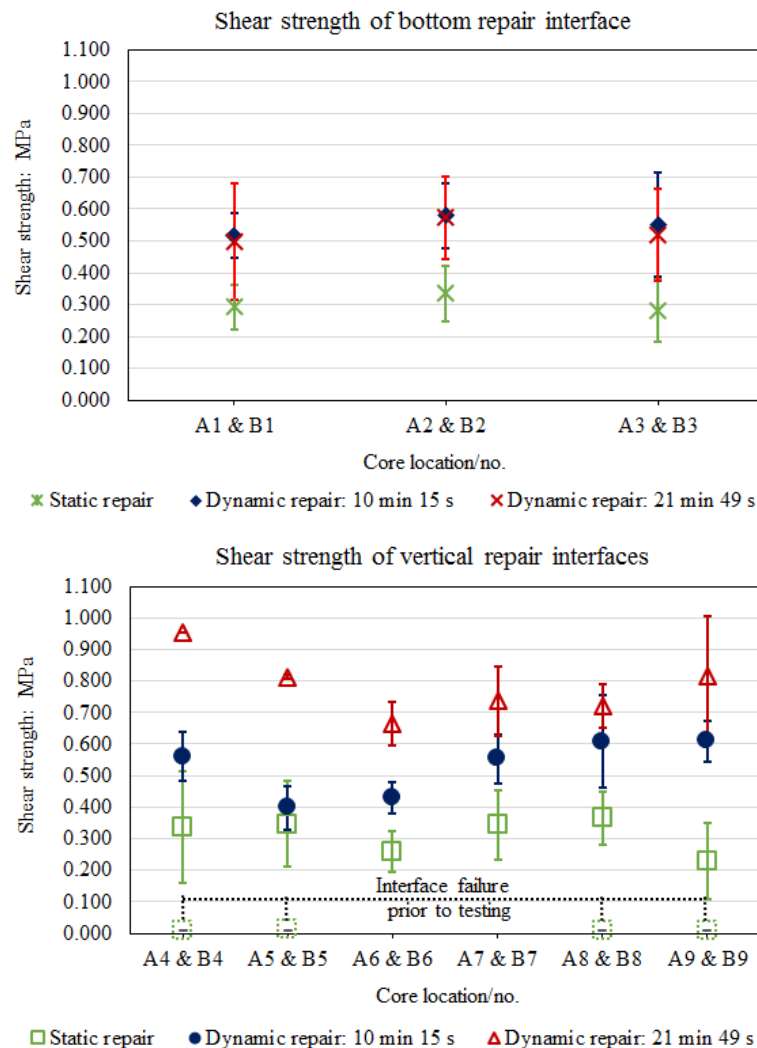
Figure 8.8 Interface shear strength for static (A) and dynamic (B) pothole repairs (sample characterisation (A1-A9 and B1-B9) is given in Figures 8.4 and 8.5, the error bars show the standard deviation (SD) of each value)

The first observation from the results is that the interface shear strengths with the dynamic repair method were significantly higher those from the static method repairs. The shear strength at the bottom repair interfaces of dynamic repairs was consistent, in the 0.499 MPa and 0.579 MPa range, averaging, 78.2% higher than static repairs. This happened because, for dynamic repairs, there was a reduction in bitumen viscosity with continuing heating. Lower viscosity means less resistance of asphalt to flow, higher interlocking between the aggregates of the host pavement and the fill mixture and adequate adhesion between repair interfaces. This justifies

also the fact that slightly higher bond strength was received for test samples A2 and B2 cored in the middle of the repairs where temperatures during preheating and repair were the highest. Between 10 minutes 15 seconds and 21 minutes 49 seconds heating durations there was no significant additional heating influence on shear bond strength on the bottom interface, in spite of the natural reduction in bitumen viscosity. This happened because the bottom face of the excavation was confined by the whole asphalt mixture of the slab during heating and repair compaction.

However, the effect of asphalt low viscosity during heating is apparent at the vertical faces of the excavation. These faces are not supported during heating and are free to move as soon as bitumen has softened, and compaction of the fill mixture started. Thus, the shear strength of test samples B4 and B5 heated for 21 minutes 49 seconds was 0.392 MPa and 0.416 MPa respectively higher than samples prepared with 10 minutes 15 seconds dynamic heating time. For test samples B6-B9 an average strength difference of only 0.185 MPa was observed. The reason that the shear strength differed between the test cores of the vertical faces of dynamic repairs was the different temperatures achieved in pothole preheating. Previous investigation, presented in Chapter 4, section 4.4.2.1, into similar dynamically heated asphalt excavations shows that, at the end of preheating, at the mid-bottom of the excavation surface, temperatures typically range from 140 ºC to 160 ºC, with the lower temperatures on the vertical faces, in the 80 ºC to 120 ºC range.

Further, the strength at the vertical repair interfaces with dynamic repair was higher than that of static repair methods. In general, the strength of test samples extracted from 10 minutes 15 seconds dynamic repairs was 68.4% higher than that of the test samples of static repairs. The strength of 21 minutes 49 seconds dynamically heated repairs more than doubled that of static repairs.

Considering the shear strength results gained for the vertical interfaces of the excavation, it seems that there is a higher influence of temperature on the strength of the interface. However, during the two heating durations of the pothole excavation, it was observed that the sides became increasingly loose after approximately 21 minutes of heating showing evidence of overheating the asphalt and heating of a larger area than expected. This is not obvious for the bottom interface since the slab is confined in its mould when the heating is applied. Besides, 21 minutes of heating would be expected to increase overall repair time which is less desirable

as reported by Wilson and Romine (2001). In addition, the interface strength of dynamic pothole repairs at the end of 10 minutes 15 seconds of heating was even higher than repairs completed with induction heating presented in Obaidi, Gomez-Meijide, and Garcia (2017).

8.2.2 WTT's

Figure 8.9 shows the permanent deformation of static and dynamic repairs at the repair vertical interface for 25 ($\pm$1) $^{\circ}$C and at 4 ($\pm$1) $^{\circ}$C test temperatures. Figure 8.10 presents the average rutting profile of these repairs along the vertical repair interface. Appendix H shows the rutting profile for all repairs individually. Six slabs were prepared for wheel tracking tests. Sets of three static and three dynamic repairs were tested for both testing temperatures. During the tests it was observed that the profile of the tested surfaces was non-uniform. This was captured from the wheel tracking machine at the first four passes with asphalt surface profile levels fluctuating between $\pm$ 1.4 mm and $\pm$ 1.7 mm for all tests. This fluctuation has been correspondingly added or subtracted from the final rutting depth in the presented results. It can be observed that for the rutting test at 25 $^{\circ}$C, dynamic repairs outperformed static repairs. The average rutting depth of dynamic repairs was 10.36 mm (with SD equal to 1.54 mm) whereas for static repairs was 14.82 mm (with SD equal to 3.73 mm). A high level of deformation was observed for the static repair constructed in slab S26. On this occasion, the rutting depth was 18.66 mm. In general, the rutting depth of static repairs was not as consistent as that of dynamic repairs. Further, no stripping was observed for all tested repairs (Figures 8.11 and 8.12) and no significant rutting for all repairs tested at 4 $^{\circ}$C (Figure 8.10b).
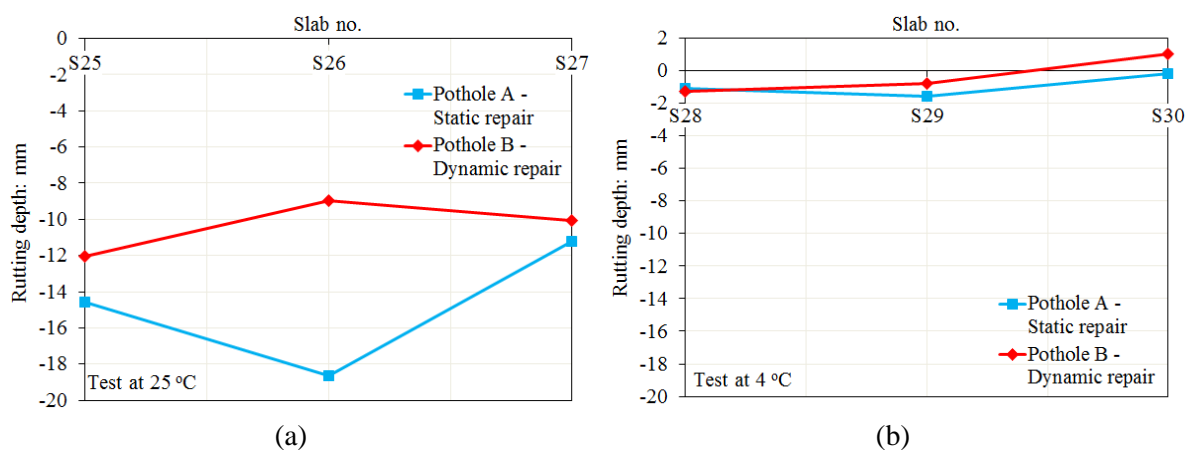
Figure 8.9 Rutting depth at (a) 25 $^{\circ}$C and (b) 4 $^{\circ}$C after 20.000 cycles

(a)

(b)
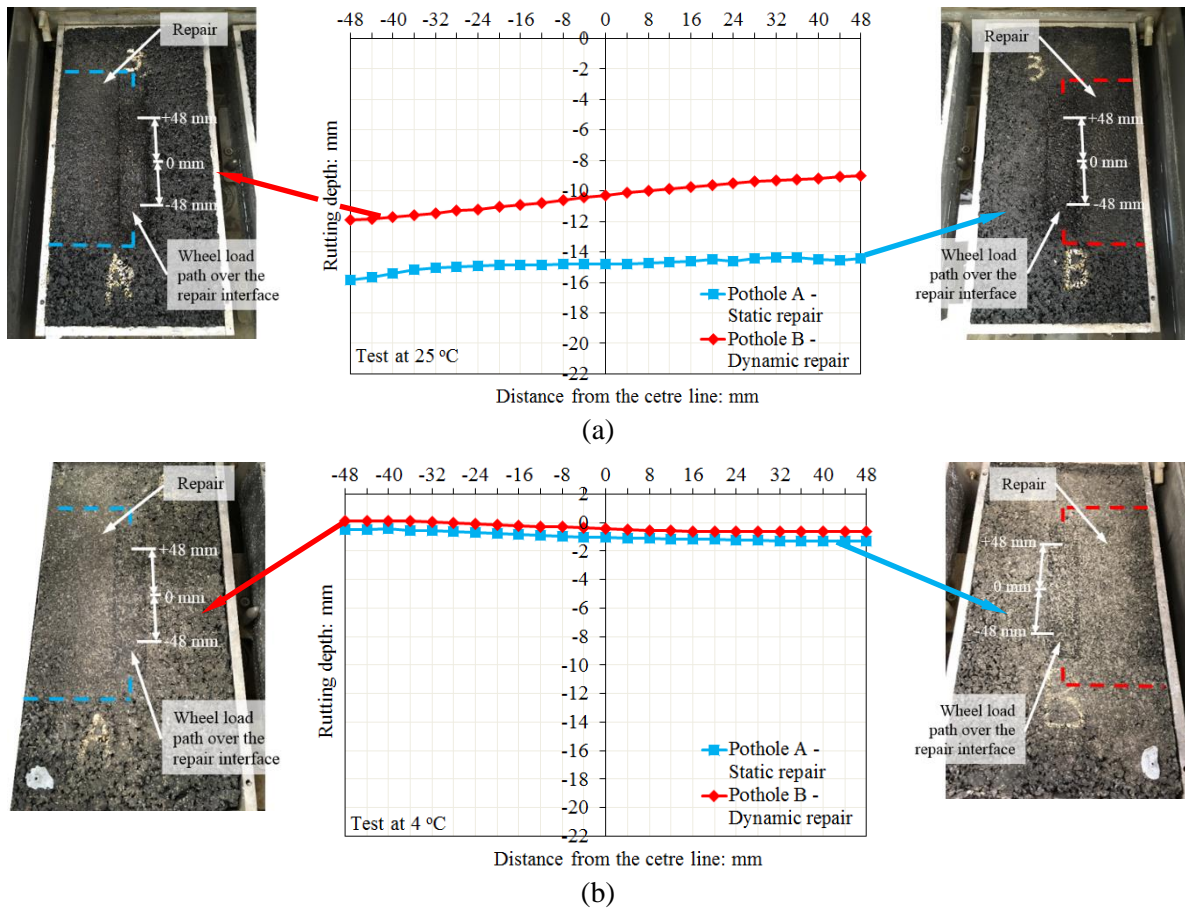
Figure 8.10 Longitudinal average rutting profile in the repair interface at (a) 25 °C and (b) 4 °C after 20.000 cycles

(a)   (b)
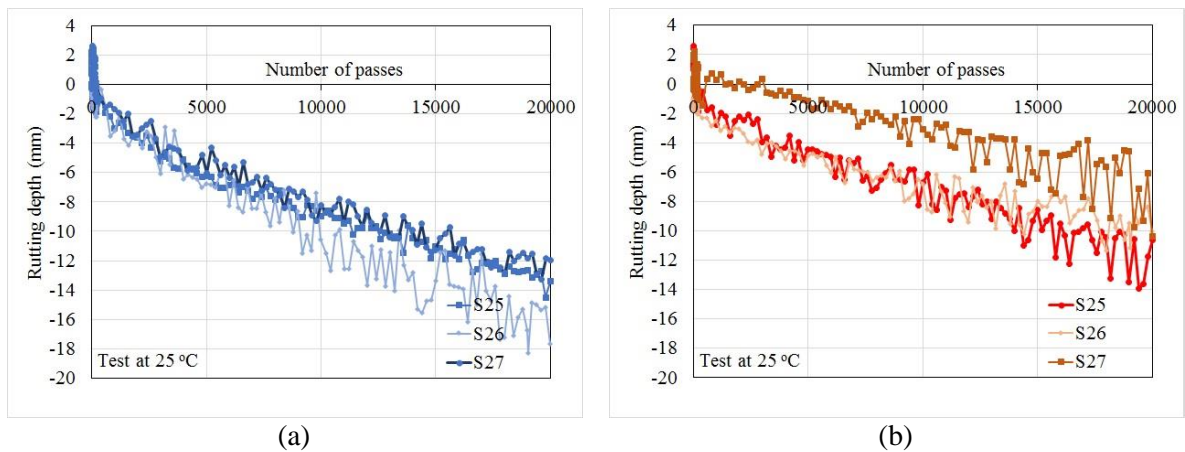
Figure 8.11 Rutting deformation profile versus number of passes at 25 °C testing temperature for (a) static repairs and (b) dynamic repairs of slabs S25, S26 and S27

(a)   (b)
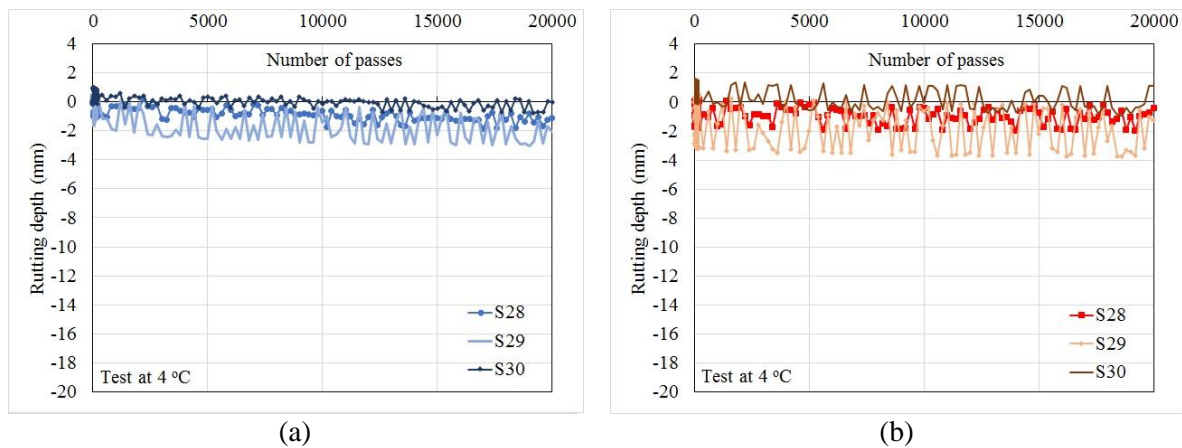
Figure 8.12 Rutting deformation profile versus number of passes at 4 ºC testing temperature for (a) static repairs and (b) dynamic repairs of slabs S28, S29 and S30

8.3   Summary

This chapter experimentally investigated the interface shear strength and rutting resistance of a method to repair potholes via dynamic infrared heating. The dynamic repairs were also compared against static repairs via similar testing. The pre-heating method for the dynamic repairs was concluded from the experimental work presented in Chapter 4. It was then used to understand the heating effects at the repair interfaces in Chapter 6 and finally assessed via SBT's and WTT's in this chapter. The next chapter presents the conclusions from this work and Chapters 3-8. It also includes recommendations for further research.

Chapter 9

Conclusions and recommendations

9.1   Conclusions

9.1.1 Experimental infrared heating equipment

The conclusions of this section relate to Chapter 3. The chapter presents the patented experimental infrared heater used in the experimental work of this Thesis. The heater offers the ability to pre-heat a pothole excavation in a controlled manner, prior to repair filling and compaction, for longer lasting pothole repairs. The study focused on the initial development and understanding of the heater operation and heating process in a laboratory controlled environment. The following conclusions were made:

- An infrared thermometer and an insulated thermocouple probe were used to measure temperatures on the heating element plate. Both equipments produced reliable and similar temperature measurements. For 80% and 100% gas supplies the infrared thermometer in comparison with the probe captured a higher concentration of temperatures in the middle area of the plate. However, the probe outlined in detail overall plate temperature distributions and showed information such as plate ignition time, temperature stabilization time and temperature distribution non-uniformities.

- The results from the plate temperature measurements with the probe showed that the plate ignites after 23 seconds to 28 seconds and temperatures on the plate stabilize for all gas levels after approximately 1 minute 40 seconds. The average temperatures after this duration of time for 20%, 40%, 60%, 80% and 100% gas feed rates were 873.60 ºC, 875.67 ºC, 894.72 ºC, 910.38 ºC and 916.82 ºC respectively.

- The experiments with the heater plate operating in heating-cooling cycles (named dynamic operation), showed that temperatures reached similar levels for all gas supplies. The temperature repetitions on the heating part of the cycles showed a difference between 1.9% and 4% for the heater gas feed rates studied. On the cooling part of the cycles, temperatures reached a difference of 2% to 9.6% for 20% to 60%

and 100% gas feed rates. However, for 80% operating gas level a difference of 16.85% was observed during the cooling part of the cycles.

- Surface heating experiments on an insulated sheet showed that there was a higher concentration of temperatures in the middle areas of the surface over which infrared heat was applied. These temperatures were higher for higher levels of gas feed rates. For example, during 300 seconds of plate operating time and at 20% gas feed rate, temperatures in the middle were at approximately 100 ºC. Whereas, for 100% gas feed rate, the middle temperatures reached 135 ºC. Even though these temperatures may not be similar when infrared heat is applied to an asphalt surface, the results offer an initial understanding of the heat pattern produced and control over asphalt pre-heating process.

- The heat powers that correspond to 20%, 40%, 60%, 80% and 100% gas feed rates are 6.6 kW, 6.7 kW, 7.1 kW, 7.5 kW and 7.7 kW respectively. These were calculated using the Stefan Boltzmann Law formula.

- A cover around the heating element plate was found to restrain the effect of air movement during heater operation and further support control of asphalt pre-heating performance.

9.1.2 Patch repair pre-heating method using dynamic heating

The conclusions of this section relate to Chapter 4. In this chapter, the application of infrared heat in heating-cooling cycles (named dynamic heating) was investigated in shallow and deep pothole excavations of asphalt slabs. The study was conducted for different height and heater gas feed rate configurations. The main conclusions drawn from the research are the following:

- Temperatures under dynamic infrared heating in 45 mm, 75 mm and 100 mm deep pothole excavations and their host pavement were non – uniformly distributed.

- There was a higher concentration of temperatures in the pothole excavation than inside the host pavement. This happened because temperatures in the excavations increase due to radiation, whereas, the temperature profile inside the host pavement depends on the thermal properties of the asphalt mixture.

- Temperatures inside the host pavement increased more for the first 10 minutes of heating than for heating between 10 minutes and 30 minutes.

- Dynamically heating a pothole excavation ensures heating up of its external surfaces and internal asphalt mixture of host pavement without burning or overheating the asphalt. For this reason and to keep patching time to a minimum, 10 minutes – 12 minutes dynamic heating time is better.

- It is suggested that 45 mm deep pothole excavation is dynamically heated for approximately 10 minutes with (a) 6.6 kW heat power and stationary heater above the pothole excavation at an offset from the asphalt surface of 230 mm and (b) 7.5 kW heat power and heater in motion at an offset of 130 mm. Method (b) is preferred for pothole areas bigger than 305×165 mm^2.

- It is suggested that a 75 mm deep pothole excavation is dynamically heated for approximately 10 minutes with 7.1 kW heat power at an offset of 230 mm.

- It is suggested that a 100 mm deep pothole excavation is dynamically heated for approximately 10 min with (a) 6.6 kW heat power and stationary heater at an offset of 230 mm and (b) 7.5 kW heat power and heater in motion at an offset of 130 mm. Method (b) is preferred for pothole areas bigger than 305×165 mm^2.

- Dynamically heating the pothole excavation is intended to improve interface pothole repair bonding and therefore repair durability over time. The suggested optimum heating may be implemented in asphalt patch repairs prior to any pothole filling and compaction and after the failed asphalt is removed and the cavity is cleaned from debris and water.

9.1.3 Thermal properties of asphalt mixtures

The conclusions of this section relate to Chapter 5. In this chapter, the thermal properties of 20 mm dense bitumen macadam (DBM), asphalt concrete (AC) 14 and AC 6 asphalt mixtures were investigated in the laboratory at three different test temperatures 19 ($\pm$1) ^{o}C, 65 ($\pm$5) ^{o}C and 80 ($\pm$5) ^{o}C. Thermal conductivity was measured with the transient line source (TLS) method for non-aged, short-term aged and long-term aged asphalt mixtures. Specific heat capacity and thermal diffusivity were calculated using formulae from the literature. The penetration of heat into the asphalt specimens during the measurements of thermal conductivity was also determined. The results were examined in terms of the (i) thermal conductivity method of measurement; (ii) effect of temperature in thermal conductivity; (iii) effect of ageing in thermal properties; (iv) effect of aggregate. The following was concluded:

- The variation of air voids (from approximately 4% to 6.5%) in compacted asphalt specimens was not found to considerably affect thermal conductivity measurements of this study.

- The results showed that thermal conductivity is affected by the volume of asphalt used by the TLS to find thermal conductivity (this can be estimated by the heat penetration depth) and the thermal contact between the needle and the asphalt surface. To increase the thermal contact, thermal paste should be applied to the needle prior to testing and the hole where the needle is inserted should be cleaned from dust and be of the right diameter.

- The most significant factor that affected thermal conductivity was temperature. Thermal conductivity considerably decreased for all asphalt mixtures at high test temperatures (from 65 $^{\circ}$C to 80 $^{\circ}$C). This showed that when thermally analysing asphalt mixtures either experimentally or via finite element modelling, the effect of thermal conductivity of asphalt mixture should be taken into consideration.

- The effect of ageing in thermal conductivity and thermal diffusivity varied between the asphalt mixtures studied in the chapter. For 20 mm DBM specimens, thermal conductivity between non-aged and aged specimens remained at similar levels at 19 $^{\circ}$C test temperature. However, at 65 $^{\circ}$C test temperature, thermal conductivity decreased by approximately 27.5%. At 80 $^{\circ}$C, it decreased by almost 50% between non-aged and long-term aged specimens. For the same mixture conditioning at 19 $^{\circ}$C, thermal diffusivity increased when thermal conductivity was increasing.

- For AC 14 and AC 6 asphalt mixture specimens, no increasing or decreasing trend was observed for thermal conductivity between non-aged and aged specimens and for test temperatures between 19 $^{\circ}$C and 80 $^{\circ}$C. For AC 14 mixture, thermal diffusivity increased in average by 34.2% between non-aged and aged specimens. For AC 6 mixture, thermal diffusivity increased by 19.2% between non-aged and short-term aged specimens and by 12% between non-aged and long-term aged specimens.

- The effect of ageing on specific heat capacity was not significant and remained almost unchanged for all asphalt mixtures and ageing conditions.

- The conducted study was not conclusive in the effect of aggregate size on thermal conductivity.

9.1.4 Temperature distribution in the interfaces of shallow patch repairs

The conclusions of this section relate to Chapter 6. In this chapter, temperatures at the interfaces of static and dynamic repairs were investigated in the laboratory using extractable thermocouples. Temperatures were measured during the pouring of the fill mixture into the excavated potholes and compaction. The following conclusions were made:

- Temperatures at the interfaces of hot mix asphalt pothole repairs were non-uniformly distributed.

- The lowest temperatures were received in vertical interfaces and corners of the repairs. This was evident mainly in static repairs.

- Same amount of temperature increase was observed in repair interfaces with initial air and slab temperatures 17 $^{\circ}$C - 22 $^{\circ}$C and 17 $^{\circ}$C - 26 $^{\circ}$C respectively.

- Dynamic heating did not considerably increase temperatures in the corners of the repair. However, this figure was improved in vertical interfaces along the length and width of the repairs.

- Comparing dynamically heated repairs of 10 minutes 15 seconds and 21 minutes 49 seconds with static repairs, showed average corner temperatures increases 10.85 $^{\circ}$C - 24.45 $^{\circ}$C and 29.51 $^{\circ}$C - 36.73 $^{\circ}$C respectively, with accompanying increases in vertical interface temperatures 34.97 $^{\circ}$C and 46.41 $^{\circ}$C respectively.

- The low temperature vertical interfaces of static repairs were attributed to high thermal contact resistance in contrast with the bottom of the repair.

- The thermal contact resistance seemed to decrease in dynamic repairs. This is due to higher actual contact spots in the repair interface and lower air voids.

9.1.5 Finite Element simulation of transient heat distribution in shallow patch repairs

The conclusions of this section relate to Chapter 7. Three simulation models were presented in this chapter. The pothole repair models and the heated excavation model were a representation of experimental work conducted by the author and described in Chapters 6 and 4 respectively. All models were validated and calibrated by experimental work presented in the Thesis. The following was concluded:

- The results from the validations of the models are promising and good correlation was found for most investigated temperature sampling points located at the repair interfaces, faces of the empty pothole excavations and inside the host pavement.

- The lowest agreement between measured and simulated temperatures was seen in the dynamic repair model mainly at the vertical faces of the repair. This happened due to the impact in the simulated temperatures from the dynamically heated pothole excavation where the lowest agreement between measured and simulated temperatures was also seen at the vertical faces of the excavation.

- It was found that thermal contact conductance plays an important role in simulating heat flow at the repair interface and that view factor significantly affects simulation of temperatures at faces subjected to radiation. Thermal contact conductance is the reciprocal of thermal contact resistance and its effect on the repair interface temperatures was also underlined in Chapter 6 and the conclusions of this chapter discussed in the previous section.

9.1.6 Performance evaluation of shallow patch repairs

The conclusions of this section relate to Chapter 8. In this chapter, static and dynamic repairs were validated in terms of interface strength and resistance to permanent deformation. The interface strength of dynamic repairs was evaluated for 10 minutes 15 seconds and 21 minutes 49 seconds pre-heating times, whereas, the dynamic repair interface resistance to rutting was assessed only for 10 minutes 15 seconds pre-heating time. The following conclusions were drawn from the research:

- Dynamically heating a pothole excavation increases pothole repair interface bonding. The longer the pre-heating time, the higher the repair bonding strength with the old pavement. This happened due to higher interlocking between the aggregates of the host pavement and the hot fill mixture.

- The shear strength of the bottom interface of dynamic repairs was found to be 78.2% higher than static repairs. Between 10 minutes 15 seconds and 21 minutes 49 seconds heating durations there was no significant additional heating influence on shear bond strength on the bottom repair interface.

- The shear strength of the vertical interfaces of dynamic repairs with 10 minutes 15 seconds pre-heating time was 68.4% higher than of the test samples of static repairs.

The strength of 21 minutes 49 seconds dynamically heated repairs more than doubled that of static repairs.

- Reflecting the above, to achieve higher interface bonding for dynamic repairs, an approximate heating time of 10 min was found to be sufficient. This avoids overheating the asphalt and heating a larger area of mixture than expected or needed.

- The rutting resistance of dynamic repairs at the repair interface was higher than that of static repairs. The average rutting depth of dynamic repairs was 10.36 mm whereas for static repairs it was 14.82 mm.

- It has been concluded that pre-heating a pothole excavation with infrared heat prior to filling and compaction increases repair durability.

Reflecting the conclusions from the study as a whole, the research has worked towards understanding the operation of infrared heat in asphalt pavement repair; how to implement infrared technology in pothole repairs; evaluated and simulated infrared heated pothole repairs and the ability of infrared technology in pothole repair bonding. Therefore, the study has established a solid foundation for building up in the future an integrated guideline of repairs from the excavation of pavement distress to its repair with infrared heat. This is shown in Figure 9.1 and further recommendations are given in the next section.
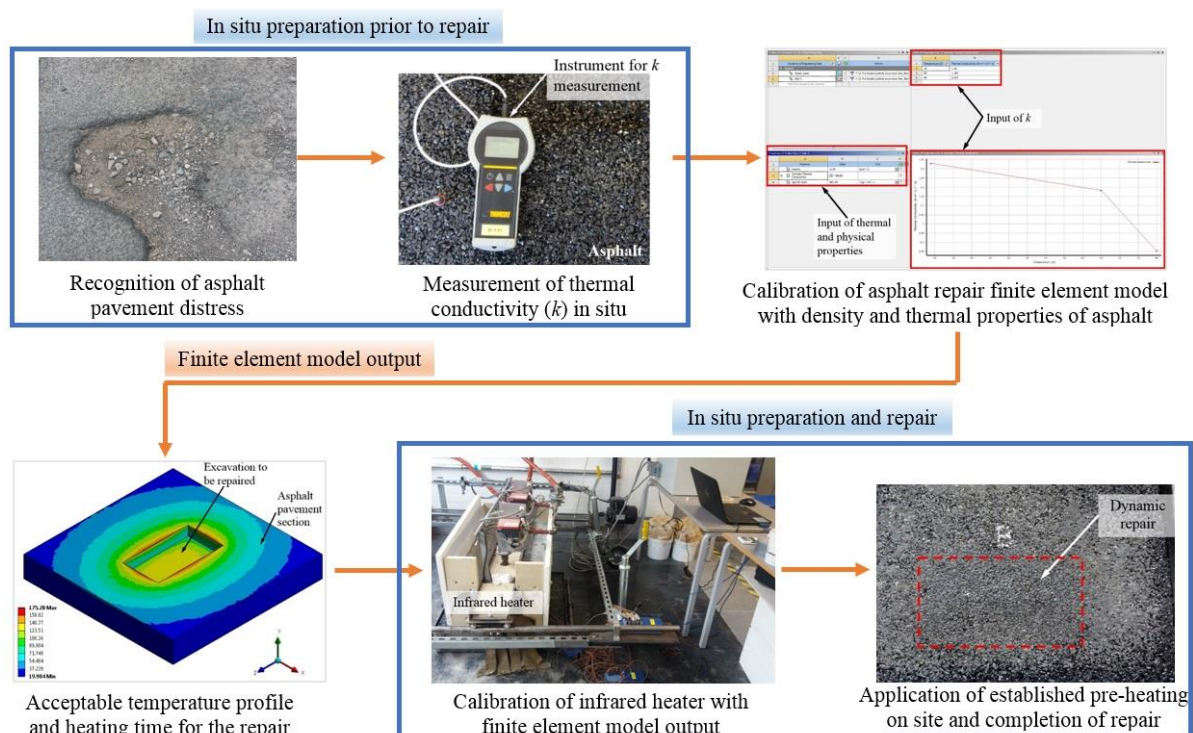
Figure 9.1 Integrated asphalt pavement repair

9.2   Recommendations

Below are recommendations for further study:

- In the present study, the experimental infrared heater was tested and used for pothole repairs completed at room temperature. Further research is recommended to evaluate the performance of the heater at low environment temperatures in order to expand the use of it for winter pothole repairs. Further, a new version of the heater is recommended with increased sensor driven control and robustness for exterior experiments.

- Future research must explore the effect of dynamic infrared heating on bitumen losses and disturbance of air voids in the old pavement when infrared heat is applied. The effect of thermal properties, asphalt absorptivity and surface roughness on infrared heated repairs should also be further investigated.

- To improve the thermal models, future work should investigate the effect in the models of the fluctuation of emissivity and thermal conductivity of the heater plate at different temperatures. Other parameters to consider are the fluctuation of air temperature between the heater and the heated excavation and thermal contact conductance in the case of the repair models. Further expansion of the models is also recommended to asphalt mixture and environment temperature variability, density and voiding in asphalt repairs.

- Regarding the assessment of the pothole repairs under the wheel load, more tests are suggested to find the stripping point and evaluate resistance to moisture damage of dynamically heated repairs.

- In this study, only 45 mm deep pothole repairs were used to find temperatures at the repair interfaces and evaluated in terms of repair interface strength and resistance to failure under the wheel load. It is recommended, that future research should perform similar experimental work for 75 mm and 100 mm deep pothole excavations for which the optimum dynamic heating method was found in this study.

- Further research is recommended to assess the durability of completed repairs using equipment under a range of climatic conditions including cyclic freezing.

- Field trials are also suggested and evaluation of how cost effective the pothole pre-heating process is compared to the traditional repair methods.

- Further research is also recommended to assess the effect of slopped pothole excavation faces in repair adhesion.

References

Adlinge, S.S. and Gupta, A. (2013) 'Pavement deterioration and its causes', *International Journal of Innovative Research and Development*, 2(4), pp. 437-450.

American Association of State Highway and Transportation Officials (2007) *AASHTO T166 Bulk specific gravity of compacted asphalt mixtures using saturated surface - dry specimens.* Washington, D.C.: American Association of State Highway and Transportation Officials.

American Association of State Highway and Transportation Officials (2006) *AASHTO R30:2006 Standard practice for mixture conditioning of hot mix asphalt*. Washington, D.C.: American Association of State Highway and Transportation Officials.

American Association of State Highway and Transportation Officials (2004) *AASHTO T324:2004 Standard method of test for Hamburg wheel-track testing of compacted hot mix asphalt (HMA)*. Washington, D.C.: American Association of State Highway and Transportation Officials.

American Society for Testing and Materials (2017) *ASTM C518:2017 Standard Test Method for Steady-State Thermal Transmission Properties by Means of the Heat Flow Meter Apparatus*. Washington, D.C.: American Society for Testing and Materials.

American Society for Testing and Materials (2016a) *ASTM D7984:2016 Standard Test Method for Measurement of Thermal Effusivity of Fabrics Using a Modified Transient Plane Source (MTPS) Instrument*. Washington, D.C.: American Society for Testing and Materials.

American Society for Testing and Materials (2016b) *ASTM E1530-11:2016 Standard Test Method for Evaluating the Resistance to Thermal Transmission of Materials by the Guarded Heat Flow Meter Technique*. Washington, D.C.: American Society for Testing and Materials.

American Society for Testing and Materials (2013a) *ASTM C1113/C1113M-09:2013 Standard Test Method for Thermal Conductivity of Refractories by Hot Wire (Platinum Resistance Thermometer Technique)*. Washington, D.C.: American Society for Testing and Materials.

American Society for Testing and Materials (2013b) *ASTM E1225:2013 Standard Test Method for Thermal Conductivity of Solids Using the Guarded-Comparative-Longitudinal Heat Flow Technique*. Washington, D.C.: American Society for Testing and Materials.

American Society for Testing and Materials (2004) *ASTM C177:2004 Standard Test Method for Steady-State Heat Flux Measurements and Thermal Transmission Properties by Means of the Guarded-Hot-Plate Apparatus*. Washington, D.C.: American Society for Testing and Materials.

American Society for Testing and Materials (2001) *ASTM D5930:2001 Standard Test Method for Thermal Conductivity of Plastics by Means of a Transient Line-Source Technique.* Washington, D.C.: American Society for Testing and Materials.

American Society for Testing and Materials (2000) ASTM D5334:2000 *Standard Test Method for Determination of Thermal Conductivity of Soil and Soft Rock by Thermal Needle Probe Procedure*. Washington, D.C.: American Society for Testing and Materials.

American Society for Testing and Materials (1995) *ASTM C335:1995 Standard Test Method for Steady-State Heat Transfer Properties of Horizontal Pipe Insulation*. Washington, D.C.: American Society for Testing and Materials.

Andersland, O.B. and Ladanyi, B. (2004) *Frozen ground engineering*. 2nd edn. Hoboken, New Jersey: John Wiley and Sons.

Anderson, D.A. and Thomas, H.R. (1984) Pothole Repair in Pennsylvania. Available at: https://docs.lib.purdue.edu/cgi/viewcontent.cgi?referer=&httpsredir=1&article=3367&context=roadschool&sei-redir=1&referer=http%3A%2F%2Fcn.bing.com%2Fsearch%3Fq%3DPothole%2BRepair%2Bin%2BPennsylvania&go%3D%25E6%258F%2590%25E4%25BA%25A4

&qs%3Dn&form%3DQBLH&pq%3Dupper%2Bgreat%2B (Accessed 20 June 2018).

Asphalt Industry Alliance (2018) *Annual Local Authority Road Maintenance Survey 2015*. Available at: http://www.asphaltuk.org/wp-content/uploads/alarm-survey-2018-FINAL.pdf (Accessed: 8 May 2018).

Asphalt Industry Alliance (2015) *Annual Local Authority Road Maintenance Survey 2015*. Available at: http://www.asphaltuk.org/wp-content/uploads/ALARM_survey_2015.pdf (Accessed: 16 August 2018).

Bergman, T.L., Incropera, F.P., DeWitt, D.P. and Lavine, A.S. (2011) *Fundamentals of heat and mass transfer*. 7th edn. Hoboken, New Jersey: John Wiley and Sons.

Blaha, J.R. (1993) *Fabrication and Testing of Automated Pothole Patching Machine*. Washington, D.C. Strategic Highway Research Program, National Research Council (No. SHRP-H-674).

Blázquez, C.S., Martín, A.F., García, P.C. and González-Aguilera, D. (2018) 'Thermal conductivity characterization of three geological formations by the implementation of geophysical methods', *Geothermics*, 72, pp. 101-111.

Bode, T.A. (2012) An Analysis of the Impacts of Temperature Segregation on Hot Mix Asphalt. Master's Thesis. University of Nebraska. Available at: https://digitalcommons.unl.edu/constructiondiss/10/ (Accessed 20 June 2018).

Bouguerra, A., Ait-Mokhtar, A., Amiri, O. and Diop, M. (2001) 'Measurement of thermal conductivity, thermal diffusivity and heat capacity of highly porous building materials using transient plane source technique', *International Communications in Heat and Mass Transfer*, 28(8), pp. 1065-1078.

British Standards Institution (2016a) *BS EN 12697-35:2016 Bituminous mixtures - Test methods, Laboratory mixing*. London: British Standards Institution.

British Standards Institution (2016b) *BS EN 13108-1:2016 Bituminous mixtures – Material specifications*. London: British Standards Institution.

British Standards Institution (2015a) *BS 594987:2015+A1-2017:2015 Asphalt for roads and other paved areas. Specification for transport, laying, compaction and product type testing protocols*. London: British Standards Institution.

British Standards Institution (2015b) *BS EN ISO 22007-2:2015 Plastics. Determination of thermal conductivity and thermal diffusivity. Transient plane heat source (hot disc) method*. London: British Standards Institution.

British Standards Institution (2013) *BS EN 12697-48:2013 Bituminous mixtures. Test methods for hot mix asphalt. Part 48. Interlayer Bonding*. London: British Standards Institution.

British Standards Institution (2012) *BS EN 12697-30:2012 Bituminous mixtures. Test methods for hot mix asphalt. Part 30. Specimen preparation by impact compactor*. London: British Standards Institution.

British Standards Institution (2010) *BS EN ISO 8894-1:2010 Refractory materials. Determination of thermal conductivity. Hot-wire methods (cross-array and resistance thermometer)*. London: British Standards Institution.

British Standards Institution (2005) *BS 594-1:2005 Hot rolled asphalt for roads and other paved areas. Specification for constituent materials and asphalt mixtures*. London: British Standards Institution.

British Standards Institution (2003) *BS EN 12667-22:2003 Bituminous mixtures. Test methods for hot mix asphalt. Part 22. Wheel tracking*. London: British Standards Institution.

British Standards Institution (2001) *BS EN 12667:2001 Thermal performance of building materials and products. Determination of thermal resistance by means of guarded hot plate*

and heat flow meter methods. Products of high and medium thermal resistance. London: British Standards Institution.

British Standards Institution (1997) *BS EN ISO 8497:1997 Thermal insulation. Determination of steady-state thermal transmission properties of thermal insulation for circular pipes*. London: British Standards Institution.

British Standards Institution (1990) *BS 598-105:1990 Sampling and examination of bituminous mixtures for roads and other paved areas. Methods of test for the determination of texture depth*. London: British Standards Institution.

Byzyka, J., Chamberlain, D.A. and Rahman, M. (2017a) 'Development of advanced temperature distribution model in hot-mix asphalt patch repair', *Proceedings of the Institution of Civil Engineers - Transport*, pp. 1-11.

Byzyka, J., Rahman, M. and Chamberlain, D.A. (2017b) 'Thermal segregation of asphalt material in road repair', *Journal of Traffic and Transportation Engineering (English Edition)*, 4(4), 360-371.

Chadbourn, B.A., Luoma, J.A., Newcomb, D.E. and Voller, V.R. (1996) Consideration of hot mix asphalt thermal properties during compaction, in Quality management of hot mix asphalt. *ASTM International*.

Chamberlain, D.A. (2004) *Pot hole repair system*. European Patent Office Patent no. GB2540044 (A). Available at:
https://worldwide.espacenet.com/publicationDetails/biblio?FT=D&date=20170104&DB=EPODOC&locale=en_EP&CC=GB&NR=2540044A&KC=A&ND=4# (Accessed: 21 June 2018).

Chatti, K., Salama, H. and El Mohtar, C. (2004) 'Effect of heavy trucks with large axle groups on asphalt pavement damage', *Proceedings of the 8th International Symposium on Heavy Vehicle Weights and Dimensions*, Muldersdrift, South Africa, date n/a. Available at:
http://road-transport-technology.org/conferenceproceedings/ishvwd-8/ (Accessed 20 June 2018).

Chaturabong, P. and Bahia, H.U. (2017) 'The evaluation of relative effect of moisture in Hamburg wheel tracking test', *Construction and Building Materials*, 153, pp. 337-345.

Clyne, T.R., Johnson, E.N. and Worel, B.J. (2010) Use of taconite aggregates in pavement applications. Saint Paul: Minnesota Department of Transportation (Publication MN/RC – 2010–24).

Commuri, S. and Zaman, M. (2008) 'A novel neural network-based asphalt compaction analyzer', *International Journal of Pavement Engineering*, 9(3), pp. 177-188.

Controls (2018) *DWT Universal AASHTO/EN Double Wheel Tracker*. Available at: http://www.controls-group.com/ita/asfaltomiscele-bituminose-testing-equipment/dwt-universal-aashtoen-double-wheel-tracker_.php (Accessed: 15 June 2018).

Cooper, M., Mikic, B. and Yovanovich, M. (1969) 'Thermal contact conductance', *International Journal of Heat and Mass Transfer,* 12(3), pp. 279-300.

Crompton, T.R. (2006) *Polymer reference book*. Shawbury, Shrewsbury, Shropshire: Smithers Rapra Publishing.

Dawson, A. (2008) *Water in Road Structures: Movements, Drainage and Effects*. Dordrecht, the Netherlands: Springer Science & Business Media.

Delgadillo, R. and Bahia, H.U. (2008) 'Effects of temperature and pressure on hot mixed asphalt compaction: field and laboratory study', *Journal of Materials in Civil Engineering*, 20(6), pp. 440-448.

Department for Transport (UK) (2008) *Manual of contract documents for Highway works. Volume 1, Specification for highway works, Series 900 Road pavements - Bituminous bound materials*. Available at: http://www.standardsforhighways.co.uk/ha/standards/mchw/vol1/pdfs/series_0900.pdf (Accessed: 6 August 2018).

Department of Transportation (2010) Standard Code of Practice, New Roads and Street Works Act 1991, Specification for the Reinstatement of Openings in Highways, 3rd ed. London: Department of Transportation.

Dong, Q., Huang, B. and Zhao, S. (2014) 'Field and laboratory evaluation of winter season pavement pothole patching materials', *International Journal of Pavement Engineering*, 15(4), pp. 279-289.

Dou, R., Ge, T., Liu, X. and Wen, Z. (2016) 'Effects of contact pressure, interface temperature, and surface roughness on thermal contact conductance between stainless steel surfaces under atmosphere condition', *International Journal of Heat and Mass Transfer*, 94, pp.156-163.

Ebay (2016) Firebrick Fire Board Heat Proof Brick Vermiculite Fireboard Resistant 1020 x 620. Available at: https://www.ebay.co.uk/itm/Firebrick-Fire-Board-Heat-Proof-Brick-Vermiculite-Fireboard-Resistant-1020-x-620/141038295589?_trkparms=aid%3D222007%26algo%3DSIM.MBE%26ao%3D2%26asc%3D49138%26meid%3D9f99a4d3afbe4ec9a97eb6bcb6855d3f%26pid%3D100623%26rk%3D1%26rkt%3D6%26mehot%3Dpp%26sd%3D221996718025&_trksid=p2047675.c100623.m-1 (Accessed: 14 May 2016)

Eppelbaum L., Kutasov I., Pilchin A. (2014) 'Methods of Thermal Field Measurements', in Applied Geothermics. *Lecture Notes in Earth System Sciences*. Springer, Berlin, Heidelberg, pp 151-159.

Flir (2018) Compact Thermal Camera FLIR C2. Available at: https://www.flir.com/products/c2/ (Accessed: 12 July 2018).

Flynn, D. (1963) 'A radial-flow apparatus for determining the thermal conductivity of loose-fill insulations to high temperatures', *Journal of Research of the National Bureau of Standards-C. Engineering and Instrumentation*, 67C(2), pp. 129.

Franco, A. (2007) 'An apparatus for the routine measurement of thermal conductivity of materials for building application based on a transient hot-wire method', *Applied Thermal Engineering*, 27(14-15), pp. 2495-2504.

Freeman, T.J. and Epps, J.A. (2012) *HeatWurx Patching at Two Locations in San Antonio*. Austin: Texas Transportation Institute, FHWA, Texas Department of Transportation (Publication FHWA/TX-12/5-9043-01-1).

Frekers, Y., Helmig, T., Burghold, E.M. and Kneer, R. (2017) 'A numerical approach for investigating thermal contact conductance', *International Journal of Thermal Sciences*, 121, pp.45-54.

Gallego, J., del Val, M.A., Contreras, V. and Páez, A. (2013) 'Heating asphalt mixtures with microwaves to promote self-healing', *Construction and Building Materials*, 42, pp. 1-4.

García, Á., Schlangen, E., van de Ven, M. and Liu, Q. (2012) 'A simple model to define induction heating in asphalt mastic', *Construction and Building Materials*, 31, pp. 38-46.

Gilmore, D. (2002) *Spacecraft thermal control handbook, Volume I: fundamental technologies*. 2nd edn. El Segundo: Aerospace Press.

Gong, L., Wang, Y., Cheng, X., Zhang, R. and Zhang, H. (2014) 'Porous mullite ceramics with low thermal conductivity prepared by foaming and starch consolidation', *Journal of Porous Materials*, 21(1), pp. 15-21.

Hartman, A., Gilchrist, M. and Walsh, G. (2001) 'Effect of mixture compaction on indirect tensile stiffness and fatigue', *Journal of Transportation Engineering*, 127(5), pp. 370-378.

Hassn, A., Aboufoul, M., Wu, Y., Dawson, A. and Garcia, A. (2016) 'Effect of air voids content on thermal properties of asphalt mixtures', *Construction and Building Materials*, 115, pp. 327-335.

Hermansson, Å. (2004) 'Mathematical model for paved surface summer and winter temperature: comparison of calculated and measured temperatures', *Cold Regions Science and Technology*, 40(1), pp. 1-17.

Hermansson A. (2001) 'Mathematical Model for Calculation of Pavement Temperatures: Comparisons of Calculated and Measured Temperatures', *Transportation Research Record: Journal of the Transportation Research Board*, 1764, pp. 180-188.

Huang, K., Xu, T., Li, G. and Jiang, R. (2016) 'Heating effects of asphalt pavement during hot in-place recycling using DEM', *Construction and Building Materials*, 115, pp. 62-69.

Huang, B., Shu, X., Chen, J. and Woods, M. (2010) 'Evaluation of longitudinal joint construction techniques for asphalt pavements in Tennessee', *Journal of Materials in Civil Engineering,* 22(11), pp. 1112-1121.

Huerne, H.L. (2004) Compaction of asphalt road pavements: using finite elements and critical state theory. HLTer Huerne, CT&M Department, Enschede, the Netherlands.

International Organization for Standardization (1991) ISO 8302:1991 *Thermal insulation - Determination of steady-state thermal resistance and related properties - Guarded hot plate apparatus*. Vernier, Geneva: International Organization for Standardization.

Islam, M.R. and Tarefder, R.A. (2014) 'Determining thermal properties of asphalt concrete using field data and laboratory testing', *Construction and Building Materials*, 67, pp. 297-306.

Janna, W.S., 1999. *Engineering Heat Transfer*. 2nd edn. Boca Raton, London, New York and Washington D.C: CRC Press.

JKS UK LTD JKS125-Drill Rig. Available at: https://www.jks-uk.com/construction-products/jks-drill-rigs/jks125-drill-rig (Accessed: 12 July 2018).

Johnson, E. (2009) *Installation and Performance Monitoring of a Pothole Patched Using Asphalt Pavement Millings and a 915 MHz Microwave*. Available at:

http://www.dot.state.mn.us/mnroad/projects/Taconite_Aggregates/PDF%27s/MnDOT_MonitoringReport_PotholePatch_10-5-09.pdf (Accessed: 15 June 2018).

Kassem, E., Liu, W., Scullion, T., Masad, E. and Chowdhury, A. (2015) 'Development of compaction monitoring system for asphalt pavements', *Construction and Building Materials*, 96, pp. 334-345.

Kloubert, H. (2009) Basic Principles of Asphalt Compaction: Compaction Methods, Compaction Equipment, and Rolling Technique. Available at: http://www.bomag.com/world/media/pdf/PRE109016_0901.pdf. (Accessed: 15 June 2018).

Knapman, C. (2013) Britain's pothole problem deepens. Available at: http://www.telegraph.co.uk/motoring/road-safety/9927061/Britains-pothole-problem-deepens.html (Accessed: 7 February 2016).

Kwon, B.J., Kim, D., Rhee, S.K. and Kim, Y.R. (2018) 'Spray injection patching for pothole repair using 100 percent reclaimed asphalt pavement', *Construction and Building Materials*, 166.

Kyriakodis, G. and Santamouris, M. (2018) 'Using reflective pavements to mitigate urban heat island in warm climates-results from a large scale urban mitigation project', *Urban Climate*, 24, pp. 326-339.

Lavin, P. (2003) *Asphalt Pavements: a Practical Guide to Design, Production and Maintenance for Engineers and Architects*. London and New York: CRC Press, Taylor and Francis Group.

Lee, D., Guinn, J.A., Khandhal, P.S. and Dunning, R.L. (1990) *Absorption of Asphalt Into Porous Aggregates*. Washington, D.C.: Strategic Highway Research Program, National Research Council (No. SHRP-A/UIR-90-009).

Leininger, C.W. (2015) Optimization of the infrared asphalt repair process. Master's Thesis. University of Maryland. Available at:

https://search.proquest.com/openview/5d63e8ff20aa8561ec9f4e81b6fc75fe/1?pq-origsite=gscholar&cbl=18750&diss=y (Accessed 20 June 2018).

Lesueur, D. and Youtcheff, J. (2013) *Asphalt pavement durability*. Edited by Hihara, L.H., Adler, R.P. and Latanision, R.M. in Environmental degradation of advanced and traditional engineering materials. Boca Raton: Taylor and Francis.

Liu, Q., Schlangen, E., van de Ven, M., van Bochove, G. and van Montfort, J. (2012) 'Evaluation of the induction healing effect of porous asphalt concrete through four point bending fatigue test', *Construction and Building Materials*, 29, pp. 403-409.

Liu, Q., García, Á., Schlangen, E. and van de Ven, M. (2011) 'Induction healing of asphalt mastic and porous asphalt concrete', *Construction and Building Materials*, 25(9), pp. 3746-3752.

Liu, Q., Schlangen, E., García, Á. and van de Ven, M. (2010) 'Induction heating of electrically conductive porous asphalt concrete', *Construction and Building Materials*, 24(7), pp. 1207-1213.

Lu, Y., Yu, W., Hu, D. and Liu, W. (2018) 'Experimental study on the thermal conductivity of aeolian sand from the Tibetan Plateau', *Cold Regions Science and Technology*, 146, pp. 1-8.

Luca, J. and Mrawira, D. (2005) 'New measurement of thermal properties of superpave asphalt concrete', *Journal of Materials in Civil Engineering*, 17(1), pp. 72-79.

Maqsood, A., Gul, I.H. and Anis-ur-Rehman, M. (2004) 'Thermal transport properties of granites in the temperature range 253–333 K', *Journal of Physics D: Applied Physics*, 37(9), p.1405.

McDaniel, R.S., Olek, J., Behnood, A., Magee, B. and Pollock, R. (2014) *Pavement Patching Practices*. Washington, D.C.: National Cooperative Highway Research Program, Transportation Research Board (No. Project 20-05, Topic 44-04).

Metals4u (2018) 1/4" od x 16swg wall Aluminium tube. Available at: https://www.metals4u.co.uk/aluminium/c1/tube/c22/6.3mm-x-1.6mm-(-14-od-x-16swg-)/p3107 (Accessed: 12 July 2018).

Mfinanga, D. A., H. Ochiai, and N. Yasufuku (1996) Traffic Loading and Environmental Effects on Asphalt Pavement Rutting. *Memoirs of the Faculty of Engineering, Kyushu University*, 56(3).

Mill, T., Tse, D., Loo, B., Yao, C. and Canavesi, E. (1992) 'Oxidation pathways for asphalt', *Preprints of Papers- American Chemical Society, Division of Fuel Chemistry*, 37(3).

Miller, J.S. and Bellinger, W.Y. (2014) *Distress identification manual for the long-term pavement performance program*. United States: Federal Highway Administration, Office of Infrastructure Research and Development (No. FHWA-HRT-13-092).

Minhoto, M., Pais, J., Pereira, P. and Picado-Santos, L. (2005) 'Predicting asphalt pavement temperature with a three-dimensional finite element method', *Transportation Research Record: Journal of the Transportation Research Board*, (1919), pp. 96-110.

Mirzanamadi, R., Johansson, P. and Grammatikos, S.A. (2018) 'Thermal properties of asphalt concrete: A numerical and experimental study', *Construction and Building Materials*, 158, pp. 774-785.

Modest, M.F. (2013) *Radiative heat transfer*. 4th ed. Oxford, Amsterdam: Academic press.

National Asphalt Pavement Association, American Association of State Highway and Transportation Officials (1997) *Segregation: Causes and Cures for Hot Mix Asphalt*. Washington, D.C.: American Association of State Highway and Transportation Officials.

Nazzal, M.D., Kim, S. and Abbas, A.R. (2014) *Evaluation of winter pothole patching methods*. Columbus: FHWA, Ohio Department of Transportation (Publication FHWA/OH-2014/2).

Nikolaides, A. (2014) Highway engineering: Pavements, materials and control of quality. Boca Raton: CRC Press, Taylor and Francis Group.

Norambuena-Contreras, J. and Garcia, A. (2016) 'Self-healing of asphalt mixture by microwave and induction heating', *Materials and Design*, 106, pp. 404-414.

Obaidi, H., Gomez-Meijide, B. and Garcia, A. (2017) 'A fast pothole repair method using asphalt tiles and induction heating', *Construction and Building Materials*, 131, pp. 592-599.

Omega (2016a) Professional Infrared Thermometer with 50:1 Field of View and Magnetic Mount. Available at: https://in.omega.com/pptst/OS425-LS.html (Accessed: 10 February 2016).

Omega (2016b) 8 Thermocouple Data Acquisition system. Available at: https://www.omega.co.uk/pptst/TC-08.html (Accessed: 14 May 2016).

Omega (2016c) High Stability, SuperOMEGACLAD™XL Thermocouple Probes - Hand-held Probes. Available at: https://www.omega.co.uk/pptst/KHXL_NHXL.html (Accessed: 13 July 2016).

Omega (2016d) Hermetically Sealed Thermocouple. Available at: http://www.omega.co.uk/pptst/HSTC.html (Accessed: 14 May 2016).

Overlockers (2018) Alumina Thermal Paste (14g). Available at: https://www.overclockers.co.uk/arctic-silver-alumina-thermal-paste-14g-th-006-ac.html (Accessed: 12 July 2018).

Pan, P., Wu, S., Hu, X., Wang, P. and Liu, Q. (2017) 'Effect of freezing-thawing and ageing on thermal characteristics and mechanical properties of conductive asphalt concrete', *Construction and Building Materials*, 140, pp. 239-247.

Pan, P., Wu, S., Xiao, Y., Wang, P. and Liu, X. (2014) 'Influence of graphite on the thermal characteristics and anti-ageing properties of asphalt binder', *Construction and Building Materials*, 68, pp. 220-226.

Pavement Interactive (2018a) *Corrugation and Shoving*. Available at: http://www.pavementinteractive.org/corrugation-and-shoving/ (Accessed: 19 June 2018).

Pavement Interactive (2018b) *Depression*. Available at: http://www.pavementinteractive.org/depression/ (Accessed: 19 June 2018).

Presley, M.A. and Christensen, P.R. (1997) 'Thermal conductivity measurements of particulate materials 2. Results', *Journal of Geophysical Research: Planets*, 102(E3), pp. 6551-6566.

Prowell, B. D., J. Zhang, and E. R. Brown (2005) *Aggregate Properties and the Performance of Superpave-Designed Hot Mix Asphalt*. Washington, D.C.: Transportation Research Board (No. Project 9-35).

Rahman, M., Grenfell, J., Arulanandam, S. and Ianakiev, A. (2013) 'Influence of thermal segregation on asphalt pavement compaction', *Transportation Research Record: Journal of the Transportation Research Board*, 2347(1), pp. 71-78.

Rahman M and Thom N (2012) *Performance of Asphalt Patch Repairs*. London: ICE.

Raposeiras, A., Castro-Fresno, D., Vega-Zamanillo, A. and Rodriguez-Hernandez, J. (2013) 'Test methods and influential factors for analysis of bonding between bituminous pavement layers', *Construction and Building Materials*, 43, pp. 372-381.

Resistalloy (2016) *Trading Limited. Fecralloy Properties: Physical and Mechanical properties*. Available at: http://www.resistalloytrading.co.uk/pages/fecralloyproperties (Accessed: 14 June 2016).

Roberts, F.L., Kandhal, P.S., Brown, E.R., Lee, D. and Kennedy, T.W. (1991) *Hot mix asphalt materials, mixture design and construction*. 2nd edn. Lanham, Maryland: National Asphalt Pavement Association Research and Education Foundation.

Rosales-Herrera, V., Prozzi, J. and Prozzi, J. (2007) *Mixture design and performance-based specifications for cold patching mixtures*. Austin: Texas Department of Transportation Report (Publication FHWA/TX-08/0-4872, 2).

Shatnawi, S. (2008) *Maintenance Technical Advisory Guide Volume I Flexible Pavement Preservation*. 2nd edn. Sacramento: State of California Department of Transportation, Office of Pavement Preservation, Division of Maintenance.

Somé, S.C., Delaunay, D. and Gaudefroy, V. (2013) 'Comparison and validation of thermal contact resistance models at solid–liquid interface taking into account the wettability parameters', *Applied Thermal Engineering*, 61(2), pp.531-540.

Stephens, R.B. and Cody, G.D. (1977) 'Optical reflectance and transmission of a textured surface', *Thin Solid Films*, 45(1), pp. 19-29.

Straube, J. F. (2000-2003) *Heat Flow Basics*. Available at:
http://www.civil.uwaterloo.ca/beg/arch264/arch264%20heat%20flow%20basics.pdf
(Downloaded: 9 August 2018).

Stroup-Gardiner, M. and Brown, E.R. (2000) *Segregation in hot-mix asphalt pavements*. Washington, D.C.: National Academy Press.

Tang, X.-W., Jiao, S.-J., Gao, Z.-Y. and Xu, X.-L. (2008) 'Study of 5.8 GHz Magnetron in Asphalt Pavement Maintenance', *Journal of Electromagnetic Waves and Applications*, 22(14-15), pp. 1975-1984.

Texas Department of Transportation (2011) *Manual Notice, Pavement Design Guide*. Texas: Texas Department of Transportation.

Textile Technologies Ltd (2016) S-TEX-CFW Silica Webbing Tape (1.5 - 2mm). Available at: http://www.textiletechnologies.co.uk/s-tex-cfw-range-1-5-2mm-thick.html (Accessed: 7 June 2016).

The Automobile Association (2016) Potholes: Plummeting road condition leaves drivers deeper in trouble. Available at: http://www.theaa.com/newsroom/news-2014/potholes-road-condition-survey-2014.html (Accessed: 6 February 2016).

Thermtest (2018) Thermtest TLS-100 Portable Thermal Conductivity Meter for Measurement of Soil, Rock, Concrete, and Polymers. Available at: https://thermtest.com/tls-100 (Accessed: 12 July 2018).

Thom, N. (2008) *Principles of pavement engineering*. London: Thomas Telford Publishing.

Thompson, M.K. and Thompson, J.M. (2007) 'Considerations for Predicting Thermal Contact Resistance in ANSYS', *17th KOREA ANSYS User's Conference*. Korea, date n/a.

Tritt, T.M. (2005) *Thermal conductivity. Theory, properties and applications*. New York, Boston, Dordrecht, London, Moscow: Springer Science & Business Media.

Tsai, B.W., Coleri, E., Harvey, J.T. and Monismith, C.L. (2016) 'Evaluation of AASHTO T 324 Hamburg-Wheel Track Device test', *Construction and Building Materials*, 114, pp. 248-260.

US Army Corps of Engineers (2000) *AC 150/5370-14 A - Hot-mix asphalt paving handbook*. Available at: https://www.faa.gov/airports/resources/advisory_circulars/index.cfm/go/document.information/documentID/1025447 (Accessed: 19 June 2018).

Uzarowski, L., Henderson, V., Henderson, M. and Kiesswetter, B. (2011) 'Innovative infrared crack repair method'. Proceedings of Congress et Exhibition de l'Association des Transports du Canada, 2011 Les Succes en Transports: Une Tremplin vers l'Avenir, Edmonton, Canada, date n/a.

Walker, D. (1984) 'How vehicle loads affect pavement performance', Wisconsin Transportation Bulletin.

Washington Asphalt Pavement Association (2018) *Slippage Cracking*. Available at: http://www.asphaltwa.com/slippage-cracking/ (Accessed: 19 June 2018).

Washington State Department of Transportation (2017) *Maintenance Manual M 51*. Washington D.C.: Washington State Department of Transportation.

West, R.C., Watson, D.E., Turner, P.A. and Casola, J.R., (2010) *Mixing and compaction temperatures of asphalt binders in hot-mix asphalt*. Washington D.C.: Transportation Research Board (No. Project 9-39).

Williams, S.G. (2011) *HMA Longitudinal Joint Evaluation and Construction*. Arkansas: University of Arkansas (TRC-0801 Final Report, AR).

Wilson, T. P., and A. R. Romine (2001) *Materials and Procedures for Repair of Potholes in Asphalt-Surfaced Pavements--Manual of Practice*. U.S. Department of Transportation. (Report No. FHWA-RD-99-168).

Yang, X. and Liu, B. (2007) 'Coupled-field Finite Element Analysis of Thermal Stress in Asphalt Pavement', *Journal of Highway and Transportation Research and Development (English Edition)*, 2(1), pp. 1-6.

Zhang, N. and Wang, Z. (2017) 'Review of soil thermal conductivity and predictive models', *International Journal of Thermal Sciences*, 117, pp. 172-183.

Zhao, D., Qian, X., Gu, X., Jajja, S.A. and Yang, R. (2016) 'Measurement Techniques for Thermal Conductivity and Interfacial Thermal Conductance of Bulk and Thin Film Materials', *Journal of Electronic Packaging*, 138(4), pp. 1-64.

Zhu, S., Shi, J., Jiang, L. and Wu, B. (2009) 'Research on heat transfer model of asphalt pavements subjected to microwave heating recycling', *Journal of Highway and Transportation Research and Development (English Edition)*, 4(2), pp. 1-5.

Appendix A

Heater heat power detailed calculations

Tables A.1 – A.5 show the calculation of heat power for the five different gas feed rates studied in Chapter 3.

Table A.1 Heat power calculation for 20% gas feed rate

Sampling temperature point no.	Temperature (T) after 2 min of heater operating time (K)	T^4 (K^4)	Emissivity	Stefan-Boltzmann Constant (W/m^2 K^4)	Heat power (W)	Heat power (kW)
1a	1227.13	$2.27 \times 10^{+12}$	0.9	5.67×10^{-8}	8687.27	8.7
1b	1185.72	$1.98 \times 10^{+12}$	0.9	5.67×10^{-8}	7572.68	7.6
1c	1183.91	$1.96 \times 10^{+12}$	0.9	5.67×10^{-8}	7526.55	7.5
2a	1180.00	$1.94 \times 10^{+12}$	0.9	5.67×10^{-8}	7427.61	7.4
2b	1182.24	$1.95 \times 10^{+12}$	0.9	5.67×10^{-8}	7484.17	7.5
2c	1157.68	$1.80 \times 10^{+12}$	0.9	5.67×10^{-8}	6881.37	6.9
3a	1172.72	$1.89 \times 10^{+12}$	0.9	5.67×10^{-8}	7246.00	7.2
3b	1162.50	$1.83 \times 10^{+12}$	0.9	5.67×10^{-8}	6996.69	7.0
3c	1139.45	$1.69 \times 10^{+12}$	0.9	5.67×10^{-8}	6458.06	6.5
4a	1176.11	$1.91 \times 10^{+12}$	0.9	5.67×10^{-8}	7330.15	7.3
4b	1158.59	$1.80 \times 10^{+12}$	0.9	5.67×10^{-8}	6903.03	6.9
4c	1137.14	$1.67 \times 10^{+12}$	0.9	5.67×10^{-8}	6405.85	6.4
5a	1177.17	$1.92 \times 10^{+12}$	0.9	5.67×10^{-8}	7356.61	7.4
5b	1151.12	$1.76 \times 10^{+12}$	0.9	5.67×10^{-8}	6726.72	6.7
5c	1140.69	$1.69 \times 10^{+12}$	0.9	5.67×10^{-8}	6486.22	6.5
6a	1121.84	$1.58 \times 10^{+12}$	0.9	5.67×10^{-8}	6067.99	6.1
6b	1151.27	$1.76 \times 10^{+12}$	0.9	5.67×10^{-8}	6730.23	6.7
6c	1113.14	$1.54 \times 10^{+12}$	0.9	5.67×10^{-8}	5881.93	5.9
7a	1158.29	$1.80 \times 10^{+12}$	0.9	5.67×10^{-8}	6895.89	6.9
7b	1127.06	$1.61 \times 10^{+12}$	0.9	5.67×10^{-8}	6181.72	6.2
7c	1117.60	$1.56 \times 10^{+12}$	0.9	5.67×10^{-8}	5976.77	6.0
8a	1140.72	$1.69 \times 10^{+12}$	0.9	5.67×10^{-8}	6486.90	6.5
8b	1132.10	$1.64 \times 10^{+12}$	0.9	5.67×10^{-8}	6293.03	6.3
8c	1100.53	$1.47 \times 10^{+12}$	0.9	5.67×10^{-8}	5619.90	5.6
9a	1145.65	$1.72 \times 10^{+12}$	0.9	5.67×10^{-8}	6599.77	6.6
9b	1148.22	$1.74 \times 10^{+12}$	0.9	5.67×10^{-8}	6659.19	6.7
9c	1113.91	$1.54 \times 10^{+12}$	0.9	5.67×10^{-8}	5898.22	5.9
10a	1134.53	$1.66 \times 10^{+12}$	0.9	5.67×10^{-8}	6347.24	6.3
10b	1147.77	$1.74 \times 10^{+12}$	0.9	5.67×10^{-8}	6648.76	6.6
10c	1117.64	$1.56 \times 10^{+12}$	0.9	5.67×10^{-8}	5977.62	6.0
11a	1160.72	$1.82 \times 10^{+12}$	0.9	5.67×10^{-8}	6953.94	7.0
11b	1142.31	$1.70 \times 10^{+12}$	0.9	5.67×10^{-8}	6523.14	6.5
11c	1116.53	$1.55 \times 10^{+12}$	0.9	5.67×10^{-8}	5953.91	6.0
12a	1121.77	$1.58 \times 10^{+12}$	0.9	5.67×10^{-8}	6066.47	6.1
12b	1084.23	$1.38 \times 10^{+12}$	0.9	5.67×10^{-8}	5294.28	5.3
12c	1133.58	$1.65 \times 10^{+12}$	0.9	5.67×10^{-8}	8687.27	6.3
				Average:		**6.6**

Table A.2 Heat power calculation for 40% gas feed rate

Sampling temperature point no.	Temperature (T) after 2 min of heater operating time (K)	T^4 (K^4)	Emissivity	Stefan-Boltzmann Constant (W/m^2 K^4)	Heat power (W)	Heat power (kW)
1a	1176.82	$1.92\times10^{+12}$	0.9	5.67×10^{-8}	7347.86	7.3
1b	1151.96	$1.76\times10^{+12}$	0.9	5.67×10^{-8}	6746.38	6.7
1c	1184.84	$1.97\times10^{+12}$	0.9	5.67×10^{-8}	7550.22	7.6
2a	1191.96	$2.02\times10^{+12}$	0.9	5.67×10^{-8}	7733.35	7.7
2b	1187.84	$1.99\times10^{+12}$	0.9	5.67×10^{-8}	7626.98	7.6
2c	1154.70	$1.78\times10^{+12}$	0.9	5.67×10^{-8}	6810.79	6.8
3a	1153.49	$1.77\times10^{+12}$	0.9	5.67×10^{-8}	6782.29	6.8
3b	1163.68	$1.83\times10^{+12}$	0.9	5.67×10^{-8}	7025.14	7.0
3c	1135.37	$1.66\times10^{+12}$	0.9	5.67×10^{-8}	6366.06	6.4
4a	1153.00	$1.77\times10^{+12}$	0.9	5.67×10^{-8}	6770.77	6.8
4b	1148.60	$1.74\times10^{+12}$	0.9	5.67×10^{-8}	6668.01	6.7
4c	1128.79	$1.62\times10^{+12}$	0.9	5.67×10^{-8}	6219.76	6.2
5a	1143.08	$1.71\times10^{+12}$	0.9	5.67×10^{-8}	6540.75	6.5
5b	1144.15	$1.71\times10^{+12}$	0.9	5.67×10^{-8}	6565.27	6.6
5c	1132.37	$1.64\times10^{+12}$	0.9	5.67×10^{-8}	6299.04	6.3
6a	1157.10	$1.79\times10^{+12}$	0.9	5.67×10^{-8}	6867.59	6.9
6b	1140.02	$1.69\times10^{+12}$	0.9	5.67×10^{-8}	6470.99	6.5
6c	1166.84	$1.85\times10^{+12}$	0.9	5.67×10^{-8}	7101.76	7.1
7a	1147.89	$1.74\times10^{+12}$	0.9	5.67×10^{-8}	6651.54	6.7
7b	1143.39	$1.71\times10^{+12}$	0.9	5.67×10^{-8}	6547.85	6.5
7c	1126.07	$1.61\times10^{+12}$	0.9	5.67×10^{-8}	6160.02	6.2
8a	1154.16	$1.77\times10^{+12}$	0.9	5.67×10^{-8}	6798.06	6.8
8b	1159.90	$1.81\times10^{+12}$	0.9	5.67×10^{-8}	6934.31	6.9
8c	1118.37	$1.56\times10^{+12}$	0.9	5.67×10^{-8}	5993.26	6.0
9a	1130.39	$1.63\times10^{+12}$	0.9	5.67×10^{-8}	6255.10	6.3
9b	1156.98	$1.79\times10^{+12}$	0.9	5.67×10^{-8}	6864.74	6.9
9c	1131.28	$1.64\times10^{+12}$	0.9	5.67×10^{-8}	6274.82	6.3
10a	1153.19	$1.77\times10^{+12}$	0.9	5.67×10^{-8}	6775.24	6.8
10b	1159.42	$1.81\times10^{+12}$	0.9	5.67×10^{-8}	6922.84	6.9
10c	1195.42	$2.04\times10^{+12}$	0.9	5.67×10^{-8}	7823.53	7.8
11a	1160.57	$1.81\times10^{+12}$	0.9	5.67×10^{-8}	6950.34	7.0
11b	1122.93	$1.59\times10^{+12}$	0.9	5.67×10^{-8}	6091.60	6.1
11c	1120.60	$1.58\times10^{+12}$	0.9	5.67×10^{-8}	6041.20	6.0
12a	1165.27	$1.84\times10^{+12}$	0.9	5.67×10^{-8}	7063.62	7.1
12b	1110.25	$1.52\times10^{+12}$	0.9	5.67×10^{-8}	5821.09	5.8
12c	1126.92	$1.61\times10^{+12}$	0.9	5.67×10^{-8}	6178.65	6.2
					Average:	**6.7**

Table A.3 Heat power calculation for 60% gas feed rate

Sampling temperature point no.	Temperature (T) after 2 min of heater operating time (K)	T^4 (K^4)	Emissivity	Stefan-Boltzmann Constant (W/m^2 K^4)	Heat power (W)	Heat power (kW)
1a	1201.62	$2.08\times10^{+12}$	0.9	5.67×10^{-8}	7987.11	8.0
1b	1170.23	$1.88\times10^{+12}$	0.9	5.67×10^{-8}	7184.65	7.2
1c	1154.81	$1.78\times10^{+12}$	0.9	5.67×10^{-8}	6813.39	6.8
2a	1199.26	$2.07\times10^{+12}$	0.9	5.67×10^{-8}	7924.54	7.9
2b	1182.40	$1.95\times10^{+12}$	0.9	5.67×10^{-8}	7488.22	7.5
2c	1167.75	$1.86\times10^{+12}$	0.9	5.67×10^{-8}	7123.94	7.1
3a	1176.76	$1.92\times10^{+12}$	0.9	5.67×10^{-8}	7346.36	7.3
3b	1162.18	$1.82\times10^{+12}$	0.9	5.67×10^{-8}	6988.99	7.0
3c	1164.66	$1.84\times10^{+12}$	0.9	5.67×10^{-8}	7048.84	7.0
4a	1189.58	$2.00\times10^{+12}$	0.9	5.67×10^{-8}	7671.77	7.7
4b	1172.14	$1.89\times10^{+12}$	0.9	5.67×10^{-8}	7231.67	7.2
4c	1175.17	$1.91\times10^{+12}$	0.9	5.67×10^{-8}	7306.74	7.3
5a	1203.42	$2.10\times10^{+12}$	0.9	5.67×10^{-8}	8035.07	8.0
5b	1151.11	$1.76\times10^{+12}$	0.9	5.67×10^{-8}	6726.49	6.7
5c	1187.29	$1.99\times10^{+12}$	0.9	5.67×10^{-8}	7612.87	7.6
6a	1199.31	$2.07\times10^{+12}$	0.9	5.67×10^{-8}	7925.87	7.9
6b	1149.38	$1.75\times10^{+12}$	0.9	5.67×10^{-8}	6686.14	6.7
6c	1166.49	$1.85\times10^{+12}$	0.9	5.67×10^{-8}	7093.25	7.1
7a	1180.74	$1.94\times10^{+12}$	0.9	5.67×10^{-8}	7446.26	7.4
7b	1146.28	$1.73\times10^{+12}$	0.9	5.67×10^{-8}	6614.30	6.6
7c	1151.53	$1.76\times10^{+12}$	0.9	5.67×10^{-8}	6736.31	6.7
8a	1174.25	$1.90\times10^{+12}$	0.9	5.67×10^{-8}	7283.89	7.3
8b	1153.16	$1.77\times10^{+12}$	0.9	5.67×10^{-8}	6774.53	6.8
8c	1125.19	$1.60\times10^{+12}$	0.9	5.67×10^{-8}	6140.79	6.1
9a	1171.24	$1.88\times10^{+12}$	0.9	5.67×10^{-8}	7209.49	7.2
9b	1148.47	$1.74\times10^{+12}$	0.9	5.67×10^{-8}	6664.99	6.7
9c	1145.16	$1.72\times10^{+12}$	0.9	5.67×10^{-8}	6588.49	6.6
10a	1184.68	$1.97\times10^{+12}$	0.9	5.67×10^{-8}	7546.14	7.5
10b	1145.87	$1.72\times10^{+12}$	0.9	5.67×10^{-8}	6604.84	6.6
10c	1167.58	$1.86\times10^{+12}$	0.9	5.67×10^{-8}	7119.80	7.1
11a	1175.22	$1.91\times10^{+12}$	0.9	5.67×10^{-8}	7307.98	7.3
11b	1133.46	$1.65\times10^{+12}$	0.9	5.67×10^{-8}	6323.33	6.3
11c	1171.37	$1.88\times10^{+12}$	0.9	5.67×10^{-8}	7212.69	7.2
12a	1186.67	$1.98\times10^{+12}$	0.9	5.67×10^{-8}	7596.98	7.6
12b	1135.91	$1.66\times10^{+12}$	0.9	5.67×10^{-8}	6378.18	6.4
12c	1184.32	$1.97\times10^{+12}$	0.9	5.67×10^{-8}	7536.98	7.5
					Average:	**7.1**

Table A.4 Heat power calculation for 80% gas feed rate

Sampling temperature point no.	Temperature (T) after 2 min of heater operating time (K)	T^4 (K^4)	Emissivity	Stefan-Boltzmann Constant (W/m² K⁴)	Heat power (W)	Heat power (kW)
1a	1250.96	$2.45\times10^{+12}$	0.9	5.67×10^{-8}	9381.98	9.4
1b	1135.93	$1.66\times10^{+12}$	0.9	5.67×10^{-8}	6378.63	6.4
1c	1163.61	$1.83\times10^{+12}$	0.9	5.67×10^{-8}	7023.45	7.0
2a	1213.40	$2.17\times10^{+12}$	0.9	5.67×10^{-8}	8304.95	8.3
2b	1183.01	$1.96\times10^{+12}$	0.9	5.67×10^{-8}	7503.68	7.5
2c	1164.00	$1.84\times10^{+12}$	0.9	5.67×10^{-8}	7032.87	7.0
3a	1209.76	$2.14\times10^{+12}$	0.9	5.67×10^{-8}	8205.74	8.2
3b	1180.73	$1.94\times10^{+12}$	0.9	5.67×10^{-8}	7446.00	7.4
3c	1199.63	$2.07\times10^{+12}$	0.9	5.67×10^{-8}	7934.33	7.9
4a	1199.10	$2.07\times10^{+12}$	0.9	5.67×10^{-8}	7920.32	7.9
4b	1185.64	$1.98\times10^{+12}$	0.9	5.67×10^{-8}	7570.63	7.6
4c	1184.74	$1.97\times10^{+12}$	0.9	5.67×10^{-8}	7547.67	7.5
5a	1175.74	$1.91\times10^{+12}$	0.9	5.67×10^{-8}	7320.93	7.3
5b	1202.24	$2.09\times10^{+12}$	0.9	5.67×10^{-8}	8003.60	8.0
5c	1193.96	$2.03\times10^{+12}$	0.9	5.67×10^{-8}	7785.38	7.8
6a	1162.07	$1.82\times10^{+12}$	0.9	5.67×10^{-8}	6986.35	7.0
6b	1195.69	$2.04\times10^{+12}$	0.9	5.67×10^{-8}	7830.60	7.8
6c	1198.42	$2.06\times10^{+12}$	0.9	5.67×10^{-8}	7902.37	7.9
7a	1170.31	$1.88\times10^{+12}$	0.9	5.67×10^{-8}	7186.62	7.2
7b	1168.99	$1.87\times10^{+12}$	0.9	5.67×10^{-8}	7154.25	7.2
7c	1202.97	$2.09\times10^{+12}$	0.9	5.67×10^{-8}	8023.06	8.0
8a	1188.36	$1.99\times10^{+12}$	0.9	5.67×10^{-8}	7640.35	7.6
8b	1163.65	$1.83\times10^{+12}$	0.9	5.67×10^{-8}	7024.42	7.0
8c	1172.73	$1.89\times10^{+12}$	0.9	5.67×10^{-8}	7246.25	7.2
9a	1178.78	$1.93\times10^{+12}$	0.9	5.67×10^{-8}	7396.94	7.4
9b	1181.79	$1.95\times10^{+12}$	0.9	5.67×10^{-8}	7472.78	7.5
9c	1210.42	$2.15\times10^{+12}$	0.9	5.67×10^{-8}	8223.66	8.2
10a	1191.72	$2.02\times10^{+12}$	0.9	5.67×10^{-8}	7727.12	7.7
10b	1134.67	$1.66\times10^{+12}$	0.9	5.67×10^{-8}	6350.37	6.4
10c	1173.18	$1.89\times10^{+12}$	0.9	5.67×10^{-8}	7257.37	7.3
11a	1168.24	$1.86\times10^{+12}$	0.9	5.67×10^{-8}	7135.91	7.1
11b	1182.76	$1.96\times10^{+12}$	0.9	5.67×10^{-8}	7497.34	7.5
11c	1188.00	$1.99\times10^{+12}$	0.9	5.67×10^{-8}	7631.09	7.6
12a	1174.37	$1.90\times10^{+12}$	0.9	5.67×10^{-8}	7286.86	7.3
12b	1180.09	$1.94\times10^{+12}$	0.9	5.67×10^{-8}	7429.87	7.4
12c	1188.90	$2.00\times10^{+12}$	0.9	5.67×10^{-8}	7654.24	7.7
					Average:	**7.5**

Table A.5 Heat power calculation for 100% gas feed rate

Sampling temperature point no.	Temperature (T) after 2 min of heater operating time (K)	T^4 (K^4)	Emissivity	Stefan-Boltzmann Constant (W/m² K⁴)	Heat power (W)	Heat power (kW)
1a	1121.47	$1.58 \times 10^{+12}$	0.9	5.67×10^{-8}	6059.99	6.1
1b	1180.95	$1.95 \times 10^{+12}$	0.9	5.67×10^{-8}	7451.56	7.5
1c	1227.83	$2.27 \times 10^{+12}$	0.9	5.67×10^{-8}	8707.11	8.7
2a	1126.11	$1.61 \times 10^{+12}$	0.9	5.67×10^{-8}	6160.90	6.2
2b	1182.89	$1.96 \times 10^{+12}$	0.9	5.67×10^{-8}	7500.64	7.5
2c	1215.39	$2.18 \times 10^{+12}$	0.9	5.67×10^{-8}	8359.56	8.4
3a	1153.43	$1.77 \times 10^{+12}$	0.9	5.67×10^{-8}	6780.88	6.8
3b	1189.05	$2.00 \times 10^{+12}$	0.9	5.67×10^{-8}	7658.11	7.7
3c	1219.03	$2.21 \times 10^{+12}$	0.9	5.67×10^{-8}	8460.16	8.5
4a	1143.83	$1.71 \times 10^{+12}$	0.9	5.67×10^{-8}	6557.93	6.6
4b	1196.96	$2.05 \times 10^{+12}$	0.9	5.67×10^{-8}	7863.93	7.9
4c	1221.44	$2.23 \times 10^{+12}$	0.9	5.67×10^{-8}	8527.26	8.5
5a	1157.57	$1.80 \times 10^{+12}$	0.9	5.67×10^{-8}	6878.76	6.9
5b	1192.34	$2.02 \times 10^{+12}$	0.9	5.67×10^{-8}	7743.22	7.7
5c	1199.19	$2.07 \times 10^{+12}$	0.9	5.67×10^{-8}	7922.69	7.9
6a	1178.38	$1.93 \times 10^{+12}$	0.9	5.67×10^{-8}	7386.90	7.4
6b	1203.99	$2.10 \times 10^{+12}$	0.9	5.67×10^{-8}	8050.31	8.1
6c	1210.33	$2.15 \times 10^{+12}$	0.9	5.67×10^{-8}	8221.22	8.2
7a	1170.36	$1.88 \times 10^{+12}$	0.9	5.67×10^{-8}	7187.85	7.2
7b	1202.22	$2.09 \times 10^{+12}$	0.9	5.67×10^{-8}	8003.07	8.0
7c	1211.18	$2.15 \times 10^{+12}$	0.9	5.67×10^{-8}	8244.34	8.2
8a	1179.70	$1.94 \times 10^{+12}$	0.9	5.67×10^{-8}	7420.06	7.4
8b	1198.76	$2.07 \times 10^{+12}$	0.9	5.67×10^{-8}	7911.34	7.9
8c	1175.80	$1.91 \times 10^{+12}$	0.9	5.67×10^{-8}	7322.42	7.3
9a	1196.94	$2.05 \times 10^{+12}$	0.9	5.67×10^{-8}	7863.40	7.9
9b	1194.32	$2.03 \times 10^{+12}$	0.9	5.67×10^{-8}	7794.78	7.8
9c	1220.38	$2.22 \times 10^{+12}$	0.9	5.67×10^{-8}	8497.70	8.5
10a	1212.06	$2.16 \times 10^{+12}$	0.9	5.67×10^{-8}	8268.32	8.3
10b	1151.80	$1.76 \times 10^{+12}$	0.9	5.67×10^{-8}	6742.63	6.7
10c	1219.57	$2.21 \times 10^{+12}$	0.9	5.67×10^{-8}	8475.16	8.5
11a	1182.95	$1.96 \times 10^{+12}$	0.9	5.67×10^{-8}	7502.16	7.5
11b	1187.70	$1.99 \times 10^{+12}$	0.9	5.67×10^{-8}	7623.39	7.6
11c	1196.62	$2.05 \times 10^{+12}$	0.9	5.67×10^{-8}	7855.00	7.9
12a	1189.73	$2.00 \times 10^{+12}$	0.9	5.67×10^{-8}	7675.64	7.7
12b	1192.14	$2.02 \times 10^{+12}$	0.9	5.67×10^{-8}	7738.02	7.7
12c	1227.32	$2.27 \times 10^{+12}$	0.9	5.67×10^{-8}	8692.65	8.7
					Average:	**7.7**

Appendix B

Construction process of HMA slabs for 75 mm and 100 mm deep pothole excavations described in Chapter 4

Figures B.1, B.2 and B.3 show the preparation and compaction of the first, second and third lift respectively of the slabs with 75 mm deep pothole excavation. Seventeen lifts were in total prepared for this type of slabs and 9 aluminum tubes were embedded between the batches to accommodate thermocouples for the thermal tests of Chapter 4. The weight of the batches, the depth of the lifts, the compacting time, the compaction equipment, the bonding of the lifts and the demoulding were similarly done as described in section 4.1.2 in Chapter 4.

For the compaction of the first lift, the 45 mm deep pothole mould was used as shown in Figure B.1. This helped to create the area of the excavation. Then, for the compaction of the second lift and in order to create the 75 mm deep excavation, the 45 mm deep pothole mould was replaced by the 75 mm deep pothole mould as shown in Figure B.2(b). The slabs were demoulded 19 hours after their construction. The pothole moulds were removed using infrared heat as described in section 4.1.2 in Chapter 4.
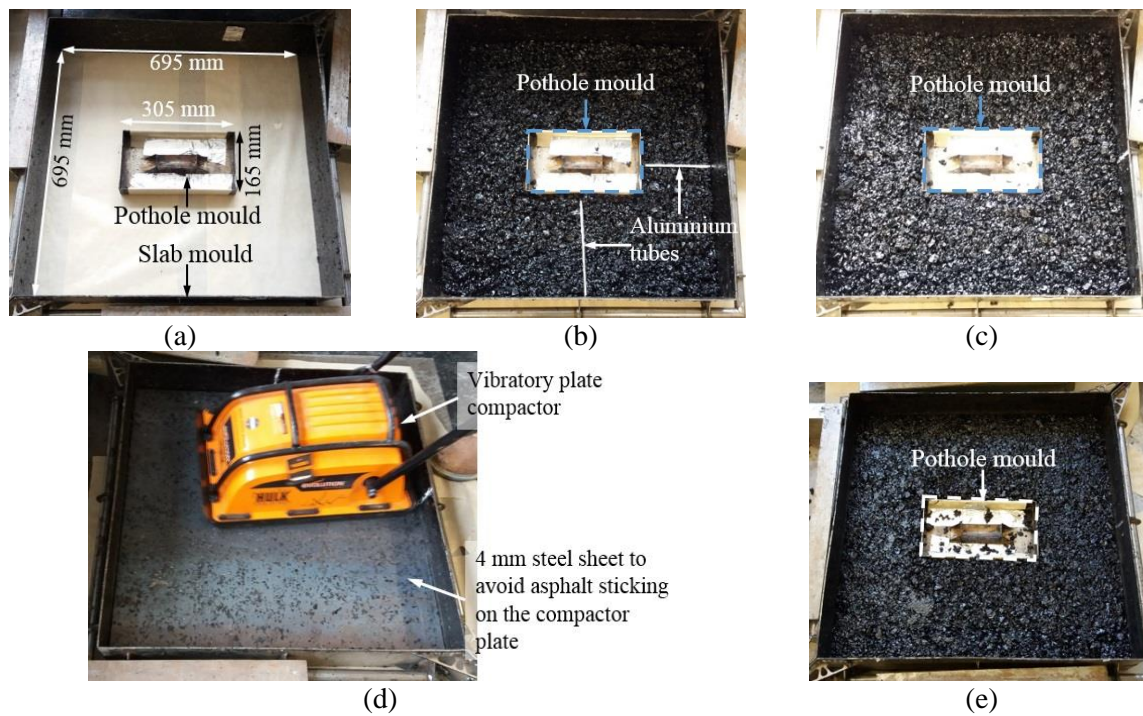
Figure B.1 Slab with 75 mm deep pothole excavation and embedded aluminium tubes to accommodate thermocouples for thermal tests of Chapter 4 – Preparation and compaction of first lift: (a) moulds set up with 45 mm deep pothole mould to create the area of the pothole excavation; (b) 3 asphalt batches poured and 2 aluminium tubes put above the batches; (c) following 3 batches poured; (d) compaction of 6 batches; (e) compacted first lift
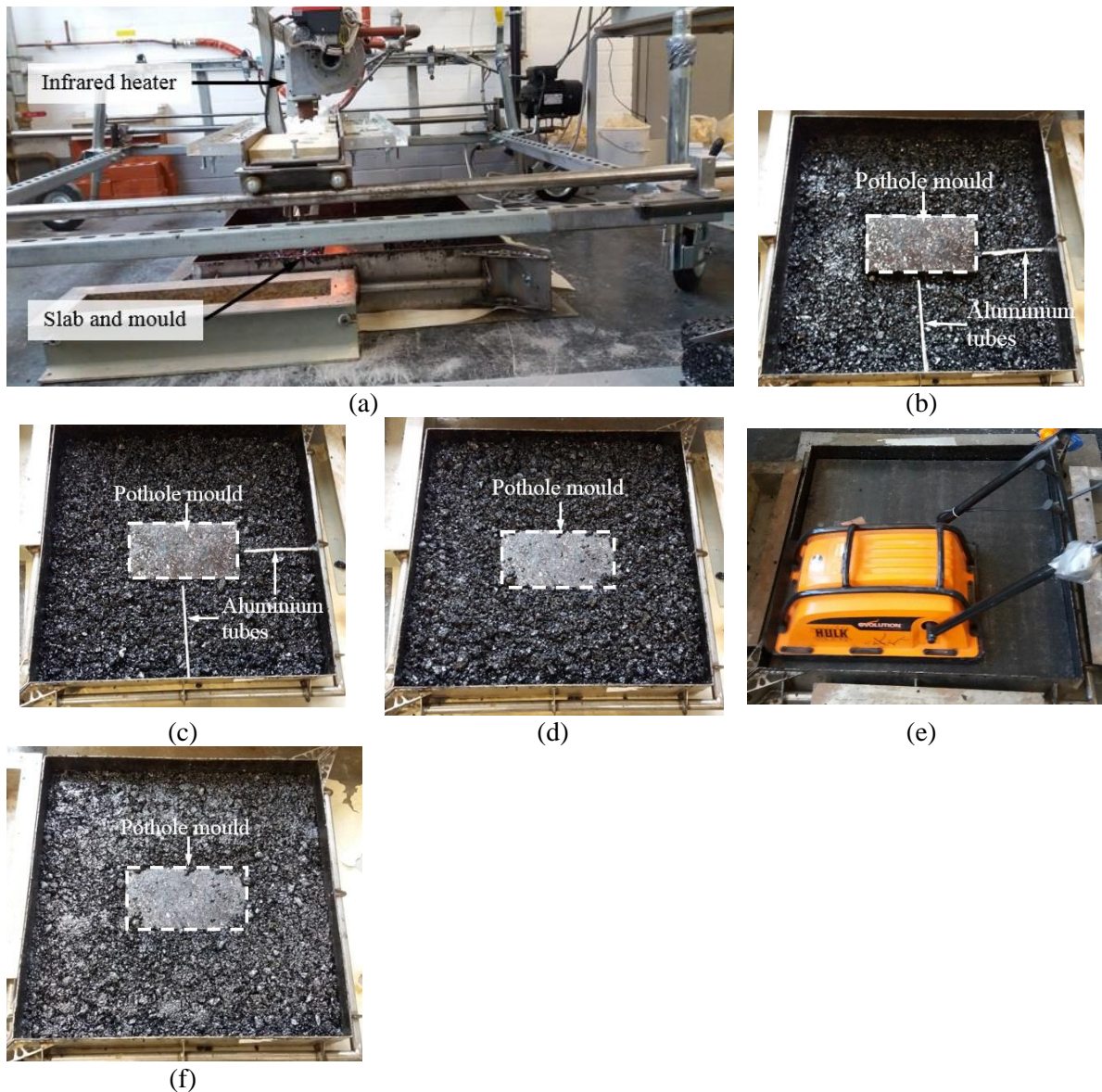
Figure B.2 Slab with 75 mm deep pothole excavation and embedded aluminium tubes to accommodate thermocouples for thermal tests of Chapter 4 – Preparation and compaction of second lift: (a) pre-heating of compacted first lift shown in Figure B.1(e); (b) 45 mm deep pothole mould replaced by the 75 mm deep mould and 2 aluminium tubes put above the compacted first lift; (c) 3 asphalt batches poured and 2 aluminium tubes put above the batches; (d) following 3 batches poured; (e) compaction of 6 batches; (f) compacted second lift
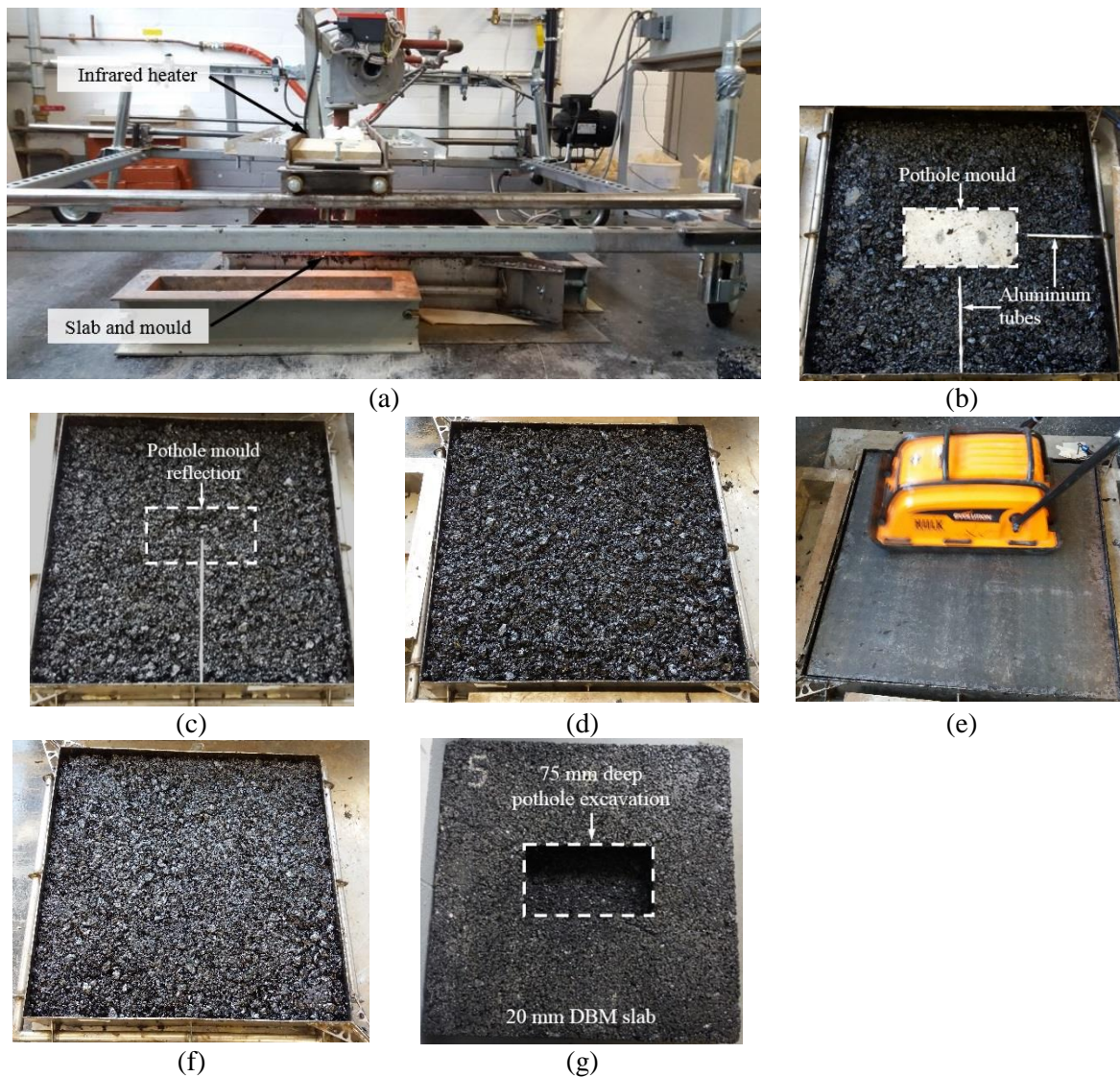
Figure B.3 Slab with 75 mm deep pothole excavation and embedded aluminium tubes to accommodate thermocouples for thermal tests of Chapter 4 – Preparation and compaction of third lift: (a) pre-heating of compacted second lift shown in Figure B.2(f); (b) 2 aluminium tubes above the compacted second lift; (c) 3 asphalt batches poured and 1 aluminium tube put above the batches; (c) following 2 batches poured and final aluminium tube put above the batches; (d) compaction of 5 batches; (e) compacted third lift; (f) constructed slab turned upside down and pothole mould removed after 19 h of construction

Figures B.4, B.5 and B.6 show the preparation and compaction of the first, second and third lift respectively of the slabs with 100 mm deep pothole excavation. Eighteen lifts were in total prepared for this type of slabs and 9 aluminum tubes were embedded between the batches to accommodate thermocouples for the thermal tests of Chapter 4. The weight of the batches, the depth of the lifts, the compacting time, the compaction equipment, the bonding of the lifts and the demoulding were similarly done as described in section 4.1.2 in Chapter 4.

For the compaction of the first and second lifts, the 45 mm and 75 mm deep pothole moulds were used respectively as shown in Figures B.4 and B.5. At the end of the compaction of the second lift, the 75 mm deep pothole mould was replaced by the 100 mm deep pothole mould. The slabs were demoulded 19 hours after their construction. The pothole moulds were removed using infrared heat as described in section 4.1.2 in Chapter 4.
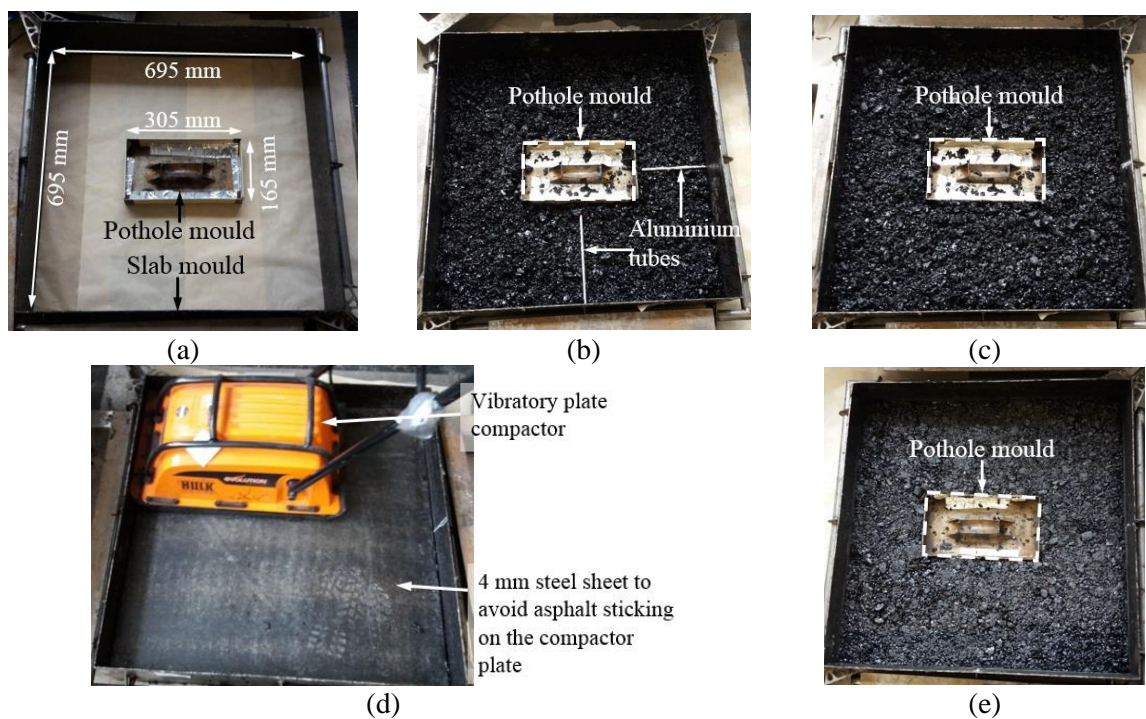
Figure B.4 Slab with 100 mm deep pothole excavation and embedded aluminium tubes to accommodate thermocouples for thermal tests of Chapter 4 – Preparation and compaction of first lift: (a) moulds set up with 45 mm deep pothole mould to create the area of the pothole excavation; (b) 3 asphalt batches poured and 2 aluminium tubes put above the batches; (c) following 3 batches poured; (d) compaction of 6 batches; (e) compacted first lift

(a)

(b)

(c)

(d)

(e)

(f)
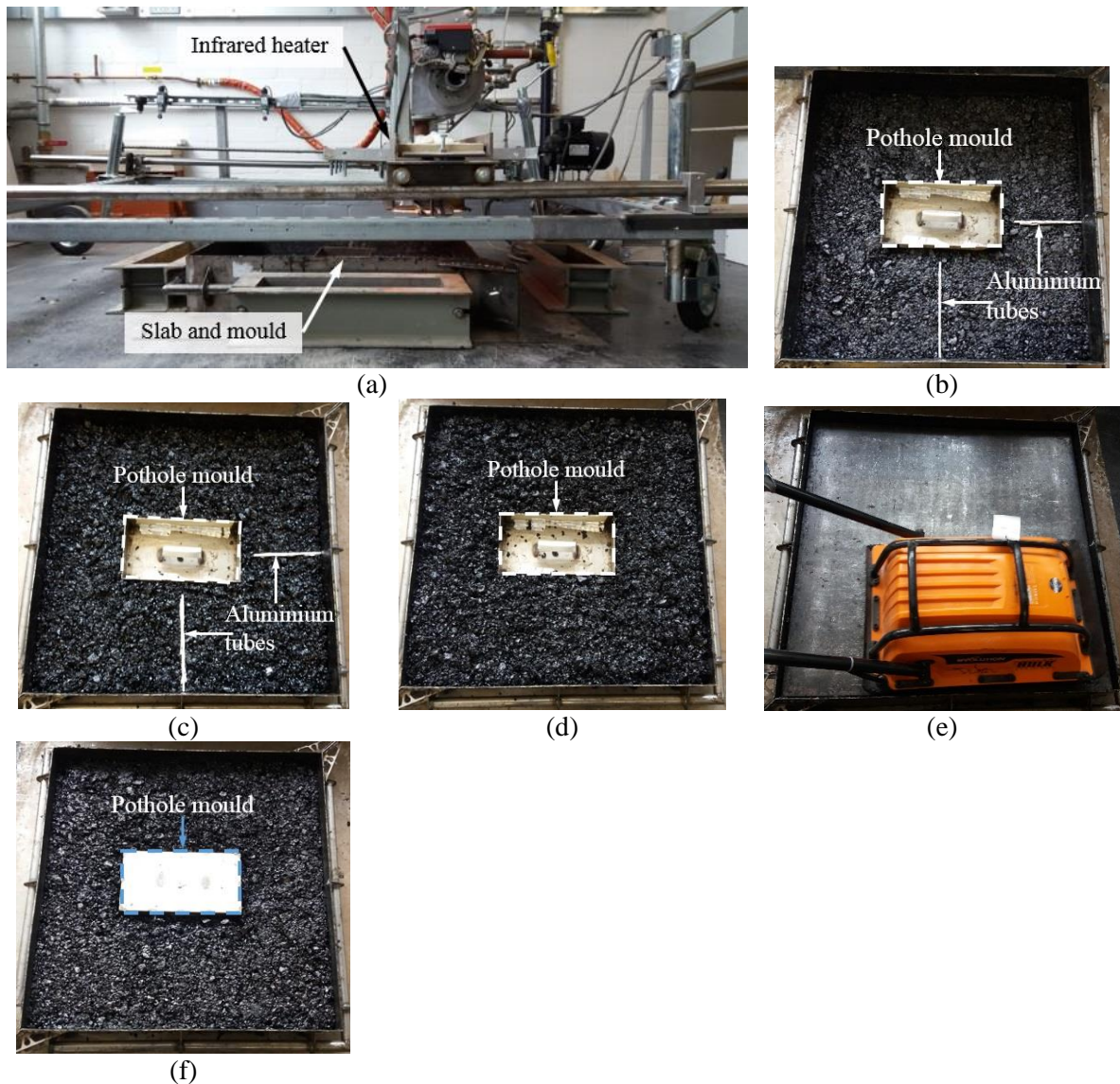
Figure B.5 Slab with 100 mm deep pothole excavation and embedded aluminium tubes to accommodate thermocouples for thermal tests of Chapter 4 – Preparation and compaction of second lift: (a) pre-heating of compacted first lift shown in Figure B.4(e); (b) 45 mm deep pothole mould replaced by the 75 mm deep mould and 2 aluminium tubes put above the compacted first lift; (c) 3 asphalt batches poured and 2 aluminium tubes put above the batches; (d) following 3 batches poured; (e) compaction of 6 batches; (f) compacted second lift - 75 mm deep pothole mould replaced by the 100 mm deep mould immediately after the compaction

(a)

(b)

(c)

(d)

(e)

(f)
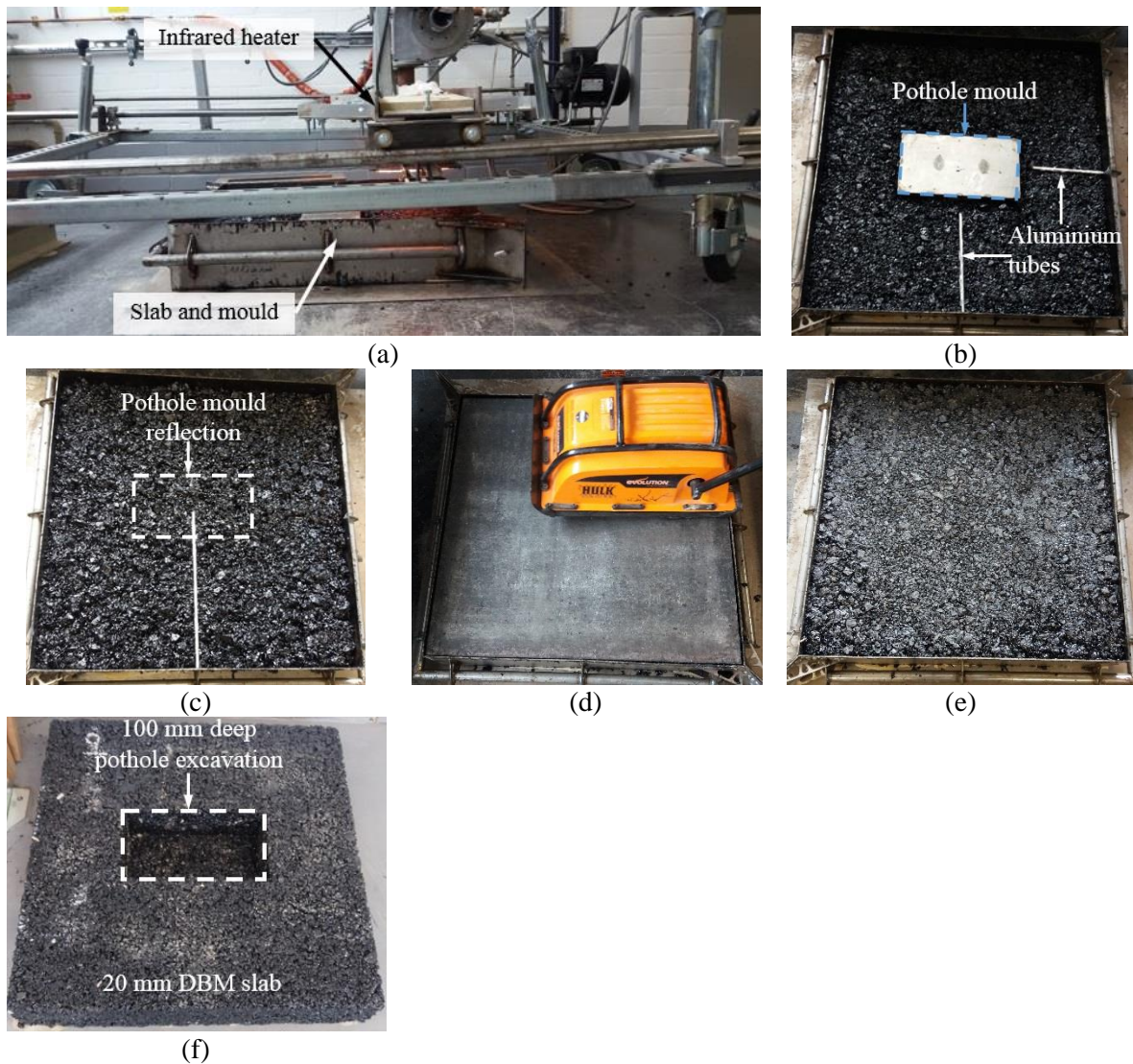
Figure B.6 Slab with 100 mm deep pothole excavation and embedded aluminium tubes to accommodate thermocouples for thermal tests of Chapter 4 – Preparation and compaction of third lift: (a) pre-heating of compacted second lift shown in Figure B.5(f); (b) 2 aluminium tubes above the compacted second lift; (c) 3 asphalt batches poured and 1 aluminium tube put above the batches; (c) following 3 batches poured and final aluminium tube put above the batches; (d) compaction of 6 batches; (e) compacted third lift; (f) constructed slab turned upside down and pothole mould removed after 19 h of construction

Appendix C

Thermophysical properties of 20 mm DBM slabs described in Chapter 4

Table C.1 Thermophysical properties of asphalt mixture of slab S1 with 45 mm deep pothole excavation

Core no.	Core diameter (mm)	Core height (mm)	Air voids content (%)	Thermal conductivity (W/m K)	Specific heat capacity (J/kg K)	Thermal diffusivity ($\times 10^{-7}$) (m²/s)
1	72	100	10.38	1.12	865.44	5.85
2	72	100	9.99	0.99	865.44	5.13
3	72	100	10.13	1.03	865.44	5.37
4	72	100	10.38	1.29	865.44	6.73
5	72	55	9.34	1.18	865.44	6.11
		Average	**10.04**	**1.12**	**865.44**	**5.84**

Table C.2 Thermophysical properties of asphalt mixture of slab S2 with 45 mm deep pothole excavation

Core no.	Core diameter (mm)	Core height (mm)	Air voids content (%)	Thermal conductivity (W/m K)	Specific heat capacity (J/kg K)	Thermal diffusivity ($\times 10^{-7}$) (m²/s)
6	72	100	10.94	0.96	865.44	5.05
7	72	100	10.71	1.25	865.44	6.57
8	72	100	10.47	0.97	865.44	5.05
9	72	100	9.92	1.02	865.44	5.31
10	72	55	11.70	1.06	865.44	5.63
		Average	**10.51**	**1.05**	**865.44**	**5.52**

Table C.3 Thermophysical properties of asphalt mixture of slab S3 with 45 mm deep pothole excavation

Core no.	Core diameter (mm)	Core height (mm)	Air voids content (%)	Thermal conductivity (W/m K)	Specific heat capacity (J/kg K)	Thermal diffusivity ($\times 10^{-7}$) (m²/s)
11	72	100	12.11	1.02	865.44	5.42
12	72	100	12.17	1.10	865.44	5.89
13	72	100	12.46	0.91	865.44	4.87
14	72	100	11.48	0.92	865.44	4.89
15	72	100	11.83	1.10	865.44	5.87
16	72	100	12.13	0.93	865.44	4.96
17	72	100	12.08	0.90	865.44	4.81
18	72	55	11.62	0.93	865.44	4.94
		Average	**11.99**	**0.98**	**865.44**	**5.20**

Table C.4 Thermophysical properties of asphalt mixture of slab S4 with 45 mm deep pothole excavation

Core no.	Core diameter (mm)	Core height (mm)	Air voids content (%)	Thermal conductivity (W/m K)	Specific heat capacity (J/kg K)	Thermal diffusivity ($\times 10^{-7}$) (m²/s)
19	72	100	11.83	1.11	865.44	5.87
20	72	100	11.26	1.05	865.44	5.54
21	72	100	11.10	1.11	865.44	5.84
22	72	100	10.09	1.08	865.44	5.62
23	72	100	11.36	1.02	865.44	5.37
24	72	100	11.63	1.06	865.44	5.63
25	72	100	11.04	1.16	865.44	6.13
26	72	55	11.14	1.19	865.44	6.28
		Average	**11.18**	**1.10**	**865.44**	**5.78**

Table C.5 Thermophysical properties of asphalt mixture of slab S5 with 75 mm deep pothole excavation

Core no.	Core diameter (mm)	Core height (mm)	Air voids content (%)	Thermal conductivity (W/m K)	Specific heat capacity (J/kg K)	Thermal diffusivity (×10⁻⁷) (m²/s)
27	72	140	12.45	1.12	865.44	5.97
28	72	140	12.64	0.97	865.44	5.21
29	72	140	11.53	1.22	865.44	6.45
30	72	140	12.44	1.32	865.44	7.05
31	72	140	12.08	1.22	865.44	6.50
32	72	140	15.41	1.33	865.44	7.36
33	72	65	15.00	1.45	865.44	8.01
34	72	65	13.09	1.34	865.44	7.20
		Average	**13.08**	**1.24**	**865.44**	**6.72**

Table C.6 Thermophysical properties of asphalt mixture of slab S6 with 75 mm deep pothole excavation

Core no.	Core diameter (mm)	Core height (mm)	Air voids content (%)	Thermal conductivity (W/m K)	Specific heat capacity (J/kg K)	Thermal diffusivity (×10⁻⁷) (m²/s)
35	72	140	11.70	1.31	865.44	6.96
36	72	140	12.90	0.84	865.44	4.52
37	72	140	12.23	0.96	865.44	5.11
38	72	140	11.98	1.00	865.44	5.31
39	72	140	11.22	1.22	865.44	6.42
40	72	140	6.56	1.23	865.44	6.16
41	72	65	14.06	1.27	865.44	6.93
42	72	65	12.55	1.02	865.44	5.46
		Average	**11.52**	**1.11**	**865.44**	**5.86**

Table C.7 Thermophysical properties of asphalt mixture of slab S7 with 75 mm deep pothole excavation

Core no.	Core diameter (mm)	Core height (mm)	Air voids content (%)	Thermal conductivity (W/m K)	Specific heat capacity (J/kg K)	Thermal diffusivity ($\times 10^{-7}$) (m²/s)
43	72	140	10.91	0.87	865.44	4.58
44	72	140	12.37	0.88	865.44	4.68
45	72	140	12.09	1.40	865.44	7.48
46	72	140	11.63	1.17	865.44	6.20
47	72	140	12.90	1.40	865.44	7.52
48	72	140	13.22	0.91	865.44	4.90
49	72	65	12.66	0.98	865.44	5.27
50	72	65	11.29	1.10	865.44	5.79
		Average	**12.25**	**1.09**	**865.44**	**5.80**

Table C.8 Thermophysical properties of asphalt mixture of slab S8 with 75 mm deep pothole excavation

Core no.	Core diameter (mm)	Core height (mm)	Air voids content (%)	Thermal conductivity (W/m K)	Specific heat capacity (J/kg K)	Thermal diffusivity ($\times 10^{-7}$) (m²/s)
51	72	140	9.60	1.13	865.44	5.85
52	72	140	11.23	1.13	865.44	5.94
53	72	140	10.97	1.33	865.44	7.02
54	72	140	11.32	1.31	865.44	6.90
55	72	140	11.62	1.36	865.44	7.19
56	72	140	8.84	1.63	865.44	8.38
57	72	65	12.57	0.83	865.44	4.47
58	72	65	11.84	1.01	865.44	5.38
		Average	**10.88**	**1.22**	**865.44**	**6.39**

Table C.9 Thermophysical properties of asphalt mixture of slab S9 with 100 mm deep pothole excavation

Core no.	Core diameter (mm)	Core height (mm)	Air voids content (%)	Thermal conductivity (W/m K)	Specific heat capacity (J/kg K)	Thermal diffusivity (×10⁻⁷) (m²/s)
59	72	140	9.78	0.98	865.44	5.09
60	72	140	12.36	0.95	865.44	5.09
61	72	140	11.97	0.97	865.44	5.14
62	72	140	11.01	0.99	865.44	5.20
63	72	140	10.09	1.03	865.44	5.37
64	72	140	11.06	0.99	865.44	5.22
65	72	140	9.61	1.05	865.44	5.45
66	72	40	10.02	1.06	865.44	5.52
		Average	**10.74**	**1.00**	**865.44**	**5.26**

Table C.10 Thermophysical properties of asphalt mixture of slab S10 with 100 mm deep pothole excavation

Core no.	Core diameter (mm)	Core height (mm)	Air voids content (%)	Thermal conductivity (W/m K)	Specific heat capacity (J/kg K)	Thermal diffusivity (×10⁻⁷) (m²/s)
67	72	140	10.62	1.10	865.44	5.77
68	72	140	10.22	1.18	865.44	6.17
69	72	140	9.41	1.13	865.44	5.82
70	72	140	11.08	1.17	865.44	6.18
71	72	140	11.38	1.19	865.44	6.27
72	72	140	11.82	1.18	865.44	6.25
73	72	140	10.41	1.20	865.44	6.26
74	72	40	11.34	1.12	865.44	5.94
		Average	**10.79**	**1.16**	**865.44**	**6.08**

Table C.11 Thermophysical properties of asphalt mixture of slab S11 with 100 mm deep pothole excavation

Core no.	Core diameter (mm)	Core height (mm)	Air voids content (%)	Thermal conductivity (W/m K)	Specific heat capacity (J/kg K)	Thermal diffusivity ($\times 10^{-7}$) (m^2/s)
75	72	140	11.19	1.17	865.44	6.16
76	72	140	10.96	1.11	865.44	5.82
77	72	140	10.28	1.29	865.44	6.71
78	72	140	11.15	1.14	865.44	5.99
79	72	140	11.06	1.17	865.44	6.19
80	72	140	10.26	1.13	865.44	5.87
81	72	140	7.50	1.22	865.44	6.19
82	72	40	12.00	1.22	865.44	6.51
		Average	**11.10**	**1.18**	**865.44**	**6.18**

Table C.12 Thermophysical properties of asphalt mixture of slab S12 with 100 mm deep pothole excavation

Core no.	Core diameter (mm)	Core height (mm)	Air voids content (%)	Thermal conductivity (W/m K)	Specific heat capacity (J/kg K)	Thermal diffusivity ($\times 10^{-7}$) (m^2/s)
83	72	140	9.70	1.25	865.44	6.48
84	72	140	10.77	1.28	865.44	6.72
85	72	140	10.13	1.33	865.44	6.92
86	72	140	10.20	1.18	865.44	6.16
87	72	140	10.92	1.23	865.44	6.45
88	72	140	10.29	1.13	865.44	5.88
89	72	140	9.64	1.30	865.44	6.76
90	72	40	10.64	1.06	865.44	5.54
		Average	**10.47**	**1.22**	**865.44**	**6.36**

Appendix D

Thermal conductivity (*k*) at 19 (±1) ºC, 65 (±5) ºC and 80 (±5) ºC for asphalt mixtures described in Chapter 5

Table D.1 Thermal conductivity of 20 mm DBM non-aged specimens

Specimen no.	Repetitions	Thermal conductivity (W/m K)		
		19 ºC	65 ºC	80 ºC
C1	k1	1.448	1.036	0.869
	k2	1.433	1.053	0.875
	k3	1.485	1.097	0.876
	Average	**1.455**	**1.062**	**0.873**
C2	k1	1.334	1.188	0.854
	k2	1.324	1.186	0.858
	k3	1.331	1.175	0.846
	Average	**1.330**	**1.183**	**0.853**
C3	k1	1.938	1.470	1.057
	k2	1.878	1.437	1.061
	k3	1.903	1.484	1.041
	Average	**1.906**	**1.464**	**1.053**
C4	k1	1.742	1.165	0.936
	k2	1.730	1.153	0.904
	k3	1.710	1.165	0.926
	Average	**1.727**	**1.161**	**0.922**
C5	k1	1.889	1.129	0.913
	k2	1.915	1.163	0.935
	k3	1.916	1.135	0.937
	Average	**1.907**	**1.142**	**0.928**

Table D.2 Thermal conductivity of 20 mm DBM short-term aged specimens

Specimen no.	Repetitions	Thermal conductivity (W/m K)		
		19 ºC	65 ºC	80 ºC
C6	k1	1.659	0.911	0.583
	k2	1.598	0.914	0.728
	k3	1.615	0.919	0.698
	Average	**1.624**	**0.915**	**0.753**
C7	k1	1.682	0.966	0.811
	k2	1.693	0.998	0.925
	k3	1.716	1.026	0.917
	Average	**1.697**	**0.997**	**0.884**
C8	k1	1.404	0.678	0.615
	k2	1.384	0.715	0.674
	k3	1.445	0.703	0.605
	Average	**1.411**	**0.699**	**0.631**
C9	k1	1.956	0.908	0.648
	k2	1.936	0.921	0.772
	k3	1.868	0.953	0.839
	Average	**1.920**	**0.927**	**0.753**
C10	k1	1.756	0.819	0.588
	k2	1.816	0.803	0.596
	k3	1.793	0.801	0.648
	Average	**1.788**	**0.808**	**0.611**

Table D.3 Thermal conductivity of 20 mm DBM long-term aged specimens

Specimen no.	Repetitions	Thermal conductivity (W/m K)		
		19 ºC	65 ºC	80 ºC
C11	k1	1.779	1.012	0.571
	k2	1.756	1.013	0.600
	k3	1.747	1.023	0.613
	Average	**1.761**	**1.016**	**0.595**
C12	k1	1.565	0.821	0.367
	k2	1.551	0.859	0.367
	k3	1.566	0.813	0.362
	Average	**1.561**	**0.831**	**0.365**
C13	k1	1.538	0.824	0.489
	k2	1.565	0.828	0.530
	k3	1.589	0.836	0.532
	Average	**1.564**	**0.829**	**0.517**
C14	k1	1.624	0.827	0.424
	k2	1.628	0.820	0.435
	k3	1.627	0.820	0.449
	Average	**1.626**	**0.822**	**0.436**
C15	k1	1.597	0.854	0.395
	k2	1.567	0.869	0.393
	k3	1.583	0.897	0.389
	Average	**1.582**	**0.873**	**0.392**

Table D.4 Thermal conductivity of AC-14 non-aged specimens

Specimen no.	Repetitions	Thermal conductivity (W/m K)		
		19 ºC	65 ºC	80 ºC
C16	k1	1.425	1.315	1.056
	k2	1.447	1.356	0.988
	k3	1.409	1.347	0.944
	Average	**1.427**	**1.339**	**0.996**
C17	k1	1.419	1.262	0.807
	k2	1.416	1.311	0.832
	k3	1.392	1.287	0.824
	Average	**1.409**	**1.287**	**0.821**
C18	k1	1.754	1.265	0.942
	k2	1.737	1.265	0.949
	k3	1.754	1.321	0.940
	Average	**1.748**	**1.284**	**0.944**
C19	k1	1.138	0.712	0.561
	k2	1.127	0.675	0.560
	k3	1.140	0.709	0.556
	Average	**1.135**	**0.699**	**0.559**
C20	k1	1.183	1.034	0.825
	k2	1.181	1.063	0.835
	k3	1.188	1.025	0.845
	Average	**1.184**	**1.041**	**0.835**

Table D.5 Thermal conductivity of AC-14 short-term aged specimens

Specimen no.	Repetitions	Thermal conductivity (W/m K)		
		19 ºC	65 ºC	80 ºC
C21	k1	1.991	1.026	0.791
	k2	1.934	1.098	0.890
	k3	1.988	1.099	0.913
	Average	**1.971**	**1.074**	**0.865**
C22	k1	1.866	1.079	0.826
	k2	1.777	1.119	0.925
	k3	1.818	1.166	0.991
	Average	**1.820**	**1.121**	**0.914**
C23	k1	1.740	1.017	0.875
	k2	1.741	1.091	0.910
	k3	1.772	1.120	0.910
	Average	**1.751**	**1.076**	**0.898**
C24	k1	1.866	0.808	1.017
	k2	1.871	0.905	0.931
	k3	1.875	0.912	0.978
	Average	**1.871**	**0.875**	**0.975**
C25	k1	1.896	0.795	0.640
	k2	1.885	0.811	0.766
	k3	1.878	0.831	0.760
	Average	**1.886**	**0.812**	**0.722**

Table D.6 Thermal conductivity of AC-14 long-term aged specimens

Specimen no.	Repetitions	Thermal conductivity (W/m K)		
		19 ºC	65 ºC	80 ºC
C26	k1	1.711	1.006	0.822
	k2	1.628	1.095	0.839
	k3	1.703	1.063	0.826
	Average	**1.681**	**1.055**	**0.829**
C27	k1	1.825	1.174	0.770
	k2	1.853	1.170	0.805
	k3	1.894	1.180	0.872
	Average	**1.857**	**1.175**	**0.816**
C28	k1	1.751	1.057	0.874
	k2	1.743	1.027	0.869
	k3	1.719	1.039	0.832
	Average	**1.738**	**1.041**	**0.858**
C29	k1	1.816	0.968	0.685
	k2	1.833	0.984	0.705
	k3	1.848	1.004	0.718
	Average	**1.832**	**0.985**	**0.703**
C30	k1	1.958	1.127	0.776
	k2	1.929	1.132	0.873
	k3	2.023	1.160	0.872
	Average	**1.970**	**1.140**	**0.840**

Table D.7 Thermal conductivity of AC-6 non-aged specimens

Specimen no.	Repetitions	Thermal conductivity (W/m K)		
		19 ºC	65 ºC	80 ºC
C31	k1	1.478	1.220	1.008
	k2	1.458	1.260	1.018
	k3	1.480	1.243	1.074
	Average	**1.472**	**1.241**	**1.033**
C32	k1	1.335	1.123	0.890
	k2	1.357	1.116	0.905
	k3	1.345	1.124	0.892
	Average	**1.346**	**1.121**	**0.896**
C33	k1	1.346	1.110	0.838
	k2	1.356	1.103	0.842
	k3	1.352	1.121	0.829
	Average	**1.351**	**1.111**	**0.836**
C34	k1	1.612	1.304	0.931
	k2	1.630	1.276	0.957
	k3	1.633	1.307	1.002
	Average	**1.625**	**1.296**	**0.963**
C35	k1	1.503	1.224	0.923
	k2	1.502	1.282	0.925
	k3	1.505	1.260	0.962
	Average	**1.503**	**1.255**	**0.937**

Table D.8 Thermal conductivity of AC-6 short-term aged specimens

Specimen no.	Repetitions	Thermal conductivity (W/m K)		
		19 ºC	65 ºC	80 ºC
C36	k1	1.644	0.733	0.805
	k2	1.700	0.786	0.863
	k3	1.665	0.817	0.897
	Average	**1.670**	**0.779**	**0.855**
C37	k1	1.895	1.030	0.827
	k2	1.839	1.041	0.827
	k3	1.915	1.112	0.824
	Average	**1.883**	**1.061**	**0.826**
C38	k1	1.707	0.686	0.672
	k2	1.751	0.765	0.768
	k3	1.765	0.780	0.756
	Average	**1.741**	**0.744**	**0.732**
C39	k1	1.646	0.755	0.800
	k2	1.659	0.802	0.849
	k3	1.687	0.807	0.800
	Average	**1.664**	**0.788**	**0.816**
C40	k1	1.735	0.758	0.832
	k2	1.755	0.818	0.806
	k3	1.732	0.817	0.814
	Average	**1.741**	**0.798**	**0.817**

Table D.9 Thermal conductivity of AC-6 long-term aged specimens

Specimen no.	Repetitions	Thermal conductivity (W/m K)		
		19 ºC	65 ºC	80 ºC
C41	k1	1.510	0.882	0.624
	k2	1.550	0.894	0.620
	k3	1.503	0.927	0.643
	Average	**1.521**	**0.901**	**0.629**
C42	k1	1.673	0.905	0.709
	k2	1.682	1.038	0.708
	k3	1.663	1.000	0.719
	Average	**1.673**	**0.981**	**0.712**
C43	k1	1.566	0.942	0.736
	k2	1.609	0.985	0.722
	k3	1.586	0.963	0.703
	Average	**1.587**	**0.963**	**0.720**
C44	k1	1.684	1.077	0.737
	k2	1.730	1.016	0.731
	k3	1.780	1.018	0.720
	Average	**1.731**	**1.037**	**0.729**
C45	k1	1.611	0.923	0.663
	k2	1.640	0.913	0.678
	k3	1.641	0.952	0.699
	Average	**1.631**	**0.929**	**0.680**

Appendix E

Thermocouple locations per slab for slabs S13-S24 described in Chapter 6

Table E.1 Post-compaction thermocouple locations in the pothole excavation of static repairs

		Pothole A - Thermocouple no.																
		T1			T2			T3			T4			T5			T6		
Coordinates (mm)		x	y	z	x	y	z	x	y	z	x	y	z	x	y	z	x	y	z
	Slab no.																		
Vertical repair interfaces	S13	200	30	175	200	25	90	300	31	90	400	31	90	505	25	90	505	24	180
	S14	200	30	180	200	30	90	305	30	90	410	26	90	505	23	90	505	27	180
	S15	200	27	180	200	21	90	305	33	90	410	28	90	505	25	90	505	25	178
	S16	200	25	175	210	26	90	305	26	90	405	29	90	505	23	90	505	25	175
	S17	200	32	180	210	28	90	300	33	90	405	32	90	505	25	90	505	23	171
	S18	200	32	180	200	29	90	310	30	90	408	30	90	505	30	90	-	-	-
		T7			T8			T9			T10			T11					
Bottom repair interface	S19	200	45	90	245	45	175	353	45	175	463	45	175	505	45	90			
	S20	200	45	90	255	45	175	355	45	175	460	45	175	505	45	90			
	S21	200	45	90	245	45	175	345	45	175	450	45	175	505	45	90			
	S22	200	45	90	255	45	175	350	45	175	454	45	175	505	45	90			
	S23	200	45	90	250	45	175	355	45	175	461	45	175	505	45	90			
	S24	200	45	90	240	45	175	310	45	175	450	45	175	505	45	90			

Table E.2 Post-compaction thermocouple locations in the pothole excavation of dynamic repairs

		Pothole B - Thermocouple no.																
		T1			T2			T3			T4			T5			T6		
Coordinates (mm)		x	y	z	x	y	z	x	y	z	x	y	z	x	y	z	x	y	z
	Slab no.																		
Vertical repair interfaces	S13	505	30	520	505	25	605	405	36	605	310	30	605	200	35	605	200	30	520
	S14	505	22	523	505	30	605	400	30	605	295	26	605	200	22	605	200	19	520
	S15	505	19	520	505	26	605	400	29	605	295	25	605	200	24	605	200	30	527
	S16	505	25	515	505	25	605	400	27	605	300	30	605	200	26	605	200	25	515
	S17	505	30	515	505	25	605	405	37	605	300	32	605	200	20	605	200	30	514
	S18	505	32	515	505	30	605	403	32	605	298	30	605	200	30	605	200	30	520
		T7			T8			T9			T10			T11					
Bottom repair interface	S19	505	45	605	505	45	520	355	45	520	246	45	520	200	45	605			
	S20	505	45	605	505	45	520	350	45	520	245	45	520	200	45	605			
	S21	505	45	605	505	45	520	345	45	520	255	45	520	200	45	605			
	S22	505	45	595	505	45	520	355	45	520	260	45	520	200	45	595			
	S23	505	45	605	505	45	520	349	45	520	250	45	520	200	45	605			
	S24	505	45	605	505	45	520	350	45	520	250	45	520	200	45	605			

Appendix F

Thermophysical properties of 20 mm DBM slabs and 6 mm AC repairs described in Chapter 6

Table F.1 Air voids content, thermal diffusivity (*a*) and specific heat capacity (*c$_P$*) of asphalt mixture of slab S13 and its corresponding repairs

Core no.	Core diameter (mm)	Core height (mm)	Air voids content (%)	Thermal diffusivity ($\times 10^{-7}$) (m^2/s)	Specific heat capacity (J/kg K)
Slab					
1	72	100	11.98	5.21	865.44
2	72	100	12.92	5.61	865.44
3	72	100	12.42	5.60	865.44
4	72	100	12.70	5.72	865.44
5	72	100	13.04	5.85	865.44
6	72	100	12.43	5.61	865.44
7	72	100	12.89	5.79	865.44
8	72	100	12.45	5.92	865.44
9	72	100	12.60	5.86	865.44
		Average	**12.61**	**5.68**	**865.44**
Static repair					
16	72	55	6.02	8.42	899.46
17	72	55	6.52	7.77	899.46
18	72	55	7.55	7.15	899.46
		Average	**6.70**	**7.78**	**899.46**
Dynamic repair					
19	72	55	5.33	7.74	899.46
20	72	55	6.98	7.99	899.46
21	72	55	5.27	7.96	899.46
		Average	**5.86**	**7.90**	**899.46**

Table F.2 Air voids content and thermal diffusivity (*a*) and specific heat capacity (*c*$_P$) of asphalt mixture of slab S14 and its corresponding repairs

Core no.	Core diameter (mm)	Core height (mm)	Air voids content (%)	Thermal diffusivity ($\times 10^{-7}$) (m^2/s)	Specific heat capacity (J/kg K)
Slab					
22	72	100	12.57	5.13	865.44
23	72	100	13.59	5.49	865.44
24	72	100	12.94	5.13	865.44
25	72	100	12.88	5.98	865.44
26	72	100	12.33	6.16	865.44
27	72	100	13.11	6.42	865.44
28	72	100	12.70	5.56	865.44
29	72	100	17.66	5.39	865.44
30	72	100	11.72	5.62	865.44
		Average	**13.28**	**5.66**	**865.44**
Static repair					
37	72	55	4.98	8.33	899.46
38	72	55	3.16	7.50	899.46
39	72	55	4.80	6.94	899.46
		Average	**4.31**	**7.59**	**899.46**
Dynamic repair					
40	72	55	4.02	7.63	899.46
41	72	55	3.77	7.72	899.46
42	72	55	4.16	7.86	899.46
		Average	**3.98**	**7.74**	**899.46**

Table F.3 Air voids content and thermal diffusivity (*a*) and specific heat capacity (*c_P*) of asphalt mixture of slab S15 and its corresponding repairs

Core no.	Core diameter (mm)	Core height (mm)	Air voids content (%)	Thermal diffusivity ($\times 10^{-7}$) (m^2/s)	Specific heat capacity (J/kg K)
Slab					
43	72	100	12.74	4.75	865.44
44	72	100	13.25	5.10	865.44
45	72	100	13.55	5.44	865.44
46	72	100	13.22	4.96	865.44
47	72	100	11.27	4.79	865.44
48	72	100	13.25	4.83	865.44
49	72	100	13.63	3.86	865.44
50	72	100	13.84	4.22	865.44
51	72	100	13.91	4.57	865.44
		Average	**13.18**	**4.73**	**865.44**
Static repair					
58	72	55	2.84	7.44	899.46
59	72	55	2.77	7.40	899.46
60	72	55	3.11	7.38	899.46
		Average	**2.91**	**7.41**	**899.46**
Dynamic repair					
61	72	55	3.76	7.97	899.46
62	72	55	2.69	7.78	899.46
63	72	55	4.23	7.80	899.46
		Average	**3.56**	**7.85**	**899.46**

Table F.4 Air voids content, thermal diffusivity (*a*) of asphalt mixture and specific heat capacity (*c_P*) of slab S16 and its corresponding repairs

Core no.	Core diameter (mm)	Core height (mm)	Air voids content (%)	Thermal diffusivity ($\times 10^{-7}$) (m²/s)	Specific heat capacity (J/kg K)
Slab					
64	72	100	14.02	6.21	865.44
65	72	100	13.52	6.06	865.44
66	72	100	11.87	5.83	865.44
67	72	100	14.03	4.77	865.44
68	72	100	12.57	4.74	865.44
69	72	100	13.50	4.84	865.44
70	72	100	13.99	4.43	865.44
71	72	100	12.27	4.51	865.44
72	72	100	13.30	4.73	865.44
		Average	**13.23**	**5.13**	**865.44**
Static repair					
79	72	55	4.99	7.71	899.46
80	72	55	4.22	7.94	899.46
81	72	55	4.04	8.21	899.46
		Average	**4.41**	**7.95**	**899.46**
Dynamic repair					
82	72	55	4.66	8.28	899.46
83	72	55	4.32	7.83	899.46
84	72	55	5.70	7.52	899.46
		Average	**4.89**	**7.88**	**899.46**

Table F.5 Air voids content and thermal diffusivity (*a*) and specific heat capacity (*c*P) of asphalt mixture of slab S17 and its corresponding repairs

Core no.	Core diameter (mm)	Core height (mm)	Air voids content (%)	Thermal diffusivity ($\times 10^{-7}$) (m²/s)	Specific heat capacity (J/kg K)
Slab					
85	72	100	13.01	4.76	865.44
86	72	100	12.59	5.04	865.44
87	72	100	11.94	5.31	865.44
88	72	100	13.72	5.82	865.44
89	72	100	13.46	6.07	865.44
90	72	100	13.55	6.08	865.44
91	72	100	14.03	5.65	865.44
92	72	100	12.50	5.83	865.44
93	72	100	12.47	6.10	865.44
		Average	**13.03**	**5.63**	**865.44**
Static repair					
100	72	55	4.96	7.42	899.46
101	72	55	4.15	7.34	899.46
102	72	55	4.77	7.37	899.46
		Average	**4.63**	**7.38**	**899.46**
Dynamic repair					
103	72	55	4.70	8.11	899.46
104	72	55	5.01	7.66	899.46
105	72	55	4.91	7.18	899.46
		Average	**4.87**	**7.65**	**899.46**

Table F.6 Air voids content and thermal diffusivity (*a*) and specific heat capacity (*c_P*) of asphalt mixture of slab S18 and its corresponding repairs

Core no.	Core diameter (mm)	Core height (mm)	Air voids content (%)	Thermal diffusivity ($\times 10^{-7}$) (m²/s)	Specific heat capacity (J/kg K)
Slab					
106	72	100	11.71	4.89	865.44
107	72	100	11.24	5.36	865.44
108	72	100	12.99	5.97	865.44
109	72	100	12.46	6.00	865.44
110	72	100	12.42	6.04	865.44
111	72	100	12.61	6.08	865.44
112	72	100	13.04	5.19	865.44
113	72	100	12.23	5.55	865.44
114	72	100	13.22	6.01	865.44
		Average	**12.43**	**5.68**	**865.44**
Static repair					
121	72	55	4.28	6.99	899.46
122	72	55	3.23	6.93	899.46
123	72	55	4.93	7.07	899.46
		Average	**4.15**	**7.00**	**899.46**
Dynamic repair					
124	72	55	5.68	7.55	899.46
125	72	55	4.99	7.72	899.46
126	72	55	5.20	7.97	899.46
		Average	**5.29**	**7.75**	**899.46**

Table F.7 Thermal conductivity (*k*) of asphalt mixture of slab S13 and its corresponding repairs

Point no.	Thermal conductivity (W/m K)
Slab	
1	0.91
2	1.04
3	1.05
4	1.09
5	1.11
6	1.05
Average	**1.04**
Static repair	
7	1.40
8	1.77
Average	**1.58**
Dynamic repair	
10	1.58
11	1.76
Average	**1.67**

Table F.8 Thermal conductivity (*k*) of asphalt mixture of slab S14 and its corresponding repairs

Point no.	Thermal conductivity (W/m K)
Slab	
12	0.96
13	0.95
14	1.11
15	1.19
16	1.01
17	1.06
Average	**1.05**
Static repair	
18	1.70
19	1.42
Average	**1.56**
Dynamic repair	
20	1.58
21	1.62
Average	**1.60**

Table F.9 Thermal conductivity (*k*) of asphalt mixture of slab S15 and its corresponding repairs

Point no.	Thermal conductivity (W/m K)
Slab	
22	0.89
23	1.00
24	0.92
25	0.90
26	0.71
27	0.84
Average	**0.88**
Static repair	
28	1.55
29	1.54
Average	**1.55**
Dynamic repair	
30	1.65
31	1.61
Average	**1.63**

Table F.10 Thermal conductivity (*k*) of asphalt mixture of slab S16 and its corresponding repairs

Point no.	Thermal conductivity (W/m K)
Slab	
32	1.14
33	1.10
34	0.88
35	0.89
36	0.81
37	0.88
Average	**0.95**
Static repair	
38	1.58
39	1.69
Average	**1.63**
Dynamic repair	
40	1.70
41	1.52
Average	**1.61**

Table F.11 Thermal conductivity (*k*) of asphalt mixture of slab S17 and its corresponding repairs

Point no.	Thermal conductivity (W/m K)
Slab	
42	0.88
43	1.00
44	1.07
45	1.12
46	1.04
47	1.14
Average	**1.04**
Static repair	
48	1.52
49	1.51
Average	**1.51**
Dynamic repair	
50	1.66
51	1.47
Average	**1.56**

Table F.12 Thermal conductivity (*k*) of asphalt mixture of slab S18 and its corresponding repairs

Point no.	Thermal conductivity (W/m K)
Slab	
52	0.92
53	1.11
54	1.12
55	1.13
56	0.96
57	1.11
Average	**1.06**
Static repair	
58	1.44
59	1.45
Average	**1.44**
Dynamic repair	
60	1.53
61	1.62
Average	**1.58**

Table F.13 Thermal conductivity (*k*) of asphalt mixture of slab S19 and its corresponding repairs

Point no.	Thermal conductivity (W/m K)
Slab	
62	1.05
63	0.99
64	0.98
65	1.20
66	1.12
67	1.19
Average	**1.09**
Static repair	
68	1.57
69	1.71
Average	**1.64**
Dynamic repair	
70	1.66
71	1.59
Average	**1.62**

Table F.14 Thermal conductivity (*k*) of asphalt mixture of slab S20 and its corresponding repairs

Point no.	Thermal conductivity (W/m K)
Slab	
72	0.87
73	1.10
74	1.06
75	0.97
76	0.97
77	1.16
Average	**1.02**
Static repair	
78	1.41
79	1.51
Average	**1.46**
Dynamic repair	
80	1.63
81	1.42
Average	**1.52**

Table F.15 Thermal conductivity (*k*) of asphalt mixture of slab S21 and its corresponding repairs

Point no.	Thermal conductivity (W/m K)
82	1.17
83	1.04
84	1.25
85	0.96
86	1.16
87	1.23
Average	**1.13**
88	1.42
89	1.51
Average	**1.46**
90	1.42
91	1.55
Average	**1.49**

Table F.16 Thermal conductivity (*k*) of asphalt mixture of slab S22 and its corresponding repairs

Point no.	Thermal conductivity (W/m K)
Slab	
92	1.23
93	0.86
94	1.10
95	1.21
96	0.96
97	1.04
Average	**1.07**
Static repair	
98	1.73
99	1.67
Average	**1.70**
Dynamic repair	
100	1.77
101	1.64
Average	**1.70**

Table F.17 Thermal conductivity (*k*) of asphalt mixture of slab S23 and its corresponding repairs

Point no.	Thermal conductivity (W/m K)
Slab	
102	1.32
103	1.18
104	1.03
105	1.12
106	0.85
107	1.34
Average	**1.14**
Static repair	
108	1.65
109	1.56
Average	**1.60**
Dynamic repair	
110	1.65
111	1.64
Average	**1.64**

Table F.18 Thermal conductivity (*k*) of asphalt mixture of slab S24 and its corresponding repairs

Point no.	Thermal conductivity (W/m K)
Slab	
112	1.32
113	0.99
114	0.93
115	1.24
116	1.01
117	1.34
Average	**1.14**
Static repair	
118	1.56
119	1.68
Average	**1.62**
Dynamic repair	
120	1.75
121	1.68
Average	**1.71**

Appendix G

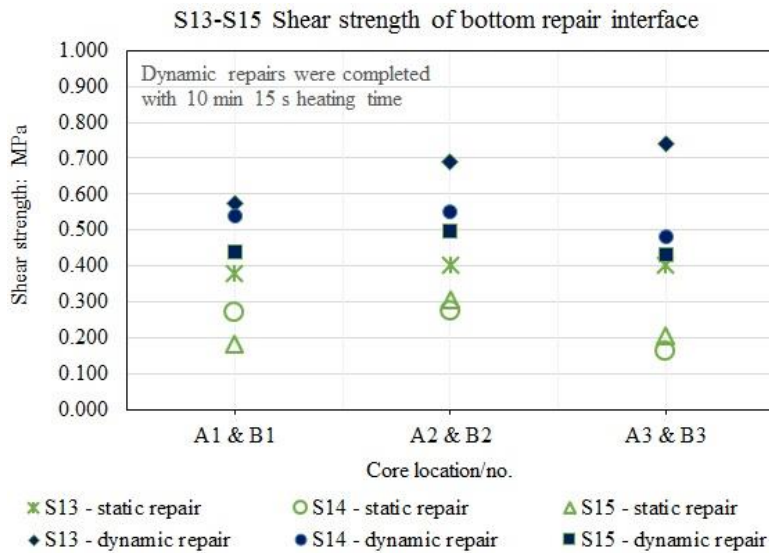**Shear strength tests (SBT's) results for specimens of Chapter 8**

Figure G.1 Bottom interface shear strength for static (A) and dynamic (B) pothole repairs with 10 minutes 15 seconds pre-heating time built in slabs S13-S15
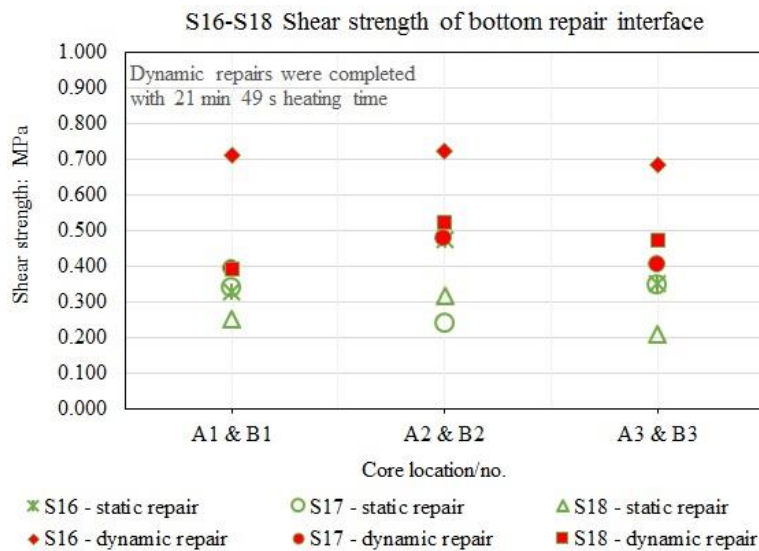

Figure G.2 Bottom interface shear strength for static (A) and dynamic (B) pothole repairs with 21 minutes 49 seconds pre-heating time built in slabs S16-S18
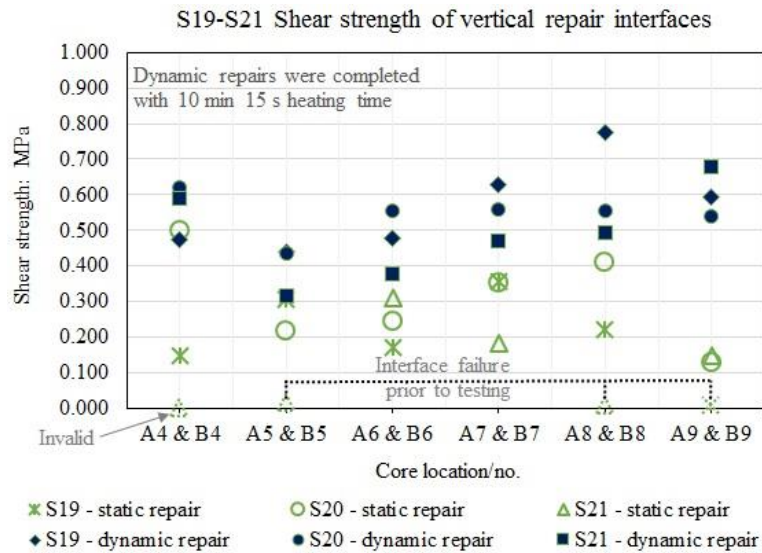
Figure G.3 Vertical interface shear strength for static (A) and dynamic (B) pothole repairs with 10 minutes 15 seconds pre-heating time built in slabs S19-S21
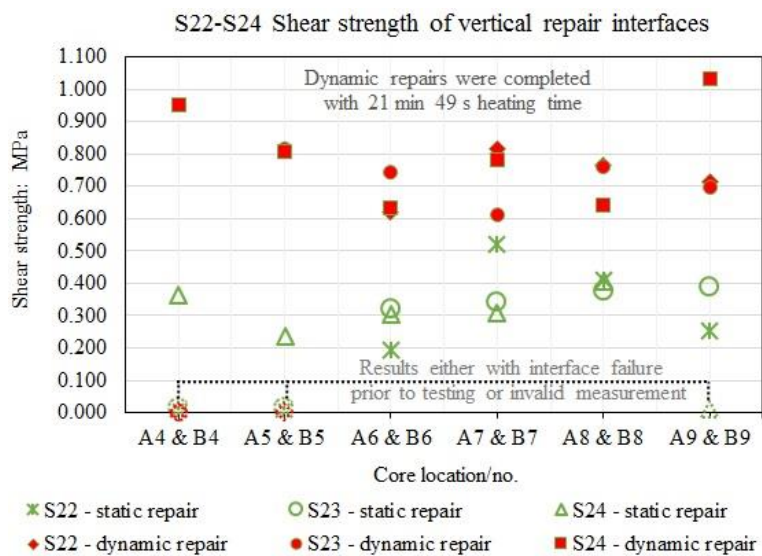

Figure G.4 Vertical interface shear strength for static (A) and dynamic (B) pothole repairs with 21 minutes 49 seconds pre-heating time built in slabs S22-S24

Appendix H

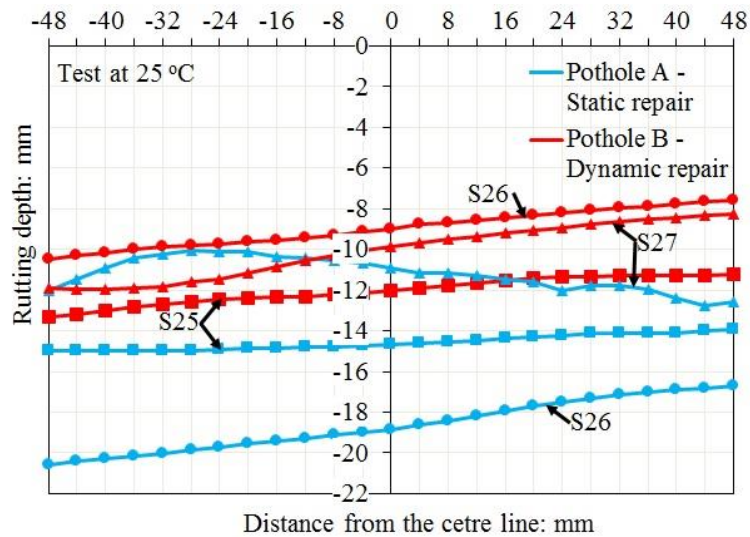Rutting profile of static and dynamic repairs completed in slabs S25-S30 described in Chapter 8

Figure H.1 Longitudinal rutting profile in the repair interface at 25 ºC after 20.000 cycles for repairs built in slabs S25-S27
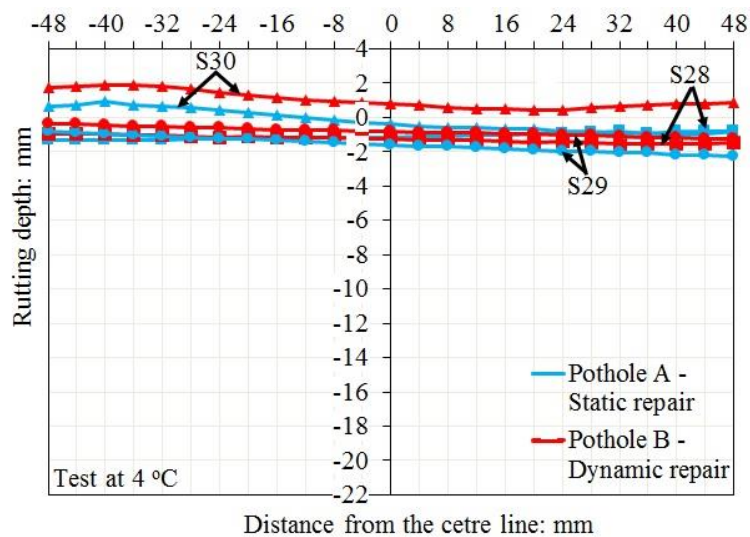

Figure H.2 Longitudinal rutting profile in the repair interface at 4 ºC after 20.000 cycles for repairs built in slabs S28-S30